Development of three-dimensional lithium-ion cells with water-based $Li(Ni_{0.6}Mn_{0.2}Co_{0.2})O_2$ thick-film cathodes using ultrafast laser ablation

Zur Erlangung des akademischen Grades eines
Doktors der Ingenieurwissenschaften (Dr.-Ing.)

von der KIT-Fakultät für Maschinenbau des
Karlsruher Instituts für Technologie (KIT)

genehmigte Dissertation

von

M. Sc. Penghui Zhu

Referent:
Prof. Dr. Wilhelm Pfleging

Korreferentin:
Prof. Dr. Britta Nestler

Tag der Einreichung: 29.07.2024
Tag der mündlichen Prüfung: 24.10.2024

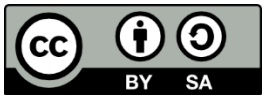

Das Leben ist kurz, und die Wahrheit wirkt fern und lebt lange – sagen wir die Wahrheit.

— Arthur Schopenhauer

Dedicated to all those who love and support me

Penghui Zhu
Karlsruher Institut für Technologie – KIT
Institut für Angewandte Materialien – Angewandte Werkstoffphysik – IAM-AWP
Laserprozesstechnik
Hermann-von-Helmholtz-Platz 1
D-76344 Eggenstein-Leopoldshafen

Tel.: +49-(0)721-608-28557
Fax: +49-(0)721-608-28557
E-Mail: penghui.zhu@kit.edu

Contents

Acknowledgment

First of all, I would like to express my deep gratitude to Prof. Dr. Wilhelm Pfleging for his valuable and constructive suggestions, as well as patient guidance and enthusiastic encouragement during the planning and development of my research work. Besides, I would also like to acknowledge Prof. Dr. Britta Nestler for accepting to be the co-referee and her valuable comments on my thesis. Special thank is given to Mrs. Alexandra Meyer for her extraordinary cooperation during the project works as well as a lot of discussion on different experiments and data analyses, as well as a lot of support in my personal life. Besides, I would like to express my special thanks to Dr. Yijing Zheng and Dr. Peter Smyrek for their invaluable support and precious experiences in slurry mixing, coating, cell assembly, and characterization which helped me a lot during my research. My sincere thanks are extended to Mr. Heino Besser and Mr. Marek Kapitz for their solid support in laser processing as well as the assembly and adjustment of optics, scan heads, and lasers. With their help all the experiments with laser were accomplished in time. In addition, I would also like to thank Mrs. Alexandra Reif for her generous support in SEM and metallographic labs, without her there would not have been so many beautiful SEM images. Furthermore, Mr. Yannic Sterzl and Mr. Ulrich Rist are also acknowledged for their help in electrochemical characterization and data processing, as well as their previous experience in anode slurry mixing and fruitful discussions. Besides, I sincerely appreciate the IT-support from Mr. Marco Klotz and precious help in software installations. Then I would also like to thank all other laser group members for their support and a comfortable team atmosphere.

My thanks are also extended to Dr. Werner Bauer, Dr. Ulrike Kaufmann for their invaluable help in providing the equipment and materials for aqueous slurry mixing, with their experiences and advice I was able to save a lot of time and avoid many mistakes. In addition, Dr. Thomas Bergfeldt is acknowledged for his help in chemical analyses, and Mrs. Vanessa Trouillet and Mr. Stefan Heißler are great acknowledged for their support in material characterization.

Finally, I would like to thank my dearest partner Ms. Sarah Sophia Keßler for her companionship and the most precious spiritual comfort as well as interesting discussions and correction during the writing of my PhD thesis. Furthermore, my deepest gratitude is given to my parents for their support and encouragement through my life, without which I would not have been able to achieve what I have now. 谢谢爸妈一直以来对我的支持和信任，感谢你们这么多年默默无闻的付出和关心，你们永远是我最坚强的后盾和温暖的港湾[1].

[1]Translation: Thank you my parent for your support and trust in me all along, and for your dedication and care over the years, you will always be my strongest support and warm harbor.

Abstract

Lithium-ion batteries have become the most crucial energy storage devices in recent years. However, it remains a great challenge to achieve high energy density while maintaining high power density. One practical method to increase energy density is to fabricate electrodes with high mass loading. In this work, $Li(Ni_{0.6}Mn_{0.2}Co_{0.2})O_2$ (NMC 622) was used as active materials, while cathodes with film thicknesses ranging from 70 to 200 µm were prepared using the state-of-the-art polyvinylidene fluoride (PVDF) binder. The cathodes were assembled in half-cells vs. lithium (Li) and electrochemically characterized using rate capability analyses, which showed a severe capacity drop for cells with thick-film electrodes when they were discharged less than 30 min. In order to compensate the capacity loss by fast charging in less than one hour, ultrafast laser ablation was applied to generate three-dimensional (3D) structures in electrodes. Line structures with pitches varying from 200 to 100 µm and hole structures with 200 µm pitch were generated for cathodes with a thickness of 150 µm to compare their performance with unstructured electrodes.

In order to evaluate the effect of particle morphology on the electrochemical performance, polycrystalline NMC 622 powder particles with different size distribution were applied for the fabrication of bilayer NMC 622 cathodes with hierarchical structures using PVDF binder and bilayer coating technique. Two NMC 622 powders with different secondary particle sizes were characterized by X-ray diffraction (XRD), laser scattering, and Brunauer-Emmet-Teller (BET) surface area analysis. In addition, reference electrodes were made with just one type of powder or with a mechanical mixture of two powders. The total film thicknesses of the different types of composite electrodes were kept constant at 150 µm, while the thickness and the position of individual layer were varied. To investigate the effect of different electrode configurations on electrochemical performance, cyclic voltammetry, rate capability analyses, lifetime analyses, and electrochemical impedance spectroscopy were conducted. In addition, laser structuring was subsequently applied on different types of electrodes to further enhance their electrochemical performance.

Conventional cathode manufacturing involves high processing costs and environmental issues due to the use of PVDF binder and the toxic solvent N-Methyl-2-pyrrolidone (NMP). In order to overcome these drawbacks, aqueous processing of thick-film NMC 622 cathodes was studied using Sodium-carboxymethyl cellulose (Na-CMC) and fluorine acrylic hybrid latex as binders. However, the reaction of cathode materials with water leads to Li leaching and a slurry pH value larger than 12. This results in chemical corrosion of aluminum (Al) current collector during coating process, leaving cavities in the dried electrodes. Acetic acid (AA) has been used in the slurry containing $Li(Ni_{0.33}Mn_{0.33}Co_{0.33})O_2$ (NMC 111) in published work and showed no negative impact on the active material. Therefore, it was added during the NMC 622 slurry mixing process to adjust the pH values between 7.4 to 12.1. Chemical corrosion of Al current collector induced by alkaline slurry was observed for slurry pH values larger than 10, and the corrosion was more severe with increasing film thickness due to longer drying time. Cyclic voltammetry analyses showed that the addition of acetic acid had no effect on the redox reaction of NMC 622 during charging and discharging, while rate capability analyses revealed that the discharge capacity decreased with a higher amount of added acid when the cells were

discharged in less than five hours. Therefore, the slurry pH values of aqueous processed NMC 622 slurries should be adjusted to 9 – 10 to acquire optimal results.

In the next stage of development, three different acids (acetic acid, citric acid, and phosphoric acid) were applied during the mixing process to adjust slurry pH value. AA was used in the previous step to determine the optimal pH range, while citric acid (CA) and phosphoric acid (PA) were applied in order to increase the electrode film adhesion to the current collector due to their cross-linking effect with CMC binder. In addition, PA might also protect NMC 622 particles by providing a coating on the surface of powder particles. X-ray photoelectron spectroscopy and Raman spectroscopy were applied to characterize the thick-film electrodes. Afterwards, 3D structures were generated in aqueous processed thick-film electrodes by ultrafast laser ablation. Rate capability analyses, cycle lifetime analyses, electrochemical impedance spectroscopy, and cyclic voltammetry were conducted to evaluate the electrochemical performance of cells with different types of cathodes. Rate capability and lifetime analyses revealed that the cells containing laser structured thick-film electrodes (3D electrodes) with PA addition outperformed the state-of-the-art (“reference cells") with PVDF as binder. In order to further enhance the performance of cells with 3D electrodes, different laser structuring strategies (with / without offset between laser scans) were applied to the electrodes with addition of PA during slurry preparation. These laser structured cathodes were afterwards assembled in pouch cells vs. graphite anodes. Rate capability analyses of pouch cells (“full-cells") were consistent to the previous results with coin cells (“half-cells”). Moreover, the pouch cells containing electrodes, in which the PA was added during the mixing process, exhibited extraordinary performance, exceeding the reference cells after 300 cycles and maintain 20 % more capacity after 500 cycles. In addition, the end-of-life of pouch cells containing 3D electrodes with PA addition during aqueous processing was extended by a factor of 3 to 4.3 in contrast to the reference cells containing unstructured electrodes with PVDF as binder.

Finally, the upscaling of the laser structuring process was discussed and the ablation depth and width using different laser repetition rates, pulse distance, and multi-beam processing were determined. The laser structuring time of a NMC 622 cathode with a film thickness of 100 µm can be reduced by 97.7 % by combining high power laser (with an average laser power of 400 W) with a 1 × 5 beam splitter (single beam to 5 beamlets) in comparison to the process with single laser beam with low laser power less than 10 W.

.

Kurzzusammenfassung

Lithium-Ionen-Batterien haben sich in den letzten Jahren zu dem wichtigsten Energiespeichersystem für viele Anwendungen wie z.B. Elektromobilität und elektronische Geräte entwickelt. Jedoch ist es immer noch eine große technologische Herausforderung, eine hohe Energiedichte zu erreichen und gleichzeitig eine hohe Leistungsdichte beizubehalten. Eine praktische Methode zur Erhöhung der Energiedichte ist die Herstellung von Elektroden mit hoher Massenbeladung. In dieser Arbeit wurde $Li(Ni_{0,6}Mn_{0,2}Co_{0,2})O_2$ (NMC 622) als Aktivmaterial für Kathoden verwendet, während Elektroden mit Schichtdicken von 70 bis 200 µm unter Verwendung des Polyvinylidenfluorid (PVDF)-Binders hergestellt wurden. Die Kathoden wurden in Halbzellen gegen Lithium (Li) verbaut und elektrochemisch mithilfe der Analyse der Hochstromfähigkeit charakterisiert. Ein starker Kapazitätsabfall wird beobachtet bei Zellen mit Dickschichtelektroden, wenn sie in weniger als 30 Minuten entladen wurden. Um einem Kapazitätsverlust infolge sich ausbildender Zellpolarisationen durch schnelles Laden (weniger als eine Stunde) entgegenzuwirken, wurde eine Laserstrukturierung mit einem Ultrakurzpulslaser zur Erzeugung von 3D Elektrodenstrukturen durchgeführt. Linienstrukturen mit Abständen von 200 bis 100 µm und Lochstrukturen mit 200 µm Abstand wurden für Kathoden mit einer Dicke von 150 µm verwendet, um ihre Leistungsfähigkeit in Knopfzellen mit denen bei Verwendung unstrukturierter Elektroden zu vergleichen.

Um die Auswirkungen der Partikelmorphologie auf die elektrochemische Performance zu bewerten, kamen polykristalline NMC 622-Pulver mit zwei verschiedenen Partikelgrößen für die Herstellung von zweischichtigen NMC 622-Kathoden mit hierarchischen Strukturen unter Einsatz von PVDF-Bindemittel und Mehrfachbeschichtungstechnik zur Anwendung. Die Charakterisierung der beiden NMC 622-Pulver erfolgte durch Röntgendiffraktion, Laserstreuung, und Brunauer-Emmet-Teller (BET)-Oberflächenanalyse. Referenzelektroden wurden mit einem Pulvertyp oder mit zwei mechanisch zusammengemischten Pulvern hergestellt. Die Gesamtschichtdicke der unterschiedlichen Arten von Kompositelektroden wurde konstant bei 150 µm gehalten, während die Dicke und die Position der einzelnen Schichten variiert wurden. Um die Auswirkungen der verschiedenen Elektrodenkonfigurationen auf die elektrochemische Leistung zu untersuchen, wurden Zyklovoltammetrie, Ratenanalyse, Lebensdaueranalyse und elektrochemische Impedanz-spektroskopie durchgeführt. Anschließend wurden verschiedene Elektrodentypen mit Laserstrahlen strukturiert, um die Leistungsfähigkeit der Zellen weiter zu steigern.

Die konventionelle Herstellung von Kathoden ist aufgrund der Verwendung von PVDF-Bindermittel und des giftigen Lösungsmittels N-Methyl-2-Pyrrolidon (NMP) mit hohen Verarbeitungskosten verbunden. Um diese Nachteile zu überwinden, wurde die wässrige Verarbeitung von Dickschichtkathoden aus NMC 622 mit Natrium-Carboxymethylcellulose (Na-CMC) und Fluor-Acryl-Hybridlatex als Bindemittel untersucht. Die Reaktion der Kathodenmaterialien mit Wasser führt jedoch zu einer Herauslösung des Lithiums aus dem Aktivmaterial und im Schlicker zu einem Ansteigen des pH-Wertes auf über 12. Dies führt zu einer chemischen Korrosion (Wasserstoffgasbildung) an der Aluminium(Al)-Stromableiter-oberfläche während des Beschichtungsprozesses und hinterlässt schließlich Kavitäten in den

getrockneten Elektrodenschichten. In der veröffentlichten Arbeit wurde Essigsäure (AA) im $Li(Ni_{0,33}Mn_{0,33}Co_{0,33})O_2$ NMC 111 Schlicker verwendet und dies zeigte keinen negativen Einfluss auf das Aktivmaterial. Daher wurde diese Säure während des Mischvorgangs zur Herstellung des Schlickers hinzugefügt, um im Schlicker einen pH-Wert zwischen 7,4 und 12,1 einstellen zu können. Die Korrosion des Al-Stromableiters erfolgte durch Kontakt mit dem alkalischen Schlicker, sofern dieser pH-Werte oberhalb von 10 aufwies. Die Dauer des Korrosionsprozesses beeinflusst maßgeblich die Kavitätsdichte und Größe der Kavitäten in den getrockneten Elektroden. Die Dauer der Korrosion wiederrum nimmt mit zunehmender Schichtdicke aufgrund der längeren Trocknungszeit zu. Die Zyklovoltammetrie-Analysen zeigten, dass die Zugabe von Essigsäure keinen Einfluss auf die Redoxreaktion von NMC 622 während des Ladens und Entladens hatte, während die Ratenanalyse darauf hinwies, dass die spezifische Entladekapazität mit einem höheren Säureanteil abnahm, wenn die Zellen in weniger als fünf Stunden entladen wurden. Der optimale pH-Wert des wässrig verarbeiteten NMC 622-Schlickers sollte daher bei 9 bis 10 liegen.

Im darauffolgenden Schritt wurden während des Mischvorgangs zur Herstellung des Kathodenschlickers drei verschiedene Säuren zugegeben, um den pH-Wert des Schlickers gezielt einzustellen. Bei den Säuren handelte es sich um Essigsäure, Zitronensäure (CA) und Phosphorsäure (PA). Essigsäure wurde im vorangegangenen Schritt verwendet, um den optimalen pH-Bereich zu ermitteln, während Zitronensäure und Phosphorsäure eingesetzt wurden, um die Schichthaftung der Elektroden am Stromableiter aufgrund der Vernetzungswirkung mit dem Na-CMC-Binder zu erhöhen. Darüber hinaus könnte PA auch die NMC 622-Partikel schützen, indem sie eine Beschichtung auf der Oberfläche der Pulverpartikel bildet. Röntgen-Photoelektronenspektroskopie und Raman-Spektroskopie wurden zur Charakterisierung der Dickschichtelektroden eingesetzt. Anschließend wurden 3D-Strukturen in den ursprünglich wässrig verarbeiteten Dickschichtelektroden mithilfe des lasergestützten Materialabtrages erzeugt. Um die elektrochemische Performance von Zellen mit verschiedenen Kathodentypen zu bewerten und untereinander vergleichen zu können, wurden Hochstromfähigkeitsanalysen, Zyklenfestigkeitsanalysen, elektrochemische Impedanzspektroskopie und Zyklovoltammetrie durchgeführt. Die Hochstromfähigkeitsanalysen und die Bestimmung der Zyklenfestigkeit zeigten, dass die Performance der Zellen mit laserstrukturierten Dickschichtelektroden (3D-Elektroden), die mit phosphorsäurehaltigem Schlicker hergestellt wurden, die Leistungsfähigkeit der Referenzzellen, deren Elektroden mit PVDF-Binder hergestellt wurden, übertrafen. Um die elektrochemische Performance der 3D-Elektroden weiter zu steigern, wurden verschiedene Laserstrukturierungsstrategien angewandt und die laserstrukturierten Kathoden, die über Phosphorsäurezugabe im Schlicker hergestellt wurden, wurden in Pouchzellen („Vollzellen“) gegen Graphitanoden verbaut. Die Ergebnisse der Hochstromfähigkeitsanalysen stimmten mit denen von Knopfzellen („Halbzellen“) überein. Darüber hinaus zeigen die Pouchzellen mit Elektroden, bei denen die PA während des Mischvorgangs zugegeben wurde, eine außergewöhnliche Steigerung der Performance, die die der Referenzzellen nach 300 Zyklen übertrafen und nach 500 Zyklen 20 % mehr Kapazität aufwiesen. Außerdem verlängerte sich die Zyklenlebensdauer der Pouchzellen, die 3D-Elektroden mit PA-Zugabe während der

wässrigen Schlickerverarbeitung enthielten, um den Faktor 3 bis 4,3, im Vergliech zu Referenzzellen mit unstrukturierten Elektroden und PVDF als Binder.

Im Hinblick auf eine Überführung der entwickelten Technologie in eine mögliche Batteriefertigung wurde abschließend die Hochskalierung des Laserstrukturierungsprozesses diskutiert und bewertet. Hierzu wird die Abtragungstiefe und -breite unter Verwendung verschiedener Laserrepetitionsraten, Pulsabstand und unter Einsatz eines Mehrstrahlabtragsprozesses bestimmt. Die Prozesszeit der Laserstrukturierung einer NMC 622 Kathode mit einer Schichtdicke von 100 µm konnte im Vergleich zu dem Verfahren mit einem einzelnen Laserstrahl mit einer Laserleistung von weniger als 10 W durch die Kombination eines Hochleistungslasers mit einer mittleren Laserleistung von 400 W und der Mehrstrahltechnologie (Einzelstrahl auf 5 Strahlen) um 97,7 % reduziert werden.

List of abbreviations and formal symbols

Abbreviation	Description
3D	Three-dimensional
AA	Acetic acid
AC	Alternating current
Al	Aluminum
BeT	Beam expanding telescope
BET	Brunauer-Emmett-Teller
BEV	Battery electric vehicles
BSE	Back-scattered electrons
CA	Citric acid
CC	Constant current
CCCV	Constant current-constant voltage
CE	Coulombic efficiency
CEI	Cathode electrolyte interphase
Co	Cobalt
CPE	Constant phase element
Cu	Copper
DMC	Dimethyl carbonate
DoD	Depth of discharge
DPSS	Diode-pumped solid-state
DS	Degree of substitution
DSC	Differential scanning calorimetry
EC	Ethylene carbonate
EDX	Energy dispersive X-ray spectroscopy
EMC	Ethyl methyl carbonate

EoL	End-of-life
FEC	Fluoroethylene carbonate
FWHM	Full-width-at-half-maximum
GITT	Galvanostatic intermittent titration technique
HAZ	Heat affected zone
HCl	Hydrochloric acid
HEV	Hybrid electric vehicles
HOMO	Highest occupied molecular orbital
ICP-AES	Inductively coupled plasma – atomic emission spectroscopy
ICP-OES	Inductively coupled plasma – optical emission spectroscopy
IEP	Isoelectric point
IR	Infrared
KIT	Karlsruhe Institute of Technology
LFP	$LiFePO_4$
Li	Lithium
LIB	Lithium-ion battery
LIBS	Laser-induced breakdown spectroscopy
LiPAA	Lithium polyacrylic acid
$LiPF_6$	Lithium hexafluorophosphate
LMO	$LiMn_2O_4$
LNMO	$LiNi_{0.5}Mn_{1.5}O_4$
LNO	$LiNiO_2$
LTO	$Li_4Ti_5O_{12}$
LUMO	Lowest unoccupied molecular orbital
MCMB	Mesocarbon microbead
Mn	Manganese
NA	Numerical aperture

Na-CMC	Sodium-carboxymethyl cellulose
NaOH	Sodium hydroxide
NG	Natural graphite
Ni	Nickel
NMC	$Li(Ni_xMn_yCo_{1-x-y})O_2$
NMC 111	$Li(Ni_{1/3}Mn_{1/3}Co_{1/3})O_2$
NMC 532	$Li(Ni_{0.5}Mn_{0.3}Co_{0.2})O_2$
NMC 622	$Li(Ni_{0.6}Mn_{0.2}Co_{0.2})O_2$
NMC 811	$Li(Ni_{0.8}Mn_{0.1}Co_{0.1})O_2$
NMR	Nuclear resonance spectroscopy
ODH	Oxygen dumbbell hopping
OEMS	Online electrochemical mass spectrometry
PA	Phosphoric acid
PC	Propylene carbonate
PE	Polyethylene
PITT	Potentiostatic intermittent titration technique
PP	Polypropylene
PTFE	Polytetrafluoroethylene
PVDF	Polyvinylidene fluoride
R	Resistor
RF	Radio frequency
R2R	Roll-to-roll
SE	Secondary electrons
SEI	Solid electrolyte interphase
SEM	Scanning electron microscope
SG	Synthetic graphite
SOC	State-of-charge
SOH	State-of-health

TEM	Transmission electron microscopy
TGA	Thermal gravimetric analysis
TM	Transition metal
TSH	Tetrahedral site hopping
UV	Ultraviolet
VC	Vinylene carbonate
Yb:YAG	Ytterbium-doped yttrium aluminum garnet
W	Warburg element
XPS	X-ray photoelectron spectroscopy
XRD	X-ray diffraction

Formal symbol	Unit	Description
A_e	cm^2	Footprint area of an electrode
A_{foot}	cm^2	Footprint area of a pouch cell
A_m	m^2/g	Electrode area per unit mass
A_R	-	Aspect ratio
C	-	BET constant
C_0	mol/cm^3	Total amount of Li-ions in a lithiated NMC 622 particle
C_{dl}	mF	Double-layer capacitance
C_{SEI}	mF	Solid electrolyte interphase capacitance
C_Q	mAh/g	Specific capacity of the active material
C_{theo}	mAh/g	Theoretical capacity of an electrode active material
D	nm	Grain size
D_{ab}	cm	Ablation depth in material
D_{eff}	cm^2/s	Effective diffusion coefficient of Li-ions in composite electrode
$D_{eff,EIS}$	cm^2/s	Effective diffusion coefficient of Li-ions in composite electrode derived from the electrochemical impedance spectroscopy
D50	µm	50 % of the particles have diameters below this value
D90	µm	90 % of the particles have diameters below this value
$\widetilde{D}$	cm^2/s	Diffusion coefficient of Li-ions in the host lattice
E	J	Energy

E_B	eV	Binding energy of an electron attracted to a nucleus
E_g	eV	Potential window of the electrolyte
E_{pulse}	J	Laser pulse energy
ED_g	Wh/kg	Gravimetric energy density of a cell
ED_v	Wh/l	Volumetric energy density of a cell
F	As/mol	Faraday constant
I	A	Current
$I(\omega)$	A	Response current at the frequency of ω
$I_{1C, cal}$	A	Calibrated current at 1C[2]
I_{cell}	A	Currently applied cell current
$I_{C/20, original}$	A	Primarily applied current at C/20[2]
I_{nC}	A	Applied current at nC[3]
I_m	A	Maximum current in an AC circuit
I_p	A	Peak current in CV analysis
L	µm	Particle size
M	g/mol	Molecular weight
M_i	g/mol	Molecular weight of element i
M_{total}	g/cm^2	Total weight of the composite electrode per unit area
M^2	-	Laser beam quality factor
N_{AV}	mol^{-1}	Avogadro number
P	mbar	Pressure

[2]The definition of nC (C-rate) can be found in page XX
[3]The definition of nC (C-rate) can be found in page XX

P_0	mbar	Saturation pressure of an adsorbate at the temperature of adsorption
P_{ele}	%	Electrode porosity
P_L	W	Average laser power
PD_g	W/kg	Gravimetric power density of a cell
PD_v	W/l	Volumetric power density of a cell
Q_{cell}	Ah	Cell capacity of a cell
Q(t)	Ah	Cell capacity at time t
Q_0	Ah	Discharge capacity of the first cycle
Q_{charge}	Ah	Charge capacity
$Q_{discharge}$	Ah	Discharge capacity
Q_{max}	Ah	Maximal cell capacity
Q_n	Ah	Discharge capacity of the n^{th} cycle
Q_{nom}	Ah	Nominal capacity of a cell
R	J/K·mol	Gas constant
R_{ct}	Ω	Charge transfer resistance
R_e	Ω	Bulk resistance
R_{SEI}	Ω	Solid electrolyte interphase (SEI) resistance
S_{BET}	m^2/g	BET surface
S_{total}	m^2	Total surface area of the measured powder
T	K	Temperature
U	V	Cell voltage
U_{OC}	V	Open circuit voltage

$U(\omega)$	V	Applied alternating voltage with a frequency of ω
U_m	V	Maximum voltage in an AC circuit
V_{ads}	m^3	Adsorbed volume
V_{cell}	cm^3	Volume of a cell
$V_{channel}$	cm^3	Volume of a single channel
$V_{channels}$	cm^3	Total volume of channels in a laser structured electrode
V_m	mmol/g	Volume of adsorbed monolayer gas
V_{total}	cm^3	Total volume of a composite electrode without current collector
W	Ω	Warburg resistance
Y_{dl}	$Fs^{\varphi-1}$	CPE capacitance of double-layer
Y_{SEI}	$Fs^{\varphi-1}$	CPE capacitance of SEI
$Z(\omega)$	Ω	The resistance of a cell in an AC circuit
Z_{re}	Ω	The real part of the resistance of a cell in an AC circuit
b	µm	FWHM of channel structures in a laser structured electrode
c_i	-	Mass ratio of component i in the composite electrode
c_p	J/g·K	Specific heat capacity at constant pressure
c_s	mol/cm^3	The concentration of lithium-ion in the active material
$c_{s,max}$	mol/cm^3	The maximum concentration of lithium-ion which can be stored in the active material
d	mm	Laser beam diameter

d_e	mm	Diameter of the incident laser beam
d_f	µm	Laser beam diameter at the focal plane
d_L	mm	Laser beam diameter on the objective lens
f	mm	Focal length of the lens
f_{rep}	kHz	Laser repetition rate
h	µm	Film thickness of electrode without current collector
h_{Al}	µm	Film thickness of the aluminum foil
h_{Ano}	µm	Film thickness of an anode
$h_{bot.ca}$	µm	Thickness of the bottom case for coin cell CR2032
h_{Cat}	µm	Film thickness of a cathode
h_{Cu}	µm	Film thickness of the copper foil
h_{cell}	µm	Thickness of a sealed coin cell
h_{doc}	mm	Doctor blade gap
h_{elect}	µm	Total thickness of an electrode (including current collector)
h_{Li}	µm	Thickness of the lithium foil
h_{Sep}	µm	Thickness of the separator
h_{spacer}	µm	Thickness of the spacer used in coin cells
h_{spring}	µm	Thickness of the spring used in coin cells
$h_{up.ca}$	µm	Thickness of the upper case for coin cell CR2032
i_{in}	A/cm^2	Current density in the cell with porous electrode
i_0	A/cm^2	Exchange current density

k_0	cm/s	Reaction rate
m_0	g	Total mass of unstructured electrode
m_{act}	g	Mass of active material in electrode
m_{Al}	g	Mass of Al foil
$m_{Al, LS}$	g	Mass of an Al foil with drilling holes
m_{Ano}	g	Mass of anode
m_{Cat}	g	Mass of cathode
m_{Cell}	g	Mass of a cell
m_{Cu}	g	Mass of Cu foil
m_{Elect}	g	Mass of electrolyte
m_i	%	Mass fraction of component i in a composite electrode
m_{LS}	g	Total mass of a laser structured electrode
m_{powder}	g	Mass of powder
m_{Sep}	kg	Mass of separator
n_e	-	Number of electrons
nC	1/h	C-rate, used to indicate the applied current or the charge / discharge time in 1/n hour(s)
$n_{channels}$	-	Total number of laser generated channels in an electrode per unit area
q	As	Elementary charge
s	m^2	Cross-section of the adsorbate
t	s	Time
t_{actual}	h	Actual discharge time

v	mm/s	Coating speed
v_{ads}	m^3/mol	Molar volume of the adsorbate
v_s	mm/s	Laser scan speed
x_i	%	Mole fraction of element i in a chemical formula
$z_{R,e}$	mm	Rayleigh length of the incident laser beam
ΔE_p	V	Voltage difference of the redox couple in CV analysis
Δx	mm	Displacement of a spring under compression
$\Delta\mu$	eV	Chemical potential difference between cathode and anode
Θ_e	°	Divergence of incident laser beam
K	-	Scherrer constant
Φ	J/cm^2	Laser peak fluence
Φ_{th}	J/cm^2	Threshold laser fluence for ablation
α	cm^2/s	Thermal diffusivity
α_a	-	Anodic transfer coefficient
α_c	-	Cathodic transfer coefficient
β	rad	FWHM of a reflex in XRD analysis
$\dot{\gamma}$	s^{-1}	Shear rate
δ	cm	Penetration depth of a laser beam in a material
η	V	Overpotential of a cell
θ	°	Position of a reflex
κ	W/cm·K	Thermal conductivity
λ	nm	Laser wavelength

μ_A	eV	Chemical potential of anode
μ_C	eV	Chemical potential of cathode
ν	mV/s	Applied scan rate in CV analysis
ρ	g/cm^3	Density
σ_w	$\Omega \cdot s^{-1/2}$	Warburg impedance coefficient
τ	s	Laser pulse duration
τ_c	s	Characteristic diffusion time
φ	degree	Phase shift between voltage and current in an AC circuit
φ_{SEI}	-	CPE parameter for SEI capacitance
φ_{dl}	-	CPE parameter for double-layer capacitance
ω	Hz	Frequency of an alternating current (or voltage) circuit
ω_0	µm	Beam radius at the beam waist

1. Introduction

Energy has been and will always be a vital topic in history and development of humanity. How to store and reuse energy and enhance the efficiency of energy usage is of significant importance for the progress of humankind and the improvement of our living standards. With the boom of electronic devices since the middle of 20th century, electrochemical energy storage systems, which are also known as batteries, have become an essential part of our daily lives. The performance of microprocessors has approximately doubled every 1.5 years according to Moore's law, while the electrical efficiency of computing (the number of computations conducted per kilowatt-hour) also doubled within the same time span [1, 2], which leads to the rapid development of cell phones, laptops, and other portable devices in the last decades. This has led to an increasing demand for batteries. Among various types of batteries, rechargeable lithium(Li)-ion batteries (LIBs) have received the most attention and have been powering stationary grids, portable devices, and electric power tools [3, 4].

In December 2019, the European Commission declared the "European Green Deal", which aims to achieve carbon neutrality by 2050 [5], meaning that no net emissions of greenhouse gases are expected by then. Measures such as applying renewable energy (e.g. solar energy, hydrogen fuel, offshore wind energy, and ocean energy) and improving energy efficiency will effectively contribute to the reduction of CO_2 emission. Besides, due to the increasingly strict CO_2-exhaust regulations, the automobile industry is seeking to find an alternative and sustainable solution for mobility. Many of them have been committed to developing hybrid electric vehicles (HEV) and battery electric vehicles (BEV). The development of BEV has led to a rapid expansion of the Li-ion battery market. However, a major barrier for BEV compared to conventional vehicles with internal combustion engines is the range of a single charge. After fully charged, the most BEV can travel from 200 to 600 km [6], which is lower than a fully fueled conventional automobile (generally 600 – 1200 km). In addition to travel range anxiety, high prices and insufficient charging infrastructure may also be major concerns limiting the market penetration of BEV [7, 8]. For example, Habla et al. [9] reported that the BEV usage in both privately held and shared vehicles is significantly lower than that in conventional diesel and gasoline vehicles in Germany due to above reasons. Meanwhile, further battery development and innovation are required to achieve batteries with high power density, high volumetric energy density, rapid chargeability, longer calendar life, while lowering the costs simultaneously.

High power density could be achieved by using thin- or ultrathin-film electrodes, whereas the energy density at cell level would be significantly reduced due to a high ratio of inactive components / active components inside the battery. To increase energy density of battery at material level, electrode materials with high specific energy density could be applied, while at cell level, high energy density can be achieved by using thick-film electrodes with thicknesses larger than 100 µm. Besides, less inactive material leads to a cost reduction of batteries. However, an increasing film thickness leads to technical issues during electrode manufacturing, such as peeling of electrodes, crack formation during drying and rewinding, and a significantly longer drying time. For roll-to-roll (R2R) processes, thick-film electrodes can be achieved by

multiple coating with thin-film electrodes (multilayer approach), since each coating requires only the already existing technology and equipment. However, increasing the film thickness results in severe capacity fade in battery due to limited Li-ion diffusion kinetics, especially at high power operations. In order to counteract the trade-off between energy and power density of cells containing thick-film cathodes, three-dimensional (3D) architectures are introduced into the electrode manufacturing, which can be realized by applying ultrafast laser ablation. Comparing to conventional mechanical techniques, laser materials processing has many advantages, such as non-contact, high precision, flexible processing, and it requires no subsequent processing steps. Besides, laser processing with a pulse duration in femtosecond (fs) range can sublimate the electrode materials directly, thereby reducing the heat affected zone, and no phase modifications in active materials could take place.

Aqueous processing of cathodes using water-soluble binders is another method to reduce the battery costs and achieve environmentally friendly electrode manufacturing by replacing the state-of-the-art polyvinylidene fluoride (PVDF) binder. On the one hand, the cost of water-soluble binder such as sodium-carboxymethyl cellulose (Na-CMC) is only 1/5 of the cost of PVDF binder, while the price of water is only about 1/150 in comparison to N-methyl-2-pyrrolidone (NMP), which is the solvent for PVDF [10]. On the other hand, the drying of aqueous processed electrode slurry is 4.5 times faster than those with NMP as solvent and consumes 10 times less energy [11]. However, reaction between active materials with water and chemical corrosion between slurry and aluminum current collector result in high porosity and inhomogeneous coating after drying process. This leads to a decrease in energy density and counteracts the benefit of applying thick-film electrode to increase energy density. Therefore, these problems need to be solved before switching from state-of-the-art PVDF binder to water-based binders.

2. Aim of the work

The primary main aim of the present work is the transfer of 3D concept to the $Li(Ni_{0.6}Mn_{0.2}Co_{0.2})O_2$ (NMC 622) cathodes. Laser ablation has been applied to generate 3D architectures in electrodes containing different active materials for LIBs, such as $LiMn_2O_4$ (LMO) [12, 13], $LiCoO_2$ [14], $Li(Ni_{1/3}Mn_{1/3}Co_{1/3})O_2$ (NMC 111) [13], $LiFePO_4$ [15, 16], and graphite [17-19], but it had not been used on NMC 622 cathodes prior to this thesis. Another important aspect is to identify the correlation between electrode architectures and their electrochemical performances. For the electrode architectures, NMC 622 cathodes with different film thicknesses (mass loading), particle sizes, dual layers with different particle size distributions, and electrodes with different 3D topography generated by laser ablation (different patterns or laser parameters), were prepared. Different methods were applied to characterize their electrochemical performances, such as rate capability and lifetime analyses, electrochemical impedance spectroscopy (EIS), and cyclic voltammetry (CV). The conducted experiments and analytics are presented in Figure 2-1.

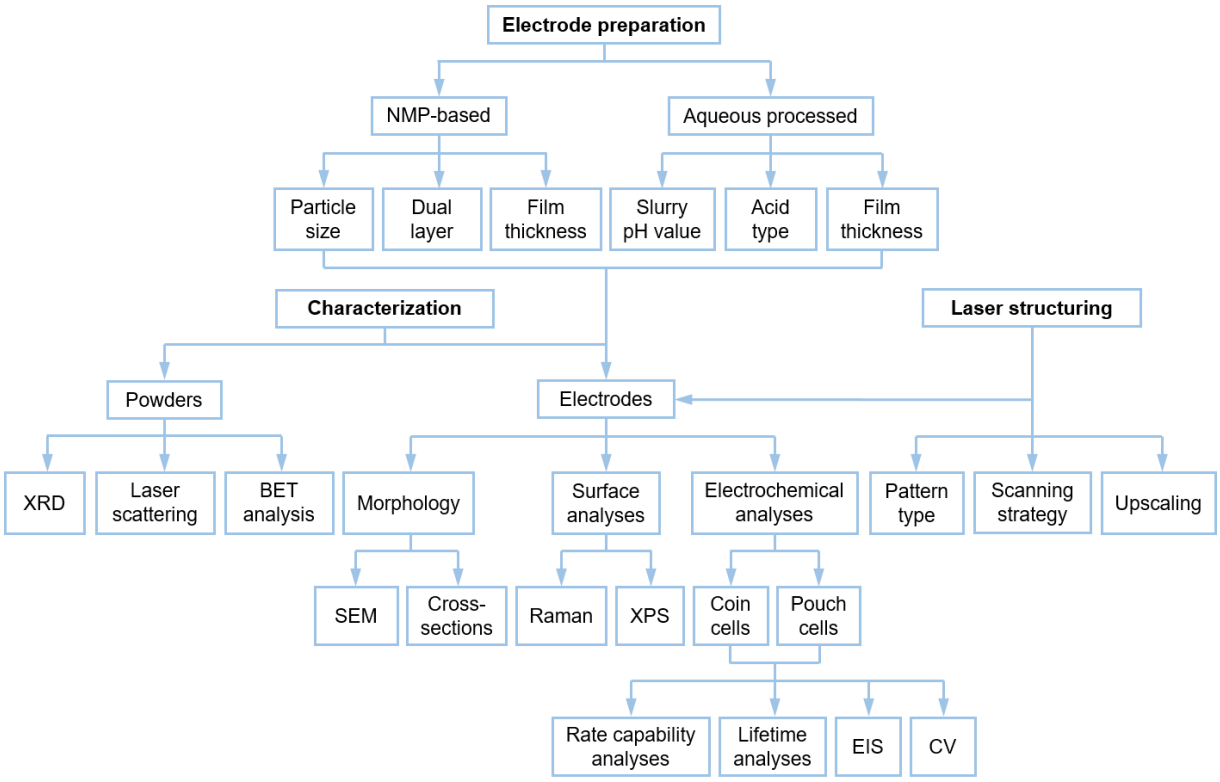

Figure 2-1. The series of experiments and analytics was carried out in accordance with the flow chart.

The film thicknesses of NMC 622 electrodes were increased by a factor of 2 to 3 compared to standard commercial electrodes with thicknesses of 65 to 80 µm [20]. Increasing the film thickness of electrodes can lower the cost at battery-pack level, since less inactive materials such as current collector foils and separators will be used [21]. However, severe capacity decrease was observed for the cells containing NMC 111 electrodes with thicknesses greater than 200 µm when the discharged rate exceeded three hours, resulting in even lower energy density in comparison to those containing thin-film electrodes with a film thickness of 70 µm

[22]. Similar trends were also observed for cells containing $LiNi_{0.8}Co_{0.15}Al_{0.05}O_2$ (NCA) [23] and NMC 622 [24] cathodes when discharged for less than one hour. This is attributed to the increasing cell polarization and a more pronounced effect of the Li-ion diffusion in the electrolyte of cells with thick-film electrodes in comparison to those with thin-film electrodes [24]. In order to counteract this drawback, laser structuring was applied to generate 3D architectures in the thick-film electrodes, which means that part of the electrode materials was removed by laser ablation. Line structures in electrodes using ultrafast laser ablation can accelerate the wettability of electrodes with liquid electrolyte [13], while line or hole structures are able to enhance the electrochemical performances such as capacity retention, high rate capability, cycle stability, and battery lifetime [16, 17, 19]. Therefore, line and hole patterns were chosen for the laser structuring of NMC 622 cathodes with different film thicknesses to study the impact of structuring patterns and mass loading on the rate capability of cells. Furthermore, different laser parameters and pitch of line structures were employed on thick-film NMC 622 cathodes in order to evaluate the possible surface layer modification of the electrode materials interacting with the laser radiation and their impact on the electrochemical performance.

In addition, in order to optimize the energy density of cells with thick-film electrodes for high power applications, the composite NMC 622 electrodes were tuned by using NMC 622 powders with two different particle sizes. In other words, hierarchical architectures in electrodes with bilayer containing NMC 622 powders with two different particle sizes were generated by applying dual-step coating. This is due to that a higher rate capability was observed with decreasing particle size while the cycling stability was enhanced for electrodes with larger particle size [25]. The NMC 622 cathodes with hierarchical architectures were afterwards laser structured and electrochemically characterized in order to investigate the correlation between hierarchical structures with 3D architectures and their electrochemical performance. Besides, the thickness ratio as well as position of each layer were varied in order to investigate their influence on the cell performance and to compare the experimental results with the existing simulation results [26], and to find the optimal electrode configuration.

The second main aim is the development of water-based NMC 622 systems with special consideration of the impact of the acids used on the slurry (viscosity, pH value) and active materials. Current cathode manufacturing in battery industries involves the use of PVDF binder and N-methyl-2-pyrrolidone (NMP) solvent. However, the price of water-soluble binders and water are significantly lower in contrast to PVDF binder and its solvent NMP [10], thus the aqueous processing of NMC 622 cathodes using water-soluble binders is a promising method to reduce the cost. Nevertheless, the reaction between NMC 622 and water leads to an increase in slurry pH value (> 12) [27] and thus results in chemical corrosion of the aluminum (Al) current collector during coating process [28], giving rise to hydrogen gas evolution and subsequently the existence of cavities inside dried electrodes. In order to solve this problem, the modification of NMC 622 slurry pH value was performed in this thesis during the mixing process by adding acid. In previous literatures, acetic acid was added into the water-based NMC 111 slurry and it was found out that its effect on the active material could be neglected because it is vaporized during the drying step [29]. Thus, this acid was firstly applied for the pH modification of NMC 622 slurry. The slurry viscosity at different pH values was determined,

while the porosity and mass loading as well as the electrochemical properties of the NMC 622 cathodes produced with different slurry pH values were investigated in order to determine the optimal slurry pH range. Besides, the aqueous processed NMC 622 cathodes having a homogenous film thickness and mass loading can ensure a successful subsequent laser structuring without affecting the current collector.

In order to study the impact of acid type on the properties of the NMC 622 electrodes and their electrochemical performance at the cell level, two other promising candidates, citric acid and phosphoric acid, were selected in addition to acetic acid. Citric acid can serve as *in situ* cross-linking agent for Na-CMC chains during the drying process and can increase the mechanical stability of the electrode [30]. Phosphoric acid is another promising pH modifier, since it is able to stabilize the interface between electrolyte and active materials such as Li-rich NMC [31] or $LiNi_{0.5}Mn_{1.5}O_4$ (LNMO) [30] and leads to higher cycling stability. The rheological properties of the slurries with different acid types were studied, while a scanning electron microscopy (SEM) was applied to investigate the possible morphology change of the dried electrodes processed with different acid types during slurry mixing. The possible coating and its species on the surface of NMC 622 particles in the dried electrodes with different acid types were analyzed by X-ray photoelectron spectroscopy (XPS), while the Li-leaching from NMC 622 particles during aqueous processing with addition of different types of acids was characterized by Raman spectroscopy. Besides, these aqueous processed NMC 622 cathodes were assembled in cells and their rate capability, lifetime, and impedance were studied in order to determine the most suitable pH modifier. Afterwards, acid-added NMC 622 cathodes were laser structured and assembled in half-cells and full-cells in order to evaluate the enhancement in electrochemical performance of aqueous processed cathodes in combination with laser structuring compared to those with PVDF-based NMC 622 cathodes. Rate capability, lifetime, as well as impedance growth during the cycling were investigated.

The third aim is to evaluate the laser ablation efficiency with regard to a possible process upscaling. To increase the laser structuring rate and to shorten the laser processing time for thick-film NMC 622 electrodes, different approaches were investigated. On the one hand, the impact of average laser power, laser repetition rate, and laser scan speed on ablation depth and width was investigated to determine appropriate laser parameters for a more efficient laser structuring of thick-film NMC 622 electrodes. On the other hand, in order to significantly increase the efficiency of laser structuring, the possibility of combining a beam splitter with a high power laser was investigated. The average laser power of each beamlet in the multi-beam setup was kept the same as that of the single beam, while the ablation depth and width as well as the areal laser structuring time were investigated.

3. Fundamentals and state-of-the-art of lithium-ion batteries and related laser processing

In this chapter, an overview is given concerning the principles and the current development of batteries, the cathode and anode materials used in LIBs, electrode manufacturing, and the characteristics of batteries, as well as laser processing techniques provided in LIBs.

3.1. Basics of lithium-ion batteries

Lithium-ion batteries are electrochemical energy storage systems consisting of several parallel and / or in series connected individual secondary cells, which provide the portability of storing chemical energy and convert it into electrical energy. The exchange between electric energy and chemical energy is almost complete reversible for those rechargeable cells, which is due to the reversible Li-ions diffusion between anode and cathode during charging and discharging.

LIBs have developed rapidly since its first commercialization more than 30 years ago and are taking over more market due to their high energy density and high power density in comparison to lead-acid, Ni-Cd, and Na- / K-ion batteries [32, 33]. In case of cylindrical cell design, the specific energy (Wh/kg) of LIBs continues to increase by about 6 % per year [34]. However, this still cannot fulfill the need of rapidly increasing electric mobility. The ‘‘generation 3’’-LIBs, which are based on liquid-state electrolyte, should achieve volumetric and gravimetric energy density of 350 – 400 Wh/kg and 750 – 1000 Wh/l, respectively; Besides, they should have a cycle life over 3000 cycles for high capacity applications and over 2000 cycles for high power applications, and most importantly, a cost below 75 €/kWh at pack level by 2030 [35]. With the rapid development of HEV and BEV, the technical requirements for batteries, such as high power, high capacity, fast charging, long calendar life, low cost, and high safety are becoming more significant for the automobile industry [36]. The advancements in LIBs are necessary to enhance the competitiveness of electric vehicles in comparison to conventional automobiles powered by internal combustion engine and thus provide the opportunity of the wide spreading of electric vehicles.

3.1.1. Components of LIBs

Although electrode materials and related cell and battery designs have been subject to major changes to date, the basic components of LIBs have remained the same. An individual lithium-ion cell consists of two electrodes (anode and cathode), current collector, separator, and electrolyte, as shown in Figure 3-1. Electrodes as well as separators are soaked with liquid electrolyte. However, for solid-state-batteries, a so-called solid-state electrolyte substitutes the liquid electrolyte and the separator. All cell components are sealed in an insulated housing; thus, they can be isolated from the external environment.

During charging, Li-ions are transported from the active material in cathodes through the electrolyte, pass the ionic permeable separators, and afterwards intercalate into the active materials in anodes, while simultaneously electrons move from cathodes through an external

circuit to the anodes. Thus, oxidation reaction takes place at cathodes while reduction happens at anode side, and vice versa for the discharging process.

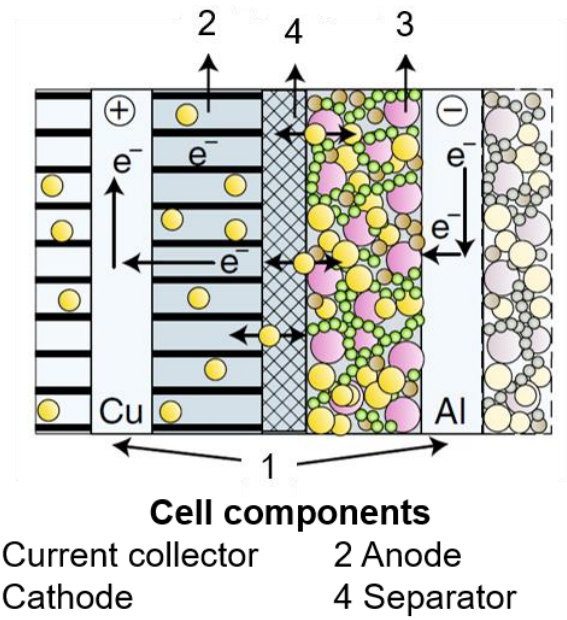

Figure 3-1. Schematic illustration of a lithium-ion cell during charging [37].

Electrodes are porous composite materials, which typically consist of active materials, conductive agents, and binders. Hereby, active materials usually take up over 90 wt% in electrodes and determine the capacity and respective specific energy density of a battery. The crystal structures and the development of active materials for cathodes and anodes will be discussed in detail in chapter 3.1.2 and 3.1.3, respectively.

Conductive agents, also known as conductive carbon or carbon black, are usually applied in electrodes with less than 5 wt% to lower the electrical resistivity of the composite electrodes. The electrochemical performance can be optimized by combining conductive agent with the binder to form conductive pathways that avoid isolation of the active material particles covered by the non-conducting polymer binder [38, 39]. Conductive agents usually have an average primary particle size smaller than 100 nm [40]. During the mixing process of slurry preparation, conductive agents can cover the surface of the active material particles and / or provide point contacts in between of the active material particles. They tend to form aggregates up to several micrometer in size, connected by weak physical forces such as van-der-Waals forces, creating continuous conduction pathways for electrons from the current collector to – in the best case – each individual active material particle [39]. Besides, Hein et al. [41] compared X-ray tomography, symmetric cells and half-cell impedance analyses with simulations using different models, and concluded that the conductive agent and binder domain should be located at the contact points of active material particles rather than being randomly distributed in the pores between the active material particles or on the surface of the active material.

Binders are used to hold the active materials and conductive agents together with the current collector while ensuring the mechanical stability of electrodes, especially the conduction pathways composed of conductive agents. Although binders account for only 2 – 5 wt% in commercial electrodes, they are very crucial for battery performance such as cell

lifetime and rate capability [42]. The state-of-the-art binder applied in the battery industry is PVDF for cathode, while water-soluble binders such as Na-CMC and styrene butadiene rubber (SBR) are widely used for anode manufacturing. In order to achieve cost reduction and environmentally friendly production, further development of cathode preparation using aqueous based binders is a key focus in current research and development [29-31, 43, 44] and will be further illustrated in chapter 3.2.

The liquid electrolyte for LIBs is commonly comprised of conductive salt – lithium hexafluorophosphate ($LiPF_6$), organic solvents such as ethylene carbonate (EC), ethyl methyl carbonate (EMC), diethyl carbonate (DEC), dimethyl carbonate (DMC) [3, 45], and further additives such as fluoroethylene carbonate (FEC) [46, 47] or vinylene carbonate (VC) [48]. $LiPF_6$ can be dissolved in carbonate solution with concentrations ranging from 0.5 to 1.3 mol/l and can provide an ionic conductivity of up to 0.01 S/cm at 25 °C due to the weakly connected and highly fluorinated anions [49]. Besides, PF_6^- anion remains stable for voltages greater than 4 V and is thus commonly applied as conductive salt for LIBs. The use of additives is essential in state-of-the-art batteries [45] due to their effect in forming a homogeneous solid electrolyte interphase (SEI) on the anodes [50], or to stabilize the interphase between active materials and electrolyte under high voltage operation (4.6 V vs. Li / Li^+) [46, 47]. Further additives such as flame retardant additives can be supplemented to the electrolyte to interrupt the self-heating chain reactions caused by electrolyte decomposition and thus prevent thermal runaway [51].

Separators are permeable membranes and physical barriers between positive and negative electrodes with thicknesses ranging from 10 µm to 30 µm. The main task of separators is to prevent short circuits in cells. Separators should be chemically and electrochemically stable, so that they can remain inert during charging and discharging (under strong oxidizing and reducing conditions) without producing impurities in the battery. Besides, separators have a porosity of 40 to 60 % and the pores serve as electrolyte reservoir to ensure low internal resistance and high ionic conductivity [52]. Separators used in the battery industries are generally classified as monolayer, multilayer, and separators modified by ceramic coating, ultraviolet (UV) or electron beam irradiation [52]. The basic framework of the separators is made of polymers such as polypropylene (PP), polyethylene (PE) [53], PVDF [54-56], or poly(methyl methacrylate) (PMMA) [57].

The composite electrodes are deposited onto current collectors, which serve to transfer electrons from cathode to anode through an external circuit. Aluminum is used as current collector for cathodes in LIBs since it is not oxidized at voltages larger than 4 V vs. Li / Li^+ due to the existence of the native oxide layer [58], whereas copper (Cu) is mostly applied as current collector for anode owing to its good electrical conductivity (5.8×10^7 S/m^{-1}) [59] and stability at low potentials (0 to 0.15 V) [60].

3.1.2. Cathode materials

Cathodes, also known as the “positive electrodes” in reference to the discharging process, are usually consisting of lithium transition metal oxides. Within this oxides the transition metal (TM) ion can undergo oxidation and reduction reactions during charging and discharging, respectively [61]. Meanwhile, the host structure of the cathode material should not be essentially changed during Li-ion de- / intercalation and should remain structurally stable at

around 4 V vs. Li / Li^+, which is limited with regard to the stability of the electrolyte [61]. The theoretical capacity (C_{theo} [mAh/g]) of an electrode material is related to the number of reactive electrons and the molar weight of the materials, as described as follows [62]:

$$C_{theo} = \frac{n_e \cdot F}{3.6 \cdot M} \tag{3.1}$$

where n_e [-] is the number of electrons transferred in the redox reaction, F [As/mol] the Faraday constant, M [g/mol] the molar weight of an active material. This equation indicates that more electrons transferred and smaller molecular weight can theoretically lead to higher capacity. However, in practice, only part of the Li-ions will be de- / intercalated from / into the active material in order to maintain the structural stability. In addition, the capacity of an electrode depends not only on the active material, but also on the charging / discharging current density, temperature, and the voltage window (the operating voltage range from lower to upper voltage) [63, 64]. Therefore, the practical capacity of an electrode material is usually lower than its theoretical capacity.

Cathode materials can generally be divided into three different classes: olivine, layered Li transition-metal oxides, and spinel, as shown in Figure 3-2 [65]. Olivine such as $LiMePO_4$ (Me = Fe, Mn, Co, or Ni) with an orthorhombic system was firstly introduced in 1997, consisting of a distorted hexagonal close-packed oxygen framework with Li- and Fe-cations locate in half of the octahedral sites and P-ions in 1/8 of the tetrahedral sites [66]. The presence of parallel one-dimensional (1D) channels allows the Li-ions diffusion in olivine structure during charging and discharging. The commonly used olivine material $LiFePO_4$ (LFP) has a theoretical specific capacity of 170 mAh/g [66, 67] and a practical specific capacity of 140 mAh/g when discharged in 10 hours with a voltage window of 3.0 to 3.8 V [68].

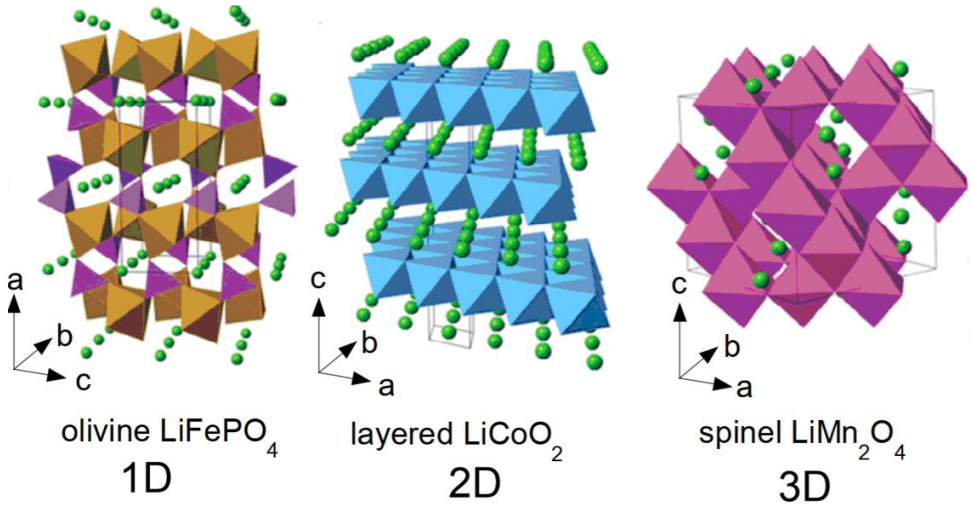

Figure 3-2. Schematic illustrations of crystal structures of three common cathode material types with one-dimensional (1D), two-dimensional (2D), and three-dimensional (3D) Li-ions diffusion pathways [65].

The spinel cathode material $LiMn_2O_4$ (LMO) with 3D diffusion pathways of Li-ions was firstly introduced by Thackeray et al. [69] in 1983. The oxygen anions are cubic close-packed in LMO and form 3D arrangement, while Li-ions occupy different sites at different discharge plateaus [70]. When discharged in 10 hours between 3.1 and 4.3 V, LMO can reach a practical specific capacity of around 120 mAh/g [71]. However, one major drawback of LMO material is

that a crystal structure transition appears when it is discharged to around 3 V, which is caused by the electrostatic repulsion between the non-bonded electrons in the p orbitals of the coordinating oxygen anions and the electrons in the d orbitals of the center Mn-cations in the oxygen octahedrons [62]. This effect is also termed as the Jahn-Teller effect.

Nowadays, layered Li transition-metal oxides are the most widely used commercial cathode material types. The first viable of this kind was $LiCoO_2$ (LCO), which was developed by Mizushima and Goodenough et al. [72] in 1980. LCO has an α-$NaFeO_2$ structure with oxygens in a cubic closed-packed arrangement, which is similar to LMO at around 4 V. It has a practical capacity of 130 mAh/g in the voltage window of 3.0 to 4.2 V, since only half of Li-ions in LCO can take part in the electrochemical reaction reversibly [61]. In order to increase the capacity of LCO, different approaches were studied. For example, derivatives $Li(Mn_{1-x}Co_x)O_2$ ($x \leq 0.5$) which are isostructural to LCO by doping Co in $LiMnO_2$ have been investigated. This material shows a capacity of 180 – 200 mAh/g in the voltage window of 2.6 to 4.8 V with a current density of 0.1 mAh/cm^2 but suffers from capacity fading due to Jahn-Teller effect [73]. The electrochemical performance of other compounds with layered structures such as $Li_{2/3}(Ni_{1/3}Mn_{2/3})O_2$ [74], $Li(Ni_{1/2}Mn_{1/2})O_2$ were reported [75-77], which exhibit 150 mAh/g (2.5 – 4.3 V) and 160 mAh/g (2.0 – 4.6 V) reversible capacity, respectively. Besides, in these materials, the Ni- and Mn-cations are assumed to have +2 and +4 oxidation state, respectively, and two-electron-transfer involving $Ni^{2+} \leftrightarrow Ni^{4+}$ happens during charging and discharging [75, 76]. Another approach by doping Al in $LiNi_{0.8}Co_{0.2}O_2$ led to the discovery of $LiNi_{0.8}Co_{0.15}Al_{0.05}O_2$ (NCA) with suppressed cell impedance rise and a specific discharge capacity of 180 – 200 mAh/g (discharged in 10 hours at 3 to 4) [3, 78]. Meanwhile, another layered cathode material type $LiNi_xMn_yCo_{1-x-y}O_2$ (NMC) has received great attention and will be discussed in the following chapter.

3.1.2.1. NMC active materials

NMC-type material was first discovered by Ohzuku et al. [79] in 2001. The layered Li-ion insertion material $LiNi_{1/3}Mn_{1/3}Co_{1/3}O_2$ (NMC 111) was synthesized by solid-state reaction at 1000 °C in air using $LiOH{\cdot}H_2O$, $CoCO_3$, and $M(OH)_2$ (M = Ni, Mn). After comparing the X-ray diffraction (XRD) patterns of NMC 111 with $LiCo_{1/2}Ni_{1/2}O_2$ and LMO, it was concluded that the crystal structure of NMC 111 is similar to that of $LiCo_{1/2}Ni_{1/2}O_2$ (space group $R\bar{3}m$), not to that of LMO with spinel structure. Besides, electrochemical analysis revealed that the half-cells containing NMC 111 cathode exhibited a reversible specific capacity of 150 mAh/g at 2.5 to 4.2 V with 0.17 mA/cm^2 current density [79]. This material was further studied by Shaju et al. [80] using XPS and XRD, and it was confirmed that the Li-ions locate at the *3a*-sites, while the TM ions and oxygen ions are at *3b*- and *6c*-sites, respectively. Their results matched the previous work from Ohzuku et al. [79] and the lattice parameters of NMC 111 obtained from XRD are $a = 2.864 \pm 0.005$ Å and $c = 14.233 \pm 0.008$ Å. XPS analysis displayed that the dominant oxidation state of Ni, Mn, and Co in NMC 111 are +2, +4, and +3, respectively, while a small amount of Ni^{3+} and Mn^{3+} ions exist at the same time [80]. Cyclic voltammetry of half-cells with NMC 111 showed two redox peaks occurring at 3.8 V and 4.6 V, which are assigned to the Ni^{2+} / Ni^{4+} and Co^{3+} / Co^{4+} redox couples, respectively [80]. Besides, differential scanning calorimetry (DSC) displayed that the exothermic reaction of NMC 111 in charged state

($Li_{0.12}Ni_{1/3}Mn_{1/3}Co_{1/3}O_2$) with liquid electrolyte is much milder than that of LCO or LNO [81]. Therefore, after the discovery of NMC 111, it was considered as a possible alternative to LCO for LIBs.

Due to the high-energy density and high-power density, NMC materials were intensive studied in the following decades and are currently the most commercially used cathode materials for LIBs in automobile industry. Although the difference in the content of each TM ion determines the type of NMC, the principal crystal structure of all NMC materials remains unchanged, which is isostructural to α-$NaFeO_2$, as shown in Figure 3-3.

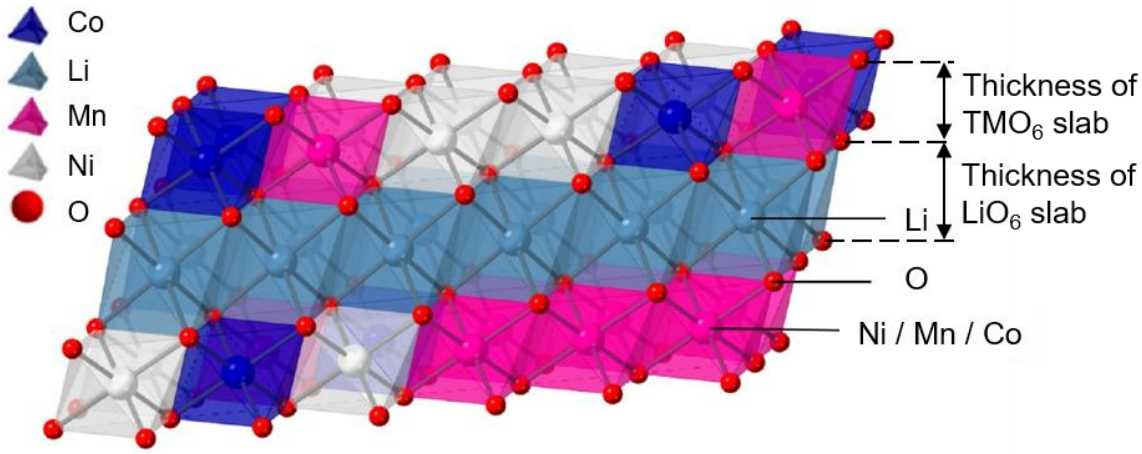

Figure 3-3. Schematic representation of the crystal structure of NMC materials [82].

In order to study the effect of content of different TM ions in NMC materials on the crystal structure and electrochemical performance, Choi et al. [83] analyzed series of Mn-rich oxides $LiNi_{0.5-y}Co_{0.5-y}Mn_{2y}O_2$ and Ni-rich $LiCo_{0.5-y}Mn_{0.5-y}Ni_{2y}O_2$. Their results revealed that the specific discharge capacity increased with increasing Ni content, but on the other side, capacity fade in Ni-rich compositions was higher in comparison to oxides with lower Ni content. In addition, impurity phase Li_2MnO_3 was found in Mn-rich oxides, while significant Li deficiency and increasing cation disorder were found for oxides with increasing Ni content [83]. At the same time, synthesis of $LiNi_{0.8}Mn_{0.1}Co_{0.1}O_2$ (NMC 811) was reported to have a specific discharge capacity of 198 mAh/g (voltage window: 3.0 – 4.3 V, current density 20 mAh/g) and it was confirmed that the presence of Mn with oxidation state of 4+ could stabilize the host structure of NMC [84]. Kosova et al. [85] studied $LiNi_{1-x-y}Co_xMn_yO_2$ with x = y = 0.1, 0.2, 0.33 using XRD, XPS, and infrared (IR) spectroscopy and found that the degree of structural disordering and TM ions – O bond covalency increased with increasing Ni content in NMC, while NMC 622 showed the highest specific discharge capacity of 170 mAh/g in comparison to NMC 111 and NMC 811. The low capacity of NMC 811 in their work is assumed due to cation mixing and surface admixtures. Besides, the previous issue owing to the cation mixing between Ni^{2+} and Li^+ on the *3b*-sites in Ni-rich NMC has been studied in other work, since Ni^{2+} has similar ionic radius (0.69 Å) in comparison to that of Li^+ (0.76 Å) [65]. The electrochemical properties as well as the structural and thermal stabilities of spherical $LiNi_xCo_yMn_zO_2$ materials with x ranging from 1/3 to 0.85 synthesized via coprecipitation method were reported by Noh et al. [86]. In contrast to the results from Kosova et al. [85], they reported that the specific capacity of NMC rises from 163 mAh/g for x = 1/3 to 206 mAh/g for x = 0.85 (20 mA/g, 3.0 – 4.3 V), however,

the residual Li amount (LiOH and Li_2CO_3) increases with increasing Ni content in NMC, especially when x is larger than 0.6 [86]. Moreover, thermal gravimetric analysis (TGA) showed that the structural stability of NMC decreases with increasing Ni content, accompanied by phase transition temperature shifting to lower temperatures, which might be owing to the decreasing particle size with increasing Ni content, since large particles are more difficult to undergo a structural transformation. DSC exhibited that the temperature peak of the exothermic reaction shifts to lower temperature along with higher heat evolution with increasing Ni content [86]. However, severe capacity fade of $LiNi_xCo_yMn_zO_2$ materials at x larger than 0.7 implies the trade-off between energy density and cycling stability should be taken into consideration and the composition of NMC needs to be cautiously selected to meet the requirement of specific applications.

3.1.2.2. NMC 622 active materials

NMC 622 with a theoretical Ni^{2+} / Ni^{3+} ratio of 1:2 and an average discharge potential of 3.71 V was first introduced by Kosova et al. [85] in 2006, and has been further studied in the following decades. In addition, XPS analysis determined that the Mn- and Co-cations in NMC 622 show the +4 and +3 oxidation states [87]. The specific capacity of NMC 622 varies from 170 to 197 mAh/g depending on the voltage window and applied current density [85, 86, 88, 89], while the lattice parameters *a* and *c* determined by XRD at room temperature are 2.8692 Å and 14.2174 Å, respectively [89]. Besides, the lattice parameters *a* and *c* are temperature dependent and increase with increasing temperature [85]. The electronic conductivity of NMC 622 measured by applying the four probe method is $1.6 \cdot 10^{-6}$ S/cm, while the TGA exhibited that there are weight losses of the delithiated NMC 622 from 235 °C, which is attributed to the release of oxygen, leading to phase transitions from layered to spinel, and a further transition to rock-salt structure at 315 °C. [86]. In comparison to NMC 111 and NMC 811, NMC 622 has the highest diffusion coefficient measured by galvanostatic intermittent titration technique (GITT) as displayed in Figure 3-4-a and a minimal temperature dependence of diffusion coefficient at -25 to 50 °C. Moreover, in contrast to other NMC materials with lower Ni content, NMC 622 exhibits higher rate capability at less than one hour of discharge [88]. Figure 3-4-b shows the results of the cyclic voltammetry (CV) analyses of a half-cell containing NMC 622 cathode vs. Li, with a distinct oxidation peak (with ascending voltage) observed at 3.85 V and a reduction peak (descending voltage) located at 3.60 V; This redox reaction corresponds to the transition of Ni^{2+} / Ni^{4+} in NMC 622 [90]. In addition, by applying different scan rates in CV analyses, the effective diffusion coefficient of Li-ion in the active material can be calculated, as will be explained in chapter 4.5.3. *In situ* XRD showed that during synthesis, rhombohedral NMC 622 reflexes appear at about 660 °C and the reflex intensities increase strongly above 760 °C, and single phase NMC 622 finally forms at above 840 °C [91].

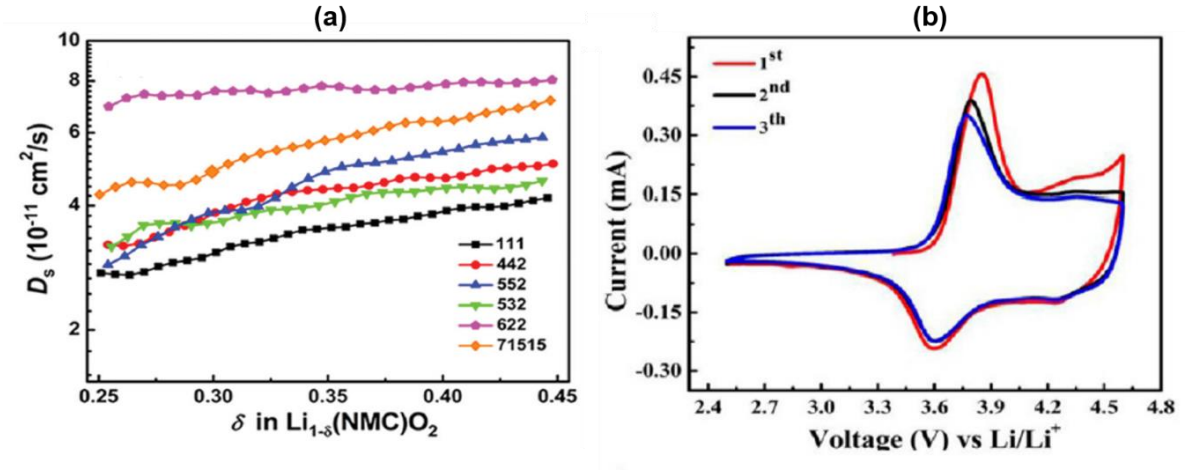

Figure 3-4. Diffusion coefficient of (**a**) NMC materials with different Ni, Mn, Co content at 25 °C measured by GITT [88]; And (**b**) cyclic voltammetry analyses of half-cell containing NMC 622 cathode using a scan rate of 0.1 mV/s with a voltage window of 2.5 to 4.6 V [90].

Wei et al. [92] investigated Li-ion diffusion kinetics in NMC using *ab initio* calculations combined with experiments, and they further developed the theory derived from Li-ion diffusion in layered transition metal oxide LCO by Van der Ven et al. [93]. There are two Li-ion diffusion mechanisms in NMC materials, which are tetrahedral site hopping (TSH) and oxygen dumbbell hopping (ODH), as shown in Figure 3-5.

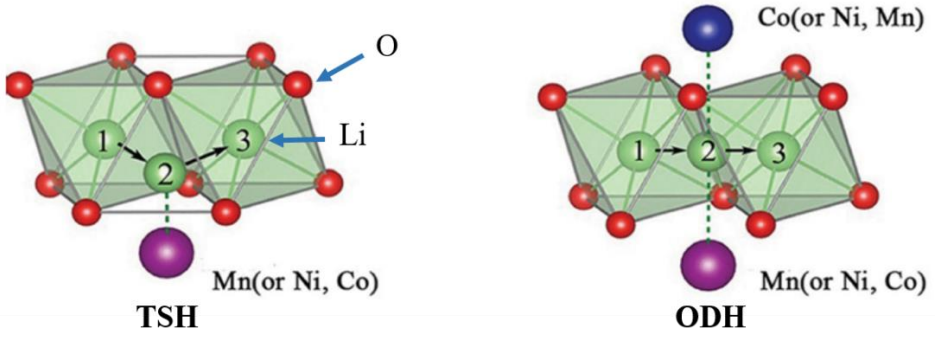

Figure 3-5. Schematic representation of two Li-diffusion mechanisms in NMC during delithiation (charge) process, which are tetrahedral site hopping (TSH) and oxygen dumbbell hopping (ODH). This image is reconstructed from the work of Cui et al. [88].

TSH means Li-ion diffusion from one octahedral site to the next by passing through an intermediate tetrahedral di-vacancy left by Li-ion diffusion with a transition metal nearby, while ODH indicates Li-ion diffusion from one octahedral to the adjacent octahedral site through the oxygen dumbbell. The activation energy of TSH is effected by the size of the tetrahedral site as well as the electrostatic interaction between Li-ion in activated state and the transition metal-ion below, in addition, the size of the saddle point of oxygen dumbbell as well as the electrostatic interaction between Li-ion in the active state and the neighboring transition metal-ions can influence the activation energy of ODH [92]. At the initial stage of charging (Li-deintercalaction), Li-ions prefer ODH, nevertheless, TSH starts to dominate the diffusion

process when 1/3 state-of-charge (SOC) is exceeded, accompanied by the oxidation of Ni^{2+} / Ni^{3+} to Ni^{3+} / Ni^{4+} and an increased activation energy [92].

Lee et al. [89] calculated the Li-slab and transition metal slab thicknesses of NMC 622 (as exhibited in Figure 3-3) using in situ XRD and proposed two stages during Li-deintercalaction: At the initial stage, the Li-slab thickness increases owing to electrostatic interaction (repulsion) and overrides the decrease in TM slab thickness due to the oxidation of transition metal-ions. With further delithiation, highly oxidized TM ions pull more electrons from oxygen, and this leads to a reduction in electron density in oxygen, which results in a decreased TM slab thickness in comparison to their initial thickness. However, the Li-slab thickness is still larger than that of initial state, indicating that the Li-ion diffusion pathways are preserved even though the *c*-lattice parameter is smaller than the original value. Besides, they argued that increasing Ni content favors Li-ions transport, lower overpotentials, smoother phase transition, decreased cation disorders, which in turn reduces charge transfer resistance and increases specific capacity after 100 cycles (charge and discharge in one hour). Similar results were reported by Zhu et al. [82] using molecular dynamics (MD) simulation of different NMC materials and they found that more Ni^{3+} to Ni^{2+} transformation occurs with increasing Ni content, and Ni^{2+} is conducive to Li-ion diffusion since the electrostatic repulsion between Li-ion and Ni^{2+} is the lowest compared to the electrostatic repulsions between Li-ion and Ni^{3+}, Co^{3+}, and Mn^{4+}.

The density of state N(E) vs. energy and the relative Fermi level of different redox couples of transition metal-ions in comparison to the anion *2p* bands of oxygen at different discharge states are shown in Figure 3-6. During charge process, the Fermi level E_F moves to lower energy state with decreasing Li^+ content in cathode material and the chemical potential difference of Li^+ in anode and cathode increases (higher voltage). However, when the Fermi level E_F of cathode reaches the top of the anion *p* bands of oxygen (at high voltage) as shown in Figure 3-6–c, the *p-d* covalent mixing could transfer correlated *d* electrons at E_F into band electrons and thus leads to lattice oxygen release [65]. This theory is supported by performing online electrochemical mass spectrometry (OEMS) as gas analysis on pouch cells with NMC 111, NMC 622 and NMC 811 vs. graphite anode by Jung at el. [94]. They found that at 4.7 V vs. Li / Li^+ for NMC 111 and NMC 622, and at 4.3 V vs. Li / Li^+ for NMC 811, oxygen evolution occurs and reacts further with the EC in electrolyte, resulting in the release of CO_2 and CO. Besides, the oxygen release at voltages larger than 4.7 V can also lead to spinel and rock-salt transformation on the surface of NMC 622, and the respective layer thicknesses are assumed to be 12 nm and 7 nm, respectively [94].

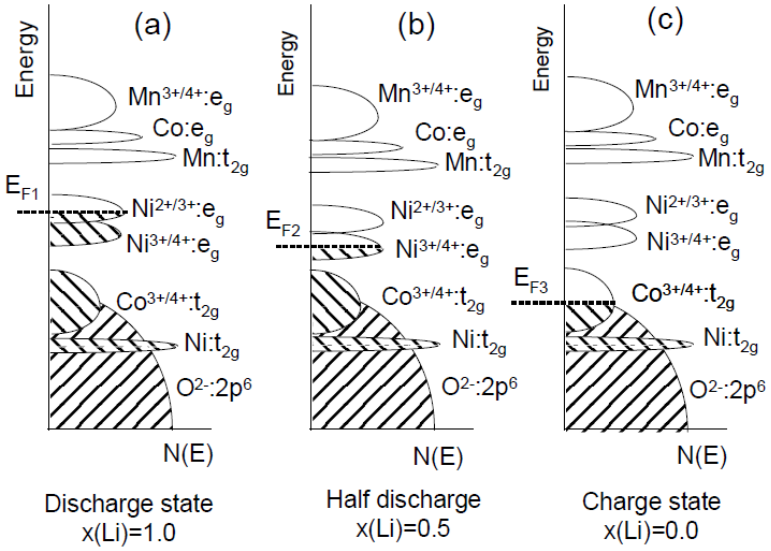

Figure 3-6. Schematics of density of state N(E) as a function of energy with respect to the Fermi level of the Ni^{3+} / Ni^{4+} and Co^{3+} / Co^{4+} redox couples for NMC materials at different charge states [65].

Considering the cycle stability of full-cells with NMC 622 cathode and graphite anode, the upper cut-off potential of cells with NMC 622 is suggested to be limited to values smaller or equal to 4.4 V [94]. However, Kim et al. [95] compared the capacity retention and thermal stability of NMC 622 with NMC 811 and $LiNi_{0.9}Co_{0.05}Mn_{0.05}O_2$, and found that NMC 622 with upper cut-off voltage up to 4.5 V showed almost the same discharge capacity and capacity retention in comparison to NMC 811 cycled up to 4.3 V and exhibited higher thermal stability. The capacity fade of Ni-rich NMC was further investigated and might be owing to the presence of intergranular nanopores ranging from 10 to 50 nm and pores inside pristine materials. Upon cycling, rock-salt regions are formed on the top of spinel-like regions at the pore boundaries with increasing thickness, which accelerate the oxygen release and strain accumulation within the primary particles [96].

3.1.3. Anode materials

The reversible intercalation of Li-ions in graphite was investigated in the 1970s, but the decomposition of the commonly used liquid electrolyte propylene carbonate (PC) and the resulting graphite peeling limited further employment of graphite in LIBs [97, 98]. Yazami et al. [99] succeeded reversible electrochemical Li intercalation in graphite by applying a solid organic electrolyte, while in 1990 liquid electrolyte containing EC was proven to be suitable for cells containing graphite as anode, since the irreversible reaction owing to the electrolyte decomposition only exists during the first cycle [100]. The stabilization of graphite in liquid electrolyte containing EC is due to the formation of a solid electrolyte interphase (SEI) on the surface of graphite, which was proposed theoretically by Peled et al. [101]. SEI can prevent the direct contact between graphite and electrolyte, thus hinders the continuous electrolyte decomposition [101, 102], and prevents the solvent co-intercalation [103]. Meanwhile, Li-ions can still infiltrate through the SEI and intercalate into the graphite [104]. The structure of SEI can be roughly divided into two layers, i.e., the inorganic layer and the organic layer. The dense layer close to the graphite particles has been reported to consist of inorganic compounds such

as Li_2O, Li_2CO_3, and LiF, while the organic layer is composed of decomposition products such as polyolefins and semi-carbonates on the top of the inorganic layer [98, 105]. The existence of SEI is the key factor that makes graphite the most commonly used anode material to date.

The theoretical specific capacity of Li-intercalated graphite LiC_6 is 372 mAh/g, while the intercalation takes place between 0.01 V and 0.25 V vs. Li / Li^+ [104]. The interlayer distance increases from 3.35 Å (without Li) to 3.70 Å (LiC_6) during Li intercalation [106]. Besides, the Li-ion diffusion coefficient is on the order of 10^{-7} cm^2/s in delithiated state and decreases to 10^{-9} cm^2/s in fully lithiated state according to the calculation by Persson et al. [107], and was experimentally measured by Levi al. [108] using potentiostatic intermittent titration technique (PITT).

In state-of-the-art commercial LIBs, mainly two kinds of graphite are used, natural graphite (NG) and synthetic graphite (SG). The corresponding particles of both materials are polycrystalline and consist of domains, however, in NG the domains are oriented in the same direction, while in SG the orientation is more random [104]. The main difference between these two graphite types is that SG is produced by heating of unsaturated carbon to 2500 °C, thus it has higher purity, better thermal stability, and lower thermal expansion in comparison to NG [109]. Therefore, SG is more suitable for applications in BEV than NG despite its 60 % higher material costs [20].

Other materials such as pure Li [110], $Li_4Ti_5O_{12}$ (LTO) [111, 112], Si [113-115], and SiO_x [115-117] are also potential anodes for LIBs. Each material has specific advantages and disadvantages, which will not be discussed further here. In comparison to other anode materials, graphite is still the most commonly used commercial anode materials for LIBs [118] and thus SG will be applied as anode material for pouch cells in this thesis.

3.1.4. Characteristics of LIBs

In this chapter, characteristics and definition of different commonly used terms in LIBs will be introduced. The working voltage (U_{OC} [V]) of a LIB is defined as the chemical potential difference ($\Delta\mu$ [eV]) between the cathode (μ_C [eV]) and anode (μ_A [eV]), and U_{OC} can also be referred to as open circuit voltage. Besides, it depends not only on the cathode and anode, but also on the potential window of the electrolyte (E_g [eV]), which is determined by the energy gap between the lowest unoccupied molecular orbital (LUMO) and the highest occupied molecular orbital (HOMO) of the electrolyte. Their relative relationship is shown in Figure 3-7. Appropriate cathode should have a μ_C above HOMO, while the μ_A of anode must locate below LUMO, otherwise the liquid electrolyte will be oxidized on the cathode and reduced on the anode [119]. The working voltage also known as the open circuit voltage of LIBs is described as follows:

$$U_{OC} = \frac{\mu_A - \mu_C}{q} \tag{3.2}$$

where q is the elementary charge e.

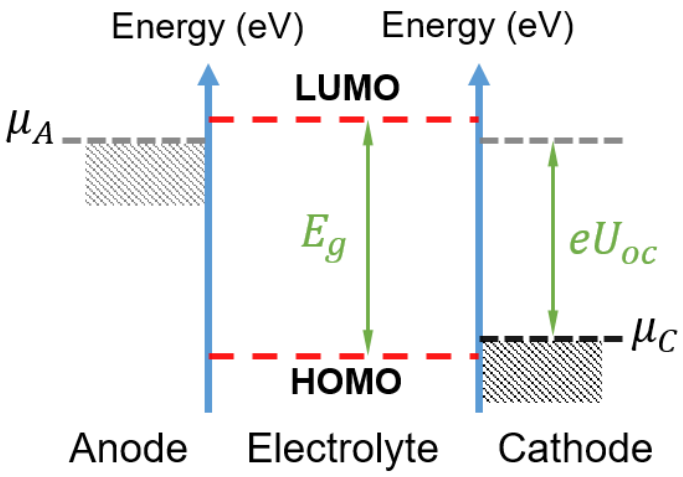

Figure 3-7. Schematic view of the LUMO and HOMO of the liquid electrolyte, relative energies of the electrolyte window Eg, the chemical potential of cathode (μC) and anode (μA). This figure is reproduced from the work of Goodenough et al. [120].

The cell capacity Q [Ah] and its relationship to electrical current I [A] and transported charge q [As] is described as:

$$Q = \int_0^{\Delta t} I dt = \int_0^{Q} dq \tag{3.3}$$

where Q is the total capacity of a LIB by the current I. This indicates that the capacity is related to the current, and generally the cell capacity decreases with increasing current.

The state-of-charge (SOC) is defined as the ratio of the currently available capacity $Q(t)$ [Ah] to the maximum stored charge Q_{max} [Ah] in a cell [121]:

$$SOC = \frac{Q(t)}{Q_{max}} \cdot 100\% \tag{3.4}$$

The SOC value ranges from 0 % to 100 %, where 0 % SOC stands for a fully discharged cell and 100 % SOC for a fully charged cell. In order to describe which electrical current is applied and how fast a battery is fully charged or discharged, the term “C-rate” nC [1/h] is introduced and defined as [122]:

$$nC = \frac{I_{cell}(t)}{Q_{nom}} \tag{3.5}$$

where $I_{cell}(t)$ [A] is the currently applied cell current, and Q_{nom} [Ah] the nominal capacity of a cell, which is usually calculated as follows:

$$Q_{nom} = \frac{m_{act} \cdot C_Q}{1000} \tag{3.6}$$

where m_{act} [g] is the mass of active material in the composite electrode, C_Q [mAh/g] is the specific capacity of the active material. Therefore, the applied cell current increases with increasing nC, while the charge and discharge time reduces with rising nC. Besides, nC also corresponds to the time required to fully charge or discharge the cell in $1/n$ hour(s).

The energy E [VAs] of a LIB is measured at a given electrical current I [A] and voltage U [V] to fully discharged state:

$$E = \int_0^{\Delta t} IU(t)dt = \int_0^{Q} U(q)dq \tag{3.7}$$

Volumetric energy density as well as gravimetric energy density are commonly used in the battery industry. The first one is of great interest for applications in portable devices such as laptops due to limited space, while both are important for the automobile industry. In order to determine the energy density, it is necessary to use a so-called full-cell configuration, including the cathodes, anodes, separators, and electrolyte. The calculations of the energy density and power density of pouch cells are shown in Appendix C. Another crucial index is the end-of-life (EoL) of a LIB, which refers to the number of cycles at which the capacity drops to 80 % of the initial capacity.

In practical applications, batteries experience cycles of charge and discharge with a hysteresis in between. It is found that the discharge potential is lower in comparison to the charge potential due to the cell polarization arising from the internal resistance [120]. A drop in potential is shown in Figure 3-8 between the end of charge and the beginning of discharge, which is termed as “IR drop”. IR drop can lead to efficiency decrease and safety issues owing to heat generation. The polarization decreases the discharge potential and increases the charge potential, and the resulted overpotential is also considered to be the driving force of the phase transitions in electrode active materials during electrochemical process [123].

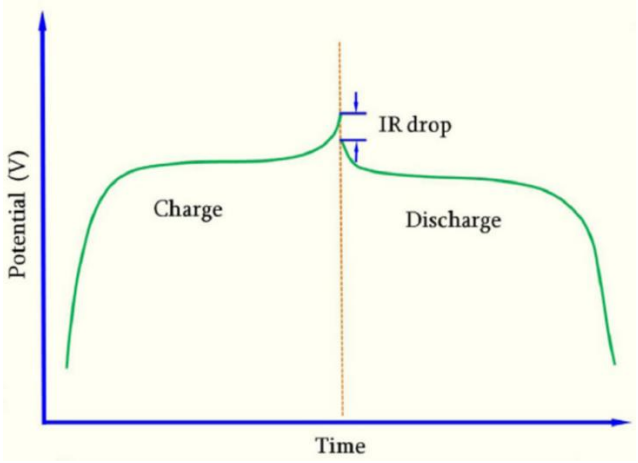

Figure 3-8. Schematic representation of the potential drop at the beginning of discharge refers to the internal resistance drop (IR drop) [62].

Irreversible capacity loss can occur in LIBs for many different reasons, e.g., the formation of SEI, limited Li-diffusion at high current densities, gas evolution due to side reactions between the electrolyte and electrodes, and / or material dissolution from the electrode [120]. Therefore, coulombic efficiency (CE) is introduced to measure the extent of irreversible capacity loss:

$$CE = \frac{Q_{discharge}(n)}{Q_{charge}(n)} \cdot 100\% \tag{3.8}$$

where $Q(n)$ [Ah] is the capacity of charge / discharge from the n^{th} cycle. Furthermore, the discharge capacity of cells is usually monitored during the lifetime analysis or in practical applications to estimate the health of the battery, and the state-of-health (SOH) is defined as following:

$$SOH = \frac{Q_n}{Q_0} \cdot 100\% \tag{3.9}$$

where Q_n [Ah] is the discharge capacity of the n^{th} cycle and Q_0 [Ah] the discharge capacity of the first cycle.

EIS was developed in the 19th century and is commonly used to determine the resistance, capacitance, and inductance of a cell by measuring the current response when alternating currents (AC) or voltages with different frequencies are applied [124]. The impedance in an AC circuit is defined as follows [124]:

$$Z(\omega) = \frac{U(\omega)}{I(\omega)} = \frac{U_m sin(\omega t)}{I_m\, sin(\omega t - \varphi)} \tag{3.10}$$

where $Z(\omega)$ [Ω] is the resistance of the cell, $U(\omega)$ [V] the applied alternating voltage with a frequency of ω [Hz], U_m [V] and I_m [A] the respective maximum voltage and current, $I(\omega)$ [A] the response current at the frequency ω, and the resulted phase shift φ [°]. Furthermore, by adapting the complex function:

$$j = exp(\frac{j\pi}{2}) \tag{3.11}$$

The equation (3.10) can be rewritten as:

$$Z(\omega) = \frac{U(\omega)}{I(\omega)} = \frac{U_m\, exp(j\omega j)}{I_m exp[j(\omega t - \varphi)]} = \frac{U_m}{I_m} exp(j\varphi) \tag{3.12}$$

And the equation (3.12) can be simplified by applying Euler's formula:

$$Z(\omega) = \frac{U_m}{I_m} exp(j\varphi) = \frac{U_m}{I_m}(cos\varphi + jsin\varphi) = Z_0(cos\varphi + jsin\varphi) = Z_0 cos\varphi + Z_0 sin\varphi j \tag{3.13}$$

where Z_0 [Ω] is the total impedance. The real part $Z_0 cos\varphi$ represents the resistance, while the imaginary part $Z_0 sin\varphi$ associates with capacitance and inductance.

Usually, impedance spectra can be presented in two methods, which are called "Bode plot" and "Nyquist plot". The first method shows the magnitude and the phase shift at applied frequencies, while the second method displays the real and the imaginary parts of the impedance. The latter one is usually combined with equivalent circuit model to analyze the LIBs. The impedance spectrum from an EIS analysis on a half-cell and its equivalent circuit model are displayed in Figure 3-9. From left to right, the frequency ω is decreasing at each measurement point. Generally, the applied AC or alternating voltages should have frequencies in the range of 100 kHz to 10 mHz in order to obtain the entire spectrum of cells [125, 126]. The equivalent circuit model consists of resistors, inductors and capacitors connected in series or parallel. Besides, elements such as constant phase element (CPE) and Warburg element (W) are applied to represent the non-ideal capacitor and Li-ion diffusion characteristics, respectively [124]. R_e at the start on the left represents the bulk resistance in a cell such as the electrolyte, current collector, and separator. The diameter of the semicircles at high-frequency range and middle-frequency range indicates the SEI resistance (R_{SEI}) and charge transfer resistance (R_{ct}), respectively. R_{SEI} comes from the impedance of the interface formed between the electrode surface and the electrolyte, and is affected by the SOC as well as the constituents of electrolyte [127]. The second semicircle corresponds to the R_{ct}, which represents the

electrochemical reaction kinetics in a cell. Furthermore, R_{ct} is more sensitive to temperature than the other two types of resistance and increases by a factor of 1000 with decreasing temperature from 20 to -60 °C, accounting for more than 90 % of the total cell resistance in the fully discharged state [128]. In the low-frequency range, a rising line with an angle of 45 ° appears, which corresponds to the Li-ion diffusion process. A Warburg element is commonly applied to fit this line and can also be used to calculate the Li-ion diffusion coefficient [129]. However, this method is only applicable to the calculation of Li-ion diffusion coefficient of electrode materials with single-phase reaction, not in the region where the phase transition takes place [130]. Thus, when calculating the effective Li-ion diffusion coefficient for NMC 622 cathodes, it is important to avoid the phase transition region of 3.70 to 3.75 V, where peaks appeared in the dQ/dV diagram [85].

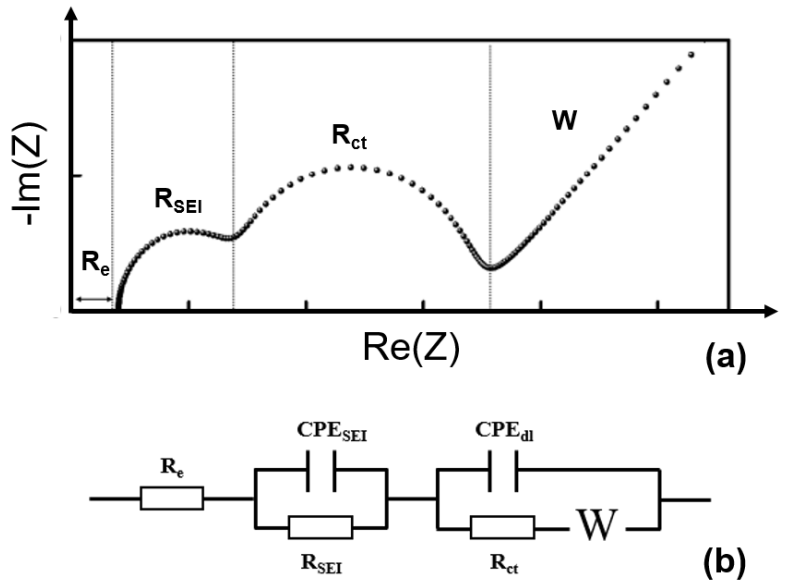

Figure 3-9. Schematic representation of the impedance spectrum from an EIS analysis using (**a**) Nyquist plot (reproduced from [124]), and (**b**) the corresponding equivalent circuit model using three resistors (R), two constant phase element (CPE), and a Warburg element (W).

Different equivalent circuit models can be applied to fit the impedance spectrum. Westerhoff et al. [131] compared different equivalent circuit models and found that the impedance spectrum could be accurately simulated by applying a model with 5 resistors and capacitors using (RC) or with a resistor and a CPE. However, the latter one required 30 less iterations to obtain the parameters. In addition, they found that the simulation accuracy using models with resistor and CPE was not improved with increasing number of equivalent circuit elements, but the number of iterations increased by four times.

The Butler-Volmer equation has been commonly used to describe the intercalation kinetics of Li-ion in cells with liquid electrolyte [132, 133], which is given as:

$$i_{in} = i_0 \left(\exp\left(\frac{\alpha_a F \eta}{RT}\right) - \exp\left(-\frac{\alpha_c F \eta}{RT}\right) \right) \tag{3.14}$$

where i_{in} [A/cm^2] is the current density in the cell with porous electrode, i_0 [A/cm^2] the exchange current density, α_a [-] and α_c [-] the anodic and cathodic transfer coefficient, respectively, and with the condition $\alpha_a + \alpha_c = 1$. F [As/mol] is the Faraday constant, η [V] the

overpotential, R [J/mol·K] the gas constant, T [K] the temperature. For the battery modeling, $\alpha_a = \alpha_c = 0.5$ is commonly applied [134]. The exchange current density i_0 proposed by Doyle et al. [135] is written in the form:

$$i_0 = k_0 F (c_s)^{\alpha_c} (c_{s,max} - c_s)^{\alpha_a} \tag{3.15}$$

where k_0 [cm/s] is a reaction rate, c_s [mol/cm^3] the concentration of Li-ion in the active material, and $c_{s,max}$ [mol/cm^3] the maximum concentration of Li-ion which can be stored in the active material, F [As/mol] the Faraday constant. In addition, the overpotential η in equation (3.14) is defined as:

$$\eta = U - U_{oc} \tag{3.16}$$

where U [V] is the cell voltage, and U_{oc} [V] the open circuit voltage. Combining equation (3.14) with (3.15) and (3.16), the following equation is acquired:

$$i_{in} = k_0 F (c_s)^{\alpha_c} (c_{s,max} - c_s)^{\alpha_a} \left(\exp\left(\frac{\alpha_a F (U - U_{oc})}{RT} \right) - \exp\left(-\frac{\alpha_c F (U - U_{oc})}{RT} \right) \right) \tag{3.17}$$

The Butler-Volmer equation and derived equations can be used to interpret the curves obtained from the CV analysis.

3.1.5. LIBs containing electrodes with 3D architectures

Batteries in general consist of a stack of thin-film anodes, cathodes, separators, and each component is considered as two-dimensional planar construction. In order to achieve enhanced gravimetric and volumetric energy density, the 3D battery concept was introduced by Long et al. [136]. The goal was to design 3D electrode architectures to achieve high power and energy density while maintaining a short Li-ion transport distance between the electrodes. For example, architectures such as interdigitated planar or cylindrical electrodes with solid electrolyte separating the anodes and cathodes are shown in Figure 3-10. However, it has to be noted that although electrodes with 3D architectures are applied, the current collector is still two-dimensional (2D). Therefore, it is a mixture of 2D and 3D structures at battery level.

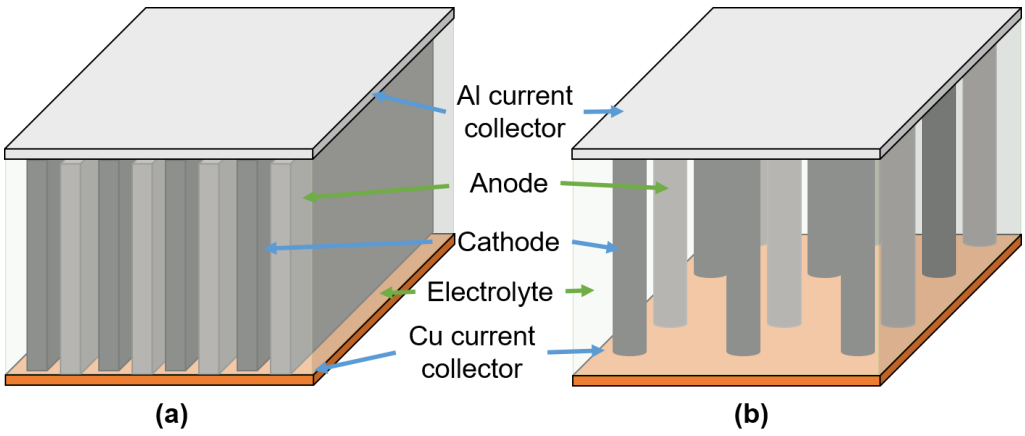

Figure 3-10. Schematic view of micro-batteries with different electrode architectures using **(a)** planar interdigitated or **(b)** cylindrical electrodes (modified from [136]).

Additive manufacturing techniques can be applied to realize architectures shown in Figure 3-10-a. Extrusion-based 3D printing of LMO cathodes with PVDF binder or with aqueous binders has been reported [137, 138], which allows the direct printing of electrodes with thicknesses larger than 100 µm. However, it is challenging to increase the manufacturing speed and precision at the same time, since small nozzle size is preferable to improve the printing resolution but leads to clogging of the nozzle and low efficiency in printing [139]. Recent studies reported the manufacturing of 3D cathodes consisting of LFP as framework with carbon nanotube networks using direct ink writing (DIW) [140, 141], this opens a new method for architecture design. Recently, micro-casting using patterned blade was reported to fabricate 3D NMC 811 cathodes with 280 µm thickness and 30 % higher capacity after 200 cycles were achieved [142]. Mechanical embossing using roller with pyramid-like structures to structure the graphite anodes with a areal capacity of 6.0 mAh/cm^2 was reported and an increase in discharge capacities at 1C and 2C of 8.7 % to 14.3 % was observed, respectively [143]. However, both technical approaches have significant drawbacks with regard to process stability, accuracy, and transferability to thick-film electrodes. Another method to achieve 3D electrode architectures is by applying laser ablation, which will be discussed in chapter 3.3.

Template-based manufacturing can be applied to generate electrodes with 3D architectures as shown in Figure 3-10-b. Salt templating of SiO_x [144] and LTO [145] anodes using NaCl particles was reported, where the NaCl particles were added into the slurry and subsequently removed by water dissolution. Additional pores with diameters of 10 – 100 µm were observed in the final dried electrodes. Wood with aligned lumina and vessels in vertical direction can also be applied as template to fabricate LCO cathodes with 3D architectures and the vertical oriented vessels are beneficial for electrolyte wetting. However, high temperature up to 700 °C is necessary to carbonize the wood template by calcination while the LCO is simultaneously sintered [146]. In addition, the 3D architecture in electrodes manufactured using this method only depends on the structure of wood template and is thus difficult to design intentionally. Ice templating is another novel process regarding to the cost efficiency, since only ice crystals are generated as templates. Recently, manufacturing of LCO cathodes [147], LFP cathodes [148], and graphite anodes [149] using this technique have been reported. For the ice templating, aqueous based slurry was prepared, poured into a freezing mould, and the ice crystals grew along the temperature gradient, which means that the alignment of ice crystals as well as the porosity, pore size and distribution are controllable. At the final step, ice crystals in the slurry were subsequently removed by freeze-drying [148]. Billaud et al. [150] demonstrated another electrode manufacturing method by applying an external magnetic field to align the Fe_3O_4 coated graphite in suspension perpendicular to the Cu current collector, while Sander et al. [151] proposed an opposite method by controlling the arrangement of pore distribution and size using a magnetic field on Fe_3O_4 coated nylon microrods in LCO suspension. The nylon microrods were subsequently removed by a pyrolysis reaction and thus vertical channels consisting of pores were generated. Template-based manufacturing offers new insights into innovative electrode manufacturing, but the most techniques are not efficient and need extra pre- or post-conditions, therefore, they are not suitable for mass production in the battery industries.

In addition to the methods described above, architectural tuning of the 3D electrodes can be achieved by adjusting the size and distribution of pores in the electrodes, or by fabricating a gradient in the size or loading of the active material [152], as shown in Figure 3-11. The simulation from Shodiev et al. [153] indicated that the porosity should be decreasing from the separator to the current collector side in order to maximize the capacity and to lower the ionic impedance. Similar results were reported for graphite anodes with multilayers consisting of different porosities, and the discharge capacity of the cells containing graphite anodes with decreasing porosities from separator to current collector was 100 mAh/g higher in comparison to those with single layer graphite anode [154]. Zhang et al. [155] prepared LFP electrodes with different pore sizes and found that the cells containing electrodes with large pores (diameters: 60 – 120 µm) and high active material loading near the separator show 30 mAh/g higher capacity than those with small pores (diameters: 20 – 40 µm) near the separator at C-rates higher than C/2. In addition, the particle size of active material affects the tortuosity. The intraparticle Li-ion diffusion pathways are less tortuous with increasing particle size, but it leads to longer diffusion within the active material, for small particle is vice versa [152]. Wood et al. [156] investigated the electrochemical performance of pouch cells containing dual-layer $Li(Ni_{0.5}Mn_{0.3}Co_{0.2})O_2$ (NMC 532) cathode and graphite anode with different active material sizes. It was found that the electrode design with small particles near the separator on the cathode side and an opposite particle size gradient on the anode side resulted in an increase of 40 mAh/g in discharge capacity at 2C in comparison to those with single layer electrodes. However, opposite results were observed in dual-gradient graphite anodes developed by Lu et al. [157], which had small particles and more porosity near the separator, and the cells achieved 80 % SOC in 10 min (6C). Thus, the effect of particle size on electrochemical performance is more complex and needs to take into account the type of electrode material, the areal loading, and electrode porosity. Further research is required to find the optimal design of the electrode architecture.

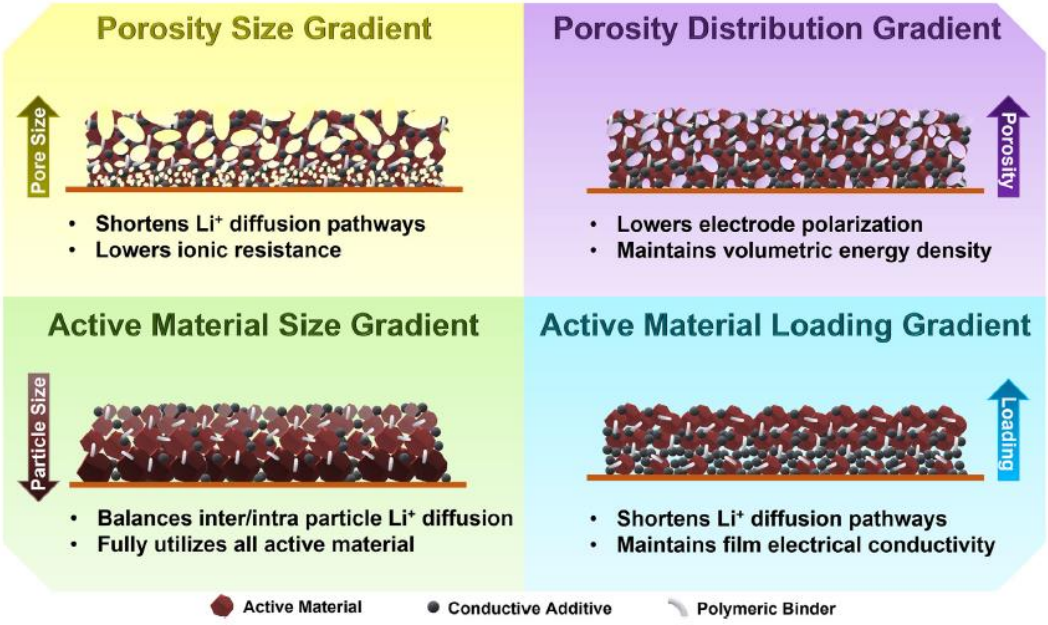

Figure 3-11. Electrodes with gradient designs using different porosity sizes, porosity distribution, different active material sizes, and active material loadings [152].

3.2. Slurry and electrode preparation

In chapter 3.1.1, different components in as-prepared electrodes for LIBs have been introduced. However, battery manufacturing includes many fabrication steps, ranging from slurry mixing to the final formation, as shown in Figure 3-12. In this chapter, the preparation of electrode from slurry mixing, coating, drying, to calendering before cell assembly will be discussed in detail.

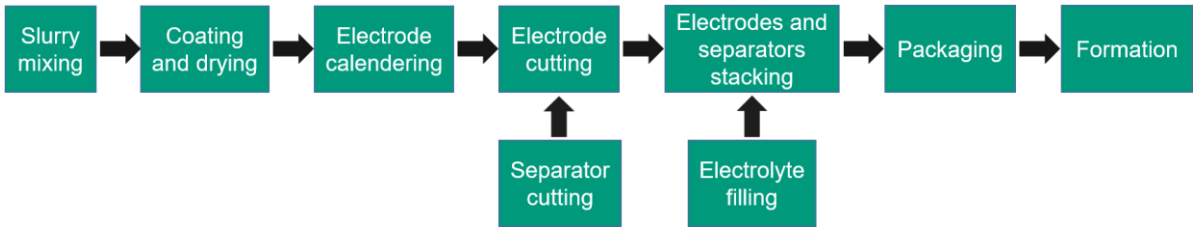

Figure 3-12. Electrode fabrication chain for a LIB, from slurry mixing to cell formation.

3.2.1. NMP-based slurry preparation

Slurry preparation refers to the solvent-based mixing process of active material, polymer binder, conductive agent, and other possible additives using mixing equipment such as ball mill, hydrodynamic shear mixer, magnetic stirrer, or ultrasonic homogenizer. A homogenous and stable slurry should be produced after the mixing process, which means that each component should be distributed homogenously and the slurry is stable against agglomeration and sedimentation [158]. Agglomeration is usually caused by van der Waals forces or in some cases by electrostatic interactions due to surface charges [159]. Therefore, external forces or dispersion additives are necessary to prevent the formation of agglomerates. Since the active material particles are much larger than the solvent molecules, the slurry can be approximated as colloidal suspension [160]. The slurry containing different components induces complex interactions that affect the subsequent coating process, thus different slurry properties are usually characterized, such as viscosity, surface tension, and agglomerate size distribution, to achieve a homogenous coating with required film thickness. PVDF is the state-of-the-art binder employed in battery industries for cathodes due to its distinct oxidation resistance and mechanical stability [3]. However, PVDF must be dispersed in NMP, an organic and toxic solvent [161]. Thus, a solvent recovery system such as ventilation is essential for production.

Bockholt et al. [162] manufactured NMC 111 slurries with PVDF binder using different dry and wet mixing devices such as low and high energy dissolver, intensive dry mixer, and planetary mixer. They found that the mixing technique had strong influence on the viscosity of slurry, pore distribution, and electric conductivity as well as electrochemical performance. Mixing with high energy (circumferential speed of 1.75 m/s) led to the lack of bind-conductive agent network between NMC 111 particles and resulted in a reduced capacity retention. Similar results were reported for $LiNi_{0.5}Mn_{1.5}O_4$ cathode slurry by comparing ball milling and magnetic stirring, where cells containing electrodes manufactured with ball milling exhibited higher capacity fade and lower coulombic efficiency [163]. Besides, the particle size of active material decreases using high energy mixing and the enlarged contact interphase between electrolyte and primary particles might results in parasitic reaction, which leads to capacity

fade and increased cell polarization. Kim et al. [164] investigated the effect of mixing sequences on the rheological properties and electrochemical properties of LCO slurry with PVDF binder and found that dry-mixing of LCO with conductive agent before adding binder solution is beneficial to increase cycling stability. However, this opinion was questioned by Bauer et al. [39], who compared the dry-mixed NMC 111 with untreated one. They argued that although this approach allows a homogenous distribution of carbon on the NMC 111 surface and may reduce electrical resistivity, it ignores the interaction between conductive agents and the binder, which can both stabilize the slurry against sedimentation and form conductive paths along the binder to prevent the existence of electrically isolated NMC 111 particles. The dry mixing pre-step using ball milling was further studied with different impact energies and frequencies of collision [165]. It showed that the film adhesion strength to the current collector is improved with increasing mixing energy, which should be owing to more contact points between NMC 111 particles and the current collector. However, the disintegration of NMC 111 and decreasing free conductive agent, which is responsible for long-range conductive pathways, will in turn deteriorate the electrochemical performance [165]. Not only the mixing process, but also the formulation of the slurry can strongly affect its properties. Bauer et al. [39] reported that the amount of conductive agent in NMC 111 slurry has significant impact on the slurry properties such as viscosity and electrical resistance. In addition, the particle size of active materials and the molecular weight of binder also affect the rheological properties of slurry and the interaction between binder and active materials [166].

3.2.2. Aqueous slurry preparation

In contrast to the state-of-the-art cathode manufacturing with NMP solvent, aqueous slurry preparation benefits the cost reduction of LIBs while reducing the environmental impact. Water-based processing shows great potential due to its low cost, reduced drying time, as well as safe production without explosion hazard [21, 167]. For instance, aqueous binders are environmentally friendly and cost an order of magnitude less than organic PVDF binder [168]. During aqueous processing, water serves as a solvent for the preparation of electrode paste, which reduces the material costs and is also favorable for the environment. Besides, although water shows 4.4 times higher enthalpy of vaporization compared to that of NMP per kilogram, the equilibrium vapor pressure of water is 35 times than that of NMP, indicating that 35 times more water vapor can be removed from the slurry per unit volume of dry air than NMP vapor; Thus as a results, the removal of water during drying is 4.5 times faster than for NMP, and the total energy required for drying process is reduced by almost 10 times according to the simulations [11]. Furthermore, Zackrisson et al. [169] reported that the life-cycle CO_2 emissions from the production of a battery pack (10 kWh) can be reduced from 4400 to 3400 kg by substituting NMP-based processing with aqueous processing.

Aqueous processing of graphite anode using CMC and SBR binders has already been implemented as a standard procedure in battery industry. Recent researches are focusing on the addition of silicon in graphite anode in order to further increase the energy density [19, 170]. However, water-based processing of cathode materials is mostly in research stage and has been intensively studied in the last decade. Li et al. [171] firstly introduced aqueous processing of LCO cathode in 2007 by applying SBR and Na-CMC as binders. The slurry pH

values were adjusted to 11.6, 9.3, and 5.7 using hydrochloric acid (HCl) and sodium hydroxide (NaOH). The isoelectric point (IEP) of 5 wt% LCO suspension was measured at different pH values and the zero potential point located at pH ≈ 6. At this point, the LCO particles had a net surface charge of zero and could form aggregates spontaneously [171], thus the slurry pH value should be as far away from this point as possible. Besides, holes with a diameter > 25 µm were observed in SEM images of dried electrode with slurry pH of 11.6. The effect of the degree of substitution (DS) of CMC on the aqueous processed carbon-coated LFP cathodes was studied and it was found that CMC with lower DS could support dispersing LFP particles; and cells containing electrodes with lower DS CMC displayed higher discharge capacity [172]. Li et al. [173] added dispersant – poly(ethyleneimine) into the aqueous processed LFP slurry and demonstrated that the addition of dispersant could reduce the agglomerate size and surface roughness of LFP cathodes. The capacity increased with increasing dispersant concentration up to 2 wt%. In addition, aqueous processing of high-voltage spinel LNMO cathode with CMC binder [30], lithium polyacrylic acid (LiPAA) [174], as well as guar gum [175] have also been reported.

Aqueous processing of NMC materials was started in 2013 when Çetinel et al. [176] and Wu et al. [177] published first results on NMC 111 and $LiNi_{0.37}Co_{0.24}Mn_{0.39}O_2$, respectively, using the same water-based binder system consisting of CMC and fluor-acrylic copolymer binder TRD202A. The previous work compared aqueous processed NMC 111 cathodes with NMP-based ones in full-cells vs. graphite anodes and found 10 mAh/g capacity drop at 1C, while TRD202A was studied in the latter work using DSC analysis and the aqueous processed electrodes exhibited higher capacity retention in contrast to reference NMP-processed electrodes. However, the surface tension of water (73 mN/m at 20 °C) is much higher than NMP (41 mN/m at 20 °C) and thus results in cracking of electrode during drying [178]. In order to compensate the crack formation and propagation during drying of aqueous processed cathodes, different approaches were reported, such as adding of isopropyl alcohol to reduce surface tension of slurry [178]; or using new binder such as poly(ethylene oxide) [179].

The major drawback of aqueous processing is the reactivity of active materials upon contact with water, which leads to phase transitions at the active materials surface [180], as well as the formation of lithium carbonate (Li_2CO_3) and lithium hydroxide (LiOH) within few minutes with a reaction layer thickness of about 10 nm due to the existence of residual Li at the NMC surface [181-183]. Besides, transition metal-ions dissolution from cathode materials in water was reported [184, 185], while Hamam et al. [186] further studied this phenomenon using inductively coupled plasma optical emission spectroscopy (ICP-OES) and found two pH-dependent regimes, where little to no transition metal dissolution was found in high pH solution (pH > 8), but the concentration of transition metal in solution increased significantly at lower pH value regimes. Another issue is the slurry pH increase owing to the Li leaching [187], which leads to chemical corrosion on Al current collector along with hydrogen gas formation during the coating process [27, 28]. The reaction can be described as follows [44]:

$$Al + OH^- + 3H_2O \rightarrow Al(OH)_4^- (s) + \frac{3}{2} H_2 (g) \quad (3.18)$$

This gives rise to the existence of huge cavities within the composite electrode with diameters ranging from 10 – 150 µm and pinholes on the electrode surface [171]. In addition, the

corrosion of Al is also observed in the water-based LTO anode slurry owing to its alkaline nature [112].

In order to enable the aqueous processing for cathodes, three methods are introduced in general to counteract the above-mentioned effects:

(i) using coated cathode materials,

(ii) providing coating on Al current collector to prevent its contact with alkaline slurry,

(iii) adjusting slurry pH with acid addition during mixing process.

Jo et al. [188] provided Li_3PO_4 coating on NMC 622 at 80 °C and subsequently dried at 500 °C, and the cells with coated NMC 622 showed higher rate capability, capacity retention, as well as lower impedance after 150 cycles in comparison to reference cells with uncoated NMC 622. Notake et al. [189] compared aqueous processed Al_2O_3 coated $Li_{1.2}(Ni_{0.18}Co_{0.03}Mn_{0.58})O_2$ with uncoated NMC 622 processed with PVDF binder and found no difference in capability retention. Furthermore, carbon, Al_2O_3, and Nb_2O_5 coating were applied for aqueous processed LNMO cathodes and the electrochemical performance was enhanced [190]. In addition to that, carbon coating on Al current collector was reported for NMC 111 [191] and LNMO [192], and the corrosion can be avoided by applying a coating with 5 µm in thickness [193]. However, the first two approaches involve additional processing steps, resulting in increased production costs, and a decreased energy density due to additional weight from coating, while the third method provides a feasible and cost-efficient solution to the aqueous processing of cathode materials.

It is worth noting that the slurry pH value and the acid type can profoundly affect the mechanical properties and electrochemical performance of aqueous processed electrodes. Loeffler et al. [194] compared the addition of phosphoric acid and formic acid in NMC 111 slurry during mixing process and validated the superior electrochemical performance of cells containing electrodes processed with phosphoric acid. Aqueous processing of NMC 111 with pH modification by adding acetic acid or using LiPAA binder was reported by Bauer et al. [29], the optimal slurry pH value was found to be at 9 regarding to the respective rate capability analysis. Other candidates such as lithium sulfate (Li_2SO_4) [195] or boric acid [196] were also reported. However, most studies have shown that the addition of phosphoric acid in different NMC materials leads to a significant improvement in electrochemical performance, such as for $LiNi_{0.4}Mn_{0.4}Co_{0.2}O_2$ (NMC 442) [197], $Li_{1.2}Ni_{0.16}Mn_{0.56}Co_{0.08}O_2$ [31], NMC 532 [43, 198, 199], NMC 622 [200, 201], and NMC 811 [202, 203]. On the one hand, the addition of phosphoric acid can adjust the slurry pH value and prevents chemical corrosion between the slurry and the Al current collector. On the other hand, it can also stabilize the interphase of NMC particles in contact with water, which could be due to the formation of a protective transition metal phosphate layer with a thickness of less than 10 nm, as confirmed for NMC 111 [194] or for LNMO [30].

3.2.3. Electrode coating, drying, and calendering

After mixing process, the anode or cathode slurry is coated onto a current collector foil and subsequently dried in ovens. Slot-die coating is the most used large-scale coating technique in battery industries. Hereby, the film thickness or mass loading can be adjusted by varying the viscosity of slurry, coating speed, or controlling the gap width between slot-die lip

and current collector [204]. Slot-die coating is usually combined with advanced roll-to-roll (R2R) process to achieve a high throughput [205]. A coating speed of 30 ± 5 m/min is typically applied in commercial LIB production, while a doctor blade with a coating speed of 0.3 to 1 m/min is usually used in laboratory for slurries with low viscosity [3, 206].

The wet slurry coated on the current collector is subsequently dried, which is a solvent evaporation process consisting of two steps – capillary action and diffusion. The film adhesion strength of water-based graphite anode decreases at a high drying rate in comparison to a low drying rate; a binder accumulation at the electrode surface is observed, while at low drying rate, the binder gradient inside the film is decreased [207]. Similar results are predicted using the mathematical model proposed by Font et al. [208]. Drying process of NMP-based NMC 111 was experimentally studied and compared with simulation results. Two dynamical regimes were observed: solvent evaporation with a constant rate (constant thickness decrease) and solvent evaporation from microstructures with low to zero evaporation rate (the film thickness remains the same) [209]. In other research, the drying process was analyzed using a continuum mathematical model and it was found that the drying was not a heat transfer controlled but a mass diffusion-controlled process. Moreover, 90 % of the drying was completed in half of the total time, while the remaining 10 % solvent was removed in another half of the total drying time [11]. The distribution of active material and conductive agent in NMP-processed NMC 622 cathodes and aqueous processed graphite anodes at different drying temperatures (from room temperature to 120 °C) were investigated: NMC 622 particles tended to concentrate on the electrode surface with increasing drying temperature, however, no significant difference in the distribution of graphite particles was observed when dried at different temperatures; The highest adhesion strength and highest rate capability were shown for the NMP-processed NMC 622 cathodes dried at room temperature, while the drying temperature had no significant influence on the electrochemical performance and adhesion strength for aqueous processed graphite anodes with a wet thickness of 300 µm [210]. In industrial production lines, long drying ovens with heating zones adjusted to different temperature are applied [211]. The stepwise drying close to the room temperature could realize a more homogenous distribution of binder and conductive agent in comparison to one-stage drying at 70 °C and achieved lower internal cell resistance and a higher capacity retention during lifetime analysis at 1C [209].

During calendering, dried electrodes are guided between rolls and subjected to pressure and temperature. This is a crucial step in increasing the volumetric energy density and improving the electronic conductivity of the electrodes. As a result, the electrode thickness and porosity will be reduced afterwards. Besides, Bockholt et al. [212] concluded that the contact area between the NMC 111 particles and the conductive agent network was increased with decreasing electrode porosity from 45% to 25% by SEM image analysis. The study of calendering on PVDF-based NMC 111 cathodes showed that a high content of active material and high amount of solvent resulted in electrodes with higher porosity even after calendering process, while a film-like conductive phase was formed after calendering with high conductive agent / PVDF content and thus resulted in enhanced electrochemical performance [213]. A study of NMC 111 cathodes with the same chemical composition showed that calendering had no significant effect on electronic conductivity, while charge transfer resistance increased with

decreasing porosity and an optimized porosity of 30 to 40% was reported [214]. Besides, calendering has impact on the electrolyte wetting, a modest calendering of graphite anode could improve the wetting due to the alignment of particles [215]. However, wetting rates for graphite anodes as well as NMC 532 cathodes decreased for strong calendering, which should be owing to the closure of micropores inside the electrodes [216].

Before cell assembly, a secondary drying process is usually performed to remove the residual water in electrodes. Recent research compared the residual moisture and discharge capacity of cells containing aqueous processed NMC 532 cathodes and found that a drying temperature of 120 °C for 2 h favored a better cell performance [217].

3.2.4. Solvent-free electrode manufacturing

Commonly applied electrode fabrication requires the slurry mixing in advance and followed by coating, drying, and calendering processes, as illustrated in Figure 3-12. However, in order to reduce the production costs and avoid solvent recovery, dry coating procedures without solvent were recently introduced and are attracting more attention [218]. Different methods such as dry R2R direct calendering [219, 220], spraying [221, 222], direct pressing [223, 224], 3D printing using fused-filament fabrication [225, 226], have been reported in the last decade.

Gyulai et al. [219] studied the effect of dry mixing intensity on the electrochemical properties of R2R calendered NMC 622 cathodes using PVDF binder (subsequently laminated to the Al foil) and found that electrodes fabricated with high-intensity dry mixing (1500 to 2000 rpm) exhibited lower electric resistivity and higher discharge capacities from C/20 to 3C in comparison to those processed with low- or medium-intensity dry mixing (500 to 1000 rpm); Besides, a coating speed of up to 5 m/min and film thicknesses of 72 to 87 µm were achieved. A similar approach was applied to fabricate solid electrolyte membranes with a thickness of 15 to 20 µm using polytetrafluoroethylene (PTFE) fibrilization for all-solid-state batteries, a capacity retention of 94 % was achieved after 250 cycles at C/3 [227]. R2R dry calendering method has the advantage of upscaling with existing equipment, however, the binders for this procedure are still limited and require further investigation. Dry spraying has been applied for the fabrication of LCO [221], NMC 111 [228], and graphite electrodes [222] using an electrostatic spray gun, but it is still challenging to accurately control the film thickness and high-voltages (10 to 25 kV) are required during this process [222]. 3D printing of electrodes for microbatteries allows for precise control of film thickness and electrode design, however, the practical capacities of cells containing printed electrodes are less than 50 % in comparison to those containing electrodes with the same active materials processed with wet coating method [225, 226].

3.2.5. Thick-film electrodes for LIBs

Employing thick-film electrodes with high mass loading is a practical strategy to increase the energy density of LIBs, since less inactive materials such as separators and current collectors are used [21]. Meanwhile, high areal capacity leads to a reduced cell assembly time and lower processing costs. Low-temperature sintered LCO cathodes with layer thicknesses ranging from 300 – 1600 µm were fabricated with sputtered gold as current collector. The ultra-thick electrodes with 1300 µm thickness showed 16 times higher areal capacity in comparison

to the commercial electrodes at C/10 [229]. Ibing et al. [230] prepared aqueous processed NMC 111 electrodes having layer thicknesses larger than 320 µm with high solid content (65 wt%) or with addition of carbon micro fibers. They found that the mechanical stability of thick-film electrodes was significantly improved without crack formation during drying and the capacity was almost as high as reference with standard active mass loading at 1C.

Numerical modeling of cells containing NCA and mesocarbon microbead (MCMB) proved that energy density increased with increasing cathode thicknesses from 60 to 240 µm at C/5, however, at higher C-rates e.g. 1C and 2C, the energy density increased at first as the cathode thickness increased, but dropped rapidly once the critical thickness was reached [23]. However, cells with thick-film electrodes generally show drawbacks such as serious capacity drop at C-rates ≥ C/2, low power capability, brittleness, as well as a low adhesion to current collector foil [24]. The capacity fade is mainly due to the accumulation of cell polarization, Li-ion diffusion limitation at high C-rates, and local material degradation, which results in an increase of charge transfer resistance [24, 231]. In general, batteries with thick-film electrodes are more suitable for stationary electrochemical storage system with low C-rates (< C/10) rather than high power applications. However, thick-film electrodes can be significantly better used in combination with the 3D battery concept, which means that 3D architectures (as shown in chapter 3.1.5) are required to counteract cell polarization, improve electrolyte wetting, and reduce mechanical issues [232].

3.3. Laser processing for LIBs

Laser is a versatile tool for electrode processing in battery industry since it can achieve precise controlled and non-contact processing of different materials. The optical laser beam shaping and especially the focusing of laser beam onto the sample surface is an important technical measure during laser processing, as shown in Figure 3-13.

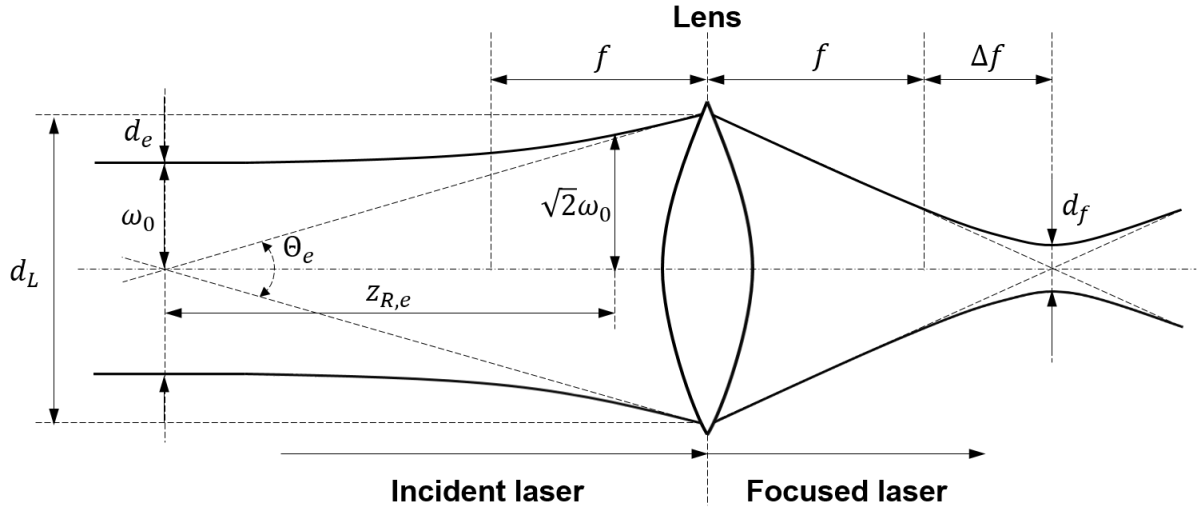

Figure 3-13. Schematic view of the focusing of a Gaussian laser beam, reproduced from [233]. d_e and d_f are the diameters of the incident and focused laser beams, respectively; ω_0 is the beam radius at the beam waist, $z_{R,e}$ is the Rayleign length of the incident laser beam, d_L is the laser beam diameter on the focusing lens; f is the focal length of the lens, Θ_e is the divergences of the incident laser beams.

The beam quality factor M^2 [-] is commonly used to measure the collimation of a Gaussian laser beam and is defined as follows [234]:

$$M^2 = \frac{\pi d_e \Theta_e}{4\lambda} \tag{3.19}$$

where Θ_e [°] is the beam divergence of the incident laser beam, λ [nm] the wavelength of the laser, d_e [mm] the diameter of the incident laser beam. The subscripts e and f indicate incident and focused laser beams, respectively. The d_e [mm] is defined as follows [233]:

$$d_e = 2\omega_0 = 2\sqrt{M^2 \frac{z_{R,e}\lambda}{\pi}} \tag{3.20}$$

where ω_0 [µm] is the beam radius at the beam waist, $z_{R,e}$ [mm] the Rayleigh length of the incident laser beam, i.e., the distance from the beam waist to the position where the beam radius is increased by a factor of $\sqrt{2}$. Thus, in order to get a laser beam with small spot size, M^2 should be as small as possible. As for the focused laser beam, the laser beam diameter at the focal plane is given by the following equation [233]:

$$d_f \approx \frac{M^2 f}{d_L}\frac{4\lambda}{\pi} \tag{3.21}$$

where d_f [µm] is the beam diameter at the focal plane, f [mm] the focal length of the lens, d_L [mm] the laser beam diameter on the focusing lens. During the laser processing, the laser diameter at the focal plane should be adjusted as small as possible in order to achieve a high energy density on the surface of samples, thus a short focal length, a small beam quality factor M^2, as well a large beam diameter on the focusing lens are beneficial according to equation (3.21). The last point indicates that the laser beam should be expanded before exposing to the focusing lens.

When the laser beam reaches the electrode surface, a part of the energy is reflected, while absorption and transmission occur simultaneously. However, no transmission was detected during laser cutting of graphite anode [235] and it is neglectable because the thickness of electrodes for LIBs is typically larger than 60 µm [20]. The energy of laser radiation is first coupled to the electrons and then transferred to their lattice atoms over a short period in the order of 1 picosecond (ps); After about 100 ps, the electrons and atoms reach a temperature equilibrium [233]. Therefore, for lasers with pulse duration larger than nanosecond (ns), there is no temperature difference in electron and lattice. However, for laser processing using lasers with pulse duration shorter than 10 ps and in femtosecond (fs) range, a two-temperature model was introduced to describe the temperature of electrons and lattice of materials during laser processing [236]. Lu et al. [237] simulated the temperature distribution of electrons and lattice and found that the temperature gradient from metal surface to bulk material decreased with decreasing pulse duration from 1 ns to 900 fs; Besides, the peak electron and lattice temperature increased at the center of laser radiation with decreasing laser pulse duration using the same total laser pulse energy. The laser-material interaction leads to extreme heating and cooling with rates of 10^3 – 10^{10} K/s in the near surface region while the bulk material remains virtually unaffected [238].

In addition, since composite electrodes consist of different materials, such as polycrystalline Li transition-metal oxide, conductive agent with sub-micrometer particle size, and polymer binder, the interaction between laser radiation and electrode materials is quite complex, including various photochemical and photothermal processes [239]. For example, the grain boundaries in polycrystalline active material leads to different absorption and transmission behavior of laser radiation in comparison to that in single crystalline [233]. Furthermore, the optical energy absorbed by the material depends on the laser wavelength, laser polarization, laser intensity, pulse duration, incident angle, temperature, as well as material properties and its surface condition [233]. Besides, the laser induced plasma, which is an electrically conductive gas medium consisting of electrons, atoms, ions, and molecules, can interact with laser radiation and changes the laser beam properties such as laser power and beam profile [240].

Ultrafast laser enables a highly precise, high-quality, and rapid processing of materials, since the most of the absorbed optical energy is used for the ablation process and the surrounding material is almost not affected by a thermally driven impact. [241]. The relation between penetration depth δ [cm] and pulse duration τ [s] can be described as [242]:

$$\delta \approx \sqrt{4\alpha\tau} = \sqrt{4\tau \frac{\kappa}{c_p \rho}} \tag{3.22}$$

here α [cm^2/s] is the thermal diffusivity of a material which is determined by the thermal conductivity κ [W/(cm·K)], the specific heat capacity c_p [J/(g·K)] and the density ρ [g/cm^3]. The penetration depth δ indicates the extent to which the laser heat can penetrate in a material, and it contributes to the size of the heat affected zone (HAZ). Equation (3.22) shows that the heat penetration depth deceases with decreasing pulse duration. Therefore, ultrafast laser processing with pulse durations in ps or fs range is most beneficial to keep the heat impact in LIBs active materials in the nanometer range [239].

Laser can be applied in different processes for LIBs, e.g., welding / brazing, cutting, annealing / drying, and structuring / surface modification [239], as presented in Figure 3-14. Laser welding of Cu and Al tabs with multiple current collector flags or the welding of battery housings have been studied and introduced into the battery industries [243-246]. In comparison to state-of-the-art ultrasonic welding, laser welding provides a contactless fast processing with limited local heat effect and thus is very suitable to achieve cost reduction in mass production. As for laser electrode cutting, pulsed ns lasers with wavelengths from 500 to 1070 nm are usually applied, the HAZ and the ablation width of coated composite electrode materials (“clearance width”) are investigated as a function of different cutting speed and average laser power, and the clearance width is usually smaller than 40 µm [235, 247-250]. Laser-assisted drying of the electrode wet coating is an alternative to conventional electrode drying using air floatation dryers and ovens. However, only laboratory scale is reported [251], which means that this technique is still in early development state and needs sufficient evaluation and development [252].

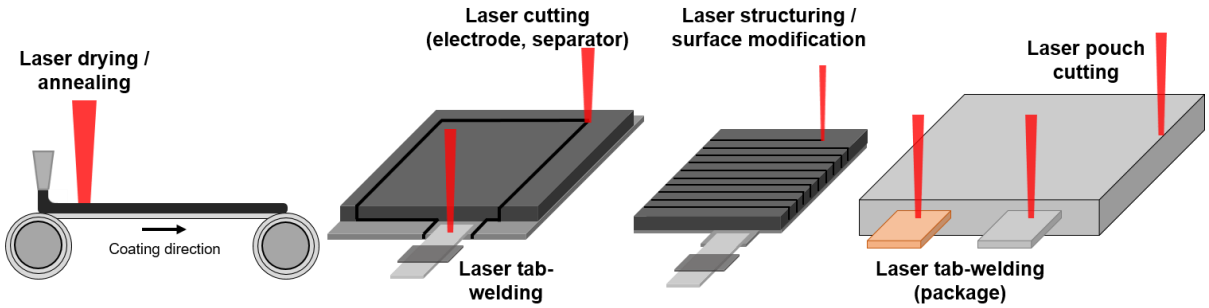

Figure 3-14. Laser processes for battery manufacturing.

Laser structuring of current collectors has been reported using direct laser interference patterning (DLIP) technique[253, 254], laser-induced periodical surface structuring (LIPSS) [12, 14, 255, 256], or direct laser ablation with wavelength ranging from 1030 nm, 515 nm [257] to 355 nm [258]. The film adhesion strength between composite graphite anode and a laser structured Cu current collector can be increased [253, 257], while the respective electrochemical performance of cells with structured current collector foils may vary with regard to the applied laser and process parameters. In another study, Cu foils were laser structured using an UV pulsed laser with a wavelength of 355 nm and were deposited with Li; The internal stress and the piercing of SEI were relieved during cycling, while full-cells containing Li deposited on the laser structured Cu foils vs. LFP cathodes showed 45 mAh/g higher capacity after 600 cycles than those with unstructured Cu foil [258]. In addition, the PP separators coated with aluminum oxide were laser structured using a fs laser with a wavelength of 515 nm, different patterns such as micro-channels with 50 µm distance and through-holes with 300 µm pitch were realized; Full-cells containing NMC 111 cathodes and graphite anodes combined laser structured separators were assembled and those containing laser structured separators with micro-channel structures showed high cycling stability with over 95 % capacity retention after 200 cycles at 2C, while cells containing unstructured separators reached 85 % capacity after the same amount of cycles; However, the ones with through-holes structured separator exhibited fast capacity drop and reached 80 % after 110 cycles [259]. The application of the laser structuring in electrodes will be further discussed in the next chapter.

3.3.1. 3D electrode architectures by using ultrafast laser ablation

Laser ablation can be applied to generate 3D electrode architectures with different designs for LIBs. This processing technique was introduced for LIBs by Karlsruhe Institute of Technology (KIT) about 15 years ago [260], LCO thin-films in a few micrometer range were fabricated using magnetron sputtering and subsequently laser structured using excimer lasers with two wavelengths (248 and 193 nm) and pulse durations of 4 to 6 ns; Cone structures were formed after laser structuring with an estimated 6-fold increase in surface area. One year later, a further study compared different pulse numbers and found that 40 to 50 pulses were optimal for the formation of conical structures in LCO thin-films; In addition, electrochemical analysis revealed that the cells with laser-treated LCO electrodes had a 30 – 40 mAh/g higher discharge capacity at C/4 in comparison to ones with unstructured electrodes, and retained over 99 % capacity after 30 cycles while the reference cells with unstructured electrodes lost 8 % of their capacity [261]. Besides, the cells with laser structured LCO electrodes retained 53

to 61 % capacity after 300 cycles at 1.25C, while those with unstructured electrodes had 10 % capacity at the end [262]. Two-step laser structuring of LCO electrode with laser fluences of 0.5 and 1.9 J/cm^2 and a laser wavelength of 248 nm was reported by Kohler et al. [263] in 2010, the laser ablation and re-deposition led to an increased cone height up to 8.4 µm, whereas the thickness of sputtered film was 3.5 µm; Besides, cells with two-step laser structured electrodes exhibited 78 mAh/g after 100 cycles at 1C, while those with unstructured electrodes showed nearly no capacity after 20 cycles under the same C-rate.

Pröll et al. [12] fabricated radio frequency (RF) magnetron sputtered LMO thin-film cathodes with free-standing conical architectures using ns excimer laser ablation by chromium / quartz mask imaging technique. It was found that the cells with structured thin-film electrodes showed higher rate capability at C/5 and C/2 in contrast to those with unstructured electrodes, and no delamination or crack formation of compact electrode materials were observed in cycled electrodes with free-standing structures. However, LMO cathodes used in their study have a thickness of 2.0 – 3.3 µm, which is much lower in comparison to state-of-the-art composite electrodes with 50 – 70 µm thickness. Thin-film as well as tape-cast LCO cathodes with respective layer thickness of 3 µm and 80 µm were laser structured using the same laser and cells with structured electrodes showed higher capacity retention at 1C after 100 cycles [14]. In the work of Pfleging et al. [13], tape cast NMC and LMO electrodes with thickness of 55 µm and 103 µm, respectively, were subsequently structured using an ns ytterbium-doped yttrium aluminum garnet (Yb:YAG) fiber laser and the wetting of liquid electrolyte was studied. They showed that the wetting process was accelerated in laser structured electrodes due to the existence of capillaries, which led to enhanced lifetimes of cells with structured electrodes in pouch cell design. Besides, the time-consuming storage of batteries after assembly could be avoided using laser structured electrodes with a perspective to reduce processing costs during electrolyte infiltration process and subsequent warm aging as well as a reduction in scrap rate. Five years later, similar conclusions were drawn by Habedank et al. [264] using *in situ* neutron radiography. The pouch cells containing laser structured electrodes with grid structures were fully wetted after 15 min, while those with unstructured electrodes reached 49 % wetting after the same time period [264].

Mangang et al. [15] investigated the influence of laser pulse duration and line energy (“average laser power” divided by “laser scan speed”) on the ablation of LFP composite cathodes by adjusting pulse duration τ from 350 fs to 200 ns and found that the aspect ratio A_R (“ablation depth” divided by “channel width”) increased with decreasing pulse duration, and the A_R reached the highest value of 2.6 for τ = 350 fs. Besides, comparing to laser structured electrodes with other pulse durations, the one with 350 fs showed the highest discharge capacity at both 1C and 2C, pouch cells with line structured LFP cathodes vs. graphite anodes showed enhanced capacity retention at C/2 after 500 cycles. The structuring of LFP cathodes by applying ns laser radiation was further studied and it was suggested that multiple laser ablation passes at low laser fluence is beneficial to achieve structures with high aspect ratio in electrodes [265]. Tsuda et al. [16] fabricated through-holes with 20 µm diameter in composite LFP cathodes and graphite anodes using ps pulsed laser radiation as shown in Figure 3-15-d. They found that the charge transfer resistance was reduced in cells with laser patterned electrodes and a clear increase in capacity retention was achieved in cells with drilled

electrodes for C-rates greater than or equal to 2C. This method was further studied in double side coated LFP cathodes with different loading on each side; And a significant degradation was found in cells with unbalanced LFP electrodes vs. Li, while cells containing laser drilled electrodes or electrodes with non-though-holes showed enhanced performance at high C-rates [266].

Line patterns with 200 µm pitch were generated in NMC 532 cathodes with layer thicknesses ranging from 100 to 210 µm and for two different electrode porosities (26 % and 50 %). It was demonstrated that the decrease of power and energy density caused by thick-film and dense electrodes can be compensated by laser structuring through the generation of expanded Li-ion diffusion pathways [267]. For thick-film cathodes made of NMC 622 with thicknesses of 91 to 250 µm, which were structured with line patterns with pitches of 200 to 600 µm, an increase in energy density was achieved for almost all cells at C rates of 1C to 5C compared to cells with unstructured electrodes [268]. Dunlap et al. [269] studied the effect of laser ablation on the chemistry and crystallography in laser-impacted regions near grooves in NMC 622 cathodes using energy dispersive X-ray spectroscopy (EDX) and XRD. They found that no phase transition of NMC 622 occurred by applying fs laser ablation, but an increase in average NMC crystallite size of 40 nm was observed, indicating a localized laser-induced annealing process during laser processing. Ultra-thick-film LCO cathodes and graphite anodes with layer thicknesses of 700 µm and 650 µm, respectively, were laser-structured with an ablation depth of 2/3 of the electrode thickness. Cells with these structured electrodes exhibited a 5 to 10 mAh/cm^2 higher areal discharge capacity at C/20, C/10, and C/5; And a lower ionic resistance was observed [270]. NMC 811 cathodes with 40 and 100 µm layer thicknesses were structured using line patterns with 200 µm pitch; The respective mass loss decreased with increasing film thickness, while cells with thick-film cathodes showed lower charge transfer resistance and 3 times higher capacity at 2C in comparison to ones with unstructured electrodes [271].

Laser patterning of composite anodes has been studied during the last decade and is recently gaining more and more attention. Grid and line patterns with 100 µm pitch were applied for the structuring of graphite or the mixture of graphite and silicon composite (Si/C) anodes, as shown in Figure 3-15-a and –b. Cells with structured graphite anodes exhibited high rate capability up to C-rates of 3C, while improved capacity retention and lifetime were observed for cells with grid structured Si/C anodes in comparison to reference cells with unstructured electrodes. In addition, *post mortem* analyses led to the conclusion that the mechanical tension in cycled Si/C anodes was significantly reduced during cell operation [19]. The influence of laser peak fluence and laser pulse repetition rate on the laser structuring of graphite anodes was studied; a high laser peak fluence (30 J/cm^2) and low repetition rates (10 – 100 kHz) were beneficial to a more sufficient laser structuring, since high repetition rates result in plasma shielding effects which in turn reduces the laser ablation efficiency [18]. The volumetric capacity of graphite anodes with mass loading in the range of 10 to 15 mg/cm^2 and a low porosity of 15 % was analyzed at different C-rates; A higher volumetric capacity was gained in cells with laser patterned anodes in comparison to ones with unstructured anodes at C-rates of C/2 and 1C [272]. In addition, the effect of calendering degree on the graphite anodes in combination with laser structuring was investigated. Hereby a shift of maximum

electrochemical performance improvement towards lower C-rates with increasing electrode density, i.e., higher calendering degree, was observed with maximum volumetric energy densities of 600 – 1000 Wh/l at power densities of 2500 – 6000 W/l for cells containing anodes with 27 % porosity [273].

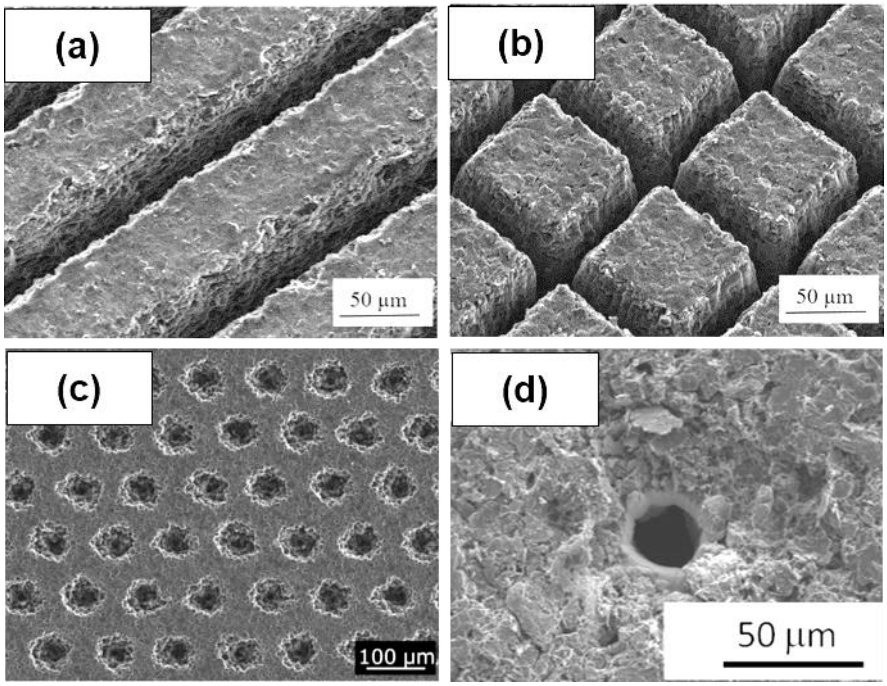

Figure 3-15. SEM images of laser structured electrodes with (**a**) line patterns (silicon / graphite composite anode) [19], (**b**) grid patterns (silicon / graphite composite anode) [19], (**c**) hole patterns without reaching the current collector (graphite anode) [274], and (**d**) through-hole patterns (drilling of the whole double-side coated electrode) from the laser incident side of graphite anode [16].

The impact of laser parameters such as laser fluence, number of laser pulses, and laser pulse duration from 0.4 – 20 ps on the structuring of graphite anodes with hole patterns were investigated. For a number of up to 10 laser pulses, a linear increase of ablation depth was observed for laser fluences smaller than 5 J/cm^2, while for fluences larger than 5 J/cm^2 the ablation depth continued to increase linearly with number of pulses; Besides, the applied pulse duration variation (0.4 to 20 ps) showed no obvious impact on the ablation rate [275]. Hille et al. [276] investigated the influence of the integration position of the laser process on the final electrochemical performance of graphite anodes. Three scenarios were considered: after coating, after drying, and after calendering. The diameter and depth of holes were analyzed by laser scanning microscopy and the first scenario – laser structuring after coating resulted in holes with diameters of 37.5 ± 9.3 µm, which is larger than other two options (24.9 – 29.8 µm). This might be explained by the evaporation of the solvent in the wet electrode, which could accelerate the ablation of the electrode materials. In addition, the peel-off analysis revealed that the adhesion strength was reduced by 90 % and 75 % for laser structuring after drying and calendering, respectively, whereas the electrodes with laser structuring after coating had almost the same adhesion strength as the unstructured electrodes. Rate capability analyses showed no difference in discharge capacity of cells containing laser structured electrodes with structuring after drying and calendering process at 1C to 5C, while at C-rates 3C to 5C, the capacity increased by 10 – 30 % in both cases in comparison to those with unstructured

electrodes. However, the cells containing laser structured electrode with laser structuring after coating exhibited 5 – 10 % higher capacity.

The combination of laser patterned cathodes and anodes with 3D architectures extends the potential of laser processing in battery industry and opens new horizons for increasing the energy density and power density of LIBs. Si/C anodes with different types of Si nano-scaled powders were laser patterned and electrochemically characterized vs. Li in coin cells or vs. NMC 622 in pouch cells. An extension in lifetime of cells with laser structured Si/C electrodes was reported; However, the overall cell degradation owing to mechanical and chemical processes could not be fully suppressed [170]. Full-cells containing graphite anodes with hole structures arranged in hexagonal design with a lateral length pitch of 70 µm vs. unstructured NMC 111 were investigated and simulated: The respective results showed that the laser structuring is beneficial at medium C-rates from 2C to 4C, where the Li concentration in structured anodes is more evenly distributed in contrast to that in unstructured ones [17]. Zheng et al. [277] quantitatively measured the Li distribution in structured graphite anodes using laser-induced breakdown spectroscopy (LIBS) and could prove for the first time that along the contour of laser-generated structures an enhanced Li-ion diffusion kinetics takes place, which indicates the formation of new Li-ion diffusion pathways in 3D electrode architectures. A similar mechanism was observed in Si/C anodes, where a homogenous Li-ion distribution was found in cycled laser structured electrodes, suggesting a high Li-ion mobility in the free electrolyte in contrast to that in the electrolyte embedded in porous composite electrode. Besides, the mechanical stress which causes degradation in cycled Si/C anodes was significantly reduced after being cycled at elevated C-rates from C/5 to 2C [278].

The electrochemical impedance and rate capability of cells with laser structured graphite anodes vs. unstructured NMC 111 cathodes were measured at different temperatures varying from -15 °C to room temperature [279]. It was found that the charge transfer resistance was reduced by laser structuring at all applied temperatures, which might be due to a reduced tortuosity in electrodes. In addition, it was proven that the improvement in discharge capacity at different C-rates varied as a function of temperature. Besides, Li-plating on laser structured anodes could be effectively reduced in comparison to unstructured ones. The capacity of pouch cells with unstructured NMC 111 cathodes vs. hole-structured graphite anodes (Figure 3-15-c) were increased up to 2.9 Ah, and the EoL of cells could be extended from 8 to 182 cycles until reaching the SOH of 80 % by applying laser structuring of graphite anodes [280]. The same type of hole pattern was generated in NMC 622 cathodes and graphite anodes with state-of-the-art thicknesses of 50 to 70 µm. The effect of laser patterning configuration in cathodes and anodes on the electrochemical performance was investigated by comparing the combination of structured / unstructured on anodes / cathodes, and it showed that the cells with both structured anodes and cathodes deliver the highest rate capability from 2C to 5C, while cells with structured anodes display the second highest discharge capacity [274]. Similar research with coin cells containing laser structured NMC 622 cathodes and graphite anodes with line structures also showed that the highest capacity increase was achieved by laser processing of both electrodes; In addition, the Li-plating on the graphite anode could be reduced; Besides, they confirmed again that the wetting of electrolyte can be significantly accelerated by patterning either one of the electrodes with line structures [269].

The electrochemical performance data of cells with laser patterned NMC 811 cathodes and graphite anodes using line, grid, and hole structures were evaluated by solely electrochemically based simulations using finite element implementation [281]. The influence of pattern pitch, ablation width, and electrode film thickness on the electrochemical performance of cells was predicted:

- at low C-rates, the capacity of cells containing structured cathodes decreases with increasing ablation width, while for high C-rates, anode structuring shows more benefit in improving the cell performance;
- laser structuring can reduce the Li-ion gradients within the electrolyte due to the additional generated diffusion pathways;
- laser patterning of cathodes is necessary for high power application or with high mass loading since the cell polarization could be reduced;
- line patterns have additional benefit in accelerating liquid electrolyte wetting due to the capillary effect.

However, in all of the above-mentioned comparative studies, the cell-balancing-factor, which refers to the areal capacity of the anode divided by the areal capacity of the cathode, was not kept constant, i.e., full-cells with laser structured electrodes were compared with reference cells with different cell-balancing-factor. It is worth mentioning that this may have an impact on performance results and the conclusions drawn. In addition, in most of the previous studies, the areal capacities of cathodes and anodes are smaller than 4 mAh/cm^2, which in general corresponds to electrode film thicknesses smaller or equal 100 µm. Therefore, so far, the advantages of laser patterning on electrodes are not fully demonstrated for the next generation batteries containing thick-film and ultra-thick-film electrodes with layer thicknesses of larger than 100 µm and 150 µm respectively. In ongoing research, it is also essential to control design pattern and active mass loss of laser structured electrodes with regard to the targeted application scenarios to achieve the most efficient full-cell configuration.

4. Experimental methods

In this chapter, each step of the electrode fabrication process will be described in detail, from electrode materials characterization, mixing, coating, to calendering and subsequent laser structuring. The electrodes were then laser cut into appropriate dimensions and assembled in coin cells vs. Li or in pouch cells vs. graphite anodes. The cells were electrochemically characterized using cyclic voltammetry (CV), rate capability analyses, lifetime analyses, and EIS analyses.

4.1. Characterization of active materials

Two different commercially available NMC 622 powders were used as active material for cathodes, which were polycrystalline NMC 622 with big particle sizes (BASF SE, Germany) and with smaller particle sizes (Targray Inc., Canada), while coke-based synthetic graphite (SPGPT808, Targray Inc., Canada) was applied as active material for anodes. Before slurry mixing, the morphology, chemical composition, particle size distribution, as well as Brunauer-Emmett-Teller (BET) surface area of active materials were characterized.

4.1.1. Composition, structure, and surface topography

The crystal structure and phase identification of two different NMC 622 powders were performed by XRD analysis (Empyrean, Malvern Panalytical Ltd., Malvern, UK). About 5 g of each powder sample was loaded onto a powder holder and pressed by a metal block. Afterwards, a razor blade was used to remove the extra powder and make the top surface of tapped NMC 622 powder flat. The XRD analysis was performed using CuKα radiation in 2θ range of 5 – 90° and 200 s per step at 40 mA and 40 kV.

To determine the concentrations of Li and the transition metals (Ni, Mn, Co), the pristine NMC 622 powders were analyzed using ICP-OES (iCAP 7000 Series, Thermo Fisher Scientific Inc., USA). The samples were firstly dissolved in acid and then pumped as an aerosol to an argon plasma. Due to the high plasma temperatures of 6000 K to 10000 K, the material is excited or atomized. The light emitted when the atoms return to their ground state is captured by a spectrometer. The intensity of the light is proportional to the concentration of the element in the sample and the elemental composition of the sample can thus be acquired by assigning to the element-specific wavelengths [282]. Oxygen content was quantitatively determined using carrier gas hot extraction method (G8 Galilei, Bruker AXS GmbH, Germany), where the oxygen in the sample was reduced by carbon to CO and CO_2 and subsequently analyzed with IR-detector [283].

A scanning electron microscope (Phenom XL G2 Desktop, Thermo Fisher Scientific Inc., Germany) was applied to obtain the high-resolution images of different NMC 622 powders. A piece of conducting carbon tape was cut and pasted on the sample holder and active material powders were tapped onto the carbon tape. 3 – 10 kV accelerating voltage and different signal types including secondary electrons (SE) and back-scattered electrons (BSE) were used for SEM imaging, while magnifications ranging from 1000 to 25000 times were applied to investigate the surface of different NMC 622 as well as graphite particles.

4.1.2. BET-surface area and particle size distribution

N_2 gas adsorption was applied to measure the BET-surface areas of different active materials using 60 mm Hg/min at room temperature (Gemini VII 2390a, Micromeritics Instrument Corporation, UK). BET theory is most commonly used to explain the adsorption isotherm of powders. The adsorption isotherm can be described as follows [284, 285]:

$$\frac{P/P_0}{V_{ads}(1-\frac{P}{P_0})} = \frac{1}{V_m C} + \frac{C-1}{C}\frac{P/P_0}{V_m} \tag{4.1}$$

Where V_{ads} [m^3] is the volume adsorbed at pressure P [mbar] and absolute temperature T [K], P_0 [mbar] is the saturation pressure of an adsorbate at the temperature of adsorption, and V_m [m^3] is the volume of adsorbed monolayer gas, C [-] is the BET constant which relates to the heat of adsorption. Equation (4.1) can be rewritten as:

$$\frac{1}{(V_{ads}/(P/P_0)-1)} = \frac{C-1}{CV_m}(\frac{P}{P_0}) + \frac{1}{V_m C} \tag{4.2}$$

Thus, a linear relationship exists with $\frac{1}{(V_{ads}/(P/P_0)-1)}$ on the y-axis and P/P_0 on the x-axis, as shown in Figure 4-1.

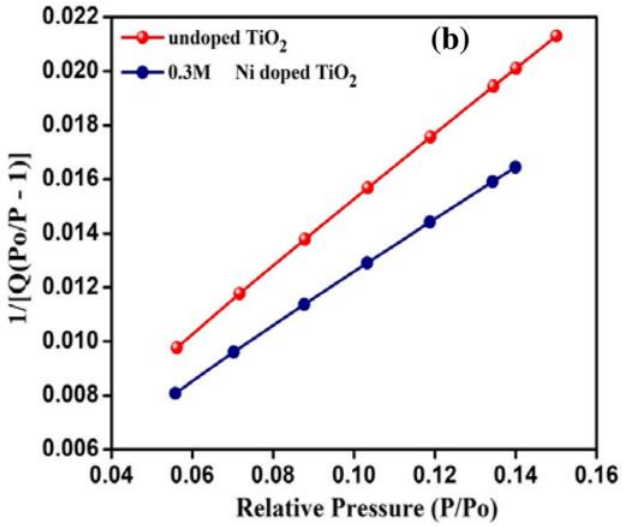

Figure 4-1. A typical multi-point linear curve for the calculation of BET surface area (here the materials are TiO_2 and Ni-doped TiO_2) [286].

The slope A [m^{-3}] and the y-intercept I [m^{-3}] derived from the plot can be applied for the calculation of V_m and C:

$$A = \frac{C-1}{CV_m} \tag{4.3}$$

$$I = \frac{1}{V_m C} \tag{4.4}$$

while the V_m and C can be rewritten by combining equation (4.3) and (4.4):

$$V_m = \frac{1}{A+I} \tag{4.5}$$

$$C = \frac{A}{I} + 1 \tag{4.6}$$

The BET surface S_{BET} [m²/g] is defined as:

$$S_{BET} = \frac{S_{total}}{m_{powder}} = \frac{V_m N_{AV} s}{v_{ads} m_{powder}} = \frac{N_{AV} s}{(A + I) v_{ads} m_{powder}} \tag{4.7}$$

where S_{total} [m²] is the total surface area, m_{powder} [g] the mass of powder sample, N_{AV} [mol^{-1}] the Avogadro number, s [m²] the cross-section surface area of the adsorbate, and v_{ads} [m³/mol] the molar volume of the adsorbate.

The particle size distribution of active materials was measured using a laser diffraction particle size distribution analyzer (LA-950, HORIBA Ltd., Japan). The powder sample was dissolved in water prior to the measurement and dispersed using ultrasonic bathing (UW2200, Bandelin GmbH & Co. KG, Germany) for 1 min. The size distribution was measured 5 times and the average value was applied. Two terms D50 [µm] and D90 [µm] were applied to characterize the particle size distribution. The former indicates that 50 % of the total volume of powder particles in the sample have diameters less than or equal to this value, whereas D90 means that 90 % of the total volume of powder particles in the sample have diameters less than this value.

4.2. Slurry preparation and coating

Subsequently to the material characterization, active materials were mixed with binder and additives in a solvent using mixing equipment to form a homogeneously distributed slurry with a specific viscosity. Afterwards, the slurry was tape-cast onto the current collector, dried at room or elevated temperature, and finally calendered to adjust the porosity of the composite electrodes.

4.2.1. Cathode slurry preparation

NMP-based slurry preparation

For the cathode slurry preparation with PVDF binder, two commercially available polycrystalline NMC 622 powders with different particle size distributions were applied as active material. PVDF powder (Solef 5130, Solvay GmbH, Germany) with a molecular weight of 1,000,000 – 1,200,000 g/mol was dissolved in NMP (Merck KGaA, Germany) with a mass ratio of 1:10 in advance. A centrifugal mixer (SpeedMixer DAC 150 SP, Hauschild & Co. GmbH, Germany) as shown in Figure 4-2 was applied for the dispersion process and the individual steps for the mixing procedure are listed in Table 4-1. The PVDF solution was stored at room temperature for 12 h for the homogenization.

Table 4-1. Parameters for mixing procedure of the PVDF solution.

Mixing of PVDF in NMP						Program	Repetition(s)
Rotating speed [rpm]	1000	1500	2000	2500	3000	P3	1
Mixing time [s]	60	60	60	60	60		
Rotating speed [rpm]	3000	3000	3000	3000	3000	P4	4
Mixing time [s]	60	60	60	60	60		

Each component was firstly weighed using an electronic balance (SECURA6102-1CEU, Sartourius AG, Germany). Afterwards, NMC 622 powder was manually stirred for three minutes with conductive agent (C-NERGY Super C65, Imerys Graphite & Carbon SA, Belgium) and compaction aid (C-NERGY KS6L graphite, Imerys Graphite & Carbon SA, Switzerland). The powder mixtures were subsequently added into the prepared PVDF solution with NMC 622: Super C65: KS6L graphite: PVDF powder = 92 : 3 : 2 : 3 (wt%). According to Bauer et al. [39], the content of conductive agent should not exceed 5 wt%, since it can lead to a rapid increase in slurry viscosity and the processability of slurry for laboratory coater using doctor blade is deteriorated. Thus, 3 wt% conductive agent was applied in this work.

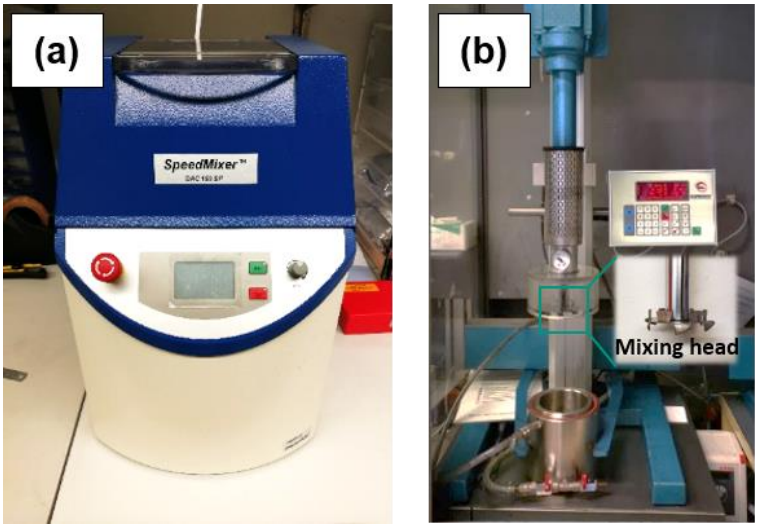

Figure 4-2. Mixers used for slurry preparation: (**a**) centrifugal mixer and (**b**) dissolver equipped with cooling system and vacuum pump.

The slurry was mixed in the same centrifugal mixer with 1500 – 3500 rpm, and extra NMP solution was added into the mixture after the first mixing step in order to adjust the slurry viscosity to 1 – 10 Pa·s at a reference shear rate of 50 s^{-1}. The solid content of the finished slurry was 66.7 wt%. The mixing steps are illustrated in detail in Table 4-2.

Table 4-2. Process parameter of mixing procedure for the NMC 622 cathode slurry with PVDF binder.

1. mixing step						Program	Repetition (s)
Rotating speed [rpm]	1000	1500	2000	2500	3000	P3	1
Mixing time [s]	60	60	60	60	60		
Rotating speed [rpm]	3000	0	3000	0	3000	P5	4
Mixing time [s]	60	60	60	60	60		
Rotating speed [rpm]	3500	0	3500	0	3500	P2	4
Mixing time [s]	30	60	30	60	30		
2. mixing step, add 5 ml NMP solvent before the mixing							
Rotating speed [rpm]	1000	1500	2000	2500	3000	P3	1
Mixing time [s]	60	60	60	60	60		
Rotating speed [rpm]	3000	0	3000	0	3000	P5	4
Mixing time [s]	60	60	60	60	60		
Rotating speed [rpm]	3500	0	3500	0	3500	P2	4
Mixing time [s]	30	60	30	60	30		

Aqueous slurry preparation

For aqueous slurry preparation, polycrystalline NMC 622 powders as well as C-NERGY Super C65 were applied, while 40 wt% solution of fluorine acrylic copolymer latex TRD 202A (JSR Micro NV, Belgium) and Na-CMC (CRT 2000PA, Dow Wolff Cellulosic GmbH, Germany) with a substitution degree of 0.82 – 0.95 were used as binder and thickening agent, respectively. Before slurry preparation, Na-CMC powder was dissolved in deionized water and mixed in a dissolver (VMA-Getzmann GmbH, Germany) with 1500 rpm for 1 h to acquire a 5 wt% CMC solution. Afterwards, NMC 622 powder and conductive agent were added to the CMC solution in four steps, 1/2, 1/4, 1/8, and 1/8 of the total powder weight. After each adding steps, the solution was mixed under vacuum using 2000 rpm rotation speed for 5 min. The container was persistently water-cooled to 20 °C. Subsequently, one of the acids, which were either 100 % liquid acetic acid (Merck KGaA, Germany), monohydrate citric acid powder (Merck KGaA, Germany), or 85 wt% aqueous phosphoric acid solution (Merck KGaA, Germany), was added into the slurry to adjust the slurry pH value. An evacuation time of 2 min was applied after the addition of acid and the slurry was afterwards stirred at 2000 rpm under atmospheric pressure for 90 min to disperse the powders homogenously. Shear sensitive latex binder TRD 202A was added into the slurry at the end and the slurry was further mixed at 500 rpm for 3 min under vacuum. The mass ratio of each constituent (only solid content) was set to NMC 622: Super C65: Na-CMC: TRD 202A = 92.6 : 2.8 : 1.8 : 2.8. The solid content of the aqueous NMC 622 slurry was 56.7 wt%. The slurry pH value was measured 15 min after the mixing procedure was finished using a pH-meter (FE30-Basic FiveEasy, Mettler-Toledo GmbH, Germany). The aqueous slurry preparation procedure of NMC 622 is summarized in Figure 4-3.

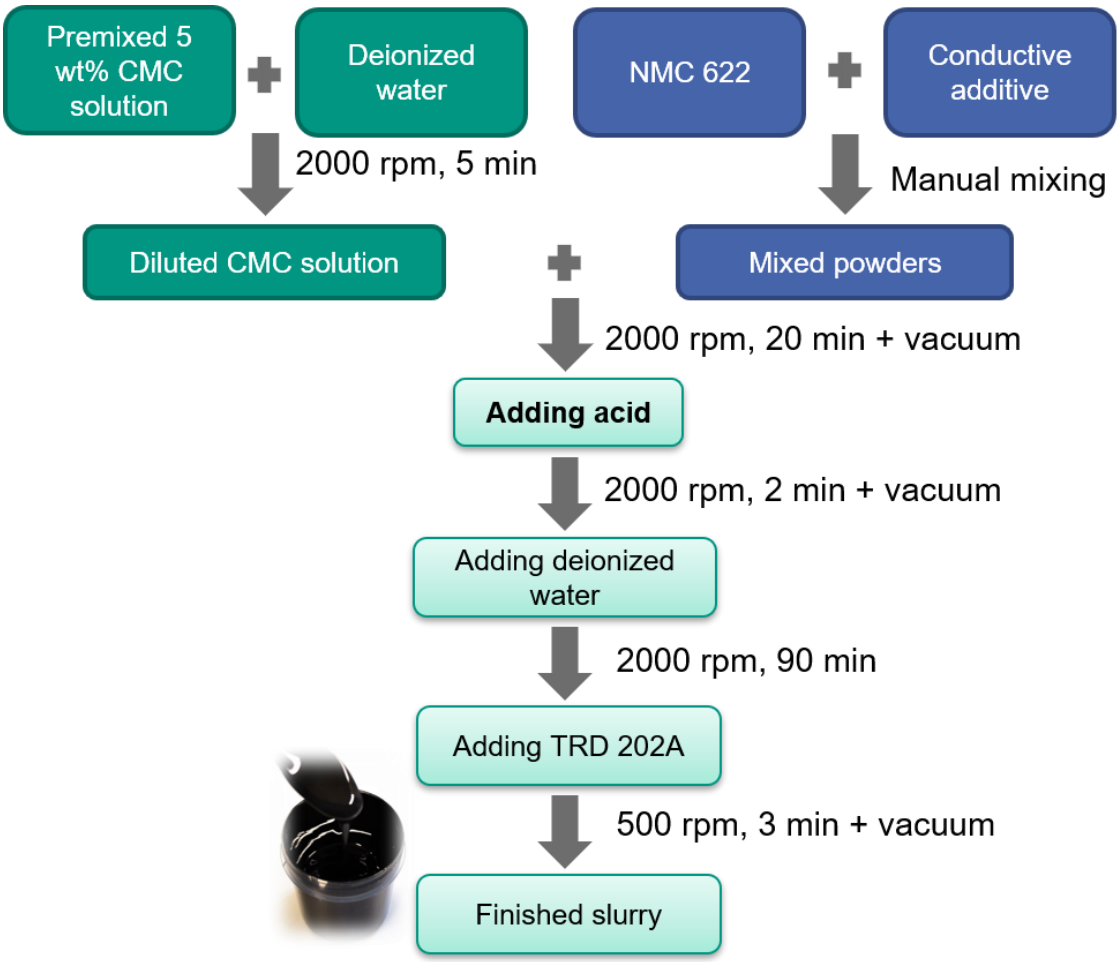

Figure 4-3. Workflow for the preparation of aqueous NMC 622 slurries.

4.2.2. Anode slurry preparation

In order to analyze the electrochemical performance of NMC 622 cathodes in full-cells, aqueous processed graphite anodes were prepared. Na-CMC powder (MTI Corporation, USA) was dispersed in deionized water to form a 2 wt% solution using a laboratory dissolver (VD-10 XP, DISTECH GmbH, Germany), see Figure 4-4. A homogenous Na-CMC solution was acquired after 1 h mixing at 1500 rpm under atmospheric pressure. The graphite powder and conductive agent (C-NERGY Super C65, Imerys Graphite & Carbon SA, Belgium) were then added into the Na-CMC solution and mixed with the same dissolver at 2500 rpm for 1.5 h. The shear-sensitive SBR (50 wt% solution, MTI Corporation, USA) was added at the end of the mixing procedure using 500 rpm for 3 min. The mass ratio of each constituent in the anode slurry was set to graphite: conductive agent: Na-CMC: SBR = 93 : 1.4 : 1.87 : 3.73. The solid content of the graphite slurry was 43 wt%. With the used dissolver, the preparation of anode slurry can be upscaled from 100 ml to 2 l, which provides the opportunity to achieve a continuous R2R coating of anodes with coating length more than 20 m (coating width: 10 cm).

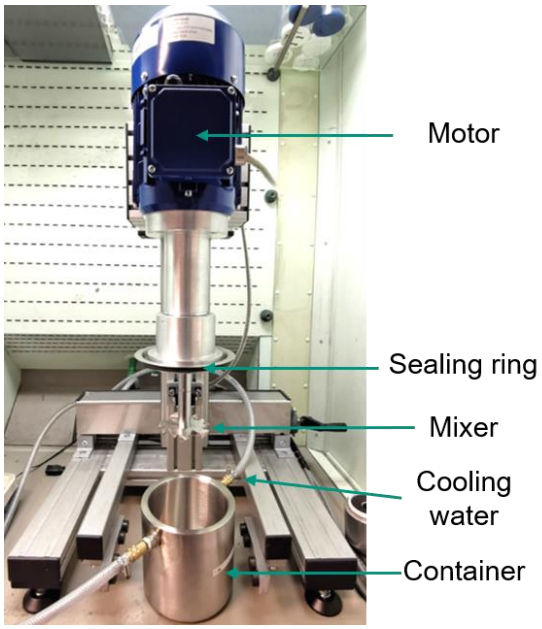

Figure 4-4. Dissolver for anode slurry preparation.

4.2.3. Viscosity analysis

After the mixing process, NMC 622 cathode slurry was transferred to a rheometer (MCR 72, Anton Paar GmbH, Austria) as shown in Figure 4-5-a for rheological analyses using the rotational flow measurements equipped with a parallel plate (PP 50, Anton Paar GmbH, Austria) shown in Figure 4-5-b, with shear rates ranging from 1 to 100 s^{-1} at the temperature of 25 °C. The shear rate $\dot{\gamma}$ [s^{-1}] of a fluid is defined as follows:

$$\dot{\gamma} = \frac{v}{h_{doc}} \tag{4.8}$$

where v [mm/s] is the coating speed and h_{doc} [mm] the doctor blade gap. The reference shear rate at 50 s^{-1} was chosen for comparison of the slurry viscosities with respect to the practical casting condition such as a coating speed of 5 mm/s and a doctor blade gap of 0.1 mm.

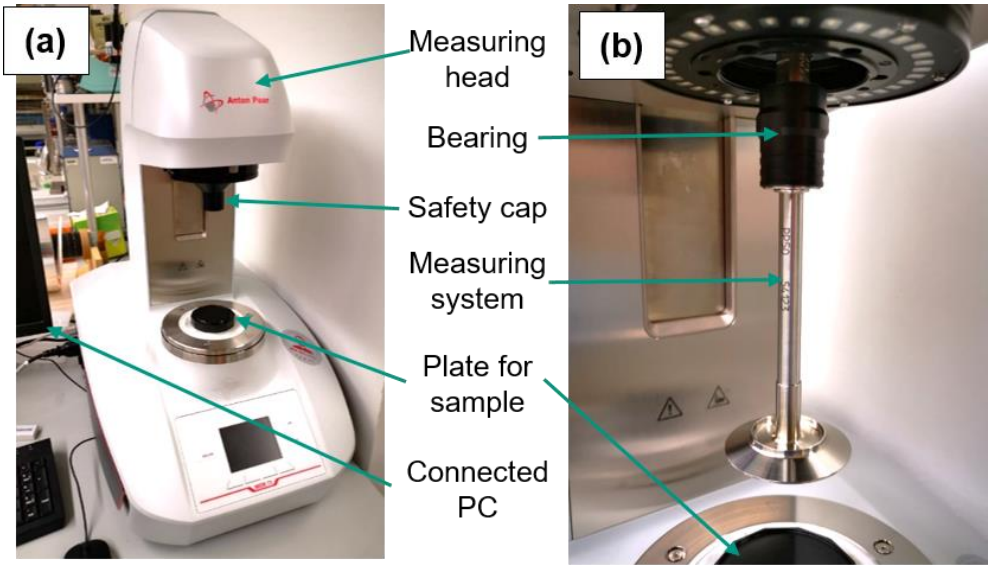

Figure 4-5. Equipment used for rheological analyses, (**a**) the rheometer and (**b**) the parallel plate.

4.2.4. Tape-casting and calendering

The slurry obtained from the previous mixing step was tape-cast with a doctor blade (ZUA 2000.100, Proceq LLC, Switzerland) onto an Al-foil (MTI Corporation, USA) with a thickness of 20 µm and a width of 240 mm. For this purpose, a film coater (MSK-AFA-L800-LD, MTI Corporation, USA) was used which was equipped with a vacuum table in order to fix the Al foil, as shown in Figure 4-6. The coating speed was 5 mm/s while the electrode wet film thickness was controlled by varying the gap of the doctor blade. The NMP-based NMC 622 slurry was dried at 90 °C for 2.5 h, while the aqueous NMC 622 slurry was dried at room temperature for 1 h to avoid possible accelerated chemical corrosion which might occur at elevated temperatures. The doctor blade gap was varied from 200 to 700 µm aiming to fabricate cathodes with state-of-the-art thickness of 50 – 70 µm and thick-film cathodes with thicknesses of 150 – 200 µm, respectively.

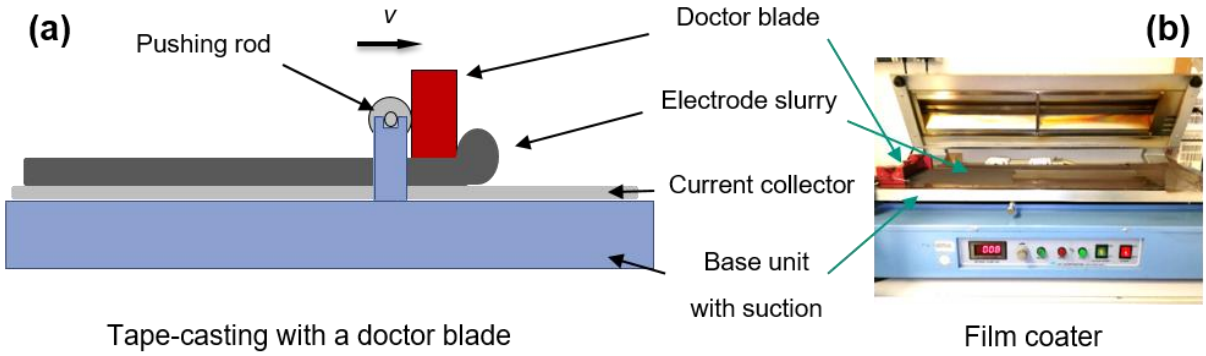

Figure 4-6. Tape casting with a doctor blade: (**a**) schematic illustration of the coating process and (**b**) view of the film coater used for electrode coating.

Dual-coating strategy was also adopted for the fabrication of thick-film NMC 622 cathodes with hierarchical structures. For this purpose, a part of the slurry was firstly cast onto the Al-foil using a doctor blade with a width of 150 mm (ZUA 2000.150, Proceq LLC, Switzerland) and was dried for 2.5 h at 90 °C. Then, the heater was turned off and the film as well as coater were cooled down to room temperature. The second film was subsequently cast on top of the previous film using a doctor blade with 100 mm width and dried at the same temperature applied for the basis film. The total film thickness was kept constant at 150 µm after calendering, while the ratios of initial individual film thicknesses, i.e., before calendering, were set to 1:1 and 1:2 (2:1). In addition, in order to investigate the impact of the position of different layers in the electrode on the electrochemical performance, three different types of cathodes were manufactured, which were with one type of NMC 622 powder; mixture of two NMC 622 powders in one film; and with two layers containing different NMC 622 powder (big particle sizes and small particle sizes). “S” represents the film containing NMC 622 powder with small particle sizes, while “B” means the film having NMC 622 powder with big particle sizes. According to the position of bottom film and upper film, different notations are used. For example, “SB” indicates that “S” layer with small particle size NMC 622 is at the bottom (close to the current collector), while “B” layer is on the top of the electrode. Therefore, “BS” suggests that in this electrode, “B” is the bottom layer and “S” is the top layer. In addition, “B&S” means

that two NMC 622 powders were added simultaneously into the slurry during mixing process, thus no bilayer exists in the final electrode. Furthermore, thin-film electrodes with 70 µm thickness with one type of powder were manufactured as references representing the state-of-the-art approach.

The coating of graphite anode is similar to that of the NMC 622 cathodes. A doctor blade (ZUA 2000.100, Proceq LLC, Switzerland) with a gap of 460 µm and a coating speed of 5 mm/s was applied to coat the anode slurry onto a Cu-foil (MTI Corporation, USA) with a thickness of 9 µm and a width of 200 mm. The drying of graphite anodes took place at room temperature.

After drying, the electrodes were calendered using an electric precision rolling press (MSK-2150, MTI Corporation, USA) at room temperature with a constant calendering speed of 35 mm/s, see Figure 4-7. The average porosity of NMC 622 cathodes with PVDF binder as well as with different acid addition was adjusted to 35 %, while the porosity of graphite anodes was reduced to 40 %. The electrode porosity P_{ele} [%] was determined by the weight percent and density of each component [268]:

$$P_{ele} = \frac{V_{total} - (\sum_i \frac{m_i}{\rho_i})}{V_{total}} = \frac{h - M_{total} \sum_i \frac{c_i}{\rho_i}}{h} \cdot 100\% \tag{4.9}$$

where V_{total} [cm^3] is the total volume of a composite electrode without current collector, m_i [g] and ρ_i [g/cm^3] the mass and density of each component, respectively, h [cm] the film thickness without current collector, M_{total} [g/cm^2] the total weight of the composite electrode per area, and c_i [-] the solid mass ratio of each component in the composite electrode.

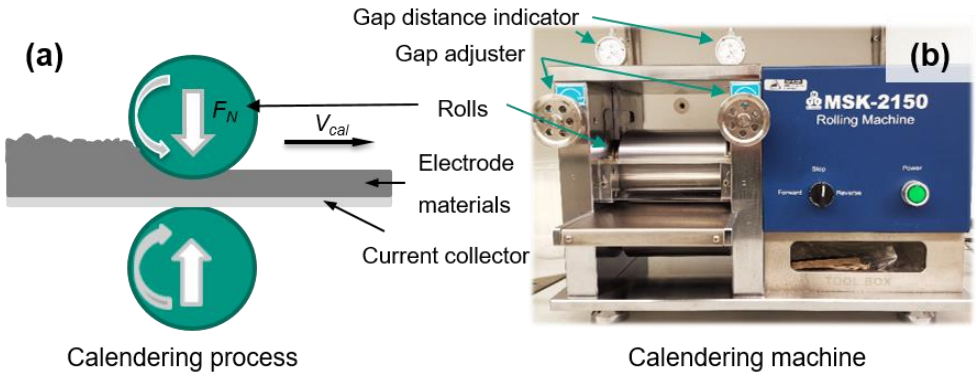

Figure 4-7. Calendering Process: (**a**) schematic representation of the calendering process and (**b**) view of the applied calendering machine.

4.3. Laser structuring of electrodes

Subsequently to the calendering process, the thick-film electrodes were structured using ultrafast laser ablation. A detailed description of the applied laser and the respective laser and process parameters for structuring and cutting will be presented in the following chapters.

4.3.1. Laser micromachining systems

A pulsed Yb:YAG fiber laser (Tangerine, Amplitude Systèmes SA, France) operating at a wavelength of 515 nm (M^2 < 1.3) with a maximal average laser power of 12 W and a pulse duration of 380 fs was used. A separate cooling unit (P310, TERMOTEK GmbH, Germany)

with cooling water flow set to 20 °C was connected to the laser to dissipate the heat generated by the laser diodes. A beam expanding telescope (BeT, S6ZOE5076/292, Sill Optics GmbH, Germany) with 3 to 5 times magnification was used to expand the incident laser beam and resulted in a final laser focus diameter of about 20 – 35 µm, which has been illustrated in chapter 3.3. A laser scan head (rhothor™, Newson NV., Belgium) and an F-Theta lens (S4LFT3161/292, Sill Optics GmbH, Germany) with a scan area of 90 × 90 mm^2 were also applied. All the above-mentioned components, as well as optical elements such as mirrors for beam reflection, were assembled and integrated into a micromachining system (PS450-TO, OPTEC SA, Belgium) for the laser patterning of the NMC 622 electrodes with different thicknesses. The schematic setup of the micromachining system is shown in Figure 4-8.

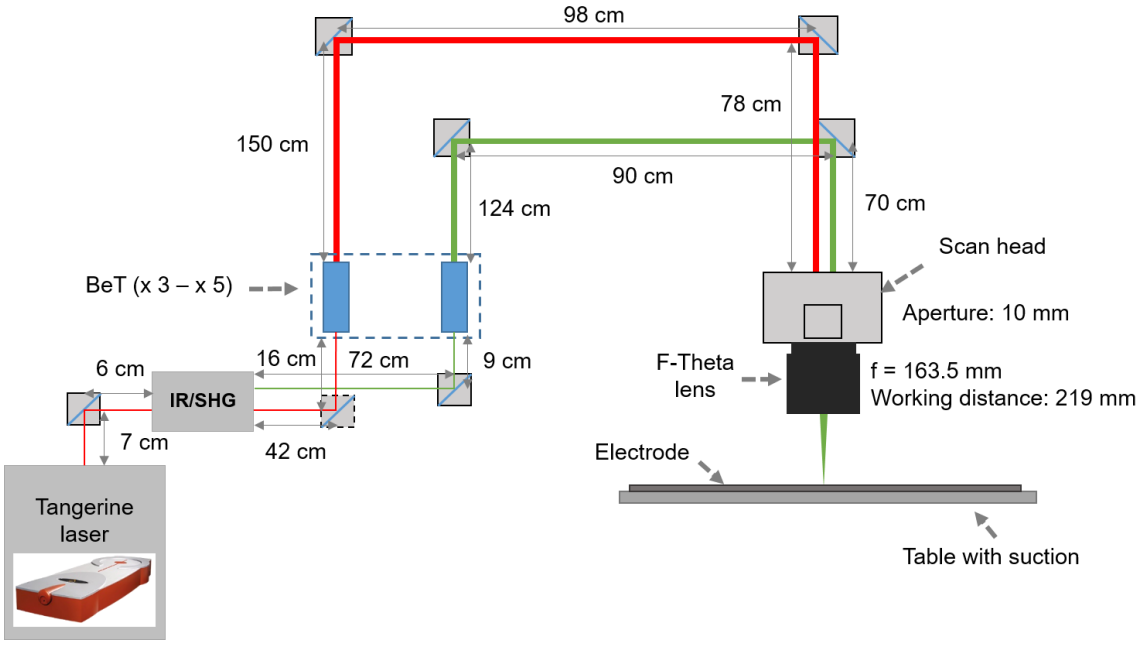

Figure 4-8. Schematic setup of the used PS450-TO micromachining system with a laser (Tangerine) operating at a wavelength of 1030 nm equipped with a second-harmonic generator (SHG) to halve the laser wavelength to 515 nm, and respective optical elements to perform laser structuring of the electrodes.

To investigate the upscaling of the laser patterning of NMC 622 cathodes, a high-power laser (PX600-1-GF, Edgewave GmbH, Germany) with a maximum average laser power of 400 W at an optimized repetition rate of 1 MHz, a wavelength of 1064 nm, a pulse duration of 12 ps, and an M^2 < 1.2 was applied as laser source. A chiller (P20500K, TERMOTEK GmbH, Germany) was applied to cool down the laser diodes to 24 °C. A high-speed scan head (Rhino 21, Novanta GmbH, Germany) with a scan speed of up to 10 m/s was used to steer the laser beam, and an additional chiller (HRSE012-A-23, SMC Corporation, Japan) was used to cool down the scan head control chips. A prototype 1 × 5 beam splitter (TOPAG Lasertechnik GmbH, Germany) and an F-Theta lens (S4LFT2256/328, Sill Optics GmbH, Germany) with a scan area of 150 × 150 mm^2 were integrated into the system. The diffraction efficiency of the beam splitter is about 86 %. The schematic of the setup using high power ps-laser radiation is depicted in Figure 4-9.

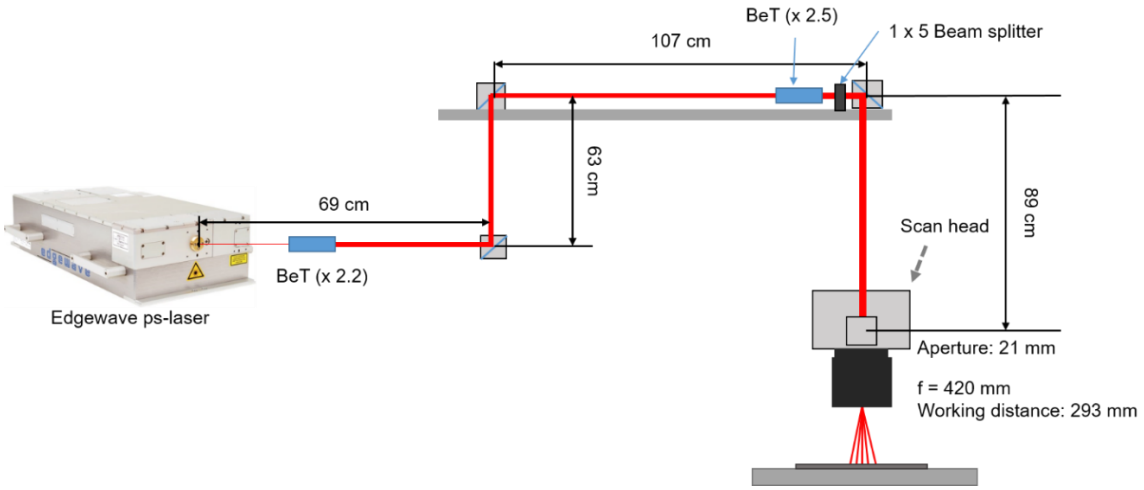

Figure 4-9. Schematic setup of the laser micromachining system consisting of high power ps-laser (wavelength: 1064 nm, pulse duration: 12 ps), beam splitter, and high speed scan head for the upscaling of the laser structuring process.

For the laser patterning of graphite anodes, a pulsed fiber laser (FX600, Edgewave GmbH, Germany) with a wavelength of 1030 nm, a pulse duration of 600 fs, and M^2 < 1.1 was used as laser source. A cooling unit (HRS050-WF-20-M, SMC Corporation, Japan) was applied to cool the laser diodes to 23 °C. Two scan heads (intelliSCAN III 20, Scanlab GmbH, Germany) equipped with F-Theta lens (JENar, Jenoptik AG, Germany) with a scan area of 150 × 60 mm^2, and a motorized BeT with 2 – 8 times expansion (Qioptiq Photonics GmbH & Co. KG, Germany) were assembled in a laser micromachining system (MSV203, M-Solv Ltd., UK), as shown in Figure 4-10.

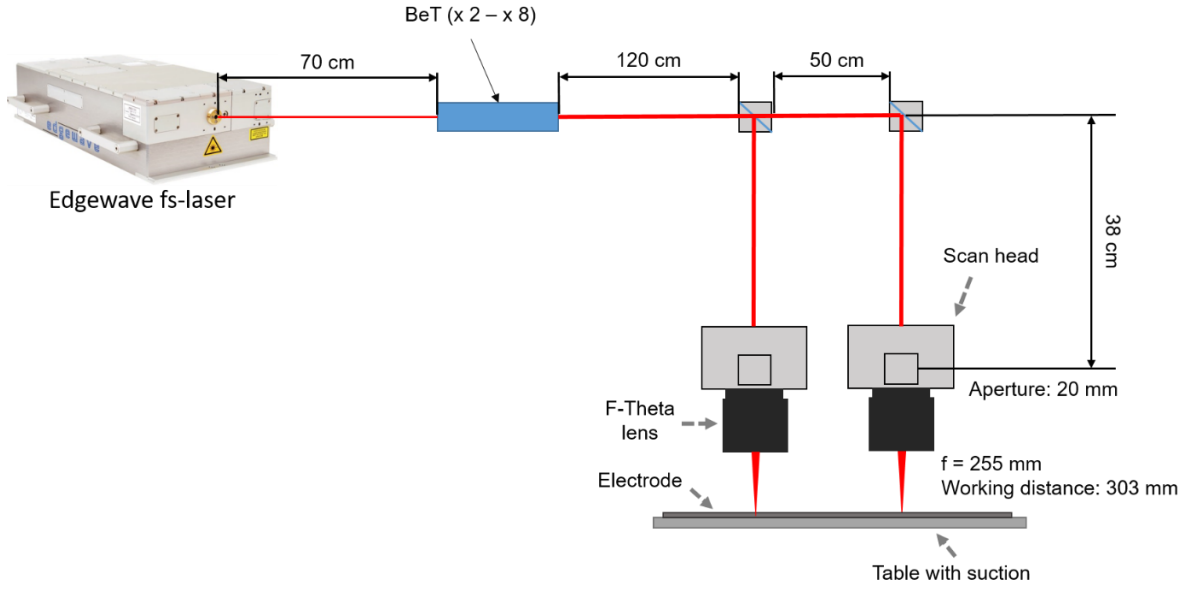

Figure 4-10. Schematic setup of the laser micromachining system equipped with an fs-laser with a wavelength of 1030 nm and two scan heads.

4.3.2. Laser parameters for electrode structuring and cutting

Setup illustrated in Figure 4-8, operating with a laser wavelength of 515 nm, was applied for the laser structuring of thick-film NMC 622 cathodes with PVDF or water-soluble binders.

Line structures with different pitch and channel width were generated with depths down to the current collector. A laser repetition rate of 500 kHz and an average laser power of 2.5 to 4.3 W were applied, while the laser scan speed was kept constant at 500 mm/s. The number of laser scans varied from 15 to 50 with regard to the cathodes with different binder and thicknesses. Other patterns such as hole structures were also applied for the laser structuring of electrodes. Since cathode material takes up about 50% of the overall material costs in a LIB [37], the mass loss due to laser ablation should be limited, which means the structured grooves should be as narrow as possible. In this work, the mass loss was adjusted below 10 %. To further investigate the upscaling of laser patterning, the setup illustrated in Figure 4-9 with high power laser was applied. The ablation efficiency of NMC 622 cathodes was studied by comparing the laser patterning at different repetition rates ranging from 100 kHz to 1 MHz and with average laser power from 3 W up to 30 W (per single beam). Besides, laser ablation of NMC 622 cathode using a 1 × 5 beam splitter with five times higher laser power (15 – 150 W) was conducted in order to prove the concept of fast laser processing.

Laser patterning of graphite anodes was performed using the setup shown in Figure 4-10. A laser repetition rate of 1 MHz and an average laser power of 37 W were applied, while the laser scan speed was set to 20 m/s and 92 laser scans were used to generate line structures with 350 µm pitch in anodes. The pitch was adjusted according to the areal capacity of the anode to achieve a cell-balancing-factor (see chapter 3.3.1) of 1.1 – 1.2.

Laser structured electrode specimens with a footprint of 2 cm × 1.3 cm were cut from the calendered cathode sheets using fs-laser radiation (Figure 4-8) for the cross-sectional analyses. The specimens were placed between two glass cover slips and held vertically with a plastic clip. Then they were placed in a holder and were afterwards filled with a mixture of resin (EpoFix Resin, Struers GmbH, Germany), hardener (Epofix Hardener, Struers GmbH, Germany), and fluorescent dye powder (EpoDye, Struers GmbH, Germany). The specimens were placed in a fume hood overnight after casting to acquire metallographic samples. Afterwards, the surface of the specimens were ground via a metallographic grinder (Qpol 250M1, QATM GmbH, Germany) using silicon carbide papers (Hermes Schleifmittel GmbH, Germany) with different P-grades from 180 to 4000 (grain sizes from 82 µm to 6 µm). The specimens were then sequentially polished with diamond suspension with a diameter of 3 µm and 1 µm, respectively. An optical microscope equipped with Leica objectives and a digital camera (DP74, Olympus Corporation, Japan) were applied to determine the width and depth of the groove structures in order to find the appropriate structuring parameters. In addition, a digital microscopy (VHX–7000, Keyence Corporation, Japan) was used for the fast analysis of the ablation depth and full-width-at-half-maximum (FWHM) of laser structured NMC 622 cathodes with different laser parameters.

In addition, fs-laser radiation with a wavelength of 515 nm was applied for the cutting of NMC 622 cathodes, graphite anodes, and separators. The laser parameters for cutting are displayed in Table 4-3. All types of laser processing were performed in ambient air with a suction device mounted on the side of the samples.

Table 4-3. Laser cutting parameters for different materials used in cells.

Materials	Av. laser power [W]	Laser scan speed [mm/s]	Laser repetition rate [kHz]	Laser scan(s) [-]
NMC 622 cathodes (70 – 150 µm)*	2.5	200	500	5 – 18
NMC 622 cathodes (150 – 200 µm)	5	200	500	15 – 40
Graphite anodes (170 – 190 µm)	2.5	200	500	8 – 10
PP separator	2.5	200	500	1

* The thicknesses refer to the composite materials without current collector.

4.4. Characterization of electrodes

After the electrodes were prepared, SEM imaging (Phenom XL, Thermo Fisher Scientific Inc., Netherlands) was applied at an accelerating voltage of 10 kV to investigate film morphology and in particular its possible modification through the use of different acids in water-based slurries. Besides, EDX analyses were applied to study possible compositional changes in laser-affected areas on electrode surfaces. In addition, in order to study the effect of aqueous processing on the NMC 622 electrodes, XPS and Raman spectroscopy analyses were performed in order to compare the possible impact of different acid additions during mixing process on the structural changes in NMC 622 particles (e.g., lithium leaching, or amount of residual Li_2CO_3) in comparison to the reference electrodes with PVDF binder. Furthermore, film adhesion strength of different types of NMC 622 cathodes were measured using a 90° peel-off test.

4.4.1. Raman spectroscopy

A Raman microscope (Senterra II, Bruker Optics GmbH & Co. KG , Germany) equipped with a diode-pumped solid-state (DPSS) laser operating at a wavelength of 532 nm was applied. An Olympus MPLAN 20 × objective with a numerical aperture (NA) of 0.45 was used for the observation of the sample surface, focusing and collimation of the backscattered light. The laser spot diameter at the sample surface was 5 µm. The spectra integration time was 40 s with four coadditions (4 × 10 s). The laser power was set to 6 mW and 2.5 mW for the detection of the electrodes and pristine NMC 622 powder, respectively, without damaging the electrode materials. For each sample, spectra were recorded at 6 to 12 randomly selected locations with a bandwidth ranging from 75 to 4000 cm^{-1}.

4.4.2. X-ray photoelectron spectroscopy (XPS)

XPS analysis was performed with a K-alpha spectrometer (Thermo Fisher Scientific Inc., UK) on NMC 622 cathodes with different acid additions during slurry preparation. Thermo Avantage software was used for data acquisition and processing. All specimens were analyzed using a microfocused, monochromated Al Kα X-ray source with a spot size of 400 µm. A Kα charge compensation system was applied during analysis using electrons of 8 eV energy and low energy argon-ions to avoid any local charge buildup. The spectra were fitted with one or more Voigt profiles (uncertainty = ± 0.2 eV) and quantified by applying Scofield sensitivity factors [287]. All spectra were referenced to the C 1s graphitic peak (sp^2) at 284.4 eV binding

energy controlled by means of the well-known photoelectron peaks of metallic copper, silber, and gold, respectively.

4.4.3. 90°-peel-off test

A static multifunctional materials testing machine (Xforce HP, ZwickRoell GmbH & Co. KG, Germany) was applied to perform the 90°-peel-off-test to measure the electrode film adhesion to the current collector with different binder and acid additions during the mixing process. The electrodes were punched into 1.7 × 8 cm^2 strips in advance and were attached with coated side downwards to a metal platform using a double-sided adhesive tape as illustrated in Figure 4-11. The electrode together with the metal platform were pressed using a hand press (MP150, msscientific Chromatographie-Handel GmbH, Germany) with a load of 0.2 t for 2 s and was fixed on the testing base. Subsequently, the uncoated current collector end was held vertically by a clamp. During the peeling test, a constant peeling speed of 10 mm/s was given while the load was recorded. After the measurement, the average force to peel-off the electrode materials from the current collector was calculated, while the film adhesion strength is defined as the average force divided by the sample width of 1.7 cm.

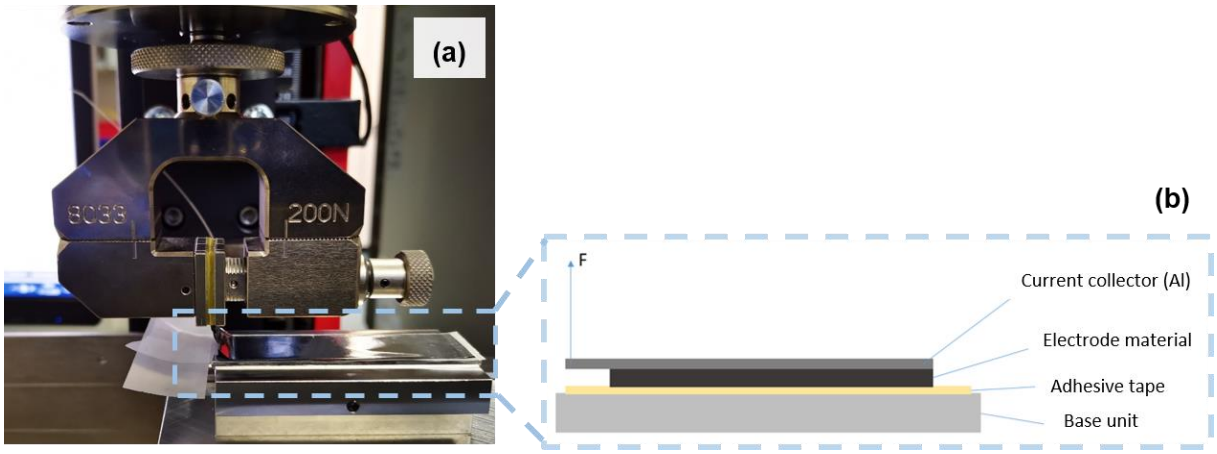

Figure 4-11. 90°-peel-off test of electrodes: (**a**) equipment for 90° peel-off test of electrodes and (**b**) a schematic view of the experimental setup.

4.5. Electrochemical analyses of the NMC 622 electrodes

All electrodes were dried at 130 °C for 12 h under vacuum in an oven (VT 6025, Thermo Fisher Scientific Inc., Germany) prior to cell assembly in order to eliminate the water content inside of the electrodes. In addition, the cross-linking of CA or PA with Na-CMC takes place between 120 – 150 °C [30], thus the drying temperature in this range is beneficial for the aqueous processed NMC 622 electrodes. Besides, the degradation of PVDF binder takes place at 400 – 510 °C [288], while CMC decomposes at 172 – 327 °C [289, 290], thus drying at 130 °C will not modify the structure and properties of the binder in the electrodes. After drying, the electrodes were transferred to an argon-filled glove box (LAB master pro sp, M. Braun Inertgas-Systeme GmbH, Germany) with H_2O< 0.1 ppm and O_2< 0.1 ppm. Due to the toxicity and high volatility of the electrolyte as well as the high reactivity of Li, all the cell assembly took place in the glove box.

4.5.1. Cell assembly

In this work, two different cell setups were used to characterize the electrochemical performance of the NMC 622 cathodes, which are coin cells CR2032 containing NMC 622 cathode vs. Li (half-cells) and pouch cells with NMC 622 vs. graphite (full-cells). The electrode design as well as cell assembly are illustrated in this chapter.

Coin cell assembly

Laser structured and unstructured NMC 622 cathodes (diameter: 12 mm) with different binders and acid addition were assembled vs. Li foil (Merck KGaA, Germany) with a thickness of 0.25 mm and a diameter of 16 mm in CR2032 coin cell. A total amount of 120 µl electrolyte (Solvionic SA, France), which is a mixture of EC / EMC (3:7, wt%) with 1.3 M $LiPF_6$ as conducting salt and 5 wt% FEC as additive was added to each cell. A polypropylene separator foil (Celgard 2500, MTI Corporation, USA) with a thickness of 25 µm was placed between the NMC 622 cathode and Li. For cells containing NMC 622 cathodes with thicknesses < 150 µm, stainless steel ring springs (a thickness of 1.2 mm and a diameter of 15.4 mm) were applied, while wave springs (a thickness of 1.6 mm and a diameter of 14.7 mm) were used for cells containing electrodes with thicknesses ≥ 150 µm, as shown in Figure 4-12-a. This is because that during experiments it was observed that the use of ring spring in cells containing thick-film electrodes with thicknesses greater than 150 µm resulted in cell failure in many cells. This might be due to insufficient wetting of the electrodes caused by excessive pressure inside the cells. Two spacers with a thickness of 0.5 mm and a diameter of 15.8 mm were used in each coin cell to ensure an evenly distributed force applied by the spring. All cell components were stacked in the order shown in Figure 4-12 and were pressed and sealed using an electric crimper (MSK-160E, MTI Corporation, USA) after stacking, see Figure 4-12-b. The pressure on the electrode with a thickness of 150 µm in a coin cell (half-cell) is 0.78 ± 0.10 MPa. The calculation of the pressure is shown in Appendix B. The cells were stored after assembly at room temperature for 24 h to enable a complete wetting of the cathode and separator prior to the electrochemical analysis.

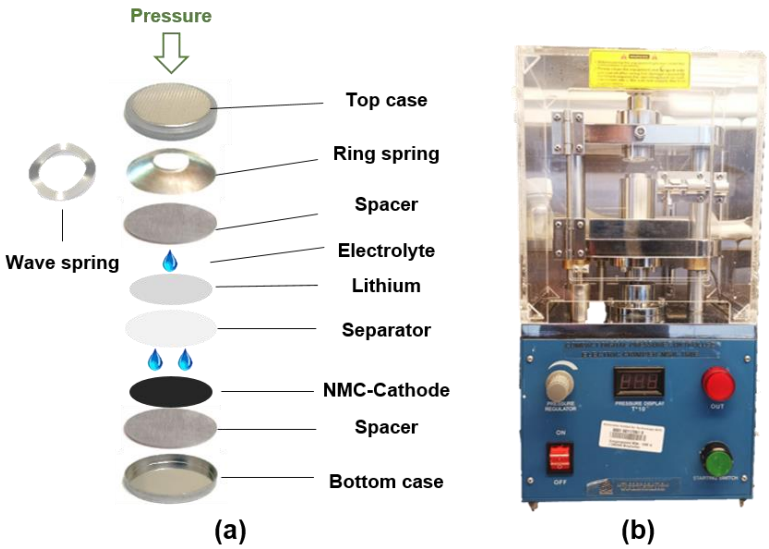

Figure 4-12. Instruction of (**a**) coin cell CR2032 assembly and (**b**) the coin cell crimper used to seal the coin cells.

Pouch cell assembly

As for pouch cell assembly, NMC 622 cathodes and graphite anodes were first laser cut into 45 × 45 mm^2 and 49 × 49 mm^2, respectively, as shown in Figure 4-13. The terminals displayed on the upper left side of the cathode and anode were uncoated Al or Cu current collectors which were subsequently welded to the Al- (EQ-PLiB-ATC8, MTI Corporation, USA) and Ni-tab (EQ-PLiB-NTA8, MTI Corporation, USA), respectively, by using an ultrasonic welding machine (DS20-B, Schunk GmbH, Germany). The length and width of both tabs was 60 mm and 8 mm, respectively, and their thickness was 90 µm.

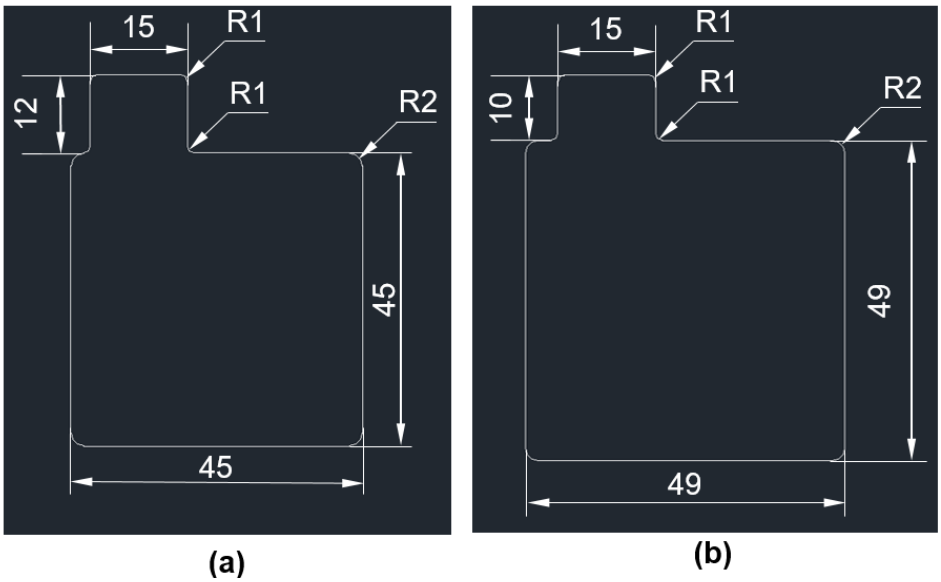

Figure 4-13. The technical drawing of electrode dimensions for (**a**) cathode and (**b**) anode.

The electrodes and PP separator (area: 60 × 60 mm^2) were then placed in the antechamber of the glovebox and were heated under vacuum to 60 °C for 12 h. This step was designed to eliminate residual water from the electrodes and separator. The drying temperature was limited to 60 °C because it was observed that higher temperatures would cause the separator to shrink during the drying process. All the components were subsequently cooled to 25 °C and were stacked in the cathode / separator / anode sequence as displayed in Figure 4-14-a. Afterwards, the stack was placed in an Al laminated polyamide pouch case (EQ-alf-480-20M, MTI Corporation, USA) consisting of polyamide + polyester-polyurethane adhesive layer + aluminum foil + PP adhesive layer. The thickness of the pouch case was 115 µm, and the length and width of pouch foil for each cell were 14.5 cm and 20 cm, respectively. After stacking, the first sealing was performed with an evacuation time of 3 s and a sealing time of 2 s (Audionvac VMS 163, Audion BV, Netherlands) in order to seal the pouch case with Ni-tab from anode and Al-tab from cathode by melting the adhesive strip made of PP and polyethylene naphthalate on the electrode tabs with pouch case. Then the same sealing parameter was used to seal the other edge perpendicular to the first sealing edge of the pouch case (second sealing). Afterwards, 1.1 ml electrolyte consisting of a mixture of EC / EMC (3:7, vol%) with 1.3 M $LiPF_6$ as conducting salt and 5 wt% FEC as additive was injected from the open side of the pouch bag into each pouch cell. After 30 min of wetting, the final sealing process was performed with an evacuation time of 15 s and a sealing time of 2 s

in order to completely seal the pouch bag. The sealing process is illustrated in in Figure 4-14-b. Finally, all pouch cells were stored at room temperature for 20 h prior to electrochemical analyses.

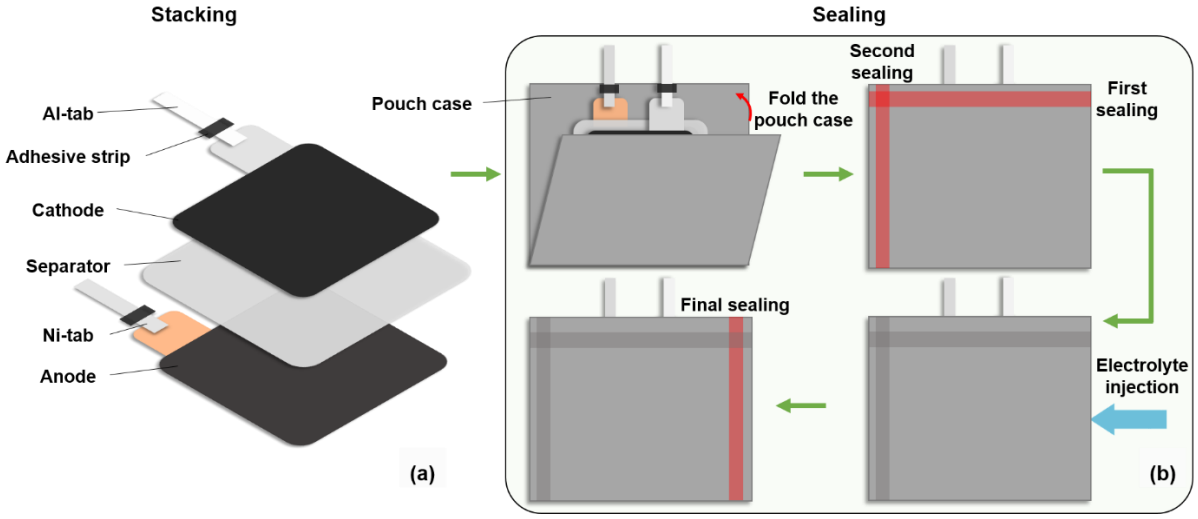

Figure 4-14. Schematic representation of (**a**) the stacking of cathode, separator and anode, and (**b**) the sealing process of electrode tabs with pouch case, including pouch case folding, first sealing, second sealing, electrolyte injection, and the final sealing.

4.5.2. Rate capability and lifetime analyses

The rate capability analyses aim to measure the specific charge transferred at a given voltage window and can indicate the fast charging as well as the energy density of a LIB. These analyses were carried out using a battery cycler (BT2000, Arbin Instruments Corporation, USA). A key influence factor on the performance and cyclic stability of the LIB is the initial cycling, a so-called “formation” step used to establish the SEI accompanied by electrolyte decomposition. Thus, slow charging and discharging at the beginning is necessary to ensure a homogeneous SEI growth. Coin cells were cycled three times at C/20 as the formation step, while the pouch cells were degassed after the first C/20 cycle, sealed, and further cycled two times at C/20. During charging, a ‘‘constant current-constant voltage’’ (CCCV) method was applied, i.e., a constant current was applied until the cell was charged to the upper voltage and thereafter the cell voltage remained constant until the electrical current decreased and reached the lower threshold current (Figure 4-15). Compared to constant current (CC) charging, the CCCV method provides many advantages, e.g., it can mitigate the capacity fading and prevents the rise of the internal resistance; In addition, it was reported that without the constant voltage charging, an inhomogeneous and porous SEI would be formed and this could lead to an accelerated loss of active Li and electrode degradation upon cycling [291, 292].

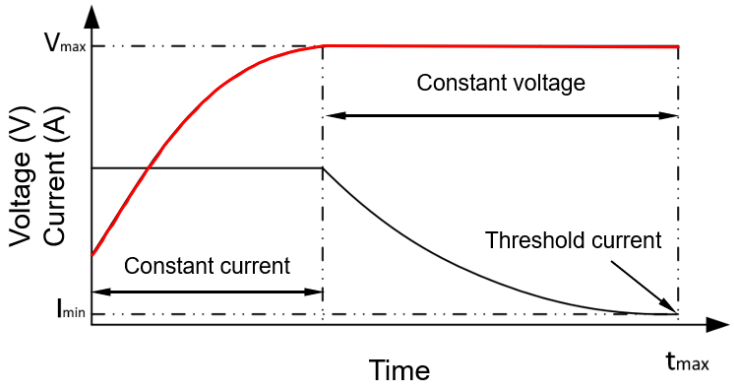

Figure 4-15. Schematic view of a CCCV charging protocol, reconstructed from Shen et al. [291].

After electrochemical priming (formation), the cells were cycled with increasing C-rates from C/10 to 3C. C/10 and C/5 were carried out for 5 cycles and the others were carried out for 10 cycles. Finally, 5 cycles at C/5 were applied to study the capacity retention after fast charging / discharging, as shown in Table 4-4. Besides, a symmetrical protocol was applied for rate capability test, which means currents for charging and discharging were the same. The C-rate was calculated based on the discharge time and applied electrical current during the formation step. In this thesis, a specific capacity of 172 mAh/g and 166 mAh/g was applied for the calculation of currents under different C-rates (I_{nC} [A]) of cells containing NMC 622 cathodes with PVDF binder and aqueous processed ones, respectively. The lower and upper voltage was 3.0 and 4.3 V for all coin cells at each C-rate, respectively, while the pouch cells were cycled using a voltage window of 3.0 – 4.2 V.

Table 4-4. The process parameters for rate capability analyses of cells with different cathodes.

Charging (CC)	C/20	C/10	C/5	C/2	1C	2C	3C	C/5
Current threshold (constant voltage)	C/50	C/20	C/10	C/10	C/10	C/10	C/10	C/10
Discharging (CC)	C/20	C/10	C/5	C/2	1C	2C	3C	C/5
Cycle number	3	5	5	10	10	10	10	5

Jafari et al. [293] studied the real-world driving data collected from different drivers and found that during driving, the batteries of BEV are most frequently discharged with C/8, followed by C/2, while higher C-rates such as 1C to 2.5C are rarely used. Thus, in this work, lifetime analyses were conducted at C/2 for coin cells and pouch cells after rate capability analyses.

4.5.3. Cyclic voltammetry

Cyclic voltammetry (CV) is commonly applied to investigate the reduction and oxidation reactions of molecular species and to study the catalytic reactions resulting from the electron transfer [294]. The most important parameter in CV is the scan rate ν [mV/s], which indicates the rate of linear change in potential during a CV analysis. A typical CV diagram of half-cells containing NMC 622 cathodes was shown in Figure 3-4-b, the closed loop indicates that the redox reaction in NMC 622 is electrochemically reversible. However, the cathodic and anodic peak potentials are at different potentials and the difference between them is defined as the

peak-to-peak separation (ΔE_p [V]). When the electron transfer barrier is low, an equilibrium can be established immediately upon applied potential. However, when the electron transfer barrier is high, the electron transfer reaction appears sluggish and more negative (positive) potentials are required to achieve the reduction (oxidation) reaction, resulting in a larger ΔE_p [294].

Furthermore, since the de- / intercalation of Li-ions from / into NMC 622 electrode is a diffusion-controlled process, the effective diffusion coefficient of Li-ions D_{eff} [cm^2/s] can be calculated using equation (4.10), which is originated from the Randles-Ševčík equation [295]:

$$\frac{I_p}{m_{act}} = 0.4463 \cdot \left(\frac{F^3}{R \cdot T}\right)^{1/2} \cdot A_m \cdot C_0 \cdot D_{eff}^{1/2} \cdot \nu^{1/2} \quad (4.10)$$

where I_p [A] is the peak current originated from CV analysis, m_{act} [g] the active mass of an electrode, F [As/mol] the Faraday's constant, R [J/mol·K] the gas constant, T [K] the temperature, A_m [cm^2/g] the electrode area per unit mass, and C_0 [mol/cm^3] the total amount of Li-ions in a lithiated NMC 622 particle.

Xie et al. [296] compared the effective Li-ion diffusion coefficients of cells containing ultrathin LCO cathode with a thickness of 0.85 µm obtained by different methods, i.e., CV, GITT, PITT, and EIS, and they suggested that the values from the PITT method were more reliable, while the Li-ion diffusion coefficients obtained by the CV was of the same magnitude as those by the PITT. In order to determine the redox reaction and to calculate the effective Li-ion diffusion coefficient of NMC 622 cathodes with different binders and acid additions, CV analyses were performed on coin cells (half-cells) after the formation step using a battery cycler (BCS-810, Biologic SAS, France). Scan rates ranging from 0.02 to 0.12 mV/s with 0.02 mV/s increment were applied, while the voltage window was set from 3.0 to 4.3 V. The electrochemical analyses were performed at a constant temperature of 18 °C.

4.5.4. Electrochemical impedance spectroscopy analyses

Electrochemical impedance spectroscopy was conducted after rate capability analyses to determine the impedance of coin cells containing different electrode types. A potentiostat (VMPS, Biologic SAS, France) was used to perform EIS analyses on cells at an open circuit voltage (OCV) of about 3.6 V, while the cells were placed in an oven with a constant temperature of 25 °C. The scanning frequency of EIS analyses varied from 0.02 Hz to 1 MHz, while a sinus amplitude of 10 mV was applied.

A battery cycler (BCS-810, Biologic SAS, France) was applied to monitor the impedance growth of the pouch cells with laser structured or unstructured aqueous processed NMC 622 cathodes vs. graphite anodes in contrast to the reference cells containing PVDF-based NMC 622 vs. graphite anodes. EIS analyses were performed at 3.6 V (50 % SOC) after the rate capability analyses and after every 100 cycles at C/2 during the lifetime analyses. The same 10 mV sinus amplitude used for coin cells was applied to the pouch cells, while the scanning frequency was set to 10 mHz to 10 kHz. ZView 2 software (Scribner LLC, USA) was employed to fit the EIS data to an equivalent electronic circuit.

In addition, the effective lithium-ion diffusion coefficient $D_{eff,EIS}$ [cm^2/s] of half-cells containing NMC 622 cathodes can be calculated from the Warburg element in EIS analyses as follows [87]:

$$D_{eff,EIS} = \frac{R^2T^2}{2A_e^2n_e^4F^4C_0^2\sigma_w^2} \quad (4.11)$$

where R [J/mol K] is the gas constant, T [k] the temperature, A_e [cm^2] the footprint area of the electrode, n_e [-] the number of electrons per molecule during oxidation (here $n = 1$), F [As/mol] the Faraday's constant, and C_0 [mol/cm^3] the total amount of Li-ions in a lithiated NMC 622 particle. σ_w [$\Omega s^{-1/2}$] is the Warburg impedance coefficient, which can be obtained from the slope by plotting the real part of the resistance Z_{re} [Ω] vs. the frequency $\omega^{-1/2}$ [$s^{1/2}$] [87]:

$$Z_{re} \propto \sigma_w \omega^{-1/2} \quad (4.12)$$

4.6. Uncertainty assessment

In this chapter, the possible variations between theoretical and experimental results in each experimental step are analyzed. The electrode density, active mass loading, areal capacity, as well as mass loss of electrodes due to laser structuring are given in values with standard deviations. The standard deviations are calculated according to the theory of uncertainty propagation described as follows [297]:

$$\sigma_f = \sum_{i=1}^{n} \left|\frac{\partial f}{\partial x_i}\right| \sigma_{x_i} \quad (4.13)$$

Slurry preparation

For the preparation of NMP-based NMC 622 slurries, each composition (NMC 622 powder, conductive agent powder, KS6L graphite powder) was weighed according to the recipe, and subsequently added into the prepared PVDF binder solution. The deviation of the amount of each component could be resulted from the precision of the balance, which is ± 0.01 mg. Besides, when weighing a component, a small portion of the powder or binder solution may stick to the weighing plate or spoon, resulting in a lower content of a component in the slurry. In addition, the slurry can stick to the wall of mixing vessel or the mixing head during and after mixing, which might cause the final obtained slurry to deviate from the intended formulation.

As for the aqueous processing of NMC 622 slurries, only acid was added between pre-mixing and homogenizing (90 min), while no alkali was added to the slurry in order to avoid introducing additional impurities. However, the slurry pH value was measured after the slurry has been homogenized, which means that it was not possible to adjust the pH value any further. Thus, the deviations of the pH values of water based NMC 622 slurries (Figure 5-36) are originated from different batches. Besides, room temperature affects the slurry pH value, so slurries modified with the same amount of acid may have slightly different pH values due to temperature fluctuation. In Table 5-17 and Table 5-19, no deviation of slurry pH values was given, since each type of cathodes was from the same batch applied for further electrochemical analyses.

Electrode characterization

After drying, the film thickness of electrode was determined by measuring on 10 – 20 random positions of an electrode sheet with a micrometer (1 µm precision). However, during

the coating, even when the screws on both sides of the doctor blade were set to the same value, the blade height may not be the same due to the aging of the threads. This means that one side of the coating may be thicker than the other. However, it is difficult to accurately determine the height difference of the doctor blade, thus only the set height (doctor blade gap) values were given in Table 5-7 and Table 5-11. Besides, the deviation of thickness increases with increasing film thickness, as shown in Table 5-7. This results in increasing errors in porosity, areal capacity, and electrode density with increasing film thickness.

Cell assembly

Most of the electrochemical analyses were conducted using CR2032 coin cells, with components such as cell case, spacer, and separator remaining the same, while the same type and amount of electrolyte and a same loading were provided for cell sealing. However, for cells containing thick-film NMC 622 cathodes with thickness more than 150 µm, wave springs were used instead of ring spring. This is due to the fact that in the previous experiments, the coin cells with thick-film electrodes using ring springs broke down after a few cycles during rate capability analyses, which might have been caused by excessive pressure inside the cells. Different pressure could result in different electrolyte amount in the electrodes and separator, since more amount of electrolyte could be squeezed out during the cell sealing. This could in turn affect the electrochemical performance. However, since the same wave springs were used for the assembly of all cells containing thick-film electrodes, the electrochemical performance of these cells are comparable with each other.

The pouch cells were assembled by hand in glovebox. Prior to cell assembly, visual inspection of all cathodes, anodes, separators, and housings was performed to identify the possible defects such as perforation, folds, or impurities as well as dust on the surface. The surface of electrodes and separators were cleaned with a bulb dust blower, while the defective electrodes or separators were not used to avoid short circuit. In addition, the position of electrodes and separators in each cell cannot be guaranteed to be exactly the same. Due to the difference in the distance between the sealing edge and the stack, the wetting behavior of the stack could be slightly different and localized dried electrode spots (lack of wetting) might be appeared in some pouch cells, resulting in reduced capacity, decreased cycling capability, and localized current density variation. Therefore, for the electrochemical analyses, at least 3 pouch cells were assembled with each type of electrode.

Laser structuring

For the laser structured NMC 622 cathodes with a thickness of 150 µm, digital microscopy was unable to characterize the ablation depth and width due to the high aspect ratio of the channel structures. Therefore, the laser structured electrodes were embedded and characterized in cross-sectional view using an optical microscope. The appropriate laser parameters such as the number of laser scans and average laser power were determined when the average ablation depth reached the current collector. However, as mentioned earlier, the film thickness of electrodes fluctuated with a deviation of ± 5 µm observed in electrodes with 150 µm thickness. Thus, laser ablation of the Al current collector was observed at some thinner spots on the electrode. This leads to a decrease of m_{Al} in equation (5.6), which means

that the calculated mass loss may be higher than the actual value. In addition, high power laser with beam splitter were employed in order to study of process upscaling (Figure 4-9). However, the power difference between five beamlets is 1.5 – 9 % (datasheet from TOPAG Lasertechnik GmbH), resulting in inhomogeneous ablation depth and width in laser generated grooves in electrodes.

Electrochemical analyses

In this work, at least 3 cells were assembled for each type of electrode. For rate capability analyses and lifetime analyses, discharge capacity with deviation was displayed. Especially for lifetime analyses, pouch cells (full-cells) showed significantly stable performance (Figure 5-70) in contrast to coin cells (half-cells) using the same electrodes (Figure 5-65). The fast degradation in coin cells might be owing to the instability of the Li electrode. However, after comparing Figure 5-64-a with Figure 5-67-a, it is found that regardless of the cell design, cells containing the same cathode types showed similar tendency in rate capability. Therefore, it is reliable to analyze the rate capability of different electrodes using coin cells, while pouch cells are preferable for the study of lifetime analyses.

Another key point is the calculation of the current applied in the rate capability analysis. Few studies have detailed how the currents were determined. In order to obtain more comparable data and minimize uncertainties, equations (3.5) and (3.6) were primarily applied to calculate the current at C/20 ($I_{C/20,original}$ [A]) for each cell. This current value was then used for the formation at C/20. Afterwards, the current at 1C ($I_{1C,cal.}$ [A]) was calibrated based on the actual discharge time (t_{actual} [h]) derived from the third cycle in the formation and was further applied to the currents at other C-rates (I_{nC} [A]):

$$I_{1C,cal.} = I_{C/20,original} \cdot t_{actual} \tag{4.14}$$

$$I_{nC} = \frac{I_{1C,cal}}{n} \tag{4.15}$$

After rate capability analyses, coin cells with different electrode setups were selected to continue the EIS analyses. A 24 h pause was engaged before EIS analyses to ensure that the voltage of all cells returned to 3.6 V (OCV). After comparing the results of cells containing different electrodes as shown in Figure 5-28 and Figure 5-61, it was found that all cells showed similar bulk resistance, which should be attributed to the fact that the coin cells and cell holders are standard industrial products. However, pouch cells were different from coin cells. As mentioned before, all pouch cells were assembled by hand, which could lead to different bulk resistance measured by the EIS analyses. Additionally, since the lifetime analyses and the EIS analyses of pouch cells were not performed on the same test instrument (the pouch cells were transferred from the Arbin battery cycler to the Biologic battery cycler after every 100 cycles), it was not guaranteed that the alligator clips on the tabs of pouch cells were always in the same position. This could result in a shift in the resistance of the electric contacts, which means that the initial position of the first semicircle obtained from the same cell can fluctuate considerably. Therefore, offsets were applied for EIS data measured after different number of cycles for each pouch cell to ensure that the EIS curves start at the same position.

5. Results and discussion

In order to determine the crystal structure, chemical composition, as well as morphology of the powder samples, all the active materials were characterized prior to the further processing. The preparation of the slurry is a fundamental process with a significant impact on subsequent processing steps. For optimizing purpose, slurries with different NMC 622 powders and with different binders were made and were coated onto the Al foil. Afterwards, the cathode films were calendered in order to adjust the porosity to values of about 35 %. Laser patterning was performed on the calendered cathodes to generate 3D structures with different pitch or pattern types. Prior to assembly, the NMC 622 electrodes with different binders and acid additions were characterized using SEM, XPS, and Raman spectroscopy. Subsequently, the cathodes were assembled into coin cells vs. Li or in pouch cells vs. graphite anodes. Electrochemical analyses such as CV, rate capability analyses, lifetime analyses, and EIS analyses were conducted to investigate the influence of electrode film thickness, electrode configuration with different NMC 622 powders and multilayers, aqueous processing, and laser structuring on the cell performance.

5.1. Characterization of electrode materials

Before slurry mixing, the chemical composition and physical properties of active materials were characterized. These are polycrystalline NMC 622 powders with two different particle size distributions which are used for cathodes, and synthetic graphite for anodes.

5.1.1. Polycrystalline NMC 622 powders

The diameters of secondary and primary particles are determined by randomly selecting 10 – 20 particles in the SEM images (Figure 5-1) by measuring their maximum horizontal length. Polycrystalline NMC 622 powder with “big” secondary particles (B-NMC 622) has spherical structures with diameters of 4.9 – 13.2 µm, as shown in Figure 5-1-a, while the primary particles show rectangular shapes with lengths of 0.3 – 0.5 µm. NMC 622 powder with “small” secondary particles (S-NMC 622), see Figure 5-1-b, shows diameters of about 3.9 to 5.5 µm in the secondary particles, while the primary particles of S-NMC 622 powder are 3 – 5 times larger (1 to 2.5 µm) compared to those in B-NMC 622 particles. The primary particles can be clearly distinguished from the secondary particles in both NMC 622 powder types.

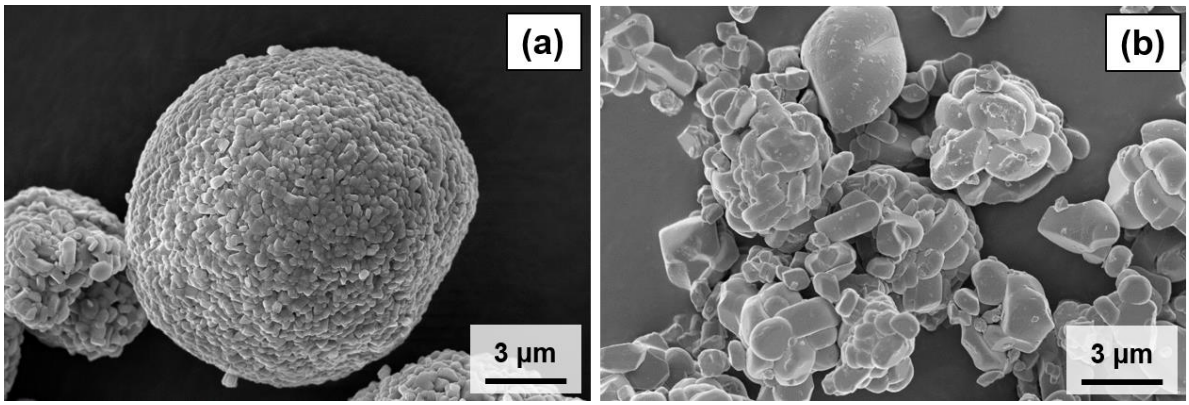

Figure 5-1. SEM images of polycrystalline NMC 622 particles with (**a**) big (B) and (**b**) small (S) secondary particles as active materials for cathodes.

The frequency distribution of the particles or the probability of finding a particle with a given diameter in the population was measured by laser scattering (Figure 5-2). The B-NMC 622 powder has a D50 (median) of 8.7 µm and a D90 of 12.8 µm, while the S-NMC 622 powder shows a D50 of 4.6 µm and a D90 of 6.7 µm. The values from this analysis are in good agreement with the diameters estimated from the SEM images (Figure 5-1).

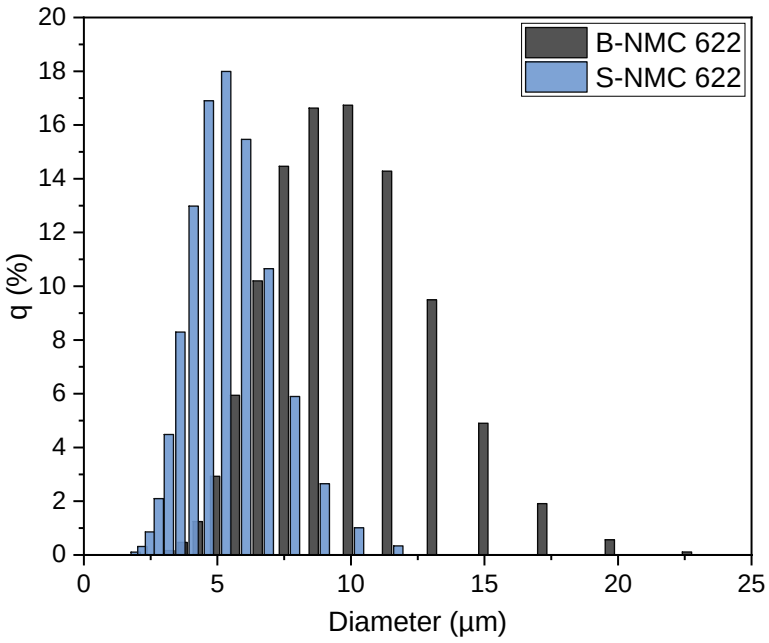

Figure 5-2. Particle distribution of the two used NMC 622 powders – B and S type. B indicates the NMC 622 powder with big secondary particles, while S refers to the NMC 622 powder with small secondary particles.

The stoichiometry of different NMC 622 powders was determined by ICP-OES and carrier gas hot extraction method. The results are shown in Table 5-1. The mole fraction x_i [%] of the respective elements in the chemical formula $Li_{x(Li)}Ni_{x(Ni)}Co_{x(Co)}Mn_{x(Mn)}O_{x(O)}$ can be calculated from the mass fraction m_i [%] of each element in combination with the molecular weight M_i [g/mol] by using the following equation:

$$x_i = \frac{m_i}{M_i} \; (i = Li, Ni, Mn, Co, O) \tag{5.1}$$

Table 5-1. Stoichiometry of different NMC 622 powders derived from chemical analyses.

Element	Molecular weight [g/mol]	B-NMC 622 powder		S-NMC 622 powder	
		Mass fraction [%]	Mole fraction [%]	Mass fraction [%]	Mole fraction [%]
Li	6.997	7.05 ± 0.15	1.01 ± 0.02	7.33 ± 0.14	1.06 ± 0.02
Mn	54.938	11.11 ± 0.21	0.20 ± 0.01	11.60 ± 0.20	0.21 ± 0.01
Co	58.933	11.93 ± 0.42	0.20 ± 0.01	11.40 ± 0.20	0.19 ± 0.01
Ni	58.693	35.74 ± 0.46	0.61 ± 0.01	35.30 ± 0.70	0.60 ± 0.01
O	15.999	34.2 ± 3.1	2.1 ± 0.2	32.9 ± 2.7	2.1 ± 0.2

The stoichiometry of B-NMC 622 powder is determined to be $Li_{1.01}Ni_{0.61}Mn_{0.20}Co_{0.20}O_{2.1}$, while the S-NMC 622 powder has a stoichiometry of $Li_{1.06}Ni_{0.60}Mn_{0.21}Co_{0.19}O_{2.1}$. In both cases NMC 622 designation is confirmed. Similar results were obtained in other works [298, 299].

Figure 5-3 represents the XRD patterns of the two NMC 622 powders, showing similar reflex positions which demonstrate that both powders have the same single-phase layered NMC 622 with a space group of $R\bar{3}m$ and equivalent chemical compositions. In addition, the sharp reflexes of both powders suggest their highly crystalline structures [300]. The Miller indices corresponding to the reflexes have been determined and they are in good agreement with data of NMC 622 from other studies [298, 299]. Furthermore, the clear reflex splitting at 2θ = 37.96 (006) and 38.36 (102) as well as at 2θ = 64.43 (108) and 65.01 (110) were detected for both NMC 622 powders, which indicates a highly crystallized and a well-ordered layered structure of the NMC 622 material [90, 301]. Besides, the reflexes of (003) and (104) show the highest intensity, and the intensity ratio of (003) to (104) reflexes ($I_{(003)}/I_{(104)}$) can be used to characterize the cation mixing of Li^+ with Ni^{2+} in NMC materials, an intensity ratio less than 1.2 indicates the appearance of cation mixing [302]. The intensity ratio $I_{(003)}/I_{(104)}$ of B-NMC 622 is 2.17, while the S-NMC 622 powder shows a higher ratio of 4.21, implying that less cation mixing exists in the S-NMC 622 particles. The average grain size D [nm] can be obtained from the XRD data using the Scherrer's formula [302]:

$$D = \frac{K\lambda}{\beta cos\theta} \tag{5.2}$$

where K [-] is the Scherrer constant (0.9), λ [nm] the wavelength of the X-ray source (0.15406 nm), β [rad] the FWHM of a reflex, and θ [°] the position of reflex. The average grain size of B-NMC 622 particles is 55.8 ± 10.6 nm, while S-NMC 622 particles exhibit a larger mean grain size of 85.3 ± 11.7 nm, which is consistent with the particle sizes obtained from the SEM images (Figure 5-1).

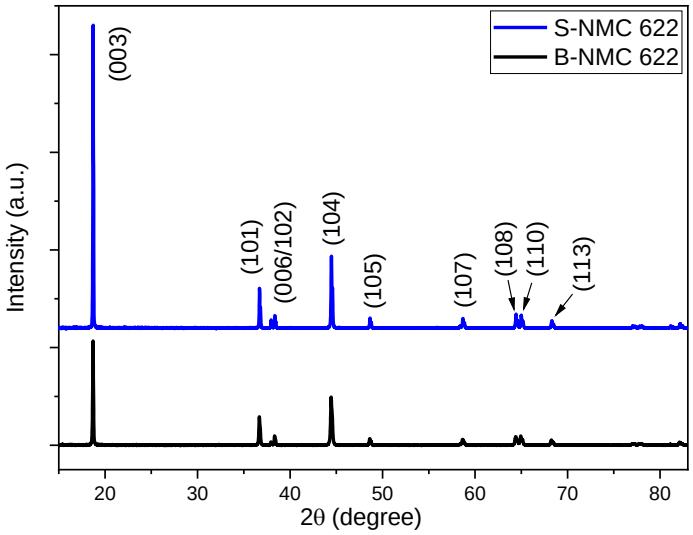

Figure 5-3. XRD patterns of the two polycrystalline B- and S-NMC 622 powders with different secondary particle sizes.

The results of the BET surface area analyses of the two NMC 622 powders are shown in Figure 5-4. The slope and the y-intercept derived from the plot are used to calculate the BET surface area using equation (4.7). The B-NMC 622 powder has a BET surface area of 0.49 ± 0.01 m^2/g, while the S-NMC 622 powder shows a larger BET surface area of 0.60 ± 0.01 m^2/g.

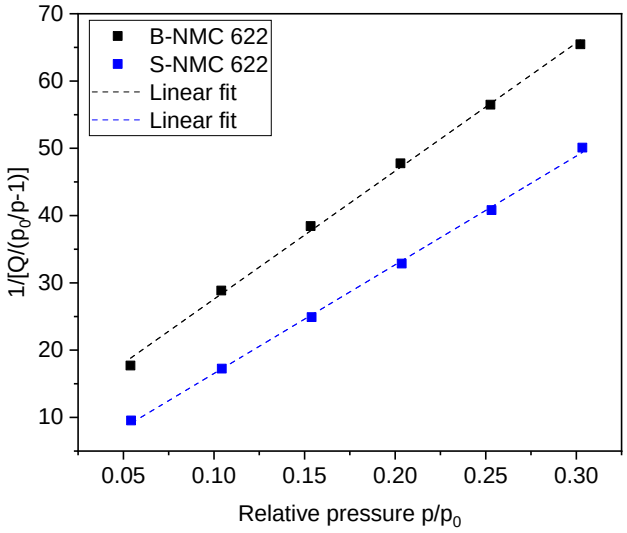

Figure 5-4. BET surface area analyses of the two different NMC 622 powders used.

5.1.2. Synthetic graphite and KS6L graphite

Two different graphite material types were used in this work with different purposes. Coke-based synthetic graphite was applied as active material for anodes, while KS6L graphite was used as compaction aid as well as conductive agent for cathodes. Although both synthetic graphite and KS6L graphite particles have a flack-like morphology as shown in Figure 5-5, their topography are quite different, since synthetic graphite powder consists of needle-like coke particles and fine grained particles, which is similar to the results from Magampa et al. [109], while KS6L graphite powder shows higher flake density with larger diameter.

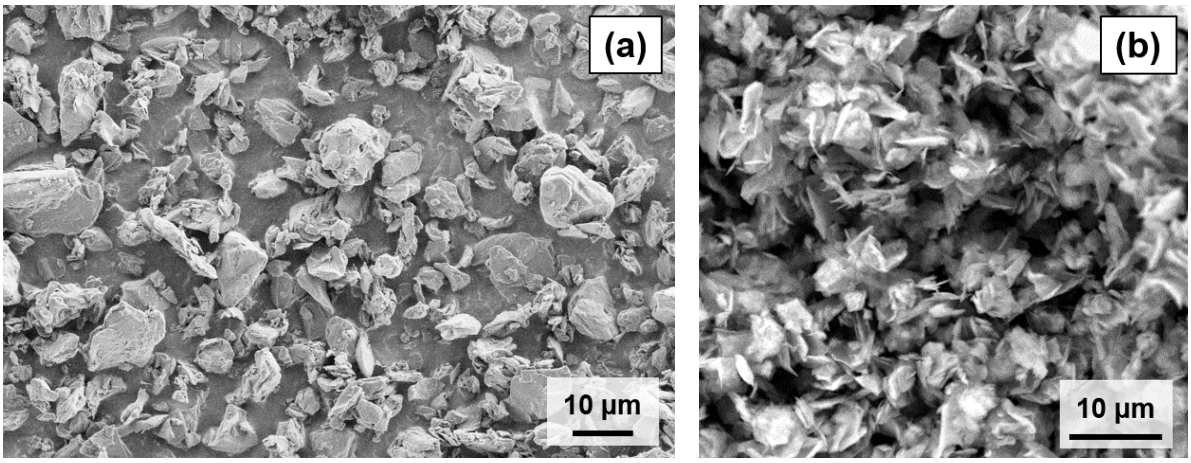

Figure 5-5. SEM images of (**a**) synthetic graphite for anode (SE detector) and (**b**) KS6L graphite as compaction aid for cathode (BSE detector).

The particle size distribution was analyzed by laser scattering, synthetic graphite powder has a D50 diameter of 4.85 µm and a D90 diameter of 6.55 µm (Figure 5-6-a), which are similar to the results from Meyer et al. [170], while KS6L graphite exhibits a larger D50 diameter of 7.47 µm and a D90 diameter of 11.04 µm, which are almost twice as large compared to the results from Jeschull et al. [303] with D50 = 3.5 µm and D90 = 6.5 µm and from Spahr et al. [38] with D50 = 3.2 µm. A possible explanation for a larger measured particle size in this work is that the ultrasonic bathing prior to the laser scattering measurement is not powerful enough to effectively break up the agglomerated KS6L graphite particles, resulting in a larger particle size that originates not only from the diameters of secondary particles but also from the agglomerated graphite particles. KS6L graphite powder has similar diameter in comparison to polycrystalline NMC 622 powder as shown in Figure 5-1-a. The BET surface areas of synthetic graphite as well as KS6L graphite are 2.02 ± 0.01 m^2/g and 18.95 ± 0.09 m^2/g, respectively (Figure 5-6-b). These results are consistent with others [170, 303].

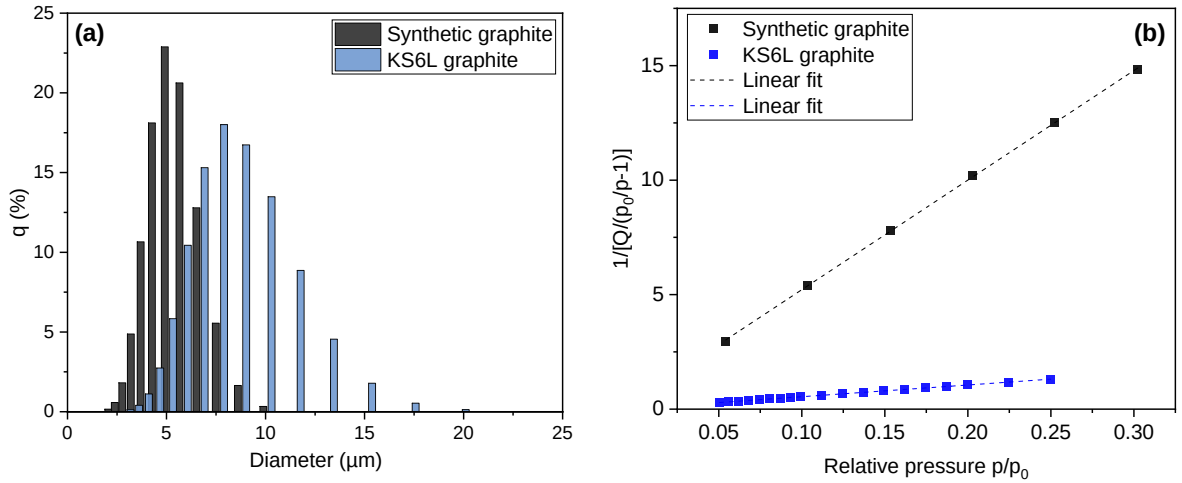

Figure 5-6. Physical properties of two different types of graphite: (**a**) particle size distribution and (**b**) BET surface area.

5.2. Electrodes processed with PVDF binder

In this chapter, NMC 622 cathode slurries with B-NMC 622 powder were prepared using state-of-the-art PVDF as binder and NMP as solvent, and subsequently tape-cast onto the Al current collector with different doctor blade gaps to achieve different film thicknesses. This allowed the investigation of the impact of film thickness and laser structuring on the electrochemical performance.

5.2.1. Slurry and electrode characterization

Prior to tape-casting, the rheological property of the NMC 622 slurry was characterized using a rheometer, see Figure 5-7. The NMC 622 slurry with PVDF binder and NMP solvent displayed a shear-thinning behavior, i.e., the viscosity decreases with increasing shear rate. This result is consistent with the results from Bauer et al. [166]. The coating speed was kept constant at 5 mm/s, whereas the doctor blade gap varied from 200 µm to 700 µm. Therefore, the practical shear rates of slurry for coating locate between 7 – 25 s^{-1}, as shown in Figure 5-7 between two red dash lines. Viscosities ranging from 6.3 to 11.3 Pa·s were applied during coating and the high viscosity can prevent the sedimentation of the NMC 622 particles by reducing the mobility of the particles in the dispersion [166], which is suitable to fabricate thick-film electrodes.

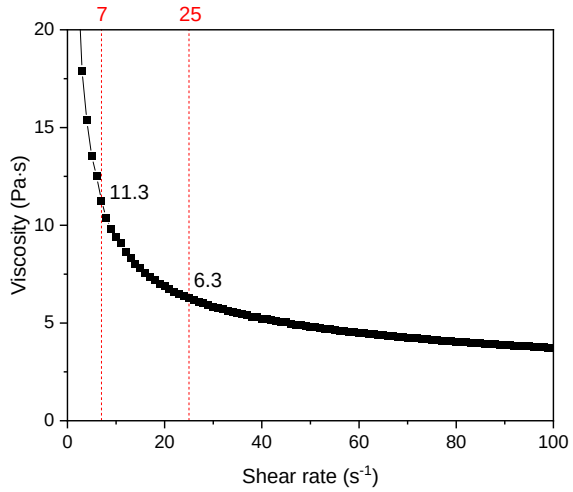

Figure 5-7. Viscosity of slurry containing polycrystalline B-NMC 622 powder with PVDF as binder at shear rates from 0 to 100 s^{-1}.

The conductive agent Super C65 has a mean primary particle diameter of 32 nm as determined by transmission electron microscopy (TEM) [38]. It can form clusters located in the gaps between NMC 622 particles with PVDF binder (Figure 5-8-a) and supports the transfer of electrons from the NMC 622 particles to the current collector [39]. The length of a stretched unbranched PVDF macro molecule can be calculated based on the molar weight (64.03 g/mol) and length (0.462 nm) of an unit cell (–CH_2CF_2–) in c-direction [304]. The molecular weight of the PVDF binder is 1,000,000 – 1,200,000 g/mol according to the datasheet. Thus, the chain length of PVDF is assumed to be 7.2 to 8.7 µm. However, the polymer chains of PVDF interact with NMP solvent and conductive agents, and this leads to the formation of random coil

structures with diameters ranging from 100 – 200 nm [166], which is larger than the conductive agent but smaller than the NMC 622 particles.

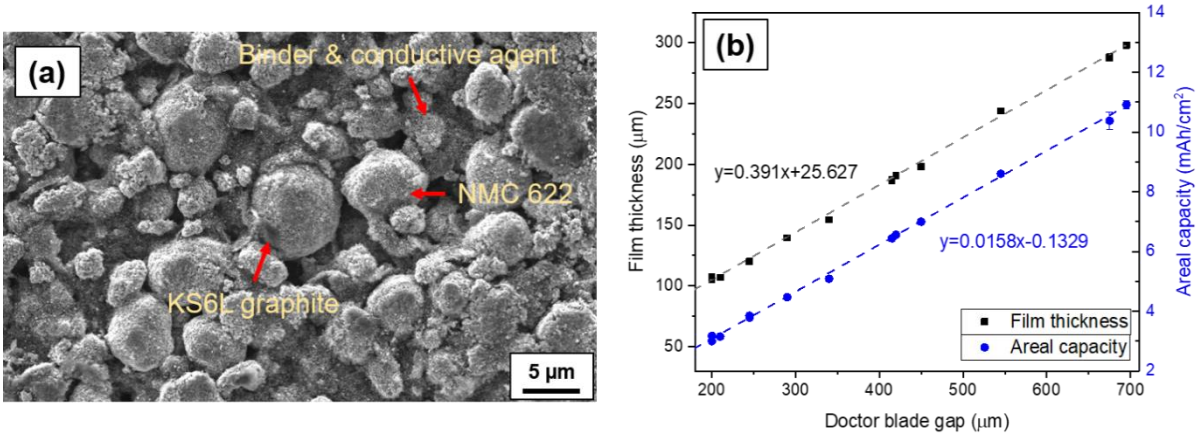

Figure 5-8. NMC 622 electrode surface topography, film thickness and respective areal capacity: SEM image of (**a**) a polycrystalline NMC 622 cathode with PVDF as binder after drying and calendering [305], and (**b**) film thickness (before calendering) and areal capacity of NMC 622 cathodes as a function of doctor blade gap.

The film thickness (after drying and before calendering) or rather the areal capacity of NMC 622 cathodes can be adjusted by varying the doctor blade gap, as shown in Figure 5-8-b. For cathode slurry with fixed composition, a linear relationship between dried film thickness and doctor blade gap is observed. This ensures a precise control of the film thickness by adjusting the gap between the doctor blade and Al foil. In this work, PVDF-based NMC 622 with a maximal film thickness of 250 µm (before calendering) was achieved. After coating, the electrodes were calendered to achieve a porosity of 35 %, which was determined using equation (4.9). State-of-the-art cathodes usually have thicknesses of 50 – 70 µm with an areal capacity of about 3 mAh/cm^2 [306], while in this work, NMC 622 cathodes with four different thicknesses of 74 µm, 100 µm, 150 µm, and 200 µm (after calendering) were selected for further electrochemical analyses. The final electrode density after calendering, active mass loading, and areal capacity of different NMC 622 cathodes are listed in Table 5-2. The active mass loading is related to the active material amount in the electrode, while a specific capacity of 172 mAh/g derived from the formation step in electrochemical analysis was applied for the calculation of areal capacity. The electrodes with 74 µm film thickness were used as reference to represent the state-of-the-art film thickness. With increasing film thickness, the mass loading of NMC 622 cathodes increases from 18 mg/cm^2 to 50 mg/cm^2, which is 2.8 times higher compared to electrodes with state-of-the-art thickness. Meanwhile, the areal capacity of the cathode increases from 3.1 mAh/cm^2 to 8.6 mAh/cm^2.

Table 5-2. Electrode density after calendering, active mass loading, and areal capacity of NMC 622 cathodes with different film thicknesses.

Film thickness [µm]*	Electrode density [g/cm^3]	Active mass loading [mg/cm^2]	Areal capacity [mAh/cm^2]
74 ± 2	2.66 ± 0.04	18.12 ± 0.24	3.12 ± 0.04
100 ± 3	2.82 ± 0.05	25.92 ± 0.37	4.47 ± 0.06
150 ± 5	2.71 ± 0.03	37.34 ± 0.35	6.44 ± 0.06
200 ± 6	2.71 ± 0.02	49.89 ± 0.28	8.60 ± 0.05

* This film thickness does not contain the thickness of Al foil (20 µm).

The XPS analysis as well as Raman spectroscopy of NMC 622 cathodes processed with PVDF binder and NMP solvent will be presented and discussed together with aqueous processed cathodes in chapter 5.4.

5.2.2. Impact of film thickness on electrochemical cell performance

As discussed in the chapter 3.2.5, increasing the film thickness is a practical strategy to increase the energy density on cell level by reducing the use of inactive material. Thus, the first step in this work is to determine the limit of rate capability of cells containing thick-film NMC 622 cathodes processed with PVDF binder.

Figure 5-9 presents the discharge capacities of cells containing NMC 622 cathodes with different thicknesses vs. Li at C-rates ranging from C/20 to 5C. Three to five cells were measured for each cell setup and the average specific discharge capacities were plotted. For the formation step, the cells were charged and discharged at C/20 for 3 cycles in order to establish a stable cathode electrolyte interphase (CEI) [307]. Both cells containing cathode with 74 µm and 100 µm thicknesses reached an initial capacity of 177 mAh/g, while cells with thicker electrodes showed a slightly lower capacity of 175 mAh/g. Besides, a capacity increase of 1 – 2 mAh/g was observed for all cells with increasing cycle number at C/20. The coulombic efficiency at the first cycle was calculated using equation (3.8). Cells containing cathodes with 74 µm and 100 µm thicknesses had 90 % CE, while others with 150 µm and 200 µm thickness cathodes had 88 % and 89 % CE, respectively. A lower initial CE suggests an increased electrolyte consumption for the CEI formation during cycling [202], in this case it might be due to an increased contact surface area between NMC 622 particles and electrolyte with increasing mass loading. The CE of cells with different thicknesses is listed in chapter 5.2.3 along with cells assembled with laser structured electrodes.

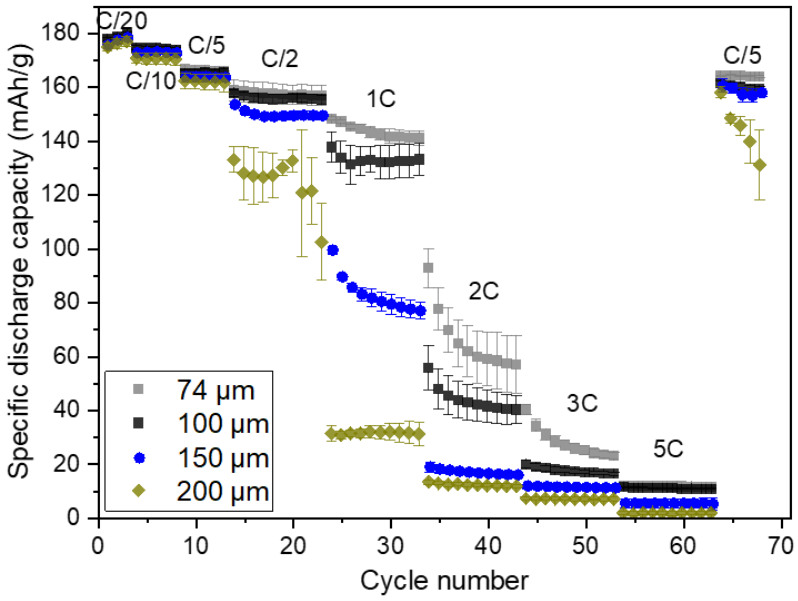

Figure 5-9. Specific discharge capacities for half-cells containing NMC 622 cathodes with different film thicknesses at different C-rates.

When the C-rate increased up to C/10 and C/5, all cells showed similar discharge capacity, while cells with 200 µm thick-film electrodes showed 2 mAh/g less discharge capacity at C/5 in comparison to others. At C/2, the discharge capacity of cells with 200 µm thick-film electrodes dropped to 126 mAh/g, and the discharge capacity deviation was significantly larger in contrast to other cells. Cells with NMC 622 cathodes having a film thickness of 74 µm and 100 µm showed no difference in specific capacity at C/2, while ones with 150 µm film thickness exhibited 150 mAh/g discharge capacity, which corresponds to a drop in capacity of about 5 mAh/g. The maximum capacity difference was achieved at 1C, where the discharge capacity decreased from 140 to 30 mAh/g with increasing electrode film thickness. For cells with the thickest electrodes, more than 78 % capacity drop was observed at 1C. At 3C and 5C, all cells showed more than 80 % drop in capacity. A serious capacity drop (degradation) in cells with thick-film NMC 622 electrodes at elevated C-rates from 1C to 5C was also reported by Heubner et al. [24], where the discharge capacity decreased from 120 mAh/g to 40 mAh/g for cells with NMC 622 cathodes having increasing thickness from 128 to 212 µm. Their results are in good agreement with the results presented here, even though they used a slightly lower NMC 622 content of 91.4 wt%.

After high rate capability analyses up to 5C, the cells were cycled again at C/5 and those having electrodes with thicknesses less than 150 µm showed almost the same capacity in comparison to the previous C/5, however, the cells with NMC 622 cathode having a film thickness of 200 µm exhibited strong degradation and the capacity dropped from 158 mAh/g to 131 mAh/g with increasing cycle number. The cells containing NMC 622 cathodes with 200 µm thickness were not able to retain the same capacity when subsequently cycled at low C-rates after being cycled at high C-rates (> 2C). This might be caused by the inhomogeneous electrolyte distribution in thick-film NMC 622 electrode, since a concentration gradient of electrolyte is formed beside electric field in order to drive the Li-ion to the cathode; And this gradient becomes stepper with increasing C-rates or film thickness [23]. It is assumed that the electrolyte concentration in the near of Al current collector in thick-film NMC 622 cathodes must be low after charging / discharging up to 5C. The Li-ion diffusion in the electrolyte becomes a limiting process and part of the NMC 622 particles near the current collector are not utilized and participate no longer in the electrochemical reaction when the cells are charged or discharged at C/5, which leads to the capacity drop during the last C/5 cycles. In contrast, cells with 150 µm electrodes maintained high-capacity retention when cycled at C/5 after being abused at high C-rates. Therefore, 150 µm film thickness (after calendering) was applied as target thickness for further studies of bilayers as well as aqueous based NMC 622 cathodes.

The charge and discharge profiles of cells from Figure 5-9 at C/10, C/2 and 1C are selected and presented in Figure 5-10. The discharge profiles at C/10 are the same as those obtained by Noh et al. [86] using the same active material. For cells with electrode film thicknesses ranging from 74 µm to 150 µm, the constant-voltage charge phase (horizontal line at the end of charge) increased with increasing C-rate. For cells containing cathodes with 150 µm thickness, almost 50 % of the discharge capacity at 1C was originated from the constant-voltage charge phase. Besides, at C/2 and 1C, the charge and discharge capacities were reduced with increasing electrode thickness. Similar trend was also observed and a significant capacity drop of 80 mAh/g was reported for cells with NCA electrodes having a film

thickness of 240 µm in comparison to those with electrodes having a film thickness of 60 µm at 1C [23].

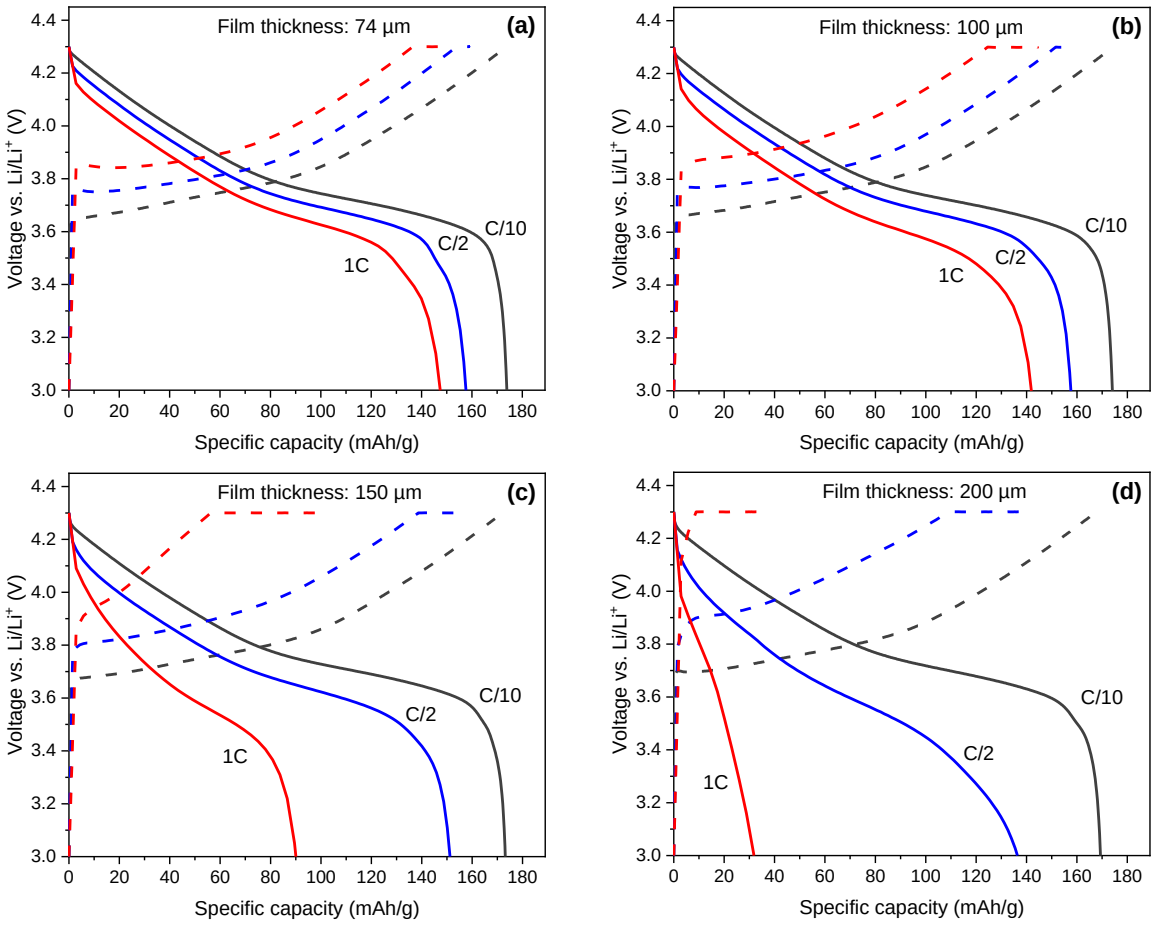

Figure 5-10. C-rate dependent specific charge (dashed lines) and discharge capacity vs. the voltage (vs. Li / Li^+) of half-cells containing unstructured NMC 622 electrodes with film thicknesses of (**a**) 74 µm, (**b**) 100 µm, (**c**) 150 µm, and (**d**) 200 µm.

The "IR-drop" illustrated in chapter 3.1.4 refers to the linear voltage drop at the beginning of a discharge curve. An IR-drop of 0.03 – 0.05 V was observed at C/10 for all cells. However, the IR-drop increased with increasing film thickness at 1C showing 0.14 V, 0.16 V, 0.21 V, and 0.32 V for cells with increasing film thicknesses from 74 µm to 200 µm, respectively. This indicates a higher ohmic resistance in cells with thicker electrodes. Besides, the discharge plateau was lower with increasing film thickness and C-rate, indicating an increasing cell polarization. Especially for cells containing NMC 622 cathodes with 200 µm film thickness, the characteristic discharge curve could hardly be observed at 1C and the cells could only reach 32 mAh/g discharge capacity, which was less than 20 % in comparison to their capacity at C/10. During electrochemical cycling, side reactions can occur, such as electrolyte oxidation with Li-ions, which can promote the growth of the resistive surface layer [308]. Another factor is the mechanical stability. Upon cycling, NMC 622 particles suffer from a volume expansion and contraction due to Li-ion de- / intercalation. The volume change can induce severe strain accumulation in thick-film electrodes, leading to an increased internal mechanical stress [309]. Especially at high C-rates above 1C, the rapid volume change will lead to crack formation or fractures in the NMC 622 secondary particles. Those cracks can cause particle isolation,

resulting in capacity loss of the cells. In addition, a limited Li-ion diffusion in the bulk thick-film electrodes can lead to higher effective current density at some local spots on the top layer of the electrode and locally increased ohmic resistance, meanwhile, the active material particles, which are close to the current collector have only reduced or no significant contribution to the overall electrochemical reaction [231]. To counteract this effect, laser structuring was employed, which will be discussed in the following chapter.

5.2.3. Impact of laser structuring on NMC 622 cathodes with PVDF binder

Impact of laser structuring on electrode morphology

The laser setup applied to structure the NMC 622 cathodes with PVDF binder and with different thicknesses was shown in Figure 4-8. The laser spot diameter at the focus plane can be determined using equation (3.21):

$$d_f \approx \frac{M^2 f}{d_L}\frac{4\lambda}{\pi} = \frac{1.2 \cdot 163\ mm \cdot 4 \cdot 515\ nm}{4.4\ mm \cdot \pi \cdot 1000} \approx 29\ \mu m \tag{5.3}$$

The repetition rate f_{rep} [kHz] and average laser power P_L [W] were kept constant at 500 kHz and 2.5 W, respectively, while the number of laser scans were varied to find the suitable parameters for the structuring of electrodes with different film thicknesses. The laser pulse energy E_{pulse} [µJ] and the peak fluence Φ [J/cm^2] applied for the laser structuring of NMC 622 cathodes with PVDF binder can be calculated as follows:

$$E_{pulse} = \frac{P_L}{f_{rep}} = \frac{2.5\ W}{500\ kHz} \cdot 1000 = 5\ \mu J \tag{5.4}$$

$$\Phi = \frac{2E_{pulse}}{\pi(\frac{d_f}{2})^2} = \frac{2 \cdot 5\ \mu J \cdot 10^{-6}}{\pi \cdot (\frac{29\ \mu m \cdot 10^{-4}}{2})^2} = 1.5\ J/cm^2 \tag{5.5}$$

In order to determine the laser ablation depth in composite electrodes, cross-sectional samples were prepared for NMC 622 cathodes with different thicknesses using different number of laser scans. The appropriate laser parameters for structuring of electrodes with different thicknesses were determined, as long as the 3D structures extend from the electrode surface to the Al current collector without damaging the current collector. The most suitable laser parameters determined from the cross-sectional analysis are listed in Table 5-3. The ablation depth of NMC 622 cathodes with PVDF binder using ultrafast laser with a wavelength of 515 nm and a laser fluence of 1.5 J/cm^2 was 5.9 ± 0.6 µm per laser scan. The laser fluence is similar to the parameters (1.5 J/cm^2) of the laser structuring of NMC 811 derived by Li et al. [310].

Table 5-3. Selected laser parameters for the structuring of NMC 622 cathodes with different thicknesses using an ultrafast laser operating at a wavelength of 515 nm (pulse duration: 380 fs, focus diameter: 29 µm, laser pulse energy: 5 µJ, and peak fluence: 1.5 J/cm^2)

Film thickness [µm]	Laser power [W]	Laser scan speed v_s [mm/s]	Repetition rate f_{rep} [kHz]	Laser scans [-]
100	2.5	500	500	17
150	2.5	500	500	22
200	2.5	500	500	38

The laser pulse overlap (PO) [%] applied for the structuring of NMC 622 cathodes is defined as:

$$PO = \frac{d_f - \frac{v_s}{f_{rep}}}{d_f} \cdot 100\% = \frac{29\ \mu m - \frac{500\ mm/s}{500\ kHz}}{29\ \mu m} \cdot 100\% \approx 96.6\% \tag{5.6}$$

where the d_f [µm] is the laser spot diameter at the focus plane, v_s [mm/s] the laser scan speed, and f_{rep} [kHz] the laser repetition rate.

The cross-sectional images of laser structured NMC 622 cathodes with film thicknesses of 100 µm, 150 µm, and 200 mm are shown in Figure 5-11. For ablation depth less than 100 µm, all channels have similar V-shape with wider opening at electrode surface. However, for electrodes with film thicknesses larger than 100 µm, the channel structures taper along the direction from the electrode surface to the current collector, reaching a channel width less than 5 µm (Figure 5-11-b and -c). Thus, the relative mass loss due to laser structuring is decreasing with increasing electrode film thickness.

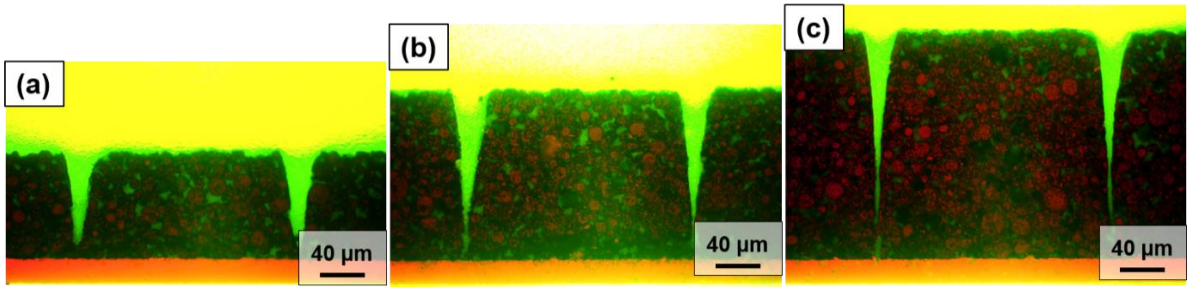

Figure 5-11. Cross-sectional view of laser structured NMC 622 cathodes containing PVDF as binder with film thicknesses of (**a**) 100 µm, (**b**) 150 µm, and (**c**) 200 µm. The laser parameters of the structuring corresponding to different film thicknesses of NMC 622 electrodes are shown in Table 5-3

The geometric information of channels in structured NMC 622 electrodes with PVDF binder and mass loss owing to the laser structuring are summarized in Table 5-4. The mass loss is calculated by weighing the difference between structured and unstructured electrode samples (with a diameter of 12 mm) from the same batch of electrode sheets, excluding the mass of the Al current collector, as shown below:

$$Mass\ loss = \frac{(m_0 - m_{Al}) - (m_{LS} - m_{Al})}{m_0 - m_{Al}} \cdot 100\% = \left(1 - \frac{m_{LS} - m_{Al}}{m_0 - m_{Al}}\right) \cdot 100\% \tag{5.7}$$

where m_0 [g] is the total mass of unstructured electrodes, m_{LS} [g] the total mass of laser structured electrode, m_{Al} [g] the mass of Al foil.

Table 5-4. Maximum width and FWHM of the laser generated groove structures in NMC 622 electrodes with different thicknesses and respective mass losses.

Film thickness [µm]	Max. width [µm]	FWHM [µm]	Mass loss [%]
100	31.1 ± 1.5	13.9 ± 1.7	5.5 ± 2.5
150	31.5 ± 1.4	11.0 ± 1.3	5.8 ± 1.6
200	31.5 ± 1.8	5.8 ± 0.4	3.8 ± 1.8

The maximum width of channels near the electrode surface are about 31 µm, which is in good agreement to the calculated spot size of approximately 29 µm of a Gaussian laser beam at focal length. The aspect ratio (film thickness : FWHM) of the channel structures increases from 7.2 to 34.5 with increasing film thickness. The mass loss was adjusted to 6 %, which is lower in comparison to results of other studies which reported about mass losses in the range of 11 – 20 % [267-269]. Since cathode material such as NMC is much more expensive in contrast to anode and other inactive components in a battery, a low mass loss is beneficial to keep a high areal capacity with increasing film thickness while ensuring that the advantage of laser structuring for thick-film electrodes at high C-rates is not counteracted.

The thermal diffusion length (or the penetration depth) which mainly defines the extent of the heat affected zone can be determined using equation (3.22). According to Gandert et al. [311], the thermal diffusivity of NMC 622 is around $4.5 \cdot 10^{-7}$ m^2/s at 20 °C, hence the respective thermal diffusion length is 0.83 nm taking into account a laser pulse duration of 380 fs. The thermal diffusion length in a NMC 622 particle is theoretically over 10,000 times smaller in comparison to the diameter of NMC 622 particles and could be thus neglected. However, in practice, the laser parameters such as repetition rate and average laser power can also affect the quality of generated 3D architectures such as channel width, sidewall smoothness, and aspect ratio. In order to investigate the effect of laser structuring on the topography and chemical composition, SEM and EDX were applied to analyze the element distribution ("elemental mapping") near a laser-material interaction zone as indicated in Figure 5-12-a. SEM images of laser generated channel with two different magnifications show that the sidewall of channel is smooth and no melted particles is observed near or inside the channels, indicating that no obvious thermal impact was induced on the NMC 622 particles. Furthermore, Dunlap et al. [269] revealed by XRD analysis that no phase modification of the active material NMC 622 took place during the ablation using ultrafast laser. In contrast, it was reported that melt formation appeared along the sidewalls of the grooves during the laser structuring of LFP cathodes with laser repetition rates higher than 200 kHz [15].

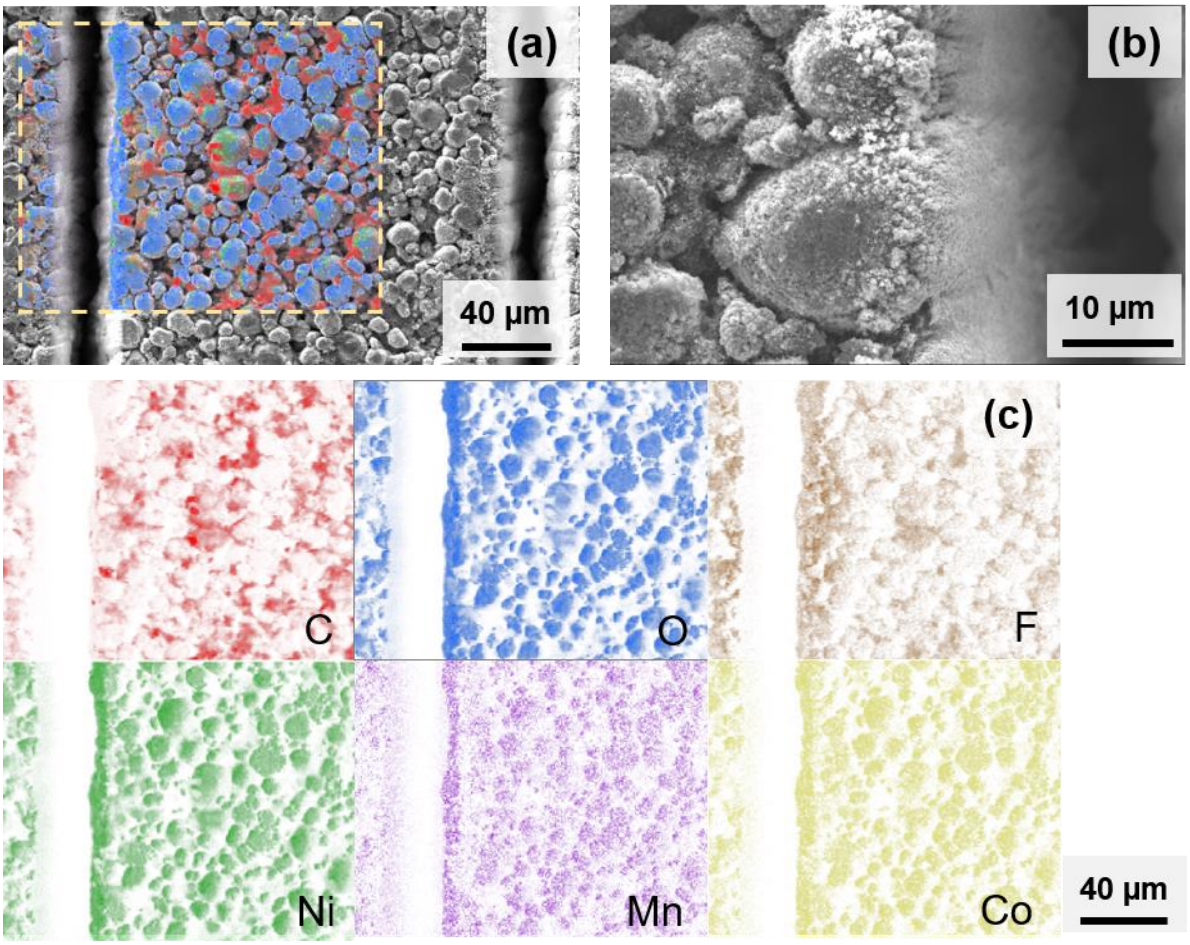

Figure 5-12. SEM and EDX analysis along the edges of a laser generated channel in NMC 622 cathode with PVDF binder. SEM images with (**a**) 2000 × and (**b**) 10,000 × magnification; (**c**) the EDX element mapping of carbon, oxygen, fluorine, nickel, manganese, and cobalt in the area indicated by the dashed rectangle.

In addition, it is worth noting that there are some nano-scaled particles at the edge of the upper surface of the grooves in structured NMC 622 electrodes (Figure 5-12-b). In order to further investigate these particles, element distribution analyses near the laser generated channel were performed (Figure 5-12-c). The carbon exists in conductive agents TIMCAL Super C65 and KS6L graphite, thus it is distributed between the NMC 622 particles. The oxygen is derived from NMC 622, therefore it overlaps with the signals from Ni, Mn, and Co, while the fluorine (F) comes only from the PVDF binder. Along the edge of the channel, no C enrichment was found, rather a depletion, while O, F, Ni, Mn, and Co concentrations are slightly elevated. Therefore, it is assumed that the nanoparticles which were detected at the edge (Figure 5-12-b) could be assigned to finely precipitated particles made of NMC 622 and PVDF binder. Subsequently to laser-induced material sublimation and plasma formation, it is quite probably that the laser generated material vapor / plasma gets in contact with the top edges of the respective channels. This in turn might lead to localized material re-deposition due to rapid cooling. The plasma-material interaction becomes increasingly relevant with increasing aspect ratio. No evidence of conductive agent re-deposition at the edges of channel structures was found while a selective depletion of carbon black via selective evaporation seems to be more probable as reported by Matsumoto et al. [312].

Impact of laser structuring on the electrochemical performance of cells with NMC 622 electrodes having different film thicknesses

The structuring pattern type and laser parameters can determine the balance between the drop in areal discharge capacity at low C-rates and the increase of specific discharge capacity at high C-rates. In our previous research, cathodes with film thicknesses of 91 to 250 µm were assembled in coin cells vs. Li and the pitch of line patterns was varied from 200 to 600 µm [268]. The study showed that the cells containing structured cathodes with 200 µm pitch exhibited significant enhancement in specific capacity at discharge rates from C/2 to 3C in contrast to others with a pitch of 400 µm and 600 µm. It was also verified using laser-induced breakdown spectroscopy (LIBS) that the Li concentration along the contour of 3D electrode architectures was significantly increased which indicates increased Li-ion mobility by providing additional diffusion pathways in liquid electrolyte [313]. Therefore, 200 µm pitch was selected for the laser structuring of NMC 622 cathodes with different thicknesses varying from 100 to 200 µm.

Figure 5-13 exhibits the rate capability analyses of coin cells containing unstructured and laser structured NMC 622 cathodes with different thicknesses vs. Li. In Figure 5-13-a, the specific discharge capacity of cells with increasing C-rates from C/20 to 5C is displayed. All cells showed a similar initial coulombic efficiency of about 89 % at the first C/20 cycle (Table 5-5), indicating that the film thickness has no impact on the CEI formation on the active materials surface. From C/20 to C/5, no significant difference was observed for the specific capacity of the cells containing cathodes with different thicknesses. However, when the C-rate was increased up to C/2, cells with unstructured 200 µm thick-film NMC 622 cathodes showed a capacity drop of about 30 mAh/g, while those with laser structured cathodes had ca. 15 mAh/g higher capacity. Other cells with structured or unstructured electrodes displayed similar results at C/2. A serious capacity drop was observed at 1C for cells containing NMC 622 cathodes with thicknesses ≥ 150 µm, but with laser structuring, a capacity increase of 10 and 30 mAh/g was observed for cells with 100 µm and 150 µm NMC 622 cathodes, respectively. At 2C, cells with laser structured 100 µm thick NMC 622 electrodes achieved almost the same specific discharge capacity in comparison to the reference cells with 74 µm thickness, while cells with laser structured 150 µm thick-film electrodes showed about 10 mAh/g higher discharge capacity in contrast to those with unstructured ones. The C/5 cycling at the end was applied to determine the capacity retention after charge/discharge at high C-rates. Cells containing unstructured and laser structured NMC 622 cathodes of 200 µm thickness exhibited the lowest capacity retention in contrast to other cells with 89.3 % and 90.9 %, respectively, while cells containing 74 µm unstructured cathodes and 150 µm un / structured cathodes showed the highest the capacity retention of more than 98 %.

Table 5-5. Initial coulombic efficiency at C/20 and the capacity retention at C/5 of cells containing unstructured and laser structured NMC 622 cathodes with different film thicknesses.

NMC 622 cathode type	Initial coulombic efficiency [%]	Capacity retention [%]
74 µm, unstructured	89.8 ± 0.6	98.7 ± 0.3
100 µm, unstructured	88.8 ± 0.2	96.9 ± 0.7
100 µm, structured	88.6 ± 0.1	95.6 ± 1.0
150 µm, unstructured	88.8 ± 0.4	98.8 ± 0.4
150 µm, structured	88.2 ± 0.6	98.9 ± 0.4
200 µm, unstructured	89.0 ± 0.3	89.3 ± 6.4
200 µm, structured	89.1 ± 0.3	90.9 ± 4.2

In industrial applications, the areal capacity of electrodes is a practical guide for the electrode manufacturing and is of great importance for the cell design, thus the areal capacities of cells containing NMC 622 cathodes with different thicknesses are determined and shown in Figure 5-13-b. At low C-rates of C/20 to C/5, the areal capacity increased with increasing film thickness. For example, cells with 200 µm electrodes showed 2.6 times higher areal capacity in comparison to reference cells with 74 µm electrodes at C/20. However, laser structuring lowered the areal capacity owing to the ablation of active material NMC 622. The capacity loss from C/20 to C/5 was the same as the mass loss as shown in Table 5-4, which was lower than 6 %. At C/2, there was no obvious difference between cells with structured and unstructured electrodes with regard to the areal capacity. Cells containing laser structured NMC 622 cathodes with 200 µm thickness showed higher areal capacity starting from C/2, while cells with laser structured 100 µm and 150 µm electrodes displayed an increase in areal capacity starting from 2C and 1C, respectively. At 1C, cells with laser structured 150 µm cathodes achieved the highest areal capacity in comparison to other cells, while further increasing the film thickness only led to deteriorated electrochemical performance. Therefore, 150µm film thickness can be considered as the "thick-film" NMC 622 cathodes, as it can demonstrate both the benefits of increasing areal capacitance with increasing film thickness and the benefits of laser-structured electrodes at high C-rates.

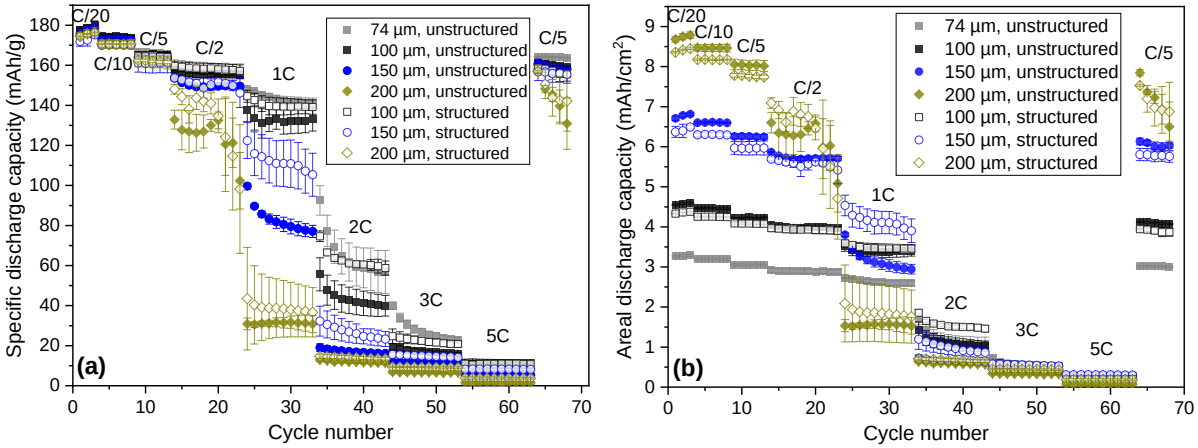

Figure 5-13. Rate capability analyses of coin cells (half-cells) containing unstructured and laser structured NMC 622 electrodes with PVDF binder and different electrode thicknesses: (**a**) specific discharge capacity and (**b**) areal discharge capacity of coin cells at increasing C-rates from C/20 to 5C.

The electrochemical impedance and lifetime analyses of cells with thick-film electrodes will be further evaluated and discussed in chapter 5.3 and 5.4 in comparison to cells containing multilayer electrodes and aqueous processed NMC 622 cathodes.

Figure 5-14 illustrates for different C-rates the relative increase of specific and areal discharge capacity of cells containing laser structured electrodes related to cells containing unstructured electrodes. A similar trend was shown for both performance parameters for C-rates ranging from C/2 to 5C. The active mass loss due to laser ablation caused in the range from C/20 to C/2 a slight decrease of areal discharge capacity by about 4 – 6 %. In addition, the gains from 3D electrode concept gradually shifted to lower C-rate as the electrode thickness increased, with main enhancement of performance data for C-rates in the range of 1C to 5C. But if one considers not only the relative but also the values of specific discharge capacities, then it becomes quite clear that an increase of more than 150 % at 5C had to be reassessed with regard to an overall decrease in capacity. Since at 5C the cells with the best performance provided less than 5 % of its initial capacity at C/20, the capacity increase at 5C can be neglected. In summary, the gain from laser structuring of NMC 622 electrodes is directly related to the film thickness and the maximum gain can be achieved between C/2 and 3C.

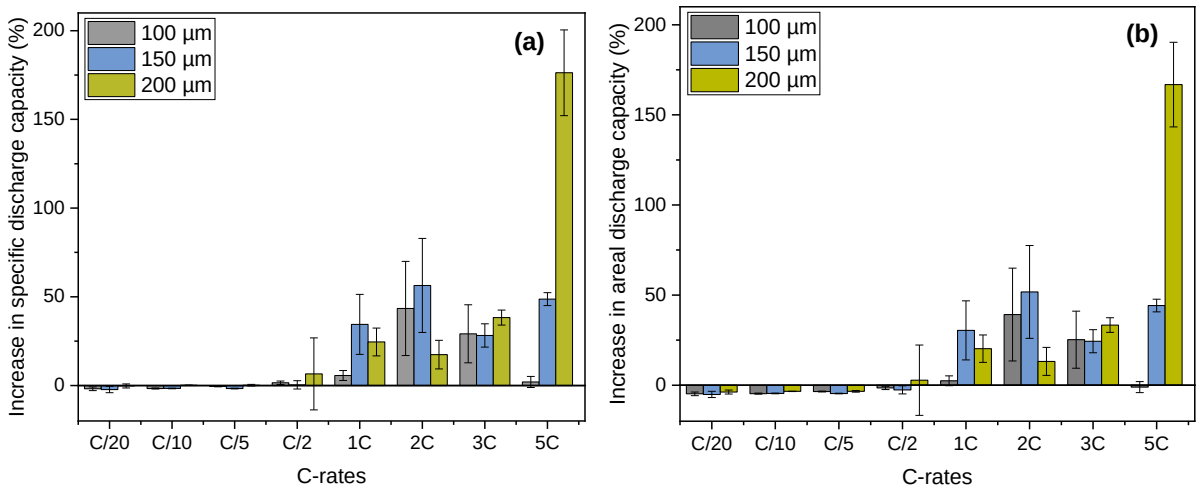

Figure 5-14. Relative increase in (**a**) specific and (**b**) areal discharge capacity of half-cells containing laser structured NMC 622 cathodes related to cells with unstructured electrodes.

At 1C, the discharge capacity of reference cell with unstructured 74 µm thick-film electrode reaches 147 mAh/g, while the cells with laser structured 100 µm and 150 µm thick-film electrodes provide 145 and 115 mAh/g, respectively (Figure 5-15). The cell with unstructured 150 µm thick-film electrode exhibited the lowest capacity. In addition, the discharge profile of cell with structured electrode having 100 µm film thickness lied above the one with unstructured electrode (Figure 5-15-a). This means that the cells with unstructured electrodes require lower voltage to achieve the same discharge capacity, i.e., the voltage window between the upper and lower voltage is increased. This indicates that the cell polarization decreases for cells with laser structured electrodes in comparison to those using unstructured electrodes. As for the cell with electrode having a film thickness of 150 µm, no difference in discharge profiles of cells with unstructured or laser structured electrode was observed from 4.3 to 3.6 V. However, the discharge curve of cell with unstructured electrode was significantly lower than those with laser structured electrode from 3.6 to 3.0 V, which corresponded to a depth of

discharge (DoD) of 50 – 100 %. Similar results were shown in full-cells, where those with laser structured NMC 622 cathodes vs. laser structured / unstructured graphite anodes exhibited higher discharge profiles than that of the cells with unstructured electrodes at C/2 [269]. Under 2C charge / discharge, cells with NMC 622 electrode having a film thickness of 74 µm showed a capacity of 80 mAh/g, while those with electrode thicknesses of 100 µm and 150 µm reached 55 and 19 mAh/g, respectively. The discharge curves of the cells with laser structured electrodes were lower than those of the cells with unstructured electrodes at voltages lower than 3.6 V (Figure 5-15-b). This is the same as the results obtained when the cells were charged or discharged with 1C.

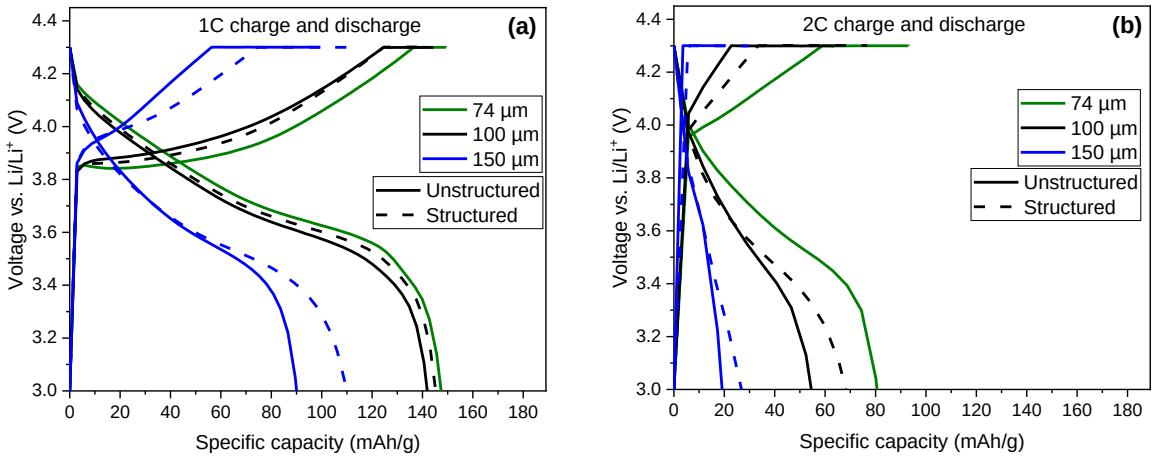

Figure 5-15. Comparison of the specific charge and discharge capacity vs. voltage (vs. Li /Li$^+$) of half-cells containing laser structured and unstructured NMC 622 electrodes with thicknesses of 74 µm, 100 µm, and 150 µm at (**a**) 1C and (**b**) 2C. A pitch of 200 µm was applied for the laser structuring of all NMC 622 electrodes.

The charge capacity derived from constant voltage phase of cells with unstructured electrodes increased from 9 % to 43 % with increasing film thickness at 1C (Figure 5-16-a), while at 2C the constant voltage - capacity fraction increased from 37 % to 79 % with increasing electrode thickness (Figure 5-16-b). Slightly higher constant voltage - capacity fraction with 30 % and 90 % in pouch cells (NMC 622 cathode with 85 µm film thickness vs. graphite anode with the same film thickness) at 1C and 2C, respectively, were reported [314]. This indicates that for cells with electrodes having film thickness larger than 100 µm, more than half of the charge capacity was obtained through the constant voltage phase at elevated C-rates larger than 1C. After laser structuring, the constant voltage - capacity share was decreased by 2 – 8 %.

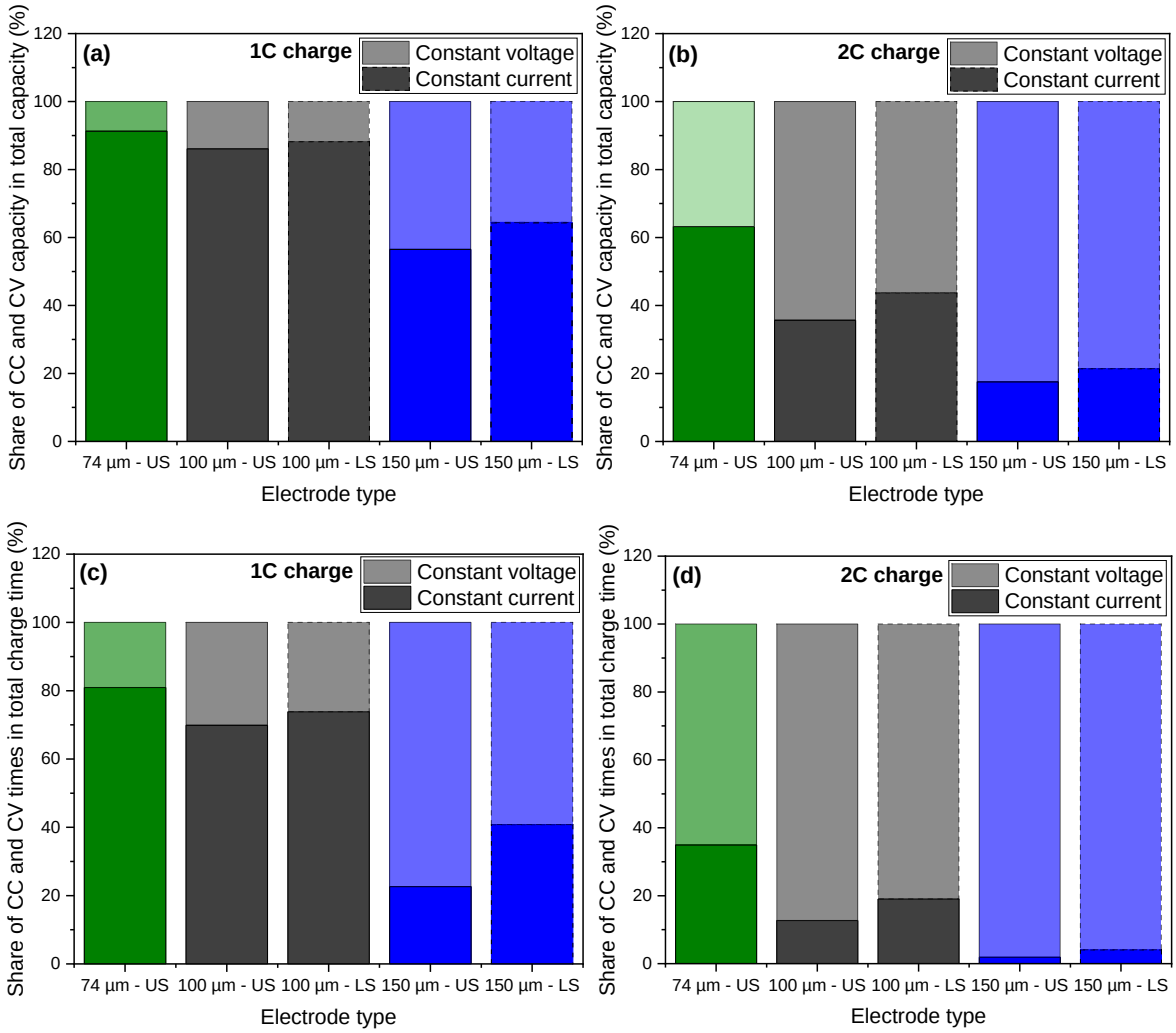

Figure 5-16. The share of charge capacity originated from constant current (dark color) and constant voltage phase (bright color) in contrast to total charge capacity at (**a**) 1C and (**b**) 2C of cells containing five different types of NMC 622 electrodes; And the share of charge time derived from constant current and constant voltage phase in comparison to total charge time at (**c**) 1C and (**d**) 2C. The data is obtained from the same cells shown in Figure 5-15. Cells containing electrodes with three different film thickness (74, 100 and 150 µm) are compared. “US” means NMC 622 electrodes are unstructured, while “LS” indicates laser structure electrodes.

The total charge time for cells containing unstructured or laser structured electrodes with different film thicknesses at 1C was 1.02 ± 0.03 h, while at 2C the total time was 0.45 ± 0.10 h. These results are in good agreement with the given C-rates. The charge time can be further subdivided into two parts, i.e., the charge time from constant current and constant voltage phase (Figure 5-16-c and -d). As the electrode thickness increased, the charge time from constant voltage rose significantly, from 19 % to 77 % at 1C and from 65 % to 98 % at 2C. Thus, at 2C, almost all the charge time of the cells with NMC 622 electrodes having a film thickness of 150 µm came from the constant voltage phase. In addition, cells with laser structured electrodes exhibited a 2 – 18 % higher share of charge time from constant current phase than those with unstructured electrodes. This trend is consistent with the capacity share shown in Figure 5-16-a and -b.

Impact of laser structuring pattern types on the electrochemical performance of cells with thick-film NMC 622 electrodes

Applying line structures can accelerates the wetting of the liquid electrolyte in laser structured electrodes due to capillary forces [13, 264, 315]. Other alternative patterns such as through-holes [16, 266, 316], or grid pattern [278] have also been reported and enhancements in rate capability and cycling lifetime of cells containing laser patterned electrodes were confirmed. Generally, cells with laser structured electrodes show enhanced capacities in comparison to those with unstructured electrodes at elevated C-rates larger than 2C. In addition, the enhancement in capacity occurs at lower applied currents with increasing electrode mass loading, as shown in Figure 5-14. In addition to the electrode mass loading, the pattern type of laser structuring can affect the capacity on the one hand, especially when the C-rates is higher than 1C; On the other hand, the laser processing efficiency is dependent on the complexity of the pattern geometry, which affects the upscaling of laser structuring and its application in battery industry. The upscaling of the laser structuring of electrodes will be discussed in chapter 5.6.

To further investigate the effect of pattern types on the electrochemical performance of cells with thick-film NMC 622 electrodes, different pitches as well as pattern geometries were applied for the structuring of thick-film NMC 622 cathodes with 150 µm thickness. A pitch of 200 µm was selected as baseline according to our previous results [268], where the cells containing laser structured NMC 622 cathode (film thickness: 151 µm) with 200 µm pitch exhibited the highest rate capability at C/2, 1C and 2C in comparison to cells containing electrodes structured with 400 and 600 µm pitched. In order to investigate whether further reduction of pitch could enhance the electrochemical performance, the pitch of line pattern was further decreased from 200 µm to 100 µm (Figure 5-17-a to -c), while the laser parameters such as laser power, repetition rate, and scan speed were kept the same for the laser structuring with different pitches in order to achieve channel structures with a high aspect ratio of 13.6 as depicted in Table 5-4. For the laser structured thick-film electrodes with 200 µm pitch (line pattern), a mass loss of 5.8 ± 1.6 % was determined, while the mass loss of laser structured NMC 622 cathodes with 150 µm and 100 µm pitch was determined as 6.6 ± 1.8 % and 8.8 ± 1.8 %, respectively.

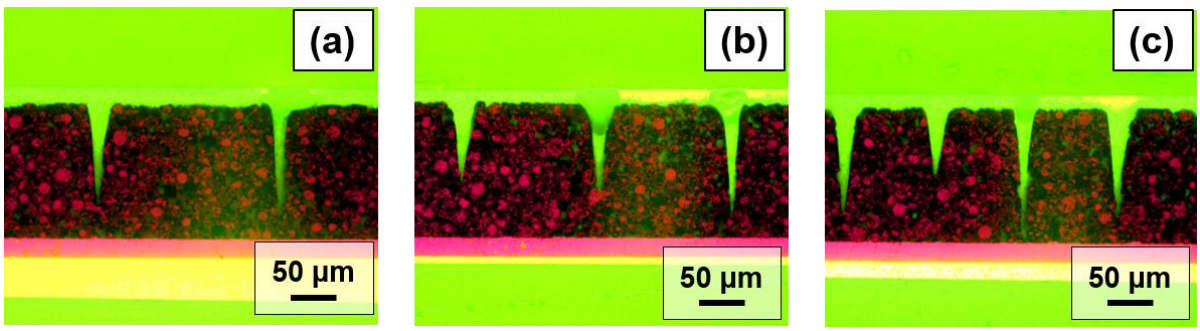

Figure 5-17. Cross-sectional images of laser structured NMC 622 cathodes (groove structures) with PVDF binder with (**a**) 200 µm, (**b**) 150 µm, and (**c**) 100 µm pitch.

In addition, through-hole pattern was applied as another alternative to the line patterns. The holes were arranged hexagonally with a distance of 200 µm between two neighboring

holes and the maximum hole diameter each was 62.6 ± 3.4 µm, as displayed in Figure 5-18. The cross-sectional view of a hole is shown in Figure S 1-a, and the FWHM of the holes was determined to be 13.0 ± 3.9 µm. Besides, Figure S 1-b exhibits an SEM image of the uncoated side of the Al current collector ("laser exit side"), where holes with a diameter of 4.8 ± 1.3 µm were observed, which is consistent with the result of the cross-section analysis. In order to accurately calculate the mass loss of composite electrode due to laser structuring as well as the specific discharge capacity of the cells with through-hole structured NMC 622 thick-film electrodes, the mass loss of the Al current collector due to laser structuring needs to be taken into account. The equation (5.7) should be rewritten as:

$$Mass\ loss = \frac{(m_0 - m_{Al}) - (m_{LS} - m_{Al,LS})}{m_0 - m_{Al}} \cdot 100\% \qquad (5.8)$$

where $m_{Al,LS}$ [g] is the mass of an Al foil with drilling holes. Considering that the average diameter of drilling holes in the Al current collector was 4.8 µm and their pitch was 200 µm, if the holes in Al foil were approximated to be cylindrical, the mass loss of the Al foil due to laser structuring is calculated to be 0.06 %. The mass loss of laser structured NMC 622 thick-film electrodes with through-hole pattern (200 µm pitch) is 1.8 ± 0.6 % compared to the unstructured electrodes, as listed in Table 5-6.

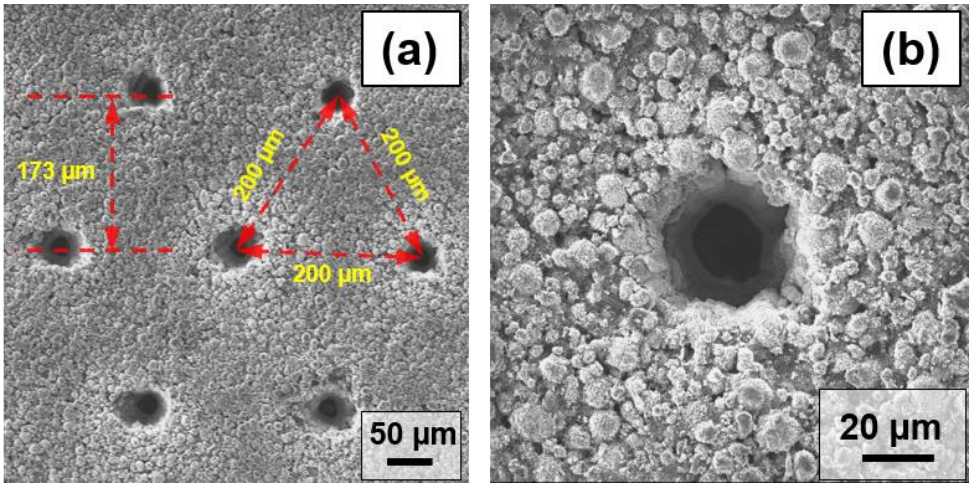

Figure 5-18. SEM images of laser structured NMC 622 cathodes with through-hole pattern with (**a**) 500 × and (**b**) 2000 × magnification ("laser entrance side").

Figure 5-19 depicts the rate capability analyses of cells containing laser structured NMC 622 cathodes (150 µm thickness) with different patterns and the respective relative increase of specific discharge capacity at different C-rates. For all cells with laser patterned electrodes, the values of initial CE at C/20 were slightly lower (0.3 – 0.5%) than that of reference cells with unstructured electrodes as displayed in Table 5-6. Similar to the results in Figure 5-13, all cells in Figure 5-19-a showed similar specific discharge capacities at C/20 and C/10, while at C/5, cells containing laser structured electrodes with line patterns exhibited lower capacities of 5 – 8 mAh/g in comparison to reference cells. At C/2, all cells with line structured electrodes showed an analogous increase in relative specific discharge capacity of about 50 % in comparison to those with unstructured electrodes (Figure 5-19-b). However, from C/20 to C/2, there was no significant difference in discharge capacity of cells containing line structured

electrodes with different pitches. As the C-rate increased to 1C, the cells containing line structured electrodes with 100 and 150 µm pitches showed similar discharge capacity of 80 – 100 mAh/g, while those having structured electrodes (line pattern) with 200 µm pitch exhibited 20 mAh/g less discharge capacity. The enhancement in discharge capacity increased as the pitch decreased (Figure 5-19-b). In the C-rate range from 2C to 5C, all cells showed a capacity loss of more than 85 % in comparison to their capacity at C/20. Therefore, reducing the pitch of groove structures from 200 µm to 150 µm in thick-film NMC 622 electrodes can slightly enhance the electrochemical performance, especially at 1C, but results in 1 % increase in mass loss in comparison to those with a 200 µm pitch. However, when the pitch was further reduced to 100 µm, there was no significant enhancement in discharge capacity in contrast to ones with a pitch of 150 µm. Meanwhile, the mass loss increased by 3 % and the laser processing time was doubled in comparison to that for line structured electrodes with a 200 µm pitch.

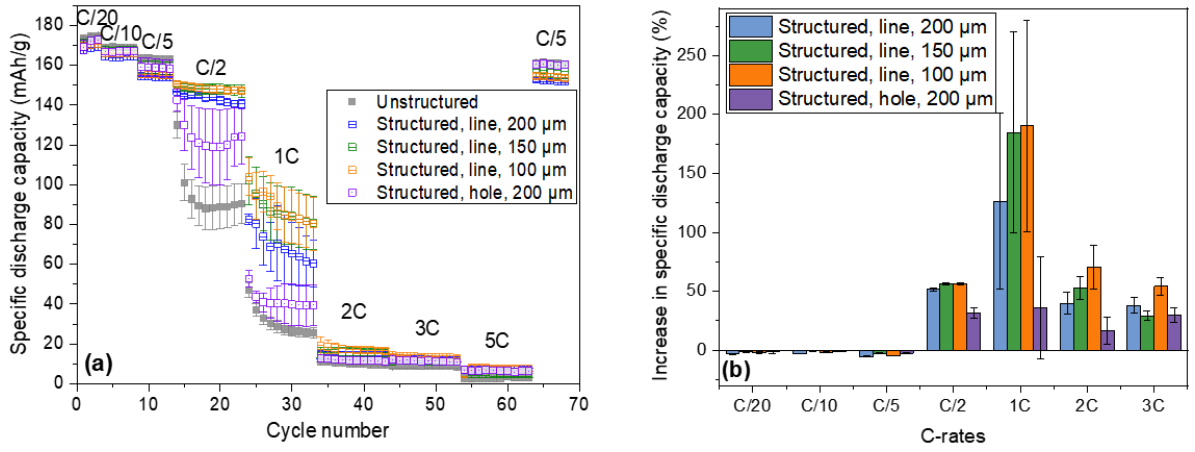

Figure 5-19. Rate capability analyses of (**a**) half-cells containing laser structured NMC 622 cathodes (150 µm thickness) with different patterns and (**b**) relative discharge capacity difference related to the reference cells.

The capacity retention is calculated by dividing the average discharge capacity of the last five cycles at C/5 by those of the previous five cycles at C/5 (Figure 5-19-a). Table 5-6 displays that the capacity retention of cells with laser patterned electrodes was equal or slightly higher than that of reference cells. In addition, the mass loss of laser structured NMC 622 electrodes with hole structure was significantly reduced in comparison to line structures with a same pitch and an increase in capacity retention at C/5 was still observed. However, Figure 5-19 shows that the discharge capacity of cells with hole structured NMC 622 cathodes was lower at C/2 in comparison to other cells with line structured electrodes, and the cells with hole structured electrodes displayed comparable specific discharge capacity as the reference cells at 1C. Thus, the enhancement of electrochemical performance of cells with line structured electrodes is in general superior to the performance of cells with hole structured electrodes. In addition, the channel structure has an unique advantage: it accelerates the electrolyte wetting due to the capillary effect [13]. Thus, line structures are preferable for the laser structuring of thick-film electrodes used in this thesis.

Table 5-6. Mass loss, initial coulombic efficiency, and capacity retention of cells containing laser structured NMC 622 cathodes with different pattern types.

Pattern type	Mass loss [%]	Initial coulombic efficiency [%]	Capacity retention * [%]
Reference	-	88.8 ± 0.2	98.8 ± 0.4
Lines, 200 µm pitch	5.8 ± 1.6	88.2 ± 0.6	98.9 ± 0.4
Lines, 150 µm pitch	6.6 ± 1.8	88.0 ± 0.4	99.3 ± 0.4
Lines, 100 µm pitch	8.8 ± 1.8	88.5 ± 0.3	99.3 ± 0.4
Holes, 200 µm pitch	1.8 ± 0.6	88.3 ± 0.2	99.1 ± 0.3

* The capacity retention is calculated by dividing the average discharge capacity of the last five cycles at C/5 by those of the previous five cycles at C/5.

The charge and discharge curves of cells containing laser patterned NMC 622 electrodes with different pattern types are displayed in Figure 5-20 for C-rates C/2 and 1C. At C/2, all cells containing laser structured electrodes with line patterns achieved 140 – 145 mAh/g capacity after fully discharged and showed higher discharge curves in comparison to the reference cell, indicating a lower cell polarization. However, no obvious difference was observed in IR-drop, which was approximately 0.11 V (from 4.30 V to 4.19 V). The reason for the IR-drop is the current flowing across the total internal resistance of cells, i.e., the resistances of the electrodes, electrolyte, and electrical contacts. In contrast, the cell containing electrode with through-hole structures exhibited a higher IR drop of 0.34 V from 4.30 V to 3.96 V, which was more than 3 times larger in comparison to other cells. Meanwhile, a more severe cell polarization was observed for this cell, although it achieved higher capacity after fully discharged compared to the reference cell at both C-rates, C/2 and 1C. The reason for the huge cell polarization of cells with through-holes structured electrode is not clear. Hille et al. [274] reported about the electrochemical performance of pouch cells containing through-hole structured NMC 622 cathodes and graphite anodes. They observed an increase of specific discharge capacity for C-rate in the range of 1C to 3C, while in the results presented here, the increase occurred at lower C-rates of C/2 and 1C. This is due to the fact that their work used relatively thin-film cathodes and anodes with thicknesses of 66 µm and 70 µm, while thick-film electrodes with a thickness of 150 µm were applied in the present work. From the previous results shown in Figure 5-13, it can be concluded that the initial C-rate shifts to a lower C-rate as the film thickness increases.

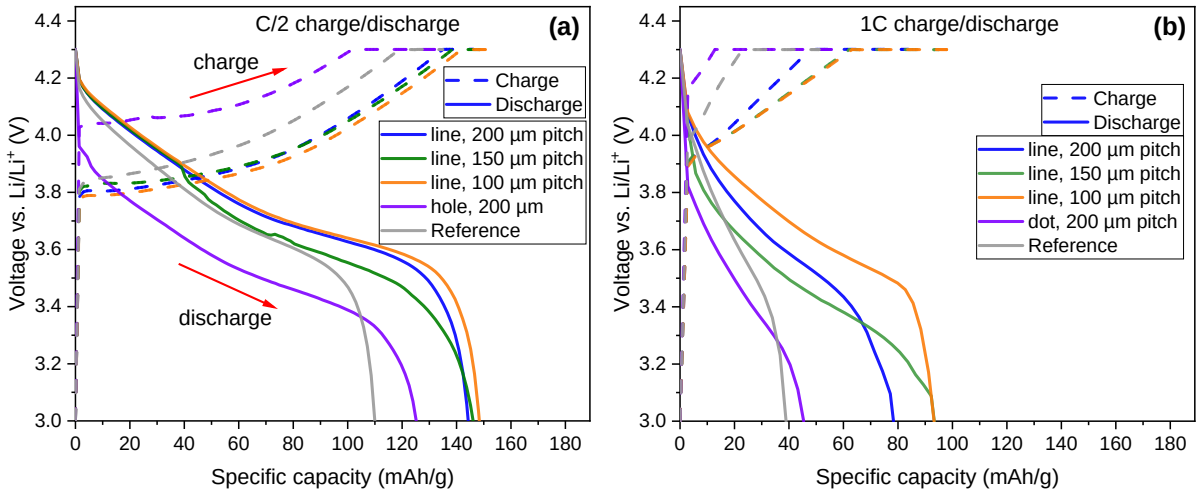

Figure 5-20. Specific charge and discharge capacity vs. voltage (vs. Li / Li^+) of half-cells containing laser structured NMC 622 electrodes with different patterns and with film thickness of 150 µm (**a**) at C/2 and (**b**) at 1C.

Laser structuring induces geometric changes in thick-film electrodes, resulting in reduced ohmic resistances, decreased tortuosity, and enhanced Li-ion diffusion kinetics. These improvements are achieved without causing thermal damage or failure of the electrode structure [270]. Besides, the Li-ion diffusion kinetics is enhanced due to the generated channels inside the laser structured electrodes filled with liquid electrolyte [232]. Laser generated channels in electrodes can reduce the diffusion distance of Li-ions in electrode pores filled with liquid electrolyte by connecting pores with the free electrolyte of the cell. Ultimately, the electrochemical performance of the electrodes can be tuned by tailoring the laser pattern types as well as the electrode thickness to meet the requirements in practical applications. Furthermore, power density and energy density are more practical to characterize the electrochemical performance for commercial applications. In order to estimate these properties and to acquire Ragone-plots (energy density vs. power density of cells) with regard to facing Pareto optimum, more information with respect to anodes, electrolyte amount, and separators are needed to perform accurate calculations. This will be further analyzed in chapter 5.5 using pouch cell (full-cell) design.

5.3. Electrodes with bilayer hierarchical architectures

Hierarchical cathodes containing polycrystalline NMC 622 powders with different particle sizes were prepared with PVDF binder and NMP solvent. The bilayer thick-film electrodes with 150 µm total film thickness were realized by dual-casting using slurries containing NMC 622 powders with different particle sizes. The individual electrode layers contain either B-NMC 622 powder with large particle size of 12.8 µm or S-NMC 622 powder with small particle size of 6.7 µm. The ratios of respective layer thicknesses were set to 1:2, 1:1, and 2:1. After drying and calendering of NMC 622 electrodes, laser structuring using laser setup shown in Figure 4-8 was performed to generate groove structures with 200 µm pitch. In addition, reference electrodes with mechanically blended NMC 622 powders (during mixing) with two different particle sizes (B&S) were analyzed. SEM and cross-sectional analyses were applied to characterize the electrodes after preparation. Afterwards, rate capability analyses, lifetime

analyses, CV, as well as EIS analyses were applied to characterize coin cells with different types of electrodes.

5.3.1. Impact of NMC 622 powder particle size on slurries and monolayer electrodes

The electrochemical performance of LIBs is highly dependent on the electrode composition, slurry and coating parameters [317], so the mixing procedure and other components such as conductive agent and binder remain the same, except for NMC 622. For the preparation of cathode slurries, 92 wt% B- or / and S-NMC 622 were used as active material, while other components and their weight percentage were kept constant. The established mixing procedure was applied as listed in Table 4-2. After mixing, the viscosity of the slurry was measured, see Figure 5-21. A doctor blade gap of about 200 µm and 420 µm was applied for different slurries to fabricate thin-film and thick-film electrodes. According to equation (4.8), the practical shear rates were 12 and 25 s^{-1}, and the corresponding slurry viscosities are shown in Figure 5-21. All slurries revealed shear-thinning behavior and the viscosity of slurry with S-NMC 622 powder was higher than that with B-NMC 622 powder. However, when these two kinds of NMC 622 powder were mixed 1:1 and added to the slurry, the viscosity was closer to that of with B-NMC 622 powder. This indicates that the NMC 622 particles with large size have a decisive influence on the viscosity of the slurry.

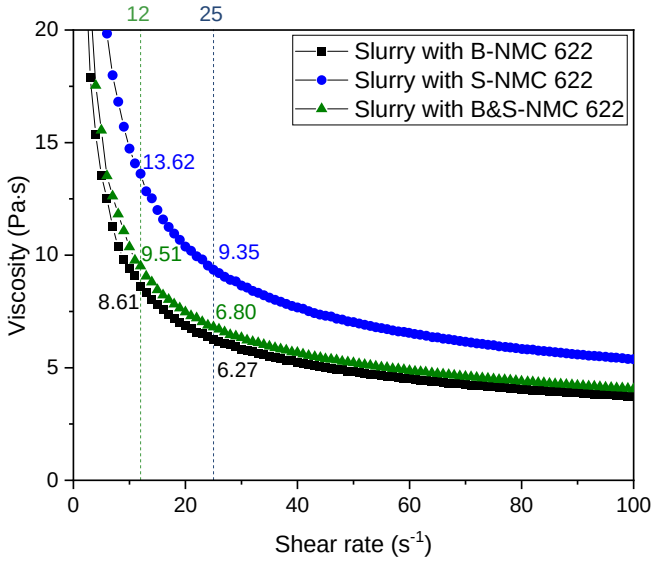

Figure 5-21. Viscosity of slurries containing B-, S-, and B&S-NMC 622 powder(s) with PVDF as binder at shear rates from 0 to 100 s^{-1}.

Two different film thicknesses, 75 µm and 150 µm (after calendering), were selected to represent the state-of-the-art thin-film and advanced thick-film electrodes, respectively. The porosities of different cathodes were reduced to 35 % after calendering. The details of various cathodes are summarized in Table 5-7. Active mass loading is the mass of NMC 622 powder per unit area and the areal capacity is calculated using a specific capacity of 172 mAh/g for NMC 622. The active mass loading and areal capacity of thick-film electrodes are doubled in contrast to those of thin-film electrodes.

Table 5-7. Film thickness, active mass loading, and areal capacity of electrodes consisting of different NMC 622 powders and different film thicknesses after calendering. The porosity of the different type of electrodes remained constant at 35 %.

NMC 622 cathode type	Doctor blade gap [µm]	Film thickness without Al foil [µm]	Active mass loading [mg/cm^2]	Areal capacity [mAh/cm^2]
B, thin	200	74 ± 2	18.12 ± 0.24	3.12 ± 0.04
S, thin	195	73 ± 2	18.17 ± 0.13	3.13 ± 0.02
B&S, thin	200	73 ± 2	18.13 ± 0.12	3.13 ± 0.02
B, thick	420	150 ± 5	37.34 ± 0.35	6.44 ± 0.06
S, thick	420	157 ± 6	38.75 ± 0.37	6.68 ± 0.06
B&S, thick	420	155 ± 5	38.32 ± 0.42	6.61 ± 0.07

Since the blended B&S-type slurry was a mechanical mixture using two different NMC 622 powders with different particle sizes, the B&S-type electrodes can be regarded as electrodes using a NMC 622 powder with bimodal particle distribution. The cross-sectional SEM images (Figure 5-22) of thick-film NMC 622 electrodes with B-, S-, and B&S-type configurations show that no significant aggregation of the NMC 622 particles was detected. In addition, the small and large particle size NMC 622 particles were homogenously mixed in B&S-type electrode (Figure 5-22-c). Besides, no agglomeration of the S-NMC 622 powder with smaller particle size was observed.

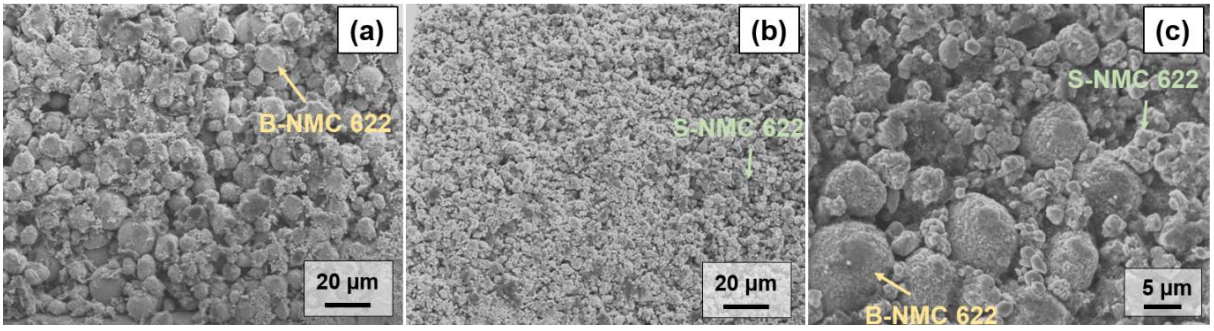

Figure 5-22. SEM images of cross-sectional view of thick-film cathodes with (**a**) B- and (**b**) S-NMC 622 powder as well as (**c**) blended (B&S) NMC 622 powder with bimodal distribution.

CV analyses of cells with monolayer NMC 622 electrodes having different particle sizes

CV analyses were performed with coin cells containing electrodes with different NMC 622 powders to investigate the impact of particle size on the redox reaction of the active material. Each cell was measured three times and the corresponding results overlap with each other, thus only the third cycles are shown in Figure 5-23-a. The recorded current signals formed a closed loop during charging and discharging and only one current peak appears during charging and discharging process, which is identical in comparison to the results from Wang et al. [90], indicating the presence of a redox reaction of Ni^{2+} / Ni^{3+} / Ni^{4+} [80, 92]. The oxidation peak of cell with B-NMC 622 cathode was located at 3.87 V, while cells with S- and B&S-NMC 622 cathodes showed an oxidation peak at 3.89 V. Meanwhile, the reduction peak shifted from 3.63 to 3.62 V for cells with S- and B&S-NMC 622 cathodes in contrast to the cell with B-NMC 622 cathode. Since B- and S-NMC 622 powders had the same chemical composition and phase as determined by ICP-OES and XRD, respectively, the redox peaks should be located at the same voltage. However, when there is a high barrier for electron transfer

between electrode and electrolyte, their reactions will be sluggish so that higher positive (negative) potentials are required to observe oxidation (reduction) reactions, giving rise to larger differences in the potential between both peaks [294].

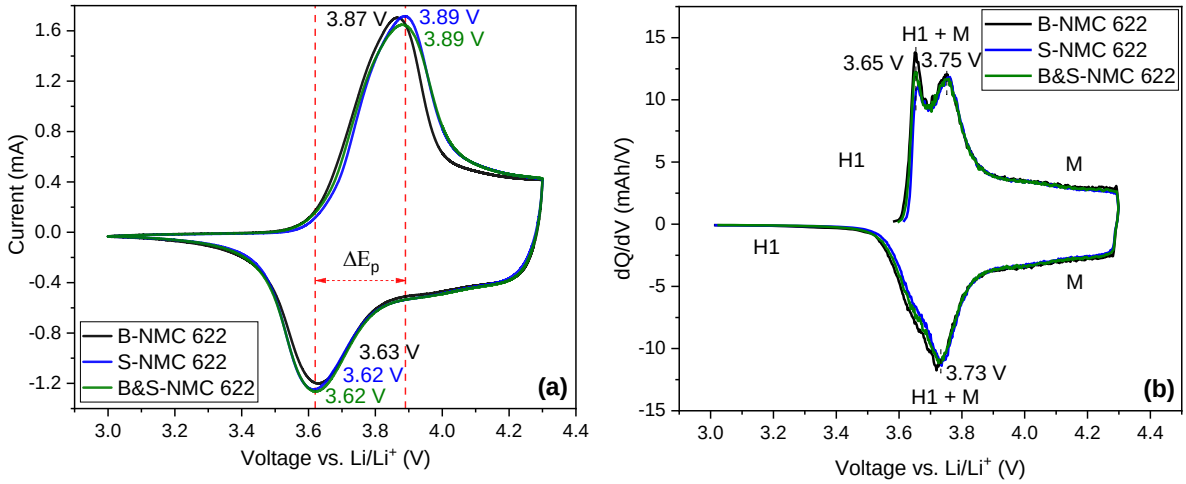

Figure 5-23. The (**a**) CV analysis and (**b**) differential capacity (dQ/dV) plots vs. voltage of the formation third cycle of cells with different types of NMC 622 cathodes.

The cell containing electrodes with B-NMC 622 powder showed a reduced peak-to-peak voltage difference of 0.24 V, while others exhibited a difference of 0.27 V. It was reported that the peak-to-peak voltage difference (or a higher overpotential η) increased as the reaction rate decreased from 1 to 10^{-4} cm/s using the simulation with Butler-Volmer equation (3.14) [133, 318]. This might imply that the reaction rate of Li-ion intercalation in S-NMC 622 and B&S-NMC 622 powders is lower in comparison to that in B-NMC 622 powder. In other words, the activation energy of the Li-ion intercalation in B-NMC 622 powder should be lower than that in other two types.

Figure 5-23-b displays the differential capacity dQ/dV of cells with different types of NMC 622 cathodes. The two peaks appeared at 3.65 V and 3.75 V during charging and the single peak at 3.72 V during discharging are identical to the results from Kim et al. [95] and Noh et al. [86]. The peaks correspond to the phase transition of NMC 622 from original layered hexagonal phase (H1) to the monoclinic phase (M) [319]. These results demonstrate that the two different NMC 622 powders undergo the same phase transition when charged and discharged from 3 V to 4.3 V, and no additional redox reaction besides the expected ones were observed.

Rate capability analyses of cells with monolayer NMC 622 electrodes having different particle sizes

Figure 5-24-a exhibits the rate capability analyses of the cells with various thin-film NMC 622 electrodes. Cells with B- or B&S-NMC 622 cathodes showed higher initial CE compared to cells with S-NMC 622 electrodes, regardless of electrode thickness, see Table 5-8. A higher CE at the first cycle indicates a reduced electrolyte consumption during CEI or SEI formation [202]. Therefore, it is assumed that a larger amount of CEI was form on the surface of S-NMC 622 particles in comparison to B-NMC 622 during formation, since the S-NMC 622 powder provided a larger BET surface area as determined in chapter 5.1.1 A larger

active surface area consumes more electrolyte during formation step [101]. Besides, during the formation, the specific discharge capacities of all cells slightly increased. For example, cells with B&S-NMC 622 electrode showed an increase in discharge capacity from 176 to 177 mAh/g, while after the third C/20 cycle cells with B- and S-NMC 622 electrode achieved 179 and 175 mAh/g, respectively. At C/10, cells with B-NMC 622 electrodes retained the highest specific discharge capacity of 174 mAh/g, while other cells showed specific discharge capacities in the range of 171 to 172 mAh/g. When the C-rate rose from C/5 to C/2, all cells exhibited similar discharge capacity, while at 1C, cells with B-NMC 622 started to show a drop in capacity from 148 to 141 mAh/g. At discharge rates of 2C and 3C, the discharge capacity of cells with thin-film electrodes decreased continuously from 120 mAh/g to 30 mAh/g. At 5C, all cells with thin-film electrode maintained about 10 mAh/g specific capacity. At high C-rates ranging from 1C to 3C, cells with cathodes having small secondary particle size exhibited higher specific discharge capacities in comparison to the cells with cathodes having blended powders or B-NMC 622 powder. These results are in good agreement with the simulation of Du et al. [320], which showed that the energy density increased with decreasing secondary particle size of cathode at high C-rates.

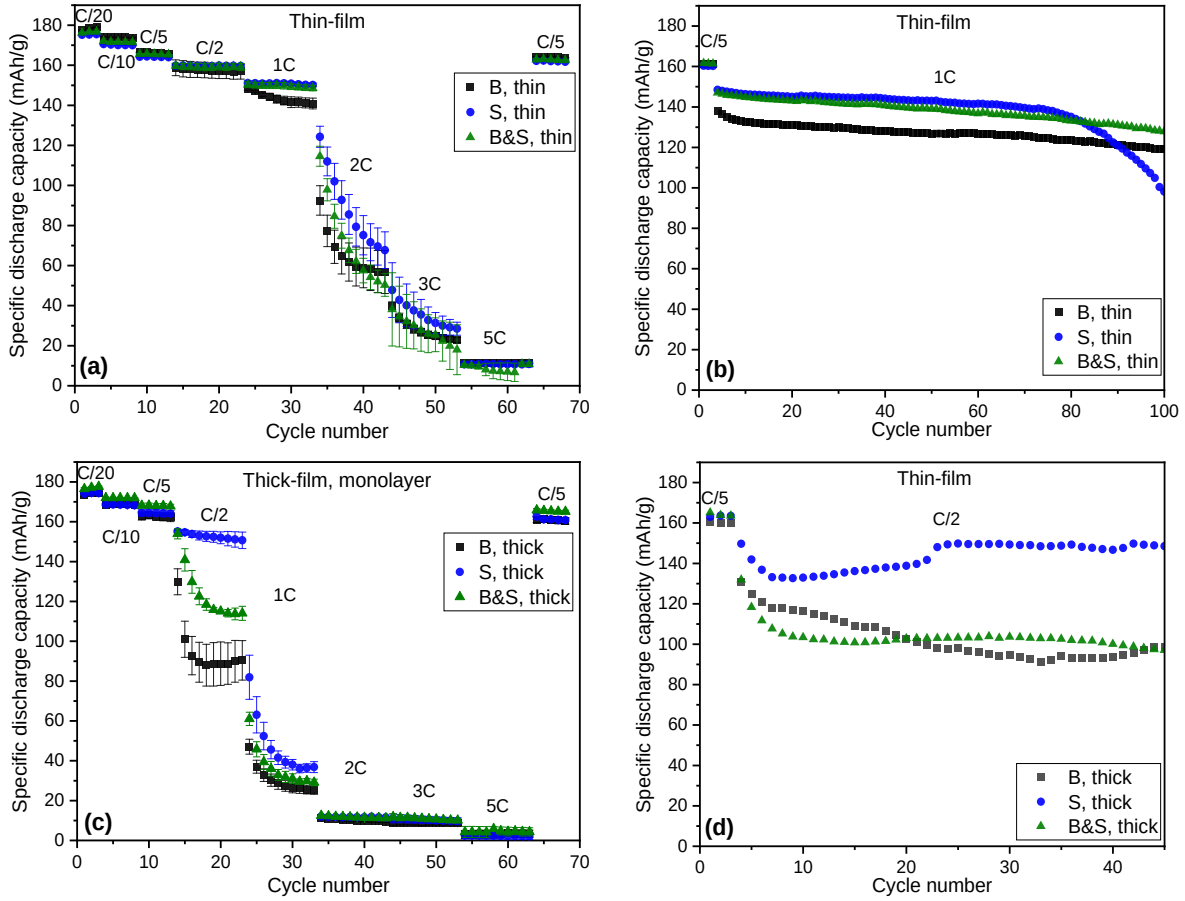

Figure 5-24. Rate capability analyses of half-cells containing (**a**) thin-film and (**c**) thick-film electrodes with different NMC 622 particles and the lifetime analyses of cells with (**b**) thin-film and (**d**) thick-film NMC 622 cathodes having different secondary particle sizes.

Subsequently to rate capability analyses, one cell from each cell type with the highest capacity retention was selected and cycled at 1C to perform lifetime analyses as shown in Figure 5-24-b. Until 70 cycles, cells with S-NMC 622 cathodes showed the highest specific

discharge capacity, followed by cells with electrodes consisting of blended B&S-NMC 622 powder and B-NMC 622 powder. However, a sudden drop in discharge capacity after 70 cycles was observed for cells with S-NMC 622 cathodes, while the other cell types showed stable behavior until the end of lifetime analyses. This implies that the cycling stability of electrodes containing large NMC 622 particles is higher in comparison to that of small particles. Besides, the cycling stability of cells with B&S-NMC 622 electrodes is comparable to that of cells with B-NMC 622 electrodes, indicating a positive impact of the blended electrode concept to stabilize the cycling performance. This can be explained as follows: with increasing particle size, the number of grain boundaries that impedes the Li-ions diffusion is decreasing, thus the electrochemical performance is enhanced [321]. Recently, Wood et al. [156] investigated the rate capability and lifetime stability of pouch cells containing NMC 532 cathodes and graphite anodes with different particle sizes. The rate capability showed that from 1C to 3C, cells containing cathodes with small particle size exhibited 5 – 40 mAh/g higher discharge capacity in comparison to cells having cathodes with big particle sizes. Besides, when being cycled at 2C, their cells with cathodes having small particles or mixed particles exhibited the highest capacity retention, while those with cathodes having large particles displayed the worst performance. This is partially consistent with the results here. However, they also found that the combination with both cathode and anode having small particles showed the lowest capacity retention at C/2, indicating that the particle size of anode also has great impact on the cycling stability.

Table 5-8. The initial coulombic efficiency at C/20 and the capacity retention (C/5) of cells with different NMC 622 cathodes, see Figure 5-24.

NMC 622 cathode type	Initial coulombic efficiency [%]	Capacity retention [%]
B, thin	89.8 ± 0.6	98.7 ± 0.3
S, thin	88.4 ± 0.8	98.7 ± 0.2
B&S, thin	89.0 ± 0.6	98.4 ± 0.2
B, thick	88.8 ± 0.4	98.8 ± 0.4
S, thick	87.6 ± 0.8	98.2 ± 0.7
B&S, thick	89.2 ± 0.3	98.4 ± 0.3

Figure 5-24-c displays the rate capability of cells containing thick-film electrodes with different NMC 622 powders. It is observed that with increasing electrode thickness, the sudden drop in discharge capacity with increasing C-rate was advanced from 2C to C/2 for cells containing B&S- and B-NMC 622 powders, showing 114 and 90 mAh/g capacity at the end of C/2 discharge, respectively, while cells with S-NMC 622 powder maintained 151 mAh/g specific capacity. At 1C, all cells showed a severe capacity loss of more than 80 % compared to of C/20, and from 2C to 5C, less than 10 mAh/g discharge capacity was shown. Besides, cells with thick-film electrodes showed a similar trend with S > B&S > B at C/2 and 1C as cells with thin-film electrodes at 2C and 3C. It is found that all cells with thick-film electrodes exhibited a similar capacity retention of about 98 % after being cycled again at C/5 (Table 5-8). Furthermore, cells with B-NMC 622 cathode exhibited the highest capacity retention of 98.8 %, followed by cells with B&S-NMC 622 cathode with 98.4 % capacity retention. This verifies the assumption that increasing the particle size of NMC 622 or adding active material with large

particle size can increase the capacity retention. Subsequently to rate capability analyses, lifetime analyses for cells with thick-film electrodes were performed at C/2, see Figure 5-24-d. C/2 was selected due to the fact that already at 1C a significant drop in specific capacity was observed, see Figure 5-24-c. A drop in capacity within the first 5 – 10 cycles was measured for all cells with thick-film electrodes, while cells with thin-film electrodes exhibited stable discharge behavior without a sudden drop in capacity. The cell with S-NMC 622 cathode exhibited the highest discharge capacity, while the cells with B- and B&S-NMC 622 showed similar trends of capacity during lifetime analyses. This is similar to the results of Sheu et al. [322] who reported a better cycling stability for cells containing LCO with smaller particle size. However, no difference in rate capability was observed in their work. The study of NCA cathodes also showed higher rate capability with decreasing particle size which should be owing to a lower charge transfer resistance [25]. Besides, the longer lifetime of cells containing electrodes with smaller particle size might be due to a faster strain relaxation during volume change caused by Li-ion insertion / extraction [65]. However, numerical simulations indicated that more Li-ion could intercalate in small particles than in large particles, resulting in higher stress level inside the particles with small size [323].

EIS analyses of cells with monolayer NMC 622 electrodes having different particle sizes

Figure 5-25 displays the Nyquist plots of cells containing unstructured thick-film electrodes with different NMC 622 powders. A Nyquist plot consists of two semicircles at high frequency and a tail at lower frequency. The first small semicircle at high frequency associates with the surface resistance of solid electrolyte interphase (SEI), while the second large semicircle from high to mid frequency is owing to the charge transfer resistance of the electrode [324]. In general, however, the two semicircles are not clearly distinguishable. The equivalent circuit model which is selected for fitting is shown in Figure 5-25. R_e represents the ohmic resistance from current collector, separator, cell case, and the electrolyte, while R_{SEI} and a constant phase element CPE_{SEI} are applied on behalf of the contribution of SEI. R_{ct} and CPE_{dl} correspond to the charge transfer resistance and double-layer capacitance, which are owing to the charge transfer behavior between electrolyte and electrode. The finite-length Warburg element W in parallel with a constant phase element (CPE) represent mainly the Li-ion diffusion in electrolyte [325].

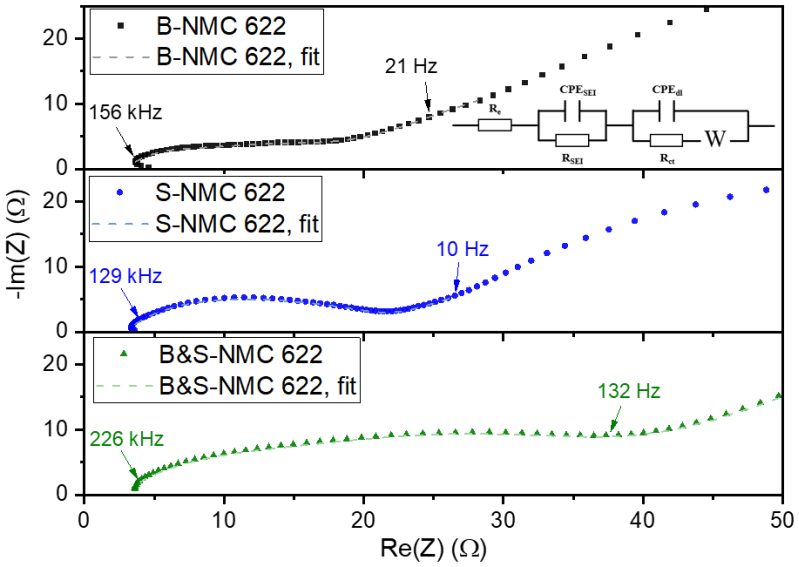

Figure 5-25. Nyquist plots of cells containing thick-film cathodes with different NMC 622 powder at OCV (3.63 V) after rate capability analyses and the fitting curves using the illustrated equivalent circuit model.

The derived ohmic resistance R_e, SEI resistance R_{SEI}, charge transfer resistance R_{ct}, SEI capacitance C_{SEI}, double-layer capacitance C_{dl}, and Warburg resistance W of cells with different types of electrodes are listed in Table 5-9. In addition, Kramers-Kronig analysis was performed for each fit to assess the mathematical connection between the real and imaginary components of the EIS results and the validity of equivalent circuit model [326], yielding χ^2 as shown in Table 5-9. In general, when the χ^2 is less than 0.01, it implies that the model has a good fitting effect [327]. After fitting, the value of CPE capacitance Y_{SEI} (or Y_{ct}) and the dimensionless CPE parameter φ (between 0 and 1) were directly obtained for each CPE connected in parallel with the resistance. When φ is equal to 1, the CPE is an ideal capacitor and the Y_{SEI} (or Y_{ct}) represents its capacitance [328]. However, when φ is smaller than 1, the SEI capacitance can be calculated as follows [329]:

$$C_{SEI} = Y_{SEI}^{\frac{1}{\varphi_{SEI}}} \left(\frac{1}{R_{SEI}}\right)^{1-1/\varphi_{SEI}} \tag{5.9}$$

where C_{SEI} [F] the SEI capacitance, Y_{SEI} [Fs$^{\varphi-1}$] the CPE capacitance of SEI, R_{SEI} [Ω] the SEI resistance, and φ_{SEI} [-] the CPE parameter. Analog to equation (5.9), the calculation of the double-layer capacitance C_{dl} [F] is given as:

$$C_{dl} = Y_{dl}^{\frac{1}{\varphi_{dl}}} \left(\frac{1}{R_{ct}}\right)^{1-1/\varphi_{dl}} \tag{5.10}$$

where C_{dl} [F] the double-layer capacitance, Y_{dl} [Fs$^{\varphi-1}$] the CPE capacitance of double-layer, R_{ct} [Ω] the charge transfer resistance, and φ_{dl} [-] the CPE parameter for double-layer. Furthermore, the equivalent time constant for a CPE with resistance in parallel is given below [328]:

$$\tau_{SEI} = (Y_{SEI} \cdot R_{SEI})^{1/\varphi_{SEI}} \tag{5.11}$$

$$\tau_{dl} = (Y_{dl} \cdot R_{ct})^{1/\varphi_{ct}} \tag{5.12}$$

where τ_{SEI} [s] and τ_{dl} [s] is the equivalent time constant of SEI capacitance and double-layer capacitance, respectively.

Table 5-9. Ohmic resistance, SEI resistance, charge transfer resistance, SEI capacitance, double-layer capacitance, and Warburg resistance of cells containing thick-film electrodes with different NMC 622 powders at an OCV of 3.63 V (50 % SOC). The χ^2 represents the Kramers-Kronig analysis.

	B-NMC 622	**S-NMC 622**	**B&S-NMC 622**
R_e [Ω]	3.0	3.0	2.7
R_{SEI} [Ω]	3.6	10.5	12.6
R_{ct} [Ω]	13.2	8.4	24.0
Y_{SEI} [Fs$^{\varphi-1}$]	$6.6 \cdot 10^{-6}$	$2.0 \cdot 10^{-5}$	$1.9 \cdot 10^{-5}$
Y_{dl} [Fs$^{\varphi-1}$]	$3.8 \cdot 10^{-4}$	$2.5 \cdot 10^{-4}$	$9.5 \cdot 10^{-5}$
φ_{SEI} [-]	0.87	0.75	0.72
φ_{dl} [-]	0.58	0.68	0.70
C_{SEI} [µF]	1.4	1.3	0.7
C_{dl} [µF]	8.4	13.9	7.4
τ_{SEI} [µs]	5.2	13.4	8.9
τ_{dl} [µs]	110.7	117.1	177.6
W [Ω]	44.0	19.6	92.1
χ^2 [-]	0.00004	0.00022	0.00021

Similar ohmic resistances R_e of around 3 Ω were observed for cells with different NMC 622 powder types, since separator, current collector, and electrolyte composition and amount were the same for each cell. However, both cells with S- or B&S-NMC 622 powder showed higher SEI resistance in comparison to the cell with B-NMC 622 powder, suggesting that the powder with bimodal distribution or with smaller secondary particle size is unfavorable to decrease the SEI resistance. Since half-cells containing NMC 622 cathodes vs. Li were applied for the EIS analyses, here the SEI refers to the CEI on the NMC 622 particle surface. With increasing particle size, the BET surface area is decreased, thus less CEI should be formed on the B-NMC 622 particle surface than on the other two types of powders during the formation. However, opposite results was reported for cells with NCA cathode, where SEI resistance was reduced with decreasing particle size [25]. In addition, cells with different types of NMC 622 cathodes had similar SEI capacitance of about 1 µF, while cell with S-NMC 622 cathode had a double-layer capacitance of about 1.5 times higher than that of cells with other two types of cathodes. The double-layer capacitance is proportional to the real surface area of surface of active material [330], and their C_{dl} are in agreement to the larger BET surface area showed in chapter 5.1.1. In addition, the τ_{SEI} of cells increased with decreasing active material size, while the τ_{dl} of cell with blended cathode was 50 % higher than those with B- or S-NMC 622 cathodes, indicating a slow charge transfer in cells with blended cathode.

R_{ct} can be changed by particle coating, phase transition, or particle size. A significant deviation is observed in the charge transfer resistance: the cell containing S-NMC 622 electrode displayed the smallest R_{ct}, while the cells with B- and B&S-NMC 622 electrodes showed higher discharge resistance. A decrease in charge transfer resistance was also reported for cells with NMC 111 electrodes having a D50 of 7.4 µm in comparison to those having a D50 of 5.1 µm, and the particle size was adjusted by using powder sieving in their

study [331]. The highest R_{ct} belongs to the cell with B&S-NMC 622 cathode, which may be due to a reduced contact surface between the NMC 622 particles and the conductive agent. Since the small NMC 622 particles can be distributed around large NMC 622 particles (see Figure 5-22-c), part of the surface of B-NMC 622 secondary particles is covered by the S-NMC 622 particles. Moreover, since KS6L and S-NMC 622 particles have a similar particle size of about 6 µm, S-NMC 622 particles can occupy the position of KS6L conductive agent. Thus, this hinders the uniform distribution of conductive agent on the surface of B-NMC 622 particles.

Figure S 2 displays a linear dependence between the real part of impedance Z_{re} and the $\omega^{-1/2}$ from the EIS analyses for all cells. This is in agreement with equation (4.12). The Warburg fitting results of cells containing three different types of NMC 622 cathodes are exhibited and the derived Warburg impedance coefficient σ_w is used to calculate the Li-ion diffusion coefficient in half-cells using equation (4.11). The Li-ion diffusion coefficients from the EIS analyses $D_{eff,EIS}$ for the cells containing different types of NMC 622 cathodes were calculated using equation (4.11). Table 5-10 shows that the cell with S-NMC 622 electrode had the highest Li-ion diffusion coefficient, while the cell with blended B&S-NMC 622 exhibited the lowest $D_{eff,EIS}$. The obtained $D_{eff,EIS}$ for the NMC 622 cathodes is in good agreement with other published results in the range of 10^{-14} cm^2/s [26, 87]. For example, Chowdhury et al. [26] reported that the cells with small NMC 622 particles having an average particle diameter of 1 µm exhibited a higher $D_{eff,EIS}$ of 6.75×10^{-14} cm^2/s than that of the cells containing big NMC 622 particles with an average particle size of 10 µm (3.45×10^{-14} cm^2/s). The higher $D_{eff,EIS}$. in cells with S-NMC 622 electrodes results in the enhanced rate capability for cells containing this type of electrodes, as shown in Figure 5-24.

Table 5-10. Warburg impedance coefficient σ_w, and the calculated Li-ion diffusion coefficient $D_{eff,EIS}$ from EIS analyses in half-cells containing different electrode types at OCV of 3.63 V.

Electrode type	σ_w [Ωs$^{-1/2}$]	$D_{eff,EIS}$ [cm^2/s]
B	34.43 ± 0.45	1.02×10^{-14}
S	17.08 ± 0.19	4.16×10^{-14}
B&S	59.73 ± 0.40	3.40×10^{-15}

Theoretically, reducing the particle size of the active materials can lead to enhanced electrochemical performance. This is due to a reduced diffusion time for Li-ions in active materials, which can be described as [65]:

$$\tau_c = L^2/4\pi\widetilde{D} \tag{5.13}$$

where τ_c [s] is the characteristic diffusion time, L [cm] the particle size and $\widetilde{D}$ [cm^2/s] the diffusion coefficient of Li-ions in the host lattice. From equation (5.13) it is known that if the particle size is reduced by half, the diffusion time of Li-ion in NMC 622 particles lattice is reduced to 1/4. Thus, cells with thick-film S-NMC 622 cathodes should have reduced τ_c in contrast to cells with B-NMC 622 cathodes, which results in their increased rate capability at C/2 and 1C. However, cells with electrodes containing smaller NMC 622 particles exhibited a lower initial CE as presented in Table 5-8, which should be due to an increased parasitic surface resulted from the exposure of larger active electrode-electrolyte interface between

active materials and electrolyte [332], because the BET surface area of S-NMC 622 powder, see Figure 5-4, is 22 % higher than that of B-NMC 622 powder. The study of Chowdhury et al. [26] compared the electrochemical performance of NMC 532 with mean particle size (D50) of 10 µm and 0.9 µm and found a large irreversible capacity loss for cells containing NMC 532 with small particle size, which is consistent with the results here. However, the study of Wagner et al. [333] had shown different results. They prepared NMC 111 with different primary and secondary particle sizes by sintering coarse or fine granules at 850 – 950 °C and found that cells containing electrodes with coarse secondary particles (D50 of 37 µm) showed higher rate capability in comparison to that with fine ones. They argued that this is due to an increased effective conductivity in NMC 111 sintered with coarse granules.

5.3.2. Impact of bilayer electrode architectures on cell performance

NMC 622 cathodes with hierarchical architectures were prepared by applying bilayer coating approach. The film thickness ratios of B- and S-layer inside hierarchical electrodes were set to 1:2, 1:1 and 2:1, while the position of B- and S-NMC 622 layers were changed in order to study the effect of the position on the electrochemical performance. All prepared NMC 622 cathodes with bilayer architectures displayed an approximate mass loading of 38 mg/cm^2 as well as an areal capacity of 6.5 – 6.6 mAh/cm^2, as shown in Table 5-11. The notation of the NMC 622 cathodes with hierarchical structures has been elaborated in chapter 4.2.4.

Table 5-11. Film thickness, active mass loading, and areal capacity of electrodes consisting of different NMC 622 particles, different film thicknesses, and with different bilayer structures.

NMC 622 cathode type	Doctor blade gap [µm]	Film thickness without Al foil [µm]	Active mass loading [mg/cm^2]	Areal capacity [mAh/cm^2]
SB – 1:2	135 + 280	152 ± 5	37.67 ± 0.19	6.50 ± 0.03
SB – 1:1	210 + 200	155 ± 6	38.48 ± 0.23	6.64 ± 0.04
SB – 2:1	275 + 135	152 ± 5	37.89 ± 0.24	6.53 ± 0.04
BS – 1:2	135 + 275	153 ± 5	37.98 ± 0.16	6.55 ± 0.03
BS – 1:1	200 + 210	151 ± 4	37.56 ± 0.18	6.48 ± 0.04
BS – 2:1	280 + 135	154 ± 5	38.32 ± 0.17	6.61 ± 0.03

Rate capability analyses

The specific discharge capacities of cells containing NMC 622 electrodes with bilayer architectures are presented in Figure 5-26. The cells containing SB – 1:2 electrodes achieved the highest capacity of 179 mAh/g, while cells containing BS – 1:1, BS – 1:2, BS – 1:1, and SB – 2:1 electrodes reached 176 mAh/g at the last C/20 cycle. The initial coulombic efficiency is listed in Table 5-12. All cells containing electrodes with B-NMC 622 as bottom layer and S-NMC 622 as top layer exhibited a lower initial CE, while the cells with BS – 1:2 cathodes showed the lowest initial CE. This indicates that the initial CE of cells can be increased either by applying S-NMC 622 as bottom layer or reducing the thickness of S-layer in BS-bilayer NMC 622 electrodes. At C/10, the cells with SB – 1:2 electrodes retained the highest specific discharge capacity of 172 mAh/g, followed by cells with BS – 2:1 electrodes. When the C-rate

rose to C/5, cells with BS – 2:1 electrodes held the highest capacity of 168 mAh/g, while the lowest specific capacity of 164 mAh/g belonged to those containing BS – 1:1 electrodes. At C/2, cells with BS – 1:2 and SB – 2:1 electrodes had the highest specific discharge capacity of about 130 mAh/g, while the lowest specific capacity of 96 mAh/g were the cells with SB – 1:2 electrodes. This suggests that the capacity at C/2 increased with increasing thickness of S-layer in the electrodes, regardless of the position of the S-layer. When the C-rate increased to 1C, cells containing BS – 2:1 cathodes showed the highest discharge capacity, while cells with SB – 1:2 and SB – 1:1 electrodes exhibited the lowest capacity. Therefore, the BS-configurations with increasing B-layer thickness can increase the capacity at 1C, while cells with SB-configurations are not suitable for high power applications. From 2C to 5C, all cells had a capacity decrease of 80 % relative to the initial discharge capacity at C/20.

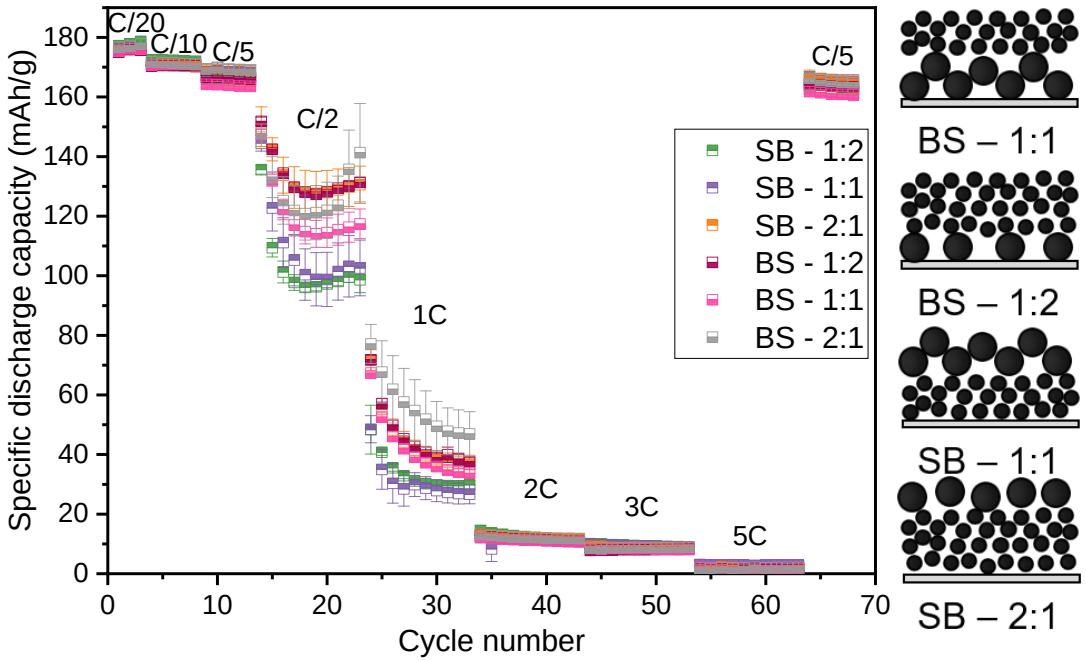

Figure 5-26. Rate capability analyses of half-cells containing thick-film bilayer NMC 622 cathodes with different configurations and their schematic views.

The capacity retention of cells with different types of NMC 622 cathodes calculated from the last five C/5 cycles in contrast to the pervious C/5 cycles is shown in Table 5-12. The highest capacity retention belonged to the cells with BS – 1:2 and SB – 2:1 cathodes, while the ones with SB – 1:2 cathodes showed the lowest value. This trend is the same as the rate capability analysis at C/2 (Figure 5-26), where the cells with BS – 1:2 and SB – 2:1 cathodes exhibited the highest discharge capacity, while the lowest value was obtained by the cells containing SB – 1:2 and SB – 1:1 cathodes. In addition, the cells containing SB – 1:2 and BS – 2:1 electrodes showed a capacity smaller than 98 % in comparison to other cells with bilayer electrodes as well as cells with monolayer electrodes (Table 5-8). This indicates that the capacity retention in cells with bilayer electrodes deteriorates with increasing thickness ratio of B:S-layers. The lifetime analyses results of cells with unstructured bilayer NMC 622 cathodes will be presented together with those of cells with structured cathodes in chapter 5.3.3.

Table 5-12. Initial coulombic efficiency at C/20 and the capacity retention (C/5) of cells containing NMC 622 cathodes with different bilayer architectures.

NMC 622 cathode type	Initial coulombic efficiency [%]	Capacity retention [%]
SB – 1:2	89.5 ± 0.2	97.4 ± 0.6
SB – 1:1	89.7 ± 0.4	98.2 ± 0.5
SB – 2:1	89.2 ± 0.1	98.4 ± 0.7
BS – 1:2	88.6 ± 0.8	98.5 ± 0.4
BS – 1:1	89.1 ± 0.3	98.3 ± 0.5
BS – 2:1	89.6 ± 0.3	97.6 ± 0.5

The cells with hierarchical bilayer NMC 622 cathodes exhibited no difference in CV analyses in comparison to cells with monolayer electrodes shown in Figure 5-23-a, displaying one oxidation and one reduction peak, see Figure 5-27-a. The oxidation peaks were located at 3.87 ± 0.01 V, while the reduction peaks were at 3.63 ± 0.01 V. Since the redox peaks of all cells were at a voltage position that varies by only 0.01 V, this indicates similar electrochemical kinetics of thick-film NMC 622 electrodes regardless of their hierarchical structures. The peak voltages which corresponded to the redox reaction of cells containing different types of thick-film NMC 622 electrodes and the peak-to-peak voltage difference are shown in Figure 5-27-b. Cells with SB – 2:1, BS – 1:2, and BS – 1:1 electrodes exhibited a minimum potential difference of 0.22 V, while the cell with S-electrode showed the largest peak-to-peak potential difference of 0.28 V, which indicates that cells with thick-film S-electrodes had a higher cell polarization in comparison to cells with other types of electrodes.

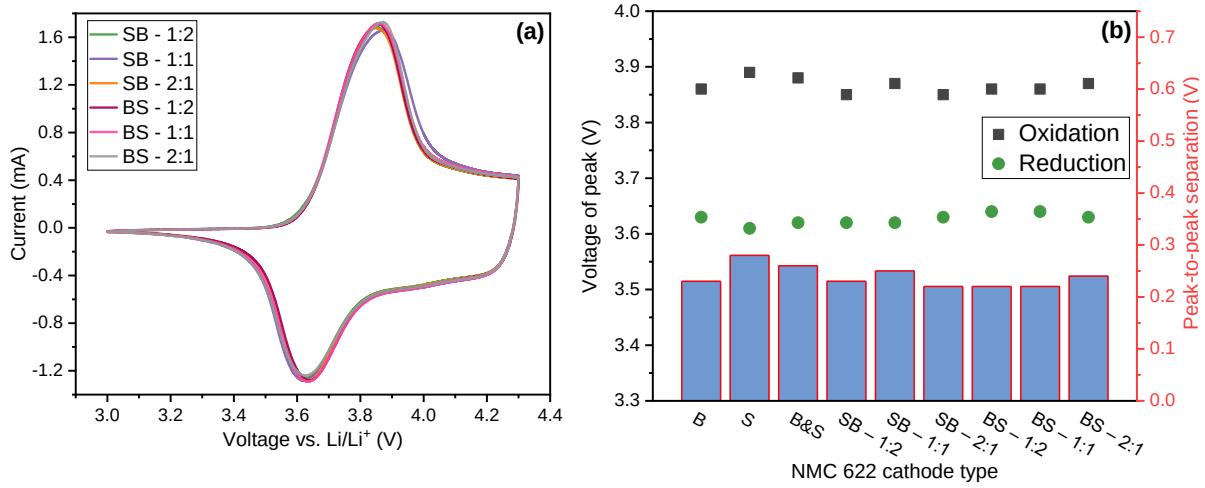

Figure 5-27. CV analyses of (**a**) cells containing bilayer NMC 622 electrodes with different configurations and (**b**) the voltages (vs. Li / Li^+) correspond to the redox peaks (points) and the separation of the oxidation and reduction peak (bars) from CV analyses of cells with different types of cathodes.

Electrochemical impedance spectroscopy

EIS analyses were performed subsequently to the rate capability analyses. Figure 5-28 shows the Nyquist plots of cells containing thick-film NMC 622 electrodes with different bilayer architectures. The EIS analyses data were fitted by using the same equivalent circuit model as described in Figure 5-25. The ohmic resistance R_e, the SEI resistance R_{SEI}, the charge transfer resistance R_{ct}, the SEI capacitance C_{SEI}, double-layer capacitance C_{dl}, and Warburg resistance W of cells containing different types of thick-film NMC 622 electrodes are

summarized in Table 5-13. Furthermore, Kramers-Kronig analyses were performed for each fit and the resulted χ^2 is exhibited in Table 5-13.

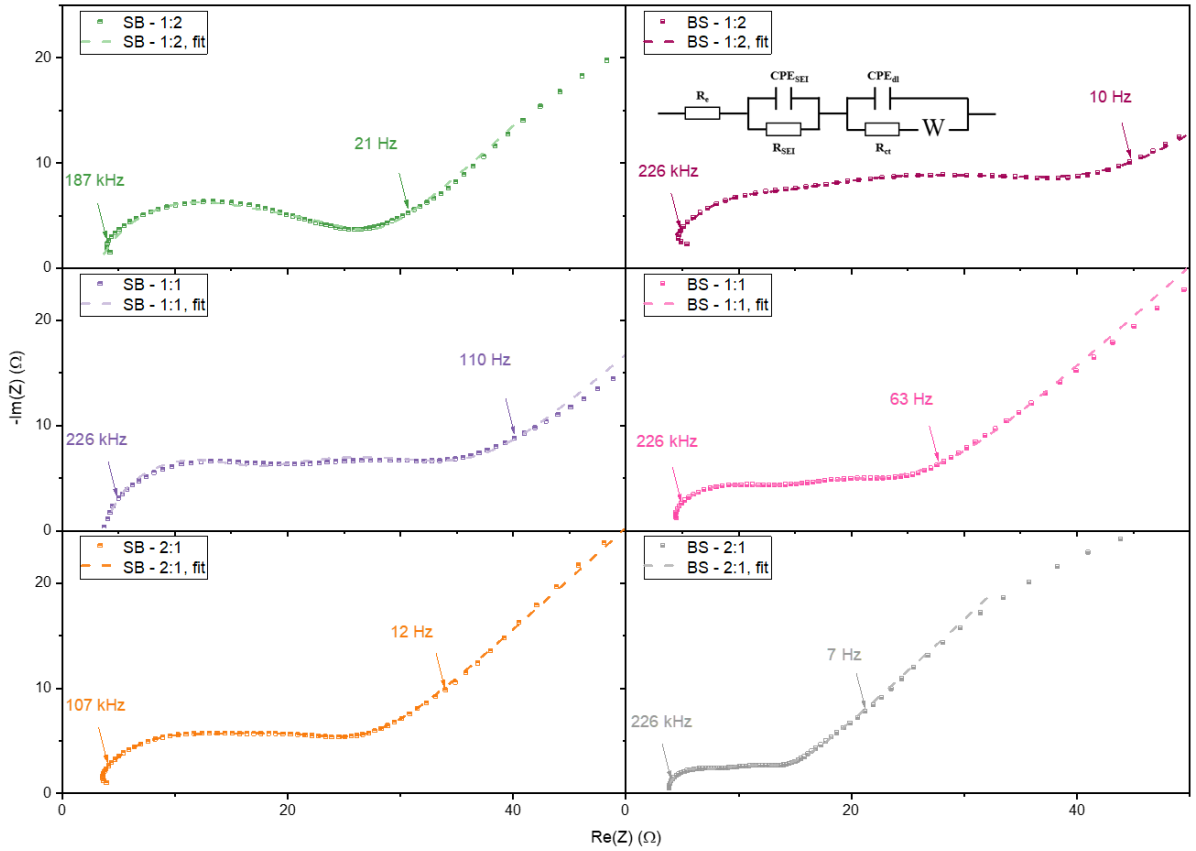

Figure 5-28. Nyquist plots of cells containing thick-film NMC 622 cathodes with different bilayer architectures at OCV (3.63 V) after rate capability analyses. The equivalent circuit model applied for fitting is the same as shown in Figure 5-25.

The ohmic resistance R_e of cells with bilayer NMC 622 cathodes was similar to that of cells with monolayer cathodes (Table 5-9), which was around 3 Ω. However, the bilayer architecture showed an impact on the charge transfer resistance R_{ct}.and the SEI resistance R_{SEI}. All cells containing electrodes with SB-configurations showed 9.1 – 9.9 Ω SEI resistance, which is similar to that of the cell with S-NMC 622 monolayer cathode (10.5 Ω), while other cells having electrodes with BS-configurations exhibited decreased R_{SEI} of 2.5 – 4.9 Ω. The cell with BS – 2:1 cathode showed the lowest charge transfer resistance of 7.8 Ω, which trends with the rate capability analyses at 1C, where cells with this architecture showed the highest discharge capacity. For cells with BS-NMC 622 cathodes, the charge transfer resistance decreased with increasing B-layer thickness. As for cells with SB-cathodes, no significant correlation between thickness ratio of S- and B-layers and charge transfer resistance was observed. However, if we compare the position of the layers individually, it is found that the R_{ct} of cell with BS – 1:1 electrode was smaller than that containing SB – 1:1 electrode, which also corresponds to their performance in rate capability analyses at C/2 and 1C.

In addition, all cells with bilayer NMC 622 electrodes except for BS – 2:1 exhibited higher charge transfer resistance in comparison to cells with monolayer electrodes. This may be due to the presence of the interface between B- and S-layer in bilayer electrodes. A clear interface

or transition area is visible in SEM images, as shown in Figure S 3. In this region, a sudden porosity change may occur, and the binder concentration must be higher than in its neighboring region (above or below). In other words, the discontinuity in the binder distribution and porosity gradient could lead to an increased resistance for Li-ion diffusion in bilayer thick-film NMC 622 electrodes than that in monolayer electrodes. However, an opposite result was reported by Chowdhury et al. [26], where cells with bilayer exhibited lower charge transfer resistance in comparison to cells containing monolayer NMC 532 cathodes with large or small particles. Yet in their study the NMC 532 powder with a small particle size of 1 µm was obtained using ball milling. Thus, the secondary particles were destroyed due to the external mechanical stress, which can be observed in their cross-sectional SEM images. This may lead to a further increase in the surface area of active material. However, the as-received large and small NMC 622 particles were not subjected to any mechanical treatment in this thesis and were applied directly for slurry preparation. Furthermore, all cells with bilayer cathodes exhibited similar C_{SEI} value as the cell with B&S-NMC 622 cathode and were lower in comparison to cells with B- or S-NMC 622 cathodes (Table 5-9). As for C_{dl}, the value increased as the interface between B- and S-NMC 622 layer moved from current collector to the electrode surface. However, the reason for this is unknown. The cells containing electrodes with BS-configurations showed lower equivalent time constant τ_{SEI} and τ_{ct} compared to those with SB-configurations and blended B&S-electrodes, suggesting a faster charge transfer and SEI formation in BS-NMC 622 electrodes. This matches the trend obtained from the rate capability analyses (Figure 5-26).

Table 5-13. Ohmic resistance, SEI resistance, charge transfer resistance, SEI capacitance, double-layer capacitance, and Warburg of cells containing thick-film NMC 622 electrodes with different bilayer architectures at OCV of 3.63 V. The χ^2 represents the Kramers-Kronig analysis.

	NMC 622 cathode type					
	SB – 1:2	**SB – 1:1**	**SB – 2:1**	**BS – 1:2**	**BS – 1:1**	**BS – 2:1**
R_e [Ω]	3.2	3.8	2.8	1.5	3.3	3.7
R_{SEI} [Ω]	9.8	9.9	9.1	3.1	4.9	2.5
R_{ct} [Ω]	14.2	21.0	13.6	38.4	17.9	7.8
Y_{SEI} [$Fs^{\varphi-1}$]	$3.6 \cdot 10^{-6}$	$6.1 \cdot 10^{-7}$	$8.5 \cdot 10^{-6}$	$1.6 \cdot 10^{-7}$	$1.1 \cdot 10^{-6}$	$1.1 \cdot 10^{-6}$
Y_{dl} [$Fs^{\varphi-1}$]	$2.9 \cdot 10^{-4}$	$2.2 \cdot 10^{-4}$	$3.2 \cdot 10^{-4}$	$2.5 \cdot 10^{-4}$	$6.2 \cdot 10^{-4}$	$6.1 \cdot 10^{-4}$
φ_{SEI} [-]	0.86	0.96	0.81	0.99	0.94	0.99
φ_{dl} [-]	0.58	0.60	0.62	0.47	0.48	0.56
C_{SEI} [µF]	0.6	0.4	0.9	0.9	0.5	1.0
C_{dl} [µF]	5.3	6.1	11.5	4.5	5.0	9.1
τ_{SEI} [µs]	6.3	3.5	8.6	2.7	2.4	2.4
τ_{dl} [µs]	74.6	128.3	156.9	56.0	89.5	71.1
W [Ω]	211.1	276.1	297.1	249.7	548.2	454.9
χ^2 [-]	0.00066	0.00077	0.00001	0.00018	0.00004	0.00034

A linear dependence between the real part of impedance Z_{re} and the $\omega^{-1/2}$ from EIS analyses in Figure 5-28 is shown in Figure S 4. The derived Warburg impedance coefficient σ_w and the lithium-ion diffusion coefficient in half-cells are listed in Table 5-14. It is noted that all cells showed similar diffusion coefficient ranging from 10^{-15} to 10^{-14} cm^2/s. The cells

containing SB – 1:2 and BS – 2:1 electrodes exhibited the highest $D_{eff,EIS}$, while the cell with BS – 1:2 electrode achieved the lowest Li-ion diffusion coefficient compared to other cells. The enhanced $D_{eff,EIS}$ of cells containing BS – 2:1 electrodes is in agreement with their high discharge capacity at C/2 and 1C in rate capability. However, no clear relationship is observed in Li-ion diffusion coefficient with respect to the variation in thickness and position of S- and B-layer in cells containing bilayer electrode.

Table 5-14. Warburg impedance coefficient σ_w, and the calculated lithium-ion diffusion coefficient $D_{eff,EIS}$ from EIS analyses in half-cells containing thick-film bilayer NMC 622 with different configurations at OCV of 3.63 V.

Electrode type	σ_w [Ωs$^{-1/2}$]	$D_{eff,EIS}$ [cm^2/s]
SB – 1:2	20.07 ± 0.19	3.02 × 10^{-14}
SB – 1:1	39.42 ± 0.36	7.82 × 10^{-15}
SB – 2:1	32.51 ± 0.25	1.15 × 10^{-14}
BS – 1:2	65.60 ± 0.40	2.82 × 10^{-15}
BS – 1:1	39.66 ± 0.26	7.72 × 10^{-15}
BS – 2:1	20.34 ± 0.13	2.94 × 10^{-14}

Furthermore, by comparing the cells with bilayer BS – 1:1 and SB – 1:1 NMC 622 cathodes with cells containing blended B&S-monolayer electrodes, we can investigate whether it is meaningful to fabricate bilayer electrodes instead of using blended NMC 622 powders with different particle sizes, since the mass ratio of S- and B-NMC 622 powders remains the same (1:1) in all three configurations.

A graphical comparison of cells containing these three different types of electrodes in terms of different electrochemical analyses are displayed in Figure 5-29. All the indexes have been normalized, higher scores indicate higher discharge capacity and higher capacity retention of the corresponding cells, while charge transfer resistance, SEI resistance, and peak-to-peak separation decrease with increasing score. Rate capability analyses showed that all these cells have similar discharge capacity at C/20 to C/5. At C/2, cells with B&S-electrodes provided 124 mAh/g discharge capacity, while cells with BS – 1:1 and SB – 1:1 electrodes retained 121 and 109 mAh/g discharge capacity, respectively. The cells with BS – 1:1 electrodes showed the highest capacity at 1C. Besides, all cells exhibit a capacity retention of 98 % in rate capability analysis. However, lifetime analyses in Figure 5-24-d and Figure 5-35-a exhibited that the cell with BS – 1:1 electrode retained 86 % discharge capacity after being cycled 40 times at C/2, while cells with B&S- and SB – 1:1 electrode showed 76 % and 57 % capacity retention after 40 cycles, respectively. In addition, EIS analyses showed that the cells with B&S-electrodes had an increased charge transfer resistance of 24.0 Ω, while cells with bilayer electrodes exhibited lower charge transfer resistance of 21.0 Ω and 17.9 Ω for those with SB – 1:1 and BS – 1:1 electrodes, respectively. Besides, cells with bilayer electrodes showed higher lithium-ion diffusion coefficients than those with B&S-electrodes. Therefore, cells containing bilayer electrodes with BS – 1:1 configuration could achieve similar rate capability in comparison to cells with blended NMC 622 cathodes, while the latter displayed higher charge transfer resistance and significantly lower cycling stability.

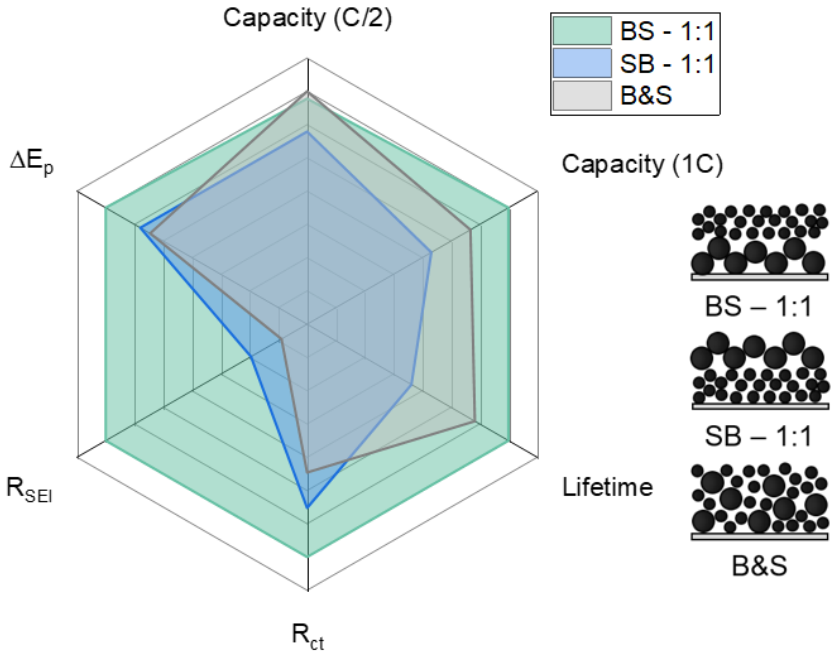

Figure 5-29. Comparison of cells containing monolayer B&S-NMC 622 cathodes with the cells containing bilayer NMC 622 cathodes with BS – 1:1 and SB – 1:1 configurations in terms of six different aspects: discharge capacity at C/2 and 1C from rate capability analyses, capacity retention from lifetime analyses, charge transfer resistance R_{ct} and SEI resistance R_{SEI} from EIS, and peak-to-peak separation (ΔE_p) from CV analyses. All Indexes are normalized to allow for the qualitative evaluation of the cells with different architectures.

Ali et al. [323] simulated the effect of particle size on the stress generation in the electrode and suggested that an architecture with increasing particle size toward the separator could alleviate stress generation in electrode during charging and discharging. However, their simulations do not involve specific electrode materials and therefore have limitations because their work showed opposite results compared to the experimental results of this work, and the simulations cannot explain the better rate capability and lower charge transfer resistance of cells with BS-configuration in contrast to cells with SB-configuration. Wood et al. [156] studied pouch cells with bilayer architectures containing NMC 532 cathodes and graphite anodes with two different secondary particle sizes. They observed a two times capacity increase at a discharge rate of 2C for cells containing NMC 532 cathodes with small particles at the top layer and large particles at the bottom layer vs. graphite anodes with large particles at the top and small particles at the bottom. Their results are consistent with the results presented in this work, where BS-configuration is beneficial for high power applications. The bottom layer with large cathode active particles results in less tortuous Li-ion transport and reduced interparticle diffusion, while an upper layer with small active material particles decreases the intraparticle solid-state diffusion ways [156].

In summary, rate capability and CV analyses indicate that in order to achieve a higher discharge capacity at high C-rates with bilayer architectures, the following methods can be applied:

(i) using bilayer NMC 622 cathodes in BS-configuration, i.e., with large NMC 622 particles as bottom layer and small particles as top layer;

(ii) increasing the thickness of the layer containing small particles.

However, if we compare the discharge capacity at low C-rates (smaller than C/2), an opposite trend is observed, which means that using SB-configuration and increasing the thickness of B-layer can increase the cell capacity at low C-rates.

5.3.3. Laser structured electrodes with bilayer architectures

In chapter 5.2.3, the laser structuring of NMC 622 electrodes with different film thicknesses was discussed. It was revealed that in the C-rates range of C/2 to 5C, the discharge capacities of cells with laser structured electrodes were increased up to 170 % in comparison to those of cells with unstructured electrodes. In this chapter, the combination of laser structuring with electrodes having bilayer architectures will be further investigated. Laser ablation was used to generate groove structures with a pitch of 200 µm in thick-film NMC 622 electrodes with different bilayer architectures. Subsequently, the laser structured electrodes were assembled into coin cell (half-cells) to study the impact of the combination of bilayer electrodes and laser structuring on the electrochemical performance.

A clear interface can be observed where the green transparent boxed are displayed in Figure 5-30. Interestingly, although the bottom layer was already dried before the casting of the upper layer, a few large B-NMC 622 particles can be found in the bottom layer, as shown in Figure 5-30-b. During the second casting, slurry with NMP solvent was cast onto the first layer with a porosity of 40 – 45 %. Before the slurry was fully dried, part of the PVDF binder near the surface of the bottom layer could redissolve into the NMP solvent. Since binder is used to maintain the mechanical stability of the dried electrode [166], dissolution of the binder can cause a localized mechanical instability, which results in relocation of NMC 622 particles, conductive agents, and binder. Meanwhile, when large NMC 622 particles are at the top, a few of them could infiltrate downward into the bottom layer due to capillary forces. Similarly, the infiltration of S-NMC 622 particles from the upper layer to the bottom B-NMC 622 layer was also observed in the BS-electrodes. However, this type of interdiffusion occurred only locally in a short period and is therefore assumed to have limited impact on the electrochemical performance at cell level.

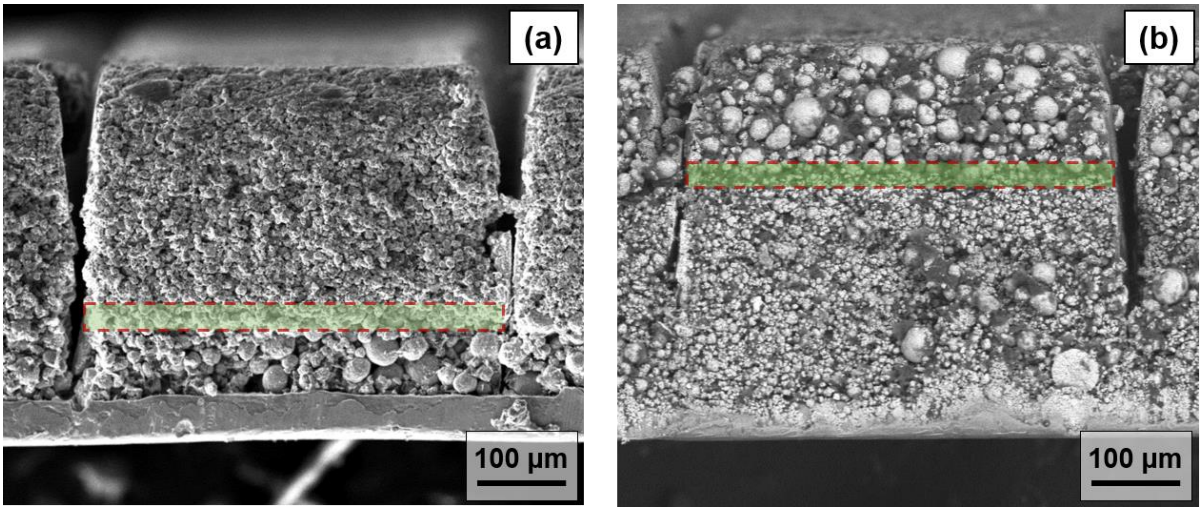

Figure 5-30. Cross-sectional SEM images of the laser structured NMC 622 electrodes with (**a**) B:S – 1:2 and (**b**) S:B – 2:1 configurations using SE and BSE detector, respectively. The green transparent boxes indicate the transition area between B- and S-layer.

In order to obtain more information such as maximum width and FWHM of the channel structures generated by laser ablation, cross-sectional analyses of embedded specimens with fluorescence powder were performed (Figure 5-31). For electrodes with monolayer or different multilayer configurations, the laser scan was adjusted to achieve channel structures from electrode surface down to the current collector. Laser structured electrodes with other configurations are shown in Figure S 5.

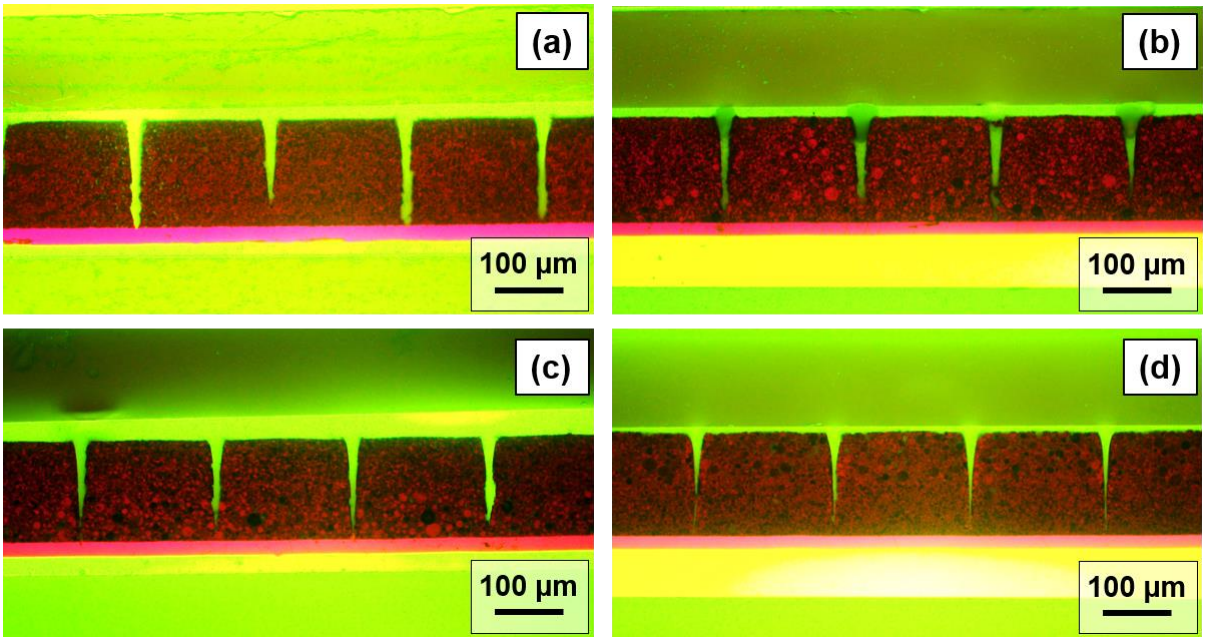

Figure 5-31. Cross-sectional views of different laser structured thick-film NMC 622 electrodes. The number of laser scans has been adjusted to enable a laser ablation down to the current collector for different types of electrodes: (**a**) S-monolayer; (**b**) B&S-monolayer; (**c**) BS – 1:1 bilayer; and (**d**) SB – 1:1 bilayer [334].

The mass loss due to laser ablation includes the removal of active material, conductive additive, and binder (equation (5.7)). Table 5-15 shows that electrodes containing B-NMC 622 powder and bilayer electrodes with B-layer on the top needed more laser scans (22 scans) in comparison to S- and BS-electrodes (14 – 16 scans) with small particles or small particles within top layer. This means that the ablation depth per laser pulse for B- and SB-electrode was about a factor of 1.5 smaller than the ablation rate for the S- and BS-electrode. Since the laser fluence was constant by applying an average laser power of 2.5 W and a laser repetition rate of 500 kHz, the difference in ablation rate may indicate a higher absorption coefficient of laser beam in S-electrode with smaller particles, as absorption takes place at grain boundaries. A higher absorption at grain boundaries could accelerate the removal of the polymer matrix and leads to wider groove structures. Figure 5-31 shows that the channels of structured S- and BS-electrodes were wider and rectangular, while B- and SB-electrodes had more Gaussian-like shaped channels with narrow width close to the current collector. In addition, the laser processing time of blended B&S-NMC 622 electrodes was reduced due to an increased ablation rate. Furthermore, it is found that the mass loss of laser structured bilayer electrode was about 5 % higher for electrodes with BS-configurations expect BS – 2:1 in comparison to ones with SB-configurations. Therefore, mass loss can be effectively reduced by using bilayers with large particle sizes in the top layer or by increasing the B-layer thickness in electrodes with BS-configurations.

Table 5-15. The number of laser scans applied for electrode structuring, active mass loading, areal capacity, maximum width and FWHM of laser structured thick-film electrodes, as well as the mass loss of structured electrodes in comparison to unstructured ones.

NMC 622 cathode type	Laser scans	Active mass loading [mg/cm^2]	Areal capacity [mAh/cm^2]	Max. width [µm]	FWHM [µm]	Mass loss [%]
B, structured	22	35.3 ± 0.1	6.09 ± 0.01	33.3 ± 1.4	10.0 ± 2.0	5.9 ± 0.9
S, structured	14	34.2 ± 0.2	5.89 ± 0.03	28.5 ± 1.2	12.5 ± 1.0	11.2 ± 1.1
B&S, structured	15	35.8 ± 0.1	6.17 ± 0.02	31.8 ± 2.1	10.9 ± 1.4	6.4 ± 1.0
SB – 1:2, structured	22	35.6 ± 0.1	6.15 ± 0.01	26.8 ± 2.6	5.4 ± 1.5	4.1 ± 0.1
SB – 1:1, structured	22	36.1 ± 0.2	6.22 ± 0.04	24.7 ± 2.1	4.1 ± 1.4	6.2 ± 1.6
SB – 2:1, structured	22	35.8 ± 0.2	6.17 ± 0.04	24.0 ± 3.0	3.9 ± 0.7	4.0 ± 1.0
BS – 1:2, structured	15	34.1 ± 0.1	5.87 ± 0.09	31.5 ± 1.4	9.4 ± 2.4	10.1 ± 2.1
BS – 1:1, structured	15	34.5 ± 0.1	5.95 ± 0.01	25.8 ± 1.7	11.7 ± 3.7	10.4 ± 0.5
BS – 2:1, structured	16	36.4 ± 0.1	6.27 ± 0.01	27.1 ± 1.0	9.5 ± 1.0	4.8 ± 0.8

Before discussing the electrochemical performance of cells containing laser structured bilayer NMC 622 cathodes, the performance of reference cells with laser structured monolayer cathodes will be reviewed. Rate capability analyses of cells with laser structured monolayer cathodes (Figure 5-32-a) show that from C/20 to C/5, cells containing laser structured electrodes provided about 5 mAh/g lower discharge capacity in comparison to cells with unstructured electrodes. This phenomenon has also been observed in previous results for cells containing laser structured NMC 622 electrodes with different thicknesses (Figure 5-13). At C/2 and 1C, a significant increase in discharge capacity was found for cells with laser structured electrodes. For example, Figure 5-32-b shows that at C/2, cells with laser structured B-electrodes displayed 48 mAh/g higher discharge capacity, while cells with B&S-electrodes exhibited a 29 mAh/g capacity increase. For cells with S-electrodes, no increase in capacity was observed at C/2, but a capacity increase of 59 mAh/g was exhibited at 1C, which is the highest increase compared to all other cells regardless of C-rates. Besides, all cells with laser structured electrodes exhibited the largest increase in discharge capacity at 1C, indicating that laser structuring can bring gains to the electrochemical performance at high C-rates above C/2 regardless of the particle size of NMC 622 used during the electrode preparation process.

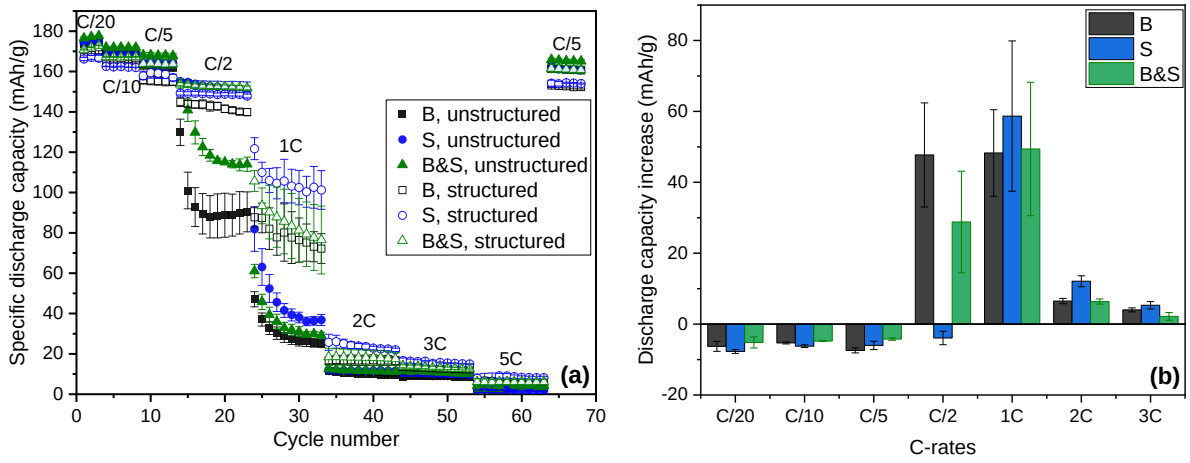

Figure 5-32. Electrochemical performance of reference cells with laser structured monolayer electrodes: (**a**) the rate capability analyses and (**b**) the discharge capacity increase of cells having structured electrodes with different monolayer electrodes in comparison to the cells with respective unstructured electrodes.

Figure 5-33 exhibits the rate capability analyses of cells containing laser structured NMC 622 cathodes with different bilayer architectures. All cells with structured electrodes showed an initial CE of around 87.5 % at the first C/20 cycle, as listed in Table 5-16, which is 2 % lower in contrast to ones with unstructured electrodes shown in Table 5-12. At C/20 to C/5, cells with laser structured bilayer electrodes showed lower discharge capacity in comparison to cells with unstructured electrodes (Figure 5-26). This discharge capacity decrease was also observed in Figure 5-13, where data of cells containing laser structured and unstructured monolayer NMC 622 cathodes with different thicknesses varying from 100 µm to 200 µm were displayed. However, at C/2, all cells with laser structured electrodes maintained about 130 – 150 mAh/g discharge capacity, while the cells with unstructured electrodes showed continuously decreasing capacity from 140 to 100 mAh/g (Figure 5-26). With increasing C-rate at 1C, the discharge capacities of cells with laser structured electrodes located at 50 – 107 mAh/g, while cells with unstructured electrodes showed 27 – 77 mAh/g capacities. When the C-rates further increase from 2C to 5C, all cells lost more than 85 % capacity in comparison to their initial capacity at C/20.

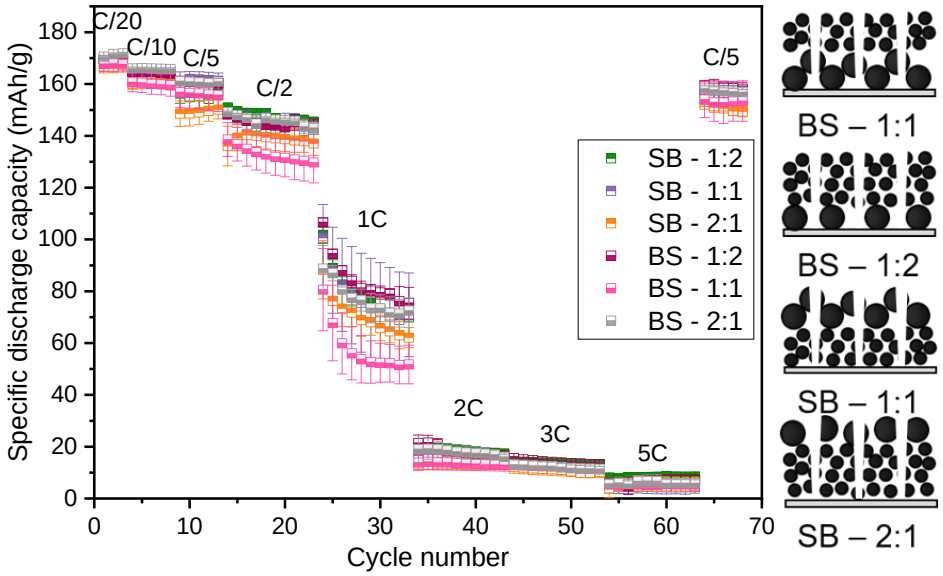

Figure 5-33. Rate capability analyses of half-cells containing laser structured thick-film NMC 622 cathodes with different bilayer architectures. The thicknesses of all electrodes without Al current collector were about 150 µm.

At the end of rate capability analyses, all cells were cycled again at C/5 and the capacity retention is calculated based on the capacity difference in comparison to the previous discharge capacity at C/5. Table 5-16 shows that all cells with laser structured bilayer electrodes exhibited about 98 % to 99 % capacity retention after being cycled up to 5C, and the capacity retention was increased for all cells containing laser structured electrodes with each bilayer configuration in comparison to cells with unstructured electrodes (Table 5-12).

Table 5-16. Initial coulombic efficiency of the first cycle at C/20 and the capacity retention (C/5) of cells containing laser structured NMC 622 cathodes with different bilayer architectures.

NMC 622 cathode type	Initial coulombic efficiency [%]	Capacity retention [%]
SB – 1:2, structured	87.8 ± 0.9	98.7 ± 0.9
SB – 1:1, structured	87.5 ± 1.0	98.0 ± 1.7
SB – 2:1, structured	86.6 ± 0.7	99.0 ± 0.7
BS – 1:2, structured	87.6 ± 0.3	98.8 ± 0.5
BS – 1:1, structured	87.3 ± 0.4	98.1 ± 0.6
BS – 2:1, structured	88.2 ± 0.1	97.9 ± 0.5

To investigate more closely the impact of different configurations on the electrochemical performance data, the differences in discharge capacity between cells with laser structured and unstructured electrodes at C/2 and 1C are compared, as shown in Figure 5-34. All cells with laser structured electrodes had higher discharge capacity at C/2 and 1C. However, the configuration of bilayer has a significant impact on the capacity increase. At C/2, for cells with SB-electrodes, the capacity increase weakened with increasing S-layer thickness, while cells with BS-electrodes showed slightly enhanced performance with increasing B-layer thickness. However, the trend was a bit different at 1C, where cells with SB – 1:1 electrodes exhibited the highest capacity increase of 47 mAh/g, followed by cells with SB – 1:2 and BS – 1:2 electrodes. The lowest discharge capacity increase at 1C belonged to the cells with BS – 1:1 electrodes. By comparing the discharge capacity increase of cells containing bilayer electrodes with cells with monolayer electrodes (Figure 5-32-b), it is found that the capacity increase at C/2 mainly

originates from the laser structured B-layer, regardless where the B-layer is located. Nevertheless, the capacity increase of cells with bilayer electrodes at 1C was lower in comparison to that of cells containing monolayer S-electrodes. Both cells with SB – 1:2 and SB – 1:1 electrodes showed high capacity increase at 1C, followed by cells with BS – 1:2 electrodes. Since cells with B- or S-monolayer electrodes exhibited similar increases in the discharge capacity after laser structuring, as shown in Figure 5-32-b, it is difficult to determine which layer is the main cause of the capacity increase. However, cells with SB-configuration showed overall higher discharge capacity increase in contrast to those with BS-configuration. In summary, B-layer as upper layer (SB-configuration) can reduce the electrode mass loss caused by laser structuring and is meanwhile beneficial to the enhancement of the discharge capacity of cells with laser structured electrodes at C-rates above C/2.

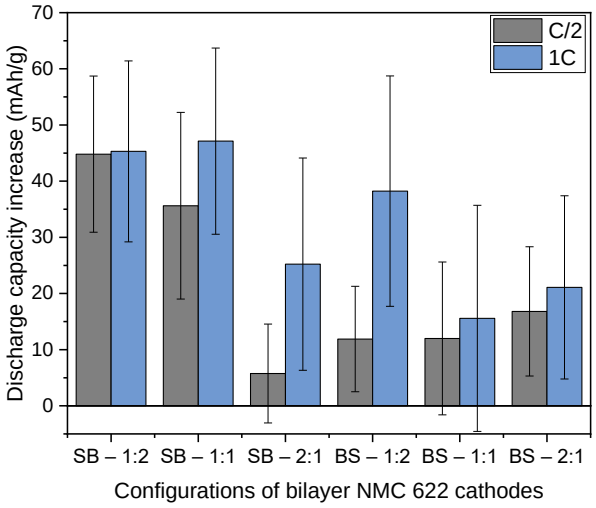

Figure 5-34. Increase in specific discharge capacity of half-cells containing laser structured bilayer NMC 622 cathodes with different configurations in comparison to the cells with unstructured electrodes at C/2 and 1C.

Park et al. [267] reported that cells with laser-structured thick-film NMC 532 cathodes (thicknesses varied from 100 to 210 µm) achieved higher rate capability in comparison to cells with unstructured electrodes at C/2 to 3C. This phenomenon is also observed in this work for all investigated cells with different bilayer configurations. However, in their work, the mass loss of electrodes due to laser structuring was 13 – 21 %, which is significantly higher than that in this work. Besides, the mass loss owing to laser structuring can be further reduced by choosing the optimal bilayer electrode configuration.

Figure 5-35-a shows the lifetime analyses of cells containing unstructured bilayer NMC 622 electrodes with different configurations. The cell with S-monolayer electrode exhibited the highest capacity retention of 98 % after 40 cycles at C/2, while the lowest capacity retention of 58 % belonged to the cell with SB – 1:1 electrode, which is lower than that of the cell with SB – 1:2 electrode (69 %) and the reference cell with B-monolayer (72 %). All cells containing electrodes with BS-configurations exhibited similar capacity retention of about 87 %, while only the cell with SB – 2:1 electrode from SB-configurations showed a capacity retention of 87 %. This indicates that for cells with unstructured bilayer electrodes, BS-configurations with small particles in the upper layer as well as increasing the S-layer thickness in SB-configurations are beneficial to improve the cycling stability. These results are consistent with

the rate capability analyses of cells containing bilayer NMC 622 cathodes with different configurations as discussed in the chapter 5.3.2. In Figure 5-35-b it can be clearly seen that the cycle stability of all cells has been significantly improved after laser structuring. For example, for cell with SB – 1:2 electrode, the cycling stability increased from 69 % to 95 % after applying laser structuring. Besides, all cells with laser structured BS-electrodes showed over 90 % capacity retention after 40 cycles at C/2. The discharge capacities of cells with unstructured thick-film electrodes deteriorated during lifetime analysis. This is due to the high internal resistance, the reduced mechanical integrity of thick-film electrodes [335] and serious reaction inhomogeneity [231]. In contrast to the cells with unstructured electrodes, all cells with laser structured thick-film electrodes are electrochemically more stable and can retain more capacity after long-term cycling. Thus, laser structuring of the thick-film electrodes is a viable approach for the high-energy battery.

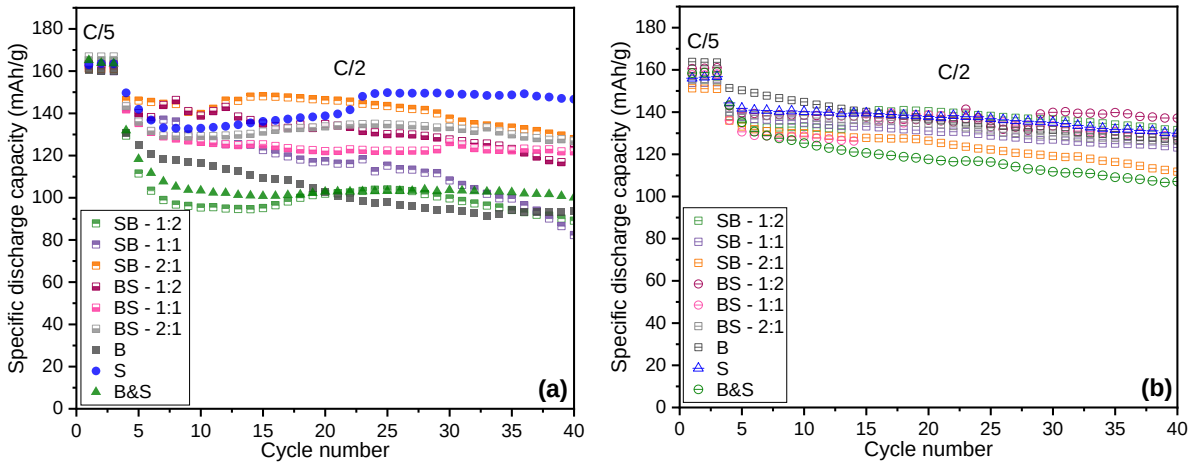

Figure 5-35. Lifetime analyses of half-cells containing (**a**) unstructured and (**b**) laser structured thick-film NMC 622 cathodes with different configurations (single layer and bilayer).

In this thesis, the impact of bilayer electrodes with different particle sizes and configurations on the electrochemical performance of the cells with laser structured electrodes is studied for the first time and is therefore of great importance to guide the selection of active materials with different particle sizes and configurations during slurry preparation and coating.

5.4. Electrodes processed with water-based binders

Conventional cathode preparation involves high processing costs and environmental issues due to the use of organic PVDF binder and highly toxic NMP solvent [10, 161]. In order to overcome these drawbacks, aqueous processing of different NMC cathode materials was investigated using Na-CMC and fluorine acrylic hybrid latex as binders [29, 189]. However, as described in chapter 3.2.2, aqueous processing of NMC materials leads to an increase in slurry pH value, and the alkaline slurry reacts with Al current collector and generates hydrogen gas during the coating process, which subsequently results in high porosity in dried composite electrodes. The effect of different types of acid addition on the cathode materials has been vastly reported [30, 175, 186]. However, only a few research groups have studied thoroughly the effect of pH value on the cathode slurry properties and the resulting electrochemical performances of NMC 622 electrodes.

In the present work, NMC 622 cathode slurries were prepared using aqueous binders Na-CMC and TRD 202A and their pH were adjusted to different values ranging from 7 to 12. First, different amounts of acetic acid were applied during the mixing process in order to examine the impact of slurry pH value on the slurry properties and the porosity of dried electrodes. Two mass loadings were chosen to represent the thin-film and thick-film electrode, respectively. The NMC 622 electrodes processed with different pH values were then assembled in half-cells to evaluate their electrochemical performance. After the optimal pH range was determined, one of the different kinds of acids was added during the slurry mixing process to adjust the slurry pH value to the same range. The electrodes processed with various acids underwent further characterization using XPS and Raman spectroscopy to identify any potential material modifications. In addition, ultrafast laser structuring of thick-film electrodes was applied to prove the feasibility of the 3D battery concept for aqueous processed NMC 622 electrodes. Afterwards, the NMC 622 electrodes with different acid additions were assembled in half-cells for electrochemical analyses.

5.4.1. Impact of slurry pH value on the properties of aqueous processed electrodes

First of all, in order to determine the optimal pH range for the electrode coating process and electrochemical performance, various amounts of acetic acid (AA) were added during the mixing process to adjust the slurry's pH value. The mass ratio of acetic acid is calculated as the ratio of the added acetic acid mass to the mass of NMC 622 powder used. The slurry pH values of slurries processed with aqueous binder were measured 10 min after completion, as the pH value of cathode slurries stabilizes after 0.1 h of immersion in water [185]. Figure 5-36 exhibits that the pH value of NMC 622 slurries without acid addition reached 12.1 after the mixing process, which is similar to already published results [27, 29]. The increase of the slurry pH value is due to the Li^+ / H^+ exchange mechanism between layered oxide electrode materials and water, which leads to the formation of LiOH and other products such as $LiHCO_3$ and Li_2CO_3 [180]. In addition, the slurry pH value declined linearly with the amount of added acetic acid. Thus, by controlling the amount of acetic acid it is feasible to obtain NMC 622 slurry with a defined pH value.

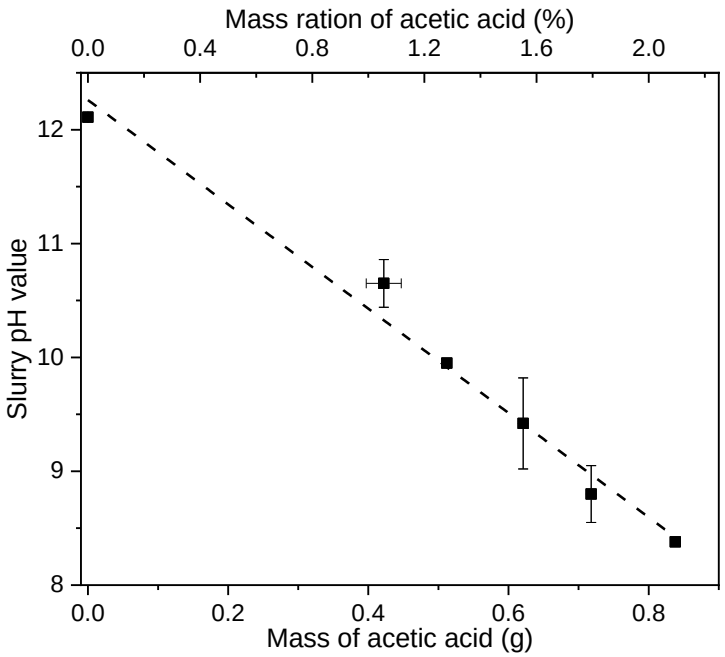

Figure 5-36. Slurry pH value as a function of the mass of added acetic acid and the mass ratio of added acetic acid to the used NMC 622 powder.

Figure 5-37-a displays the viscosities of slurries with different pH values measured at shear rates from 0 to 100 s^{-1}. The slurries with different pH values exhibited similar shear thinning behavior as the slurry with PVDF binder (Figure 5-7). This shear thinning behavior is a typical rheological behavior of Na-CMC binder, which is often used as a thickening agent in suspension due to its long-chain molecular and network structures [336]. The long-chain molecules tend to align themselves in the direction of flow as the shear stress increases, resulting in a decrease in shear resistance and viscosity [337]. With increasing slurry pH value, a distinct decrease in slurry viscosity was observed, suggesting that a higher shear force is needed to break the agglomerates in slurries with lower pH values. Figure 5-37-b shows the viscosity of slurries at a reference shear rate of 50 s^{-1} as a function of slurry pH values. An approximately linear correlation between viscosity and slurry pH value is obtained. In addition, it is observed that with an increasing amount of added acetic acid, the slurry pH value decreased from 12 to 8, while the viscosity increased from 2 to 9 Pa·s at the shear rate of 50 s^{-1}. Nevertheless, the trend of slurry viscosity at different pH values in this work is not consistent with the viscosity of NMC 111 slurries reported by Bauer et al. [29], where the viscosity remained constant at around 4 Pa·s over a pH range of 8 to 11. However, the viscosity rise with decreasing pH value from 12 to 8 is consistent with the study on the viscosity of Na-CMC solution under different pH values from Lee at al. [338]. The chemical groups and the resulting topography of Na-CMC can be modified by slurry pH value changes. Thus, the variation of slurry pH value affects the protonation of the derivative sites on the Na-CMC, which in turn impacts the molecular conformation [339]. For pH values around 7, the dissociation of Na-CMC produces negatively charged polymer chains, the mutual repulsion among carboxylate ions (–COO–) results in an expansion of the network chains to form a hydrogel [340] and thus leads to a high viscosity. When the pH value raises to the alkaline region, Na-ions are dissolved from Na-CMC into water. The amount of dissolved Na-ions increases with

increasing pH value, inhibits the extension of the tangled molecular chains in the hydrogel, leading to a decrease in viscosity [340].

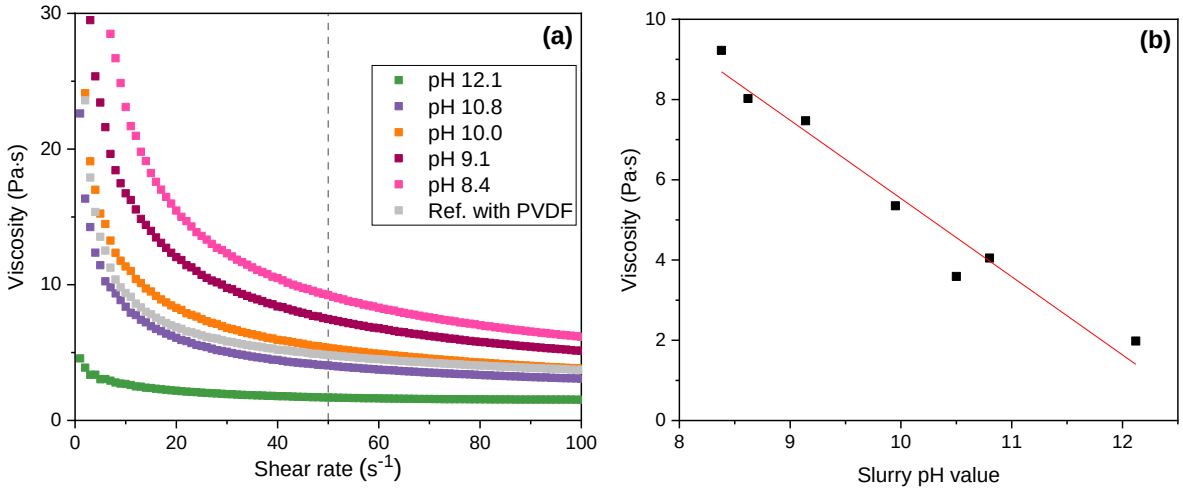

Figure 5-37. Viscosity of slurries with different pH values as a function of (**a**) shear rate and (**b**) slurry pH value at the reference shear rate of 50 s^{-1} [206].

The rheological property of the slurry has a significant influence on the cathode fabrication processes, e.g., mixing and coating. High viscosity can limit the sedimentation of active material particles, convection of conductive additives, and binder migration [167]. Therefore, slurry with high viscosity is of great importance for the coating process, especially for the preparation of thick-film electrodes. Typically, high viscosity can be achieved by reducing the solvent content or increasing the binder content in the slurry. In the present work, it is observed that the acid addition not only adjusts the slurry pH value but also increases the slurry viscosity, which in turn facilitates the preparation of thick-film NMC 622 electrodes.

Slurries with different pH values were tape cast onto Al-foil with 20 µm thickness and subsequently dried in ambient air. The details of the electrode characteristics are summarized in Table 5-17. Since the porosity of different electrodes varies greatly, the highly porous electrodes processed with a slurry pH value above 10 were calendered by reducing their film thicknesses by 10 – 20 %, while other cathodes were calendered to 35 % porosity. The electrode density refers to the density of composite electrodes after the calendering process. The NMC 622 thick-film electrodes were produced with a mass loading of 37 to 48 mg/cm^2, while the thin-film electrodes were produced with a mass loading of approximately 11 mg/cm^2 to represent the state-of-the-art standard.

Table 5-17. Film thickness (before calendering), porosity, mass loading, and areal capacity of NMC 622 electrodes processed with different slurry pH values.

Slurry pH Value	Film thickness without Al [µm]	Initial porosity [%]	Electrode density [g/cm^3]	Mass Loading [mg/cm^2]	Areal capacity [mAh/cm^2]
12.1	247 ± 12	57.5 ± 0.2	1.49 ± 0.08	36.9 ± 0.2	6.13 ± 0.03
10.8	185 ± 10	36.6 ± 0.2	2.17 ± 0.12	40.1 ± 0.1	6.66 ± 0.02
10.0	180 ± 14	35.6 ± 0.3	2.64 ± 0.21	47.5 ± 0.1	7.89 ± 0.02
9.0	185 ± 9	35.1 ± 0.4	2.40 ± 0.13	44.4 ± 0.3	7.26 ± 0.05
8.6	186 ± 6	35.5 ± 0.4	2.33 ± 0.09	43.4 ± 0.2	7.21 ± 0.03
8.4	191 ± 3	31.7 ± 0.5	2.48 ± 0.05	47.3 ± 0.3	7.86 ± 0.05
12.0	110 ± 3	68.1 ± 0.2	1.25 ± 0.04	13.7 ± 0.1	2.28 ± 0.02
10.7	61 ± 2	57.7 ± 0.2	1.69 ± 0.09	10.3 ± 0.2	1.71 ± 0.03
9.2	51 ± 2	38.8 ± 0.4	2.22 ± 0.11	11.3 ± 0.1	1.88 ± 0.02
7.4	56 ± 2	40.7 ± 0.5	2.32 ± 0.14	13.0 ± 0.3	2.16 ± 0.05

Interestingly, it is found that without acid addition, the cathodes had a high porosity of about 60 % and a low electrode density of 1.2 – 1.5 g/cm^3. Therefore, although the thick-film cathodes produced with a slurry pH value of 12.1 had a film thickness approximately 60 µm greater than those produced with a slurry pH value of 10.8 film, their mass loadings were reduced by a value of 3 mg/cm^2. Similar results were also observed in thin-film NMC 622 electrodes, where electrodes without acid addition had the lowest electrode density of 1.25 mg/cm^3 in contrast to other electrodes with acid addition. Therefore, the electrode density increased with decreasing slurry pH value, while the initial porosity decreased with decreasing slurry pH value.

Figure 5-38 displays the cross-sectional images of electrodes processed with different slurry pH values. When exposed to alkaline slurries, the natural oxide layer on the Al current collector undergoes local breakdown, leading to corrosion of the Al substrate and H_2 gas formation [28, 341, 342]. In the absence of acid addition, the generation of H_2 along the interface between the Al foil and the slurry resulted in a high porosity of above 57 % in dried electrodes (Table 5-17) and cavities having diameters greater than 100 µm in the interior of the electrodes after drying process, as shown in Figure 5-38-a and -b. These cavities were spread throughout the whole electrode film, leaving open pits on the electrode surface with diameters ranging from 25 to 105 µm. As the slurry pH value decreased to 10.8, the size of cavities was reduced, as shown in Figure 5-38-c. Meanwhile, the number of cavities was decreased. For example, Figure 5-38-d shows a segment of the cathode processed with a slurry pH value of 10.8 without obvious cavities. With further decrease of slurry pH values to 10.0 and 9.0, the dried electrodes became homogenous and no cavities were detected, as shown in Figure 5-38-e and -f.

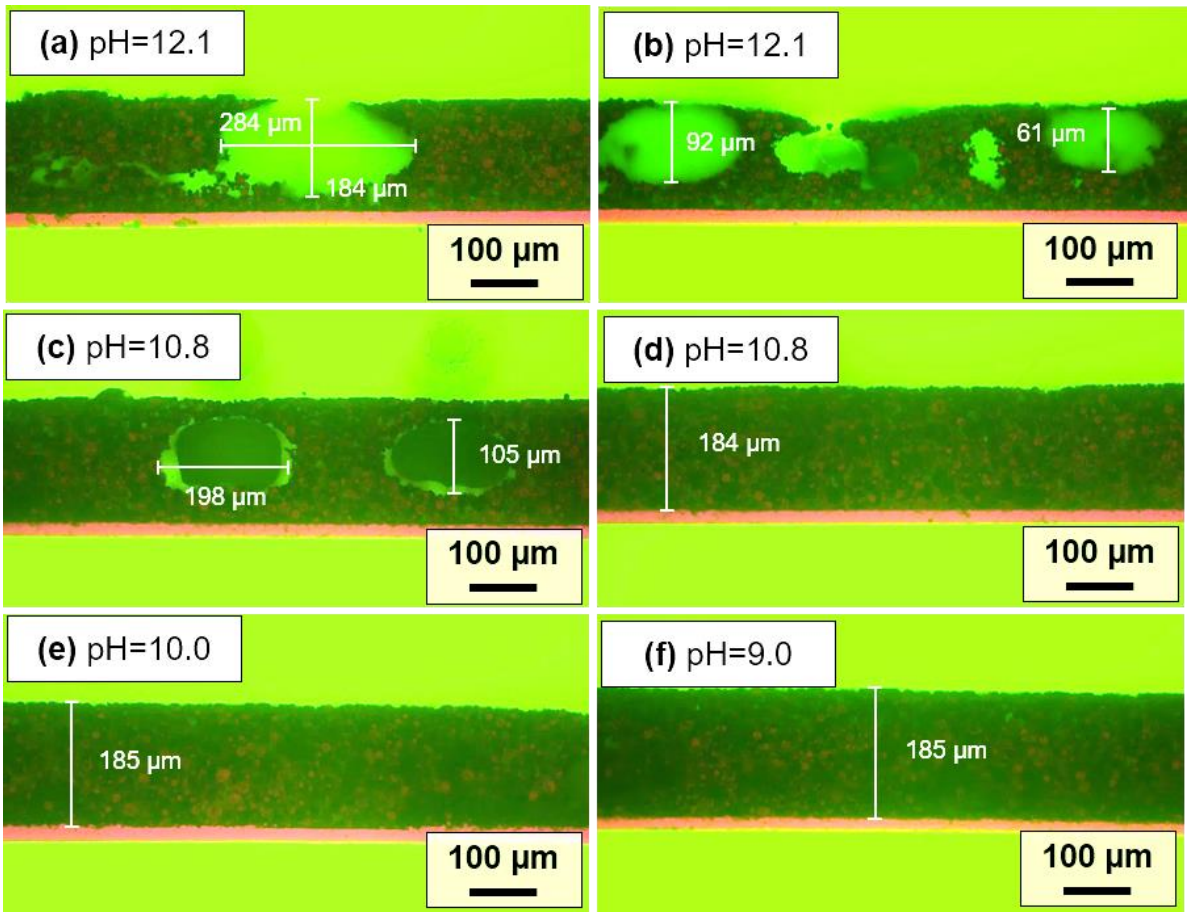

Figure 5-38. Cross-sectional views of uncalendered thick-film NMC 622 cathodes processed with different slurry pH values: (**a**) and (**b**) pH = 12.1; (**c**) and (**d**) pH = 10.8; (**e**) pH = 10.0 and (**f**) pH = 9.0 [206].

The size and number of cavities in the electrode are assumed to depend not only on the slurry pH value but also on the wet film thickness, i.e., the doctor blade gap, and the drying temperature. In this work, all aqueous processed electrodes were dried at room temperature of 20 °C, i.e., the influence of temperature was neglected. An inhomogeneous surface morphology with different layer thickness was observed in aqueous processed thick-film electrodes (Figure 5-39-a to -c). The dark regions marked with red polygons are craters caused by the inward collapse of the electrode materials during drying. For thick-film cathodes processed with a slurry pH value of 12, craters with diameters ranging from 150 µm to 700 µm were detected. With increasing wet film thickness, the drying time was increased, which led to a longer reaction time between alkaline slurry and Al current collector. This can be verified from the SEM images in Figure 5-39, where the thin-film electrodes showed fewer craters on the electrode surface (resulted by the gas evolution during coating process) compared to the thick-film electrode at the same slurry pH value. For example, for the thin-film electrodes processed with a slurry pH value of 12.0, the craters were 80 – 150 µm in diameter, which is about a quarter of the size of those in thick-film electrodes. After lowering the slurry pH value to 10.8, the craters on the surface became smaller and shallower, with diameters of 190 – 200 µm. In thin-film electrodes with slurry pH values of 10.7, the active material particles were evenly distributed and there were no obvious cavities on the electrode surface.

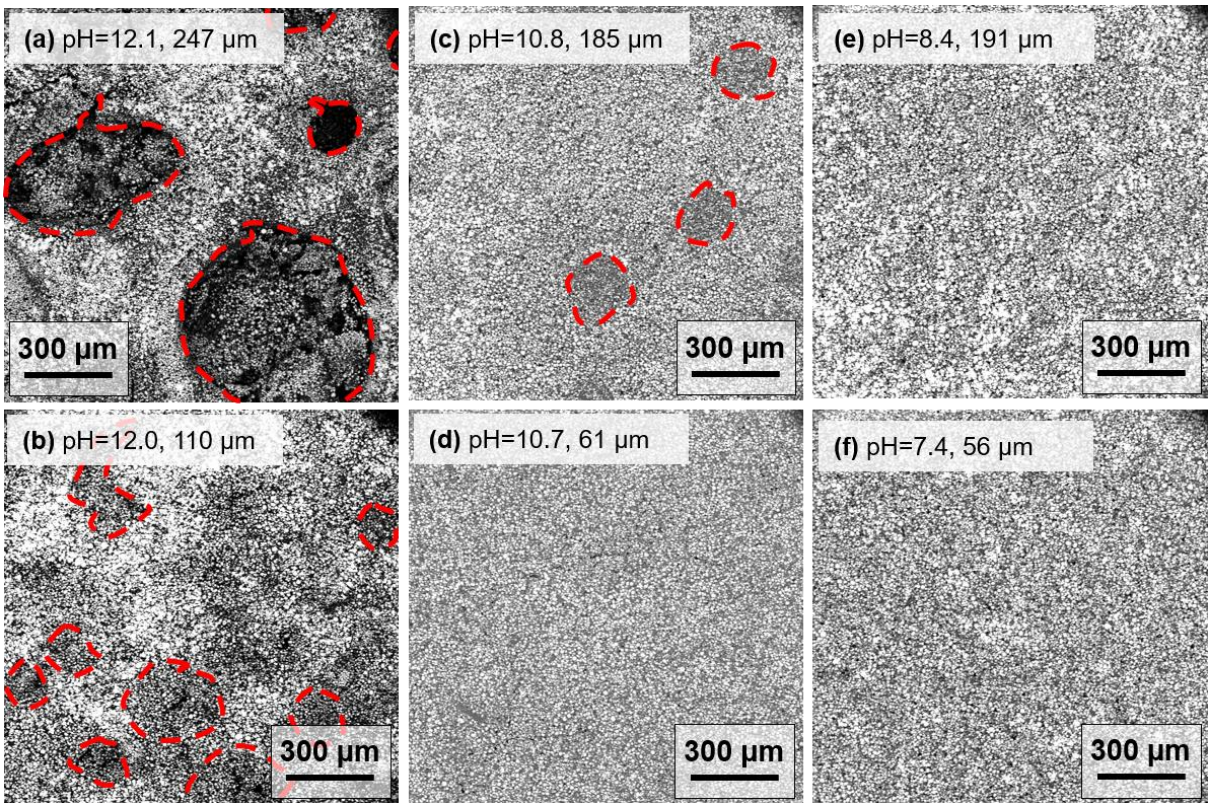

Figure 5-39. SEM images of NMC 622 cathodes processed with different slurry pH values and different film thicknesses: (**a**) pH = 12.1, 240 µm; (**b**) pH = 12.0, 130 µm; (**c**) pH = 10.8, 189 µm; (**d**) pH = 10.7, 82 µm; (**e**) pH = 8.4, 191 µm; (**f**) pH = 7.6, 76 µm. The craters on the electrode surface with different diameters are marked with red dot lines. Figure-a to -d are reproduced from own published results [206].

During the drying process, the surface of the deposited slurry is dried faster due to air convection, while the slurry close to the current collector stay humid for a longer period. The formation of H_2 along the current collector surface continues until the electrode is completely dried. As a result, the hydrogen bubbles are trapped within the film during the drying process, forming craters and pits on the surface as seen in the cross-sectional images in Figure 5-38 and the SEM images of Figure 5-39. Corrosion products such as $Al(OH)_3$ can impede the electric contact between active material, conductive agent with current collector and thus cause unsatisfied electrochemical performance [193]. Besides, high porosity is detrimental to achieving a high volumetric energy density and thus counteracts the benefit of increasing the electrode thickness. In addition, cracking and flaking issues were also observed in the aqueous processed NMC 811 electrodes without pH modification and became more severe with increasing doctor blade gap [44], which is consistent with the results of this work. The corrosion of the Al current collector in thick-film electrodes has a greater impact compared to that in thin-film electrodes, which is due to the longer drying time of thick-film electrodes. Therefore, the slurry pH value adjustment is of great importance for fabricating aqueous-based electrodes. A slurry pH value less than 10 ensures homogeneity of dried electrodes, without the existence of craters or cavities, thus providing better conditions for subsequent laser processing.

According to Sukiman et al. [341], the Al current collector is chemically stable in the pH value range of 4 – 9 due to the existence of a natural alumina passivation layer. In order to study the impact of slurry pH value on Al foil, the cathodes were soaked in deionized water and subsequently dissolved using an ultrasonic cleaner device (Elmasonic X-tra 50H, Elma

Schmidbauer, Germany). Afterwards, the Al foils were dried and subsequently characterized by SEM (Figure 5-40). Corrosion induced pitting was observed on the surface of the Al current collector, corresponding to the craters found in the composite cathodes. For the thick-film electrode with a slurry pH value of 12.1 and a thickness of 247 µm, the most severe corrosion effect was observed on the Al foil, leaving surface corrosion craters with diameters ranging from 8 to 15 µm. More pitting was formed around the deep surface corrosion. With decreasing slurry pH values or reducing wet film thickness, the corrosion and pitting were alleviated. For example, an Al foil of cathode film processed with slurry pH value of 12.0 and 110 µm film thickness had similar amount of corrosion in comparison to those with slurry pH value of 10.8 and 185 µm film thickness. As for cathodes processed with slurry pH value of 10.7 and 61 µm electrode thickness, the surface corrosion was hardly to be found. However, there were still some residual active material particles on the surface. When the slurry pH value was decreased to 8.4 and 8.0, no corrosion traces were visible on the Al surface.

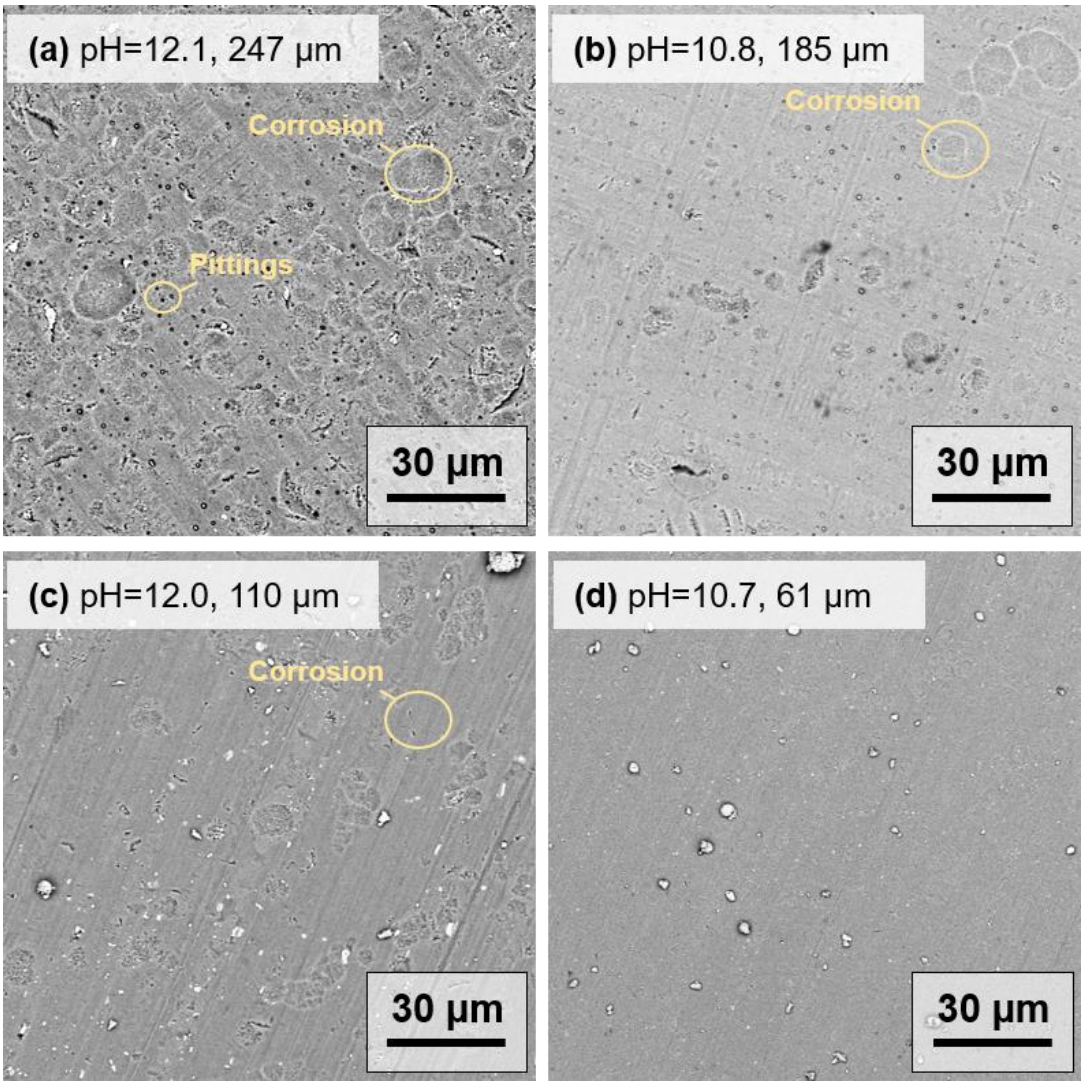

Figure 5-40. SEM images of Al foils after removal of the dried NMC 622 coating with (**a**) slurry pH value of 12.1 and 247 µm electrode thickness; (**b**) slurry pH value of 10.8 and 185 µm electrode thickness; (**c**) slurry pH value of 12.0 and 110 µm electrode thickness; and (**d**) slurry pH value of 10.7 and 61 µm electrode thickness.

5.4.2. Impact of slurry pH value on cell performance

As discussed in the previous chapter, aqueous processed electrodes are significantly affected by the slurry pH value. An increase in slurry pH value leads to the formation of large cavities within the electrodes, which in turn has an impact on tortuosity, mechanical stability and areal capacity. In this chapter, the electrochemical performance of half-cells containing thick-film and thin-film NMC 622 cathodes processed with different slurry pH values is presented, including CV analyses, rate capability analyses, and lifetime analyses. The average porosity of the thick-film NMC 622 cathodes was adjusted to 35 %, while a reduction of 10 – 15 % in the thicknesses of thin-film cathodes were applied.

CV analyses

The current peaks in CV correspond to redox reactions and can be assigned to different phase transitions of NMC 622 (see Figure 3-4). The recorded current signals in Figure 5-41-a during charging and discharging formed a closed loop with hysteresis. For each sample, the measured three cycles for each cell overlapped with each other, which proves good cycle stability of the cells containing aqueous processed NMC 622 electrodes. During each charging and discharging cycle, only one current peak was detected, which is similar to the results of cells containing NMC 622 with PVDF as binder (Figure 5-23). This indicates that no additional redox reaction exists in cells containing aqueous processed NMC 622 cathodes with different slurry pH values besides the well-known redox reactions of Ni^{2+} / Ni^{3+} / Ni^{4+} on the cathode side. During charging process, the peak maximum shifted from 3.80 V to 3.86 V with decreasing slurry pH value from 12.0 to 10.8, respectively. However, when the slurry pH value decreased further below 10.8, the corresponding peak remained at a voltage of 3.87 V. In discharging process, the maximum peak shifted from 3.70 V to 3.66 V voltage with decreasing slurry pH value to 10.8, while the voltages of the peak maximum remained unchanged at 3.64 V for cells with electrodes prepared with slurry pH values from 9.2 to 7.4.

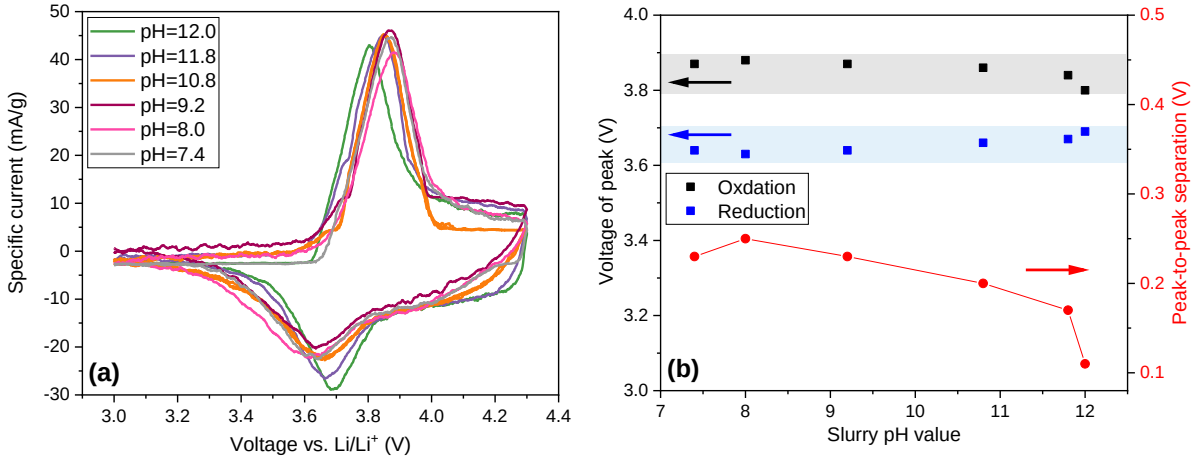

Figure 5-41. CV plots of (**a**) the cells containing NMC 622 cathodes processed with different slurry pH values, and (**b**) the corresponding voltage of oxidation and reduction peaks as well as the peak-to-peak separation of different cells [206].

Figure 5-41-b summarize the voltage of each redox peak as function of pH value and the corresponding voltage difference of the redox couple (ΔE_p) extracted from CV analyses. As

the slurry pH value decreased, the oxidation and reduction peaks shifted to higher and lower potential, resulting in an increase in peak-to-peak separation of the redox couples. The rise in ΔE_p indicates an increased cell polarization and therefore a sluggish electrochemical reaction [294]. Besides, according to equation (3.17), the decrease in ΔE_p with increasing slurry pH value indicates that the reaction rate of Li-ion intercalation in cells containing electrodes processed with higher slurry pH value is higher than those processed with lower slurry pH values. This occurs mainly as a result of the less porous structure in the electrode. Due to the increased size and number of cavities within the electrodes processed with higher slurry pH values, the contact area between the electrode and the electrolyte is enlarged and the Li-ion diffusion kinetics from the liquid electrolyte to the bulk electrode is therefore enhanced compared to the electrodes with lower porosity.

Rate capability analyses

The specific discharge capacity of cells with aqueous processed thick-film NMC 622 electrodes is shown in Figure 5-42-a. At the C/20 formation step, the specific capacities of all cells with thick-film electrodes were slightly increased. For example, for cells containing electrodes produced from slurries having pH values of 10.0 and 9.0, the specific capacity increased from 153 to 158 mAh/g after formation, while cells containing cathodes produced with slurry pH values of 8.6 and 8.4 exhibited a capacity increase from 146 to 156 mAh/g at C/20. This phenomenon was also observed in half-cells with NMC 622 electrodes [200] and pouch cells with NMC 811 cathodes vs. graphite anodes [202]. Since the Li^+ / H^+ cation exchange only takes place on the edges of the NMC 622 active material, a part of the H^+ in the surface of NMC 622 particles can be swapped with Li^+ in electrolyte upon cycling. This may explain that the discharge capacity increase during formation in the cells with aqueous based cathodes was more profound than that in the cells containing electrodes with PVDF as binder. The highest specific capacity of 147 mAh/g was achieved for cells containing electrodes produced with a slurry pH value of 9.0 at C/10, while ones having the electrodes produced with a slurry pH value of 8.4 showed the lowest specific capacity of 137 mAh/g. As the C-rate rose to C/5 and C/2, cells containing electrodes produced with a slurry pH value of 12.1 held the highest capacity of 130 mAh/g and 100 mAh/g at C/5 and C/2, respectively, while the lowest specific capacities (90 mAh/g at C/5 and 37 mAh/g at C/2) belonged to the ones containing electrodes produced with a slurry pH value of 8.4. At 1C and 2C, all cells with thick-film electrodes suffered more than 80 % capacity drop with regard to the initial capacity, except those containing electrodes that were prepared without acid addition (slurry pH value 12.1), who maintained the highest capacity of 57 mAh/g at 1C and 12 mAh/g at 2C. At discharge rates of 3C and 5C, all cells with thick-film electrodes hardly exhibited any specific capacity.

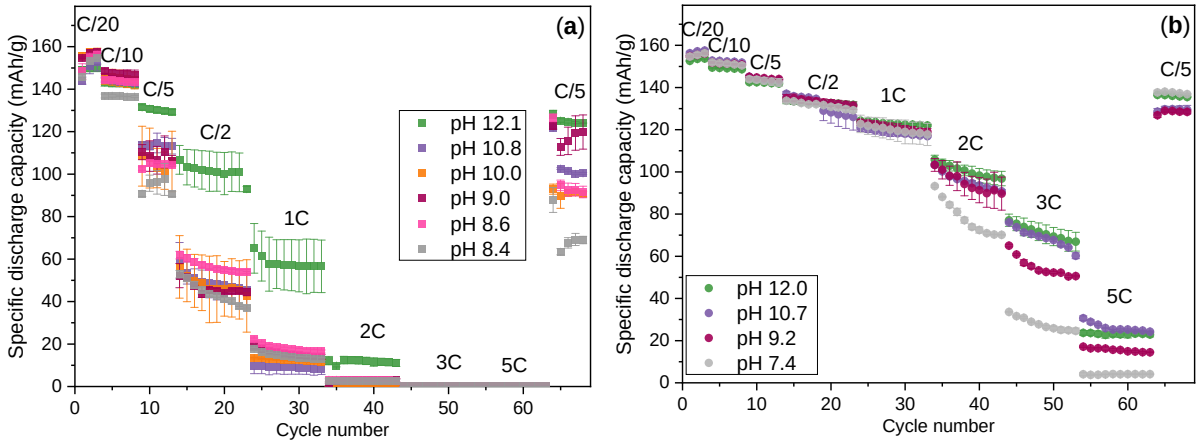

Figure 5-42. Specific discharge capacity of half-cells containing aqueous processed (**a**) thick-film and (**b**) thin-film NMC 622 electrodes prepared with different slurry pH values.

Figure 5-42-b depicts the specific capacities of cells containing thin-film NMC 622 electrodes processed with slurry pH values ranging from 12.0 to 7.4. Cells with thin-film electrodes exhibited higher discharge capacity than those containing thick-film electrodes produced with the same slurry pH value, especially at discharge rates above C/2. This result is similar to the rate capability analyses of cells containing NMC 622 cathodes with PVDF binder and with different thicknesses (Figure 5-9). After the C/20 formation step, all cells achieved similar specific capacities of 154 – 157 mAh/g, which are similar to those obtained with thick-film electrodes. With increasing C-rate, the specific capacity of all cells showed successive deterioration. From C/10 up to 1C, cells with thin-film electrodes showed similar discharge capacities: 151 mAh/g at C/10, 143 mAh/g at C/5, 132 mAh/g at C/2, and about 120 mAh/g at 1C. In this C-rate range, electrodes produced with different slurry pH values showed no significant difference in capacity. However, from 2C to 5C, the discharge capacity of cells containing thin-film electrodes decreased with increasing cycle number, especially for cells containing electrodes produced with a slurry pH value of 7.4. In addition, cells with NMC 622 electrodes processed with a slurry pH value of 7.4 exhibited the lowest discharge capacity in contrast to other cells at 2C to 5C. The drop in capacity at elevated C-rates for cells containing thin-film electrodes processed with low slurry pH values was also detected for cells with thick-film electrodes. The initial coulombic efficiencies of cells containing NMC 622 cathodes processed at different slurry pH values and thicknesses are listed in Table 5-18. For the cells with thick-film electrodes, the initial CE was around 85 % for all cells, except the ones containing electrodes processed with a slurry pH value of 8.4, which had a lower CE of 81.9 % at the first C/20 cycle. In comparison to cells containing NMC 622 electrodes with PVDF binder, shown in Table 5-5, all cells with aqueous processed NMC 622 electrodes showed about 1 % – 3 % lower initial CE. This indicates an increased electrolyte consumption to form the CEI during the first charging / discharging process [202]. As for cells with thin-film electrodes, the initial CE was similar for cells whose electrodes were processed with slurry pH value of 12.0 and 10.7 in comparison to those with thick-film electrodes and similar pH values. However, the initial CE of cells with thin-film electrodes was slightly increased from 85 % to 87 % with decreasing slurry pH value.

Table 5-18. The coulombic efficiency of the first cycle at C/20 and the capacity retention (C/5) of half-cells containing NMC 622 cathodes processed aqueously at different slurry pH values and for different thicknesses.

Electrode type	Initial coulombic efficiency [%]	Capacity retention [%]
pH 12.1, thick	85.2 ± 0.2	96.1 ± 1.9
pH 10.8, thick	85.6 ± 1.2	89.1 ± 1.5
pH 10.0, thick	86.7 ± 0.1	86.6 ± 3.5
pH 9.0, thick	84.8 ± 4.6	86.7 ± 4.4
pH 8.6, thick	85.4 ± 1.5	89.1 ± 2.1
pH 8.4, thick	81.9 ± 4.4	71.5 ± 5.2
pH 12.0, thin	85.3 ± 2.1	95.6 ± 0.5
pH 10.7, thin	85.7 ± 0.3	89.9 ± 0.7
pH 9.2, thin	87.1 ± 1.1	88.8 ± 0.9
pH 7.4, thin	87.2 ± 1.2	96.0 ± 0.7

In order to measure the capacity retention of the electrodes after cycling at high discharge rates up to 5C, the C-rate was reduced to C/5 after the last 5C cycles. All cells showed less specific capacity compared to the previous C/5 cycles. Cells containing cathodes which were processed without acid addition provided the highest specific capacity of 125 mAh/g with a capacity retention of 96 %, while the ones containing thick-film electrodes processed at a slurry pH value of 8.4 exhibited the lowest capacity retention of 72 %. The capacity retention decreased slightly with decreasing slurry pH value for cells with thick-film electrodes, while no significant difference was observed for cells containing thin-film electrodes processed with slurry pH values from 10.7 to 9.2. However, the capacity retention of cells containing electrodes processed with a slurry pH of 7.4 increased to 96 %, which was almost the same as that of the ones containing electrodes without acid addition. This trend is different from that observed in cells with thick-film electrodes, suggesting that the film thickness has an impact on capacity retention. Furthermore, studies on pH modification with different types of acids indicated that the electrochemical performance of cell with aqueous processed cathode deteriorated when the slurry pH value is lower than 9 [29, 230], which is similar to the results obtained here. The increase in capacity at high C-rates of cells containing thick-film electrodes processed without acid addition may be directly related to their high porosity. Since the porosity of these electrodes is much higher than that of other electrodes processed at lower slurry pH values. The pores and cavities within the electrodes could serve as electrolyte reservoirs, while mitigating the impact of volume changes of the NMC 622 particles during charging and discharging. However, the distribution and the size of cavities and pores is random and uncontrollable, which can lead to mechanical instability and uneven current density distribution in the electrodes, resulting in more severe ageing effect and cell breakdown.

Figure 5-43 gives an overview of the specific discharge capacity vs. C-rate for cells containing thick-film and thin-film electrodes prepared using different slurry pH values. The capacity of the cells with aqueous processed electrodes decreased by about 10 mAh/g compared to the cells with NMP-based electrodes as shown in Figure 5-9, which could be attributed to the loss of Li-ions and dissolution of transition metal-ions from the outer surface of NMC 622 particles during aqueous processing [185]. Li-ions close to the surface of NMC particles react with water during slurry mixing, forming LiOH that dissolves in the electrolyte,

which leads to a delithiated outer layer [43]. Inductively coupled plasma atomic emission spectroscopy (ICP-AES) analyses in previous researches revealed that NMC 532 and NMC 111 showed a similar dissolution trend of Li >> Ni > Co > Mn near the particle surface of NMC after immersion in water [43, 194]. A reorganization of the outer layer where cation mixing (Ni^{2+} replacing the Li sites) is most likely due to their similar ionic radii [43], while Shkrob et al. [180] suggested that the a cation exchange process with protons intercalating into NMC could take place for the charge compensation.

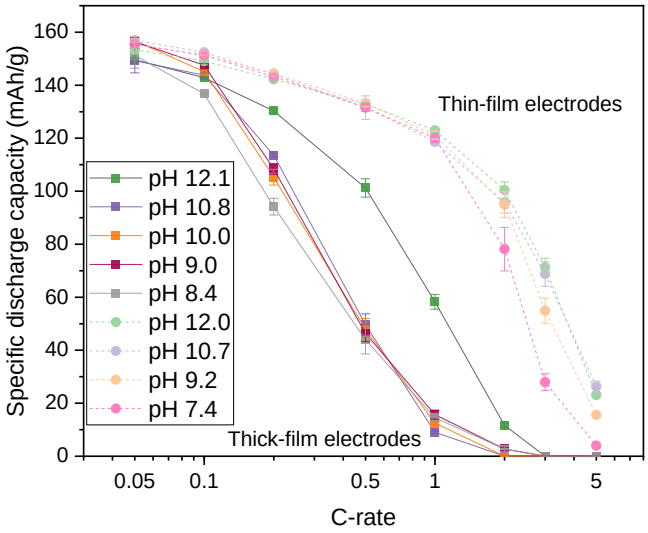

Figure 5-43. Average discharge capacity as a function of C-rate for half-cells containing thin-film and thick-film electrodes processed at different slurry pH values ranging from 12.1 to 7.4 [206].

In addition, the specific discharge capacity is found to be strongly related to the electrode thickness and applied discharge rate. Cells with thick-film electrodes suffered severe capacity fade with increasing discharge current, losing over 60 % of the capacity at C/2 compared to the initial capacity at C/20. Although cells with non-acid treated electrodes showed the highest discharge capacity at C-rates above C/10, the extremely high porosity of around 60 % hinders the possibility of achieving high volumetric energy densities. Additionally, the adhesion strength of cathode materials to the current collector is reduced with increasing porosity. Not to mention the shedding of the electrode materials during handling, which makes post-processing of the electrodes more difficult, such as calendaring, winding, laser structuring, cutting, and packaging. In addition, the cells containing thick-film electrodes produced at a slurry pH value of 8.4 and thin-film electrodes produced at a slurry pH value of 7.4 showed the lowest discharge capacity above C/10 and 2C, respectively. This suggests that excessive amount of acid deteriorates the electrochemical performance of the cells at high C-rates regardless of the mass loading, leading to a reduced discharge capacity. Similar results were reported for half-cells having NMC 111 cathodes processed with different slurry values varying from 7 to 11, where the cells containing cathodes processed at slurry pH 7 exhibited 10 – 20 mAh/g lower discharge capacity at 1C to 3C compared to those processed at slurry pH values of 8 – 11 [29]. Furthermore, Ibing et al. [199] compared the cells containing NMC 532 cathodes processed at slurry pH values of 12.5 and 7.6 with reference cells with PVDF binder. They found that the cells processed with a slurry pH value of 7.6 exhibited severe capacity fade during lifetime analyses, losing over 40 mAh/g discharge capacity after 500 cycles, while

the cells with other two types of cathodes lost about 20 mAh/g capacity. This can be explained that as the slurry pH value decreases from 12 to 7, the high dispersing potential of the acid leads to a reduction in the size and number of carbon black agglomerates, which leads to a decrease in the electronic conductivity of the electrodes, causing a decrease in discharge capacity [29]. Therefore, the pH of the NMC 622 slurry should be adjusted to 9 – 10, taking into account a suitable balance between rate capability, mechanical stability of electrode, pore distribution and size, and current collector corrosion.

Figure 5-44 depicts the discharge profiles of cells with different electrode types at selected C-rates of C/5, 1C, 3C, and the last C/5 to discuss the impact of slurry pH value and film thickness on the electrochemical performance. At initial C/5, the discharge capacities of cells with thin-film electrodes showed no substantial difference, whereas ones with thick-film electrodes showed a difference of 40 mAh/g between electrodes processed at different slurry pH values. With decreasing pH value, the Li insertion along the voltage plateau is shortened. From 1C to 3C, the discharge capacities of cells containing thick-film electrodes dropped sharply from less than 50 mAh/g to 0 mAh/g, while the discharge capacities of cells with thin-film electrodes reduced by 20 mAh/g for each step. A sudden voltage drop (IR-drop) could be observed at the beginning of the respective discharge curves. At 1C, the IR-drop of cell with thin-film electrode processed at a slurry pH value of 7.4 was higher (from 4.20 V to 3.87 V, 146 Ω) in comparison to cells containing electrodes with slurry pH values of 12.0 and 10.7 (from 4.20 V to 3.99 V, 92 Ω), which indicates a 59 % higher ohmic resistance for the cell containing thick-film electrodes produced at lower slurry pH values.

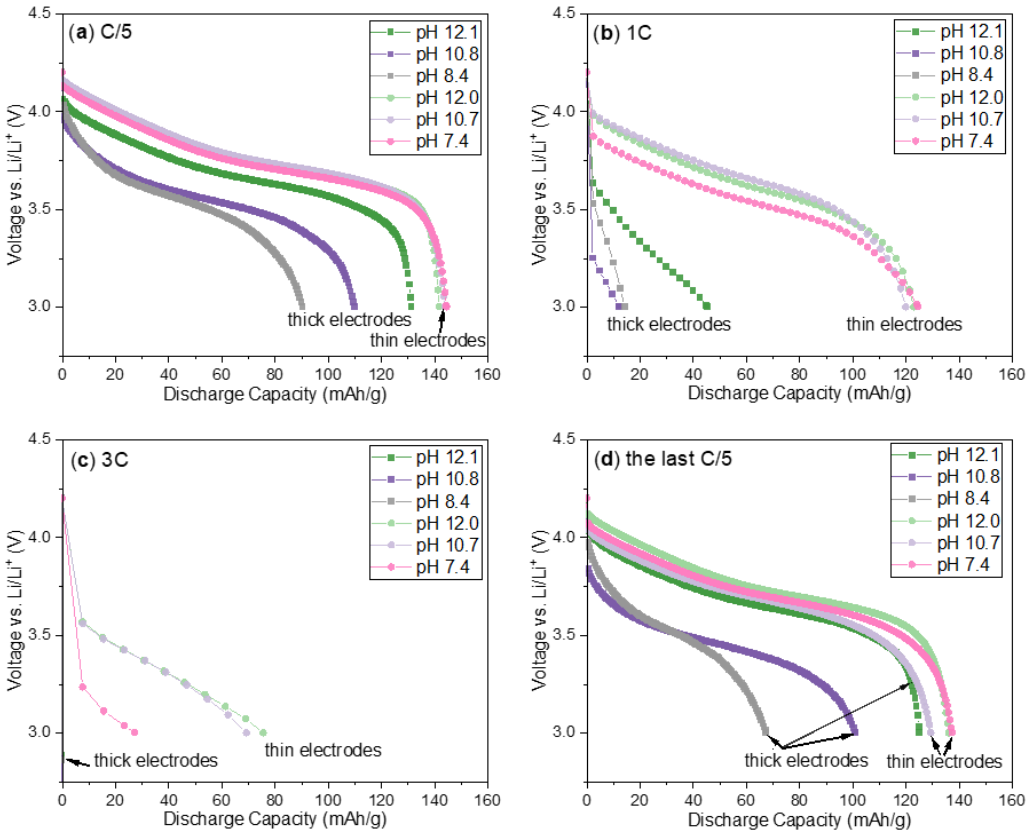

Figure 5-44. Comparison of the specific discharge capacity vs. voltage (vs. Li / Li^+) of half-cells containing thin-film and thick-film cathodes prepared at slurry pH values of 12, 11, and 8 from rate capability shown in Figure 5-42 at discharge rates of (**a**) C/5, (**b**) 1C, (**c**) 3C, and (**d**) the last C/5 cycle [206].

The lowering of the discharge curve at a high C-rate is due to cell polarization which is generally caused by ohmic resistance, charge transfer resistance, and Li-ion diffusion overpotential [335]. Electrodes with increasing film thicknesses have in average longer diffusion and migration pathways of Li-ions in liquid electrolyte within the bulk electrode. The NMC 622 particles in the upper region of the electrode are kinetically favored and can intercalate more Li-ions than particle from underlying regions. Finally, a Li-ion concentration gradient along the electrode thickness is built-up leading to an overpotential in the electrode which contributes to additional mass transport losses. Obviously, this effect is more pronounced for thick-film electrodes, which require higher electrical current densities to overcome the mass transport potential. As a result, the increase of cell impedance with increasing electrode thickness has a significant contribution by an increasing diffusion overpotential [343]. However, increasing the film thickness causes also additional ohmic losses, e.g., by an increased charge transfer resistance, which can be directly observed in IR-drop at the initial voltage change in each cycle.

5.4.3. Impact of acid type on the electrode properties

In the previous chapter, the impact of slurry pH value on the electrode coating and electrochemical performance of cells containing NMC 622 cathodes have been investigated and it was found that the slurry pH value should be adjusted to 9 – 10 in order to mitigate the chemical corrosion between alkaline cathode slurry and Al current collector. In this chapter, aqueous processing of NMC 622 cathode is further studied using three different types of acid additives, i.e., acetic acid (AA), citric acid (CA), and phosphoric acid (PA). The reasons for choosing these three acids to adjust the slurry pH value have been illustrated in chapter 2. Meanwhile, the slurry pH values were kept constant at 9 – 10. XPS and Raman spectroscopy were performed to identify possible surface modifications of NMC 622 electrodes processed with different acid additions in comparison to the reference electrodes with PVDF binder.

During the slurry preparation process as described in Figure 4-3, the amount of each component, i.e., NMC 622 powder, conductive agent, and binders, as well as the mixing steps remained identical expect for the type and amount of acid. For the viscosity analyses, two reference shear rates at 12 and 25 s^{-1} were chosen since doctor blade gaps of 200 µm and 500 µm were used for the tape casting of thin-film and thick-film electrodes, respectively, at a constant coating speed of 5 mm/s. NMC 622 slurries with PVDF binder or water-soluble binders (added with different acids) exhibited similar shear-thinning behavior as shown in Figure 5-45. The slurry with CA reached the highest viscosity of 10.8 Pa·s at 12 s^{-1}, while the slurry without acid addition had the lowest viscosity of 2.5 Pa·s. It is worth noting that all slurries with acid addition showed 2 – 4 times higher viscosity in comparison to the reference slurry without acid addition. This means that the addition of acid can not only adjust the slurry pH value to avoid chemical corrosion on the Al foil, but also increases the viscosity, which is advantageous for the coating of thick-film electrodes, since the sedimentation of large NMC 622 particles in the slurry can been reduced.

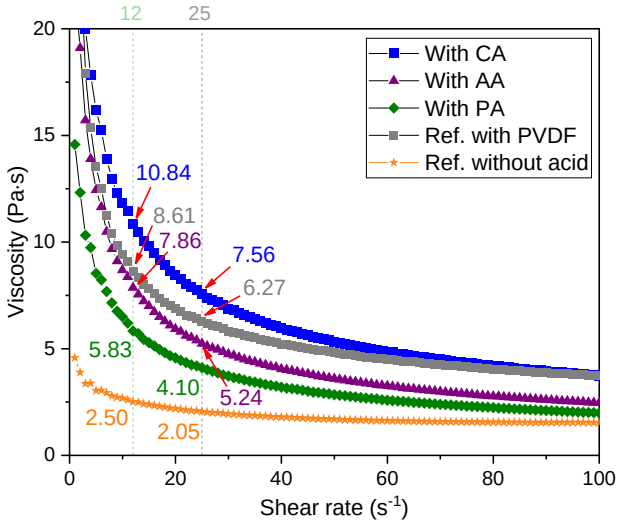

Figure 5-45. The viscosities of the aqueous processed NMC 622 slurries with different acid additions in comparison to the reference slurry without acid addition and NMP-based slurry at shear rates from 0 to 100 s^{-}

The slurries with different acid additions were coated onto the Al foil and subsequently dried at room temperature. Table 5-19 summarizes the amount of acid, the slurry pH value, as well as other details of the various electrodes. The mass loading of NMC 622 cathodes increases from 17 – 19 mg/cm^2 to about 34 – 38 mg/cm^2 with increasing film thickness, which is almost twice higher compared to that of thin-film electrodes. For the calculation of areal capacity, specific capacities of 172 mAh/g and 166 mAh/g were applied for NMP-based and aqueous processed NMC 622 electrodes, respectively. This is due to the hydrolysis of NMC 622 during aqueous mixing process, which results in the exchange of Li-ions from the surface of NMC 622 particles with protons in electrolyte [180]. The Li-leaching effect leads to a lower specific capacity of NMC 622 in aqueous processed electrodes.

Table 5-19. The amount of acid, slurry pH value, film thickness, active mass loading, and areal capacity of NMC 622 electrodes prepared with different types of binders or acid additions.

Electrode type	Acid amount * [wt. %]	Slurry pH value	Film thickness [µm]	Active mass loading [mg/cm^2]	Areal capacity [mAh/cm^2]
Reference with PVDF binder	-	-	74 ± 2	18.8 ± 0.2	3.24 ± 0.04
With CA	2.3	9.3	73 ± 2	17.0 ± 0.1	2.83 ± 0.02
With AA	1.4	9.4	71 ± 2	16.1 ± 0.2	2.68 ± 0.04
With PA	0.9	9.5	73 ± 2	16.9 ± 0.3	2.80 ± 0.09
Reference with PVDF binder	-	-	150 ± 5	36.9 ± 0.9	6.36 ± 0.16
With CA	2.3	9.3	160 ± 6	38.9 ± 1.4	6.46 ± 0.24
With AA	1.4	9.4	149 ± 4	33.9 ± 0.2	5.63 ± 0.03
With PA	0.9	9.5	149 ± 4	35.3 ± 0.3	5.87 ± 0.06

* The acid amount is calculated by dividing the mass of acid by the mass of added NMC 622 powder in the slurry.

Figure 5-46-a displays that the NMC 622 particles were homogenously covered with the mixture of PVDF binder and conductive agent, while the flake-like KS6L graphite particles were distributed between the NMC 622 particles. Due to the high apparent density and compressibility of KS6L graphite, the direct contact area between the NMC 622 particles as

well as the contact between the NMC 622 and conductive agents is increased, resulting in a lower electrical resistivity [38]. The conductive agent Super C65 has a primary particle diameter of less than 50 nm [38, 40], which is beyond the resolution of SEM. However, in Figure 5-46-b and -d, conductive agent clusters on the NMC 622 surface and between NMC 622 particles can be detected. These small particles in the slurry help to unfold the CMC polymer coils during the mixing process, which leads to extended bridging between the particles [29]. In Figure 5-46-c, cracks in some NMC 622 particles are observed from the top view of the as-prepared electrodes with CA addition, which are assumed to be originated from the calendering process.

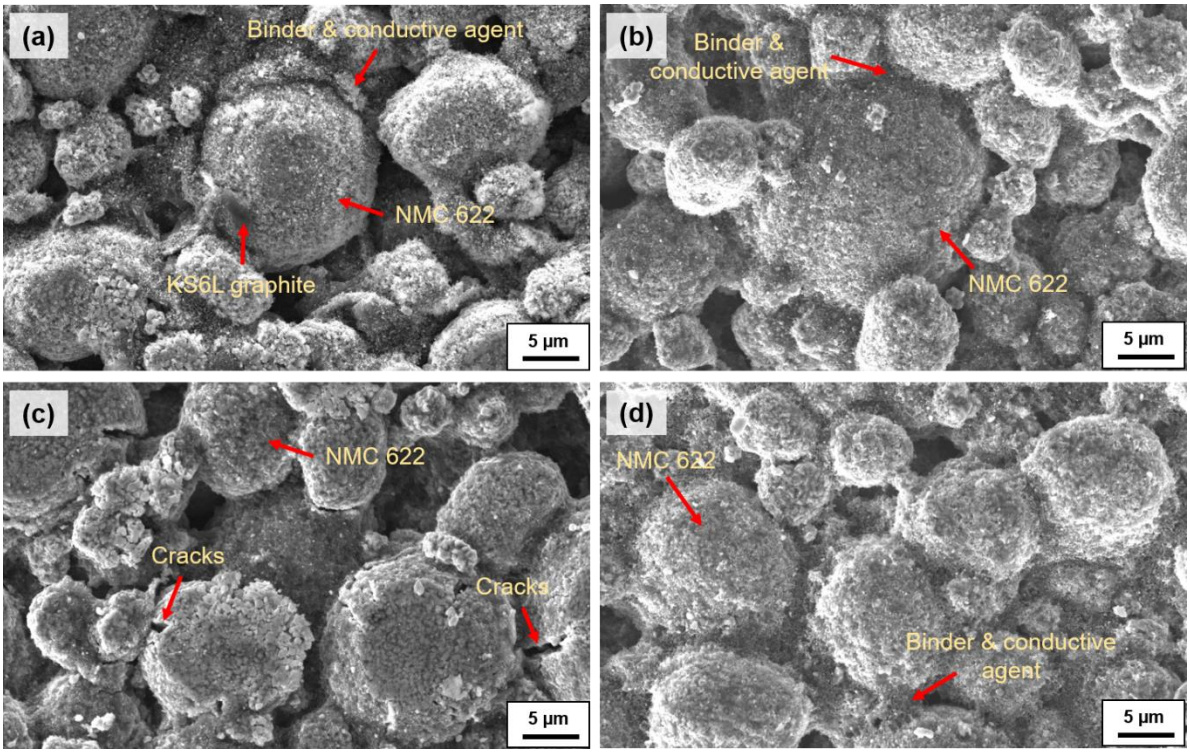

Figure 5-46. SEM images of (**a**) NMP-based NMC 622 cathodes and aqueous processed cathodes with addition of (**b**) citric acid, (**c**) acetic acid, and (**d**) phosphoric acid.

XPS analyses were conducted to characterize the surface chemistry of the dried electrodes prepared with different acid additions during the slurry mixing process as well as the reference electrodes without acid addition and those with PVDF binder. Figure 5-47-a exhibits the C 1s spectra of different NMC 622 electrodes. The peak at a binding energy E_B = 284.4 eV is assigned to the carbon black (conductive agent) in electrodes, while the signal at 285.4 eV corresponds to C-C / C-H bonds; The low intensity peaks at 290.4 eV are attributed to lithium carbonate species formed on the surface of NMC 622 during aqueous processing [344]. Chen et al. [183] reported that Li_2CO_3 and LiOH are formed on the surface of NMC 622 powders when they are stored at room humidity above 80 %. Therefore, it is assumed that the formation of Li_2CO_3 on the surface of the NMC 622 particles would be significant during the aqueous mixing process. Nevertheless, a direct comparison of the Li_2CO_3 amount in aqueous processed electrodes with the reference NMP-based electrode is intractable due to the overlap of the CF_2 peak, which is characteristic for PVDF binder in the reference electrodes, with CO_3^{2-} peak at E_B = 290.4 eV. In addition, CF_2 was detected on the surface of the aqueous processed electrodes, which was proven to be originated from the TRD

202A binder, since 0.2 at.% at 290.7 eV was detected in this dried binder. However, the amount of TRD 202A binder remained constant in all aqueous processed electrodes with different acid additions. Thus, its contribution can be neglected. Since the carbon black amount remained the same in different aqueous processed electrodes, the trend of Li_2CO_3 content in the electrodes with different acid additions can be derived by calculating the atomic ratio between the peak at 290.4 eV and carbon black peak at 284.4 eV. However, there was no significant difference in the amount of Li_2CO_3 in the different acid-containing electrodes compared to the reference electrode without acid addition, and the Li_2CO_3 concentrations detected on the NMC 622 surface in all electrodes were very low (1.0 ± 0.2 at.%). Therefore, it cannot be concluded from the XPS analyses that the acid addition results in a decrease of Li_2CO_3 on the NMC 622 surfaces.

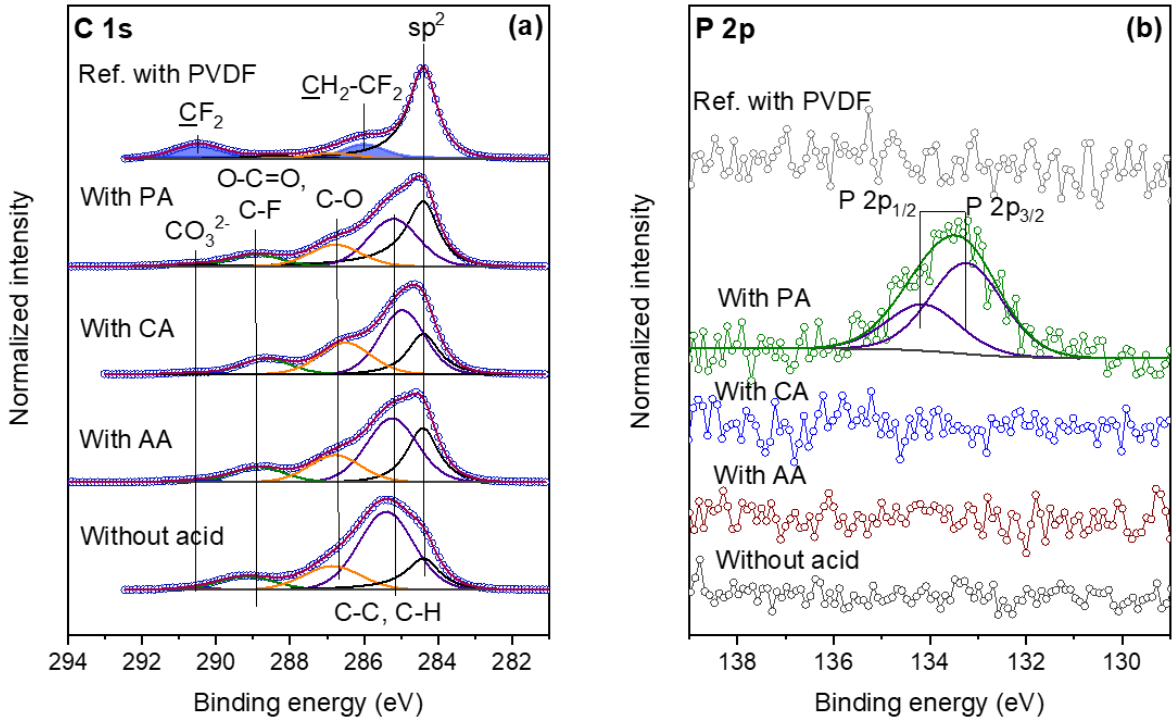

Figure 5-47. XPS spectra of the (**a**) C 1s and (**b**) P 2p lines of electrodes prepared with different binders or with different acid additions during slurry mixing process [305].

Figure 5-47-b displays the P 2p spectra of different types of NMC 622 electrodes. Only the aqueous processed electrode with PA addition showed a peak at the binding energy of 133.3 eV with an atomic percent of about 0.3 %. This may indicate the formation of water-insoluble substances such as Li_3PO_4 [31, 194, 198, 345], or $M_3(PO_4)_2$ (M as transition metal) [346] on the surface of aqueous processed NMC 622 particles. However, from the XPS spectra one cannot conclude whether the phosphates were bound or absorbed to the NMC 622 surface. Thus, more evidence is needed, especially with regard to the impact on the electrochemical performance of cells containing different types of electrodes. Furthermore, Li with 2.4 – 2.7 at.% on the surface of NMC 622 was measured, which is distinctly higher than the corresponding concentration of Ni, Mn, or Co in NMC 622. This might be related to the Li leaching and re-deposition of Li after electrode drying. According to Hamam et al. [186], Li-ions / protons exchange and transition metal-ion dissolution occur in NMC 532 in solutions with

pH values from 7 – 10, and the removal rate is increased when the slurry pH value is below 7. In this work, the slurry pH values were adjusted to 9 – 10. As a result, Li leaching occurs during mixing and the concentration of Li-ions in the water was increased compared to its amount on the surface of NMC 622. However, with the elimination of water after drying, Li-ions dissolved in water might be redeposited on the surface of NMC 622, resulting in an increased Li concentration on the NMC 622 surface.

Stokes Raman scattering was applied to investigate the local structures of NMC 622 in cathodes processed with different acids and the spectrum of pristine NMC 622 powder as well as that of reference electrode with PVDF binder, since Raman spectroscopy is sensitive to the short-range environment of oxygen around the cations in the lattice of an oxide [347]. The Raman active modes of NMC 622 particles were observed in Figure 5-48 between 400 and 650 cm^{-1}, which are associated to the vibrational modes of different transition metal-ions (Ni, Mn, and Co). For the NMC 622 pristine powder as well as the electrodes processed with different acids, two Raman-active modes, A_{1g} at 570 cm^{-1} and E_g at 470 cm^{-1} were detected. These two modes represent the symmetrical movement of oxygen atoms along the *c*-axis (M–O, M = Ni, Co, or Mn), and the opposing displacements of oxygen atoms along adjacent oxygen layers (O–M–O), respectively [348]. The band at higher wavenumber is usually assigned to A_{1g} since it represents the stretching of M–O and is typically stiffer than the bending mode [349]. Besides, the A_{1g} band shifts from 600 cm^{-1} to lower wavenumber as the Ni content in $LiNi_{1-x}Co_xO_2$ increases [350]. In this work, the A_{1g} band of NMC 622 pristine powder was located at around 570 cm^{-1}, which is lower in comparison to other studies exhibiting A_{1g} bands at 609 cm^{-1} and 597 cm^{-1} [348, 349]. The band shift may be resulted from inhomogeneous polycrystalline, crystalline size and orientation, and the wavelength of excitation source [349]. The excitation laser applied in the present work has a wavelength of 532 nm, while the laser wavelength used in their study is 632.8 nm. This may lead to a band shift to a lower wavenumber for A_{1g}.

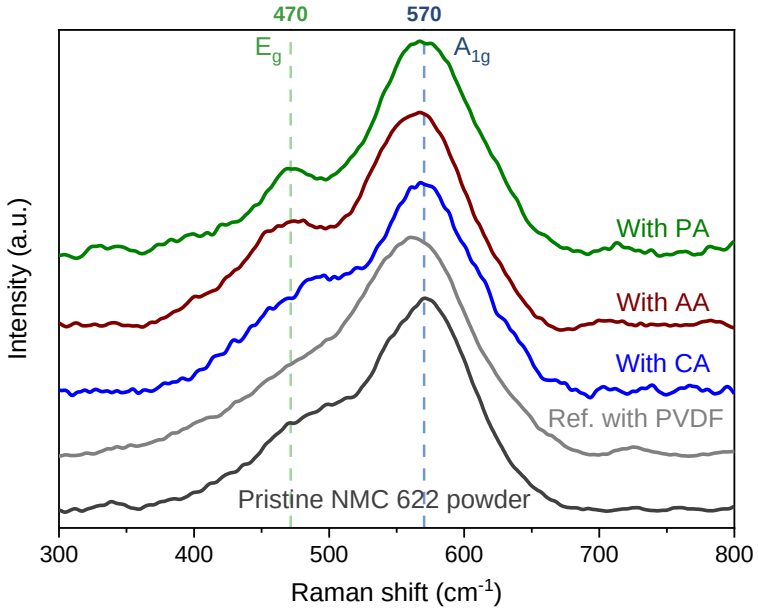

Figure 5-48. Raman spectra of aqueous processed NMC 622 electrodes with addition of citric acid (CA), acetic acid (AA), phosphoric acid (PA) in comparison to reference electrode with PVDF binder and pristine NMC 622 powder [305].

The Raman spectra of NMC 622 electrodes and pristine NMC 622 powder are envelopes consisting of highly overlapping bands of different transition metal-ions, thus it is difficult to assign the band to each vibration mode exactly. However, by comparison with the results of other studies, it is assumed that the bands above 600 cm^{-1} correspond to the E_g and A_{1g} of Mn, while the shoulder band at 465 cm^{-1} can be assigned to the E_g mode of Ni. Between 470 cm^{-1} and 590 cm^{-1}, the bands should in turn belong to the E_g mode of Co, A_{1g} mode of Co, and A_{1g} of Ni with increasing wavenumber. Since the A_{1g} band decreases significantly with increasing Li de- / intercalation [349], and due to the fact that Raman spectroscopy has a detection depth of only a few hundred nanometers, the intensity of A_{1g} / E_g can be utilized to determine the Li leaching from the NMC 622 surface in aqueously processed electrodes [183]. The A_{1g} / E_g ratios for the pristine NMC 622 powder and PVDF-containing reference electrode are 2.4 – 2.5, whereas the ratios for the aqueous processed electrodes containing CA and AA are lower at 2.1 – 2.2, indicating a higher degree of Li leaching during the mixing process with addition of these two acid types. However, the electrode with PA displays an A_{1g} / E_g ratio of 2.5, which is higher in comparison to that for other aqueous processed electrodes. This further supports the assumption that a protective layer was formed on the NMC 622 surface with PA addition, which could attenuate Li leaching during slurry preparation. Thus, the appearance of the new peak at 133.3 eV in P 2p spectra from XPS analyses suggests that the addition of PA results in the formation of a protective layer on the surface of the NMC 622 particles. However, since PA has a melting point of around 40 °C [201] and would be dense and highly crystallized after drying at 130 °C, the existence of residual PA in dried electrodes cannot be excluded. Very recently, Tolchard et al. [201] studied the fast aqueous processing of NMC 622 cathodes (approx. 45 min mixing time) with addition of PA using nuclear resonance spectroscopy (NMR), and proved that a protective phosphate layer on the NMC 622 particles were formed. However, rapid cell failure was still observed in their study within 100 cycles, which might be due to the reaction of acid residues with electrolytes. Furthermore, this effect can be suppressed by electrode washing with ethanol. Thus, electrochemical analyses can help to investigate whether the residual PA may have a detrimental effect on the performance of the cells, which will be discussed in the following chapter.

The adhesion strengths of uncalendered NMC 622 electrodes prepared with different acid additions were measured using the 90°-peel-off setup shown in Figure 4-11. Electrodes with CA and AA addition exhibited similar adhesion strength of about 12 N/m, while electrodes with PA addition had the lowest adhesion strength of 1 N/m. In contrast showed the reference electrodes with PVDF binder significantly higher adhesion strength of 82 N/m, see Figure 5-49. Hawley et al. [351] also reported that the adhesion strength of NCA cathodes with PVDF binder was 4.3 times higher than those aqueous processed NCA electrodes with PAA as binder. An extreme drop in adhesion strength in NMC 111 electrodes processed at slurry pH values below 10 regardless of the type of acid added during the slurry preparation was reported by Bauer et al. [29]. The adhesion between the binder and the current collector could be due to weak Van-der-Waals force, electrostatic force, and acid-based interaction [352]. In aqueous slurries, alumina surfaces are amphoteric with both basic and acidic sites [353], thus base / acid bonds with electron donating or accepting sites of the polymer are formed. The acids used in this work are strong Lewis acids, which can move to the interface and hinder the attraction required

for adhesion. As a result, the adhesion strength is reduced. In addition, CMC and TRD 202A acrylic latex binders are charged polyelectrolytes that can be affected by electrostatic force [29]. Alumina has been reported to have an IEP at a pH value of 9.5 [352], thus, when coated with a slurry having a pH values of around 9.5, the surface of alumina is likely to be electroneutral, which would substantially weaken the adsorption of polymer binder to the Al current collector, resulting in severe decrease in adhesion strength. In addition, the NMC 622 electrodes with PA addition exhibited the lowest adhesion strength compared to other aqueous processed electrodes. This may be due to that during drying process, PA reacts with the oxide layer on the Al current collector, and the reaction with PA is faster than that with CA or AA, occupying more sites where binder can interact. Thus, less binder molecules could be attached to the surface of oxide layer and this caused the loss of adhesion strength.

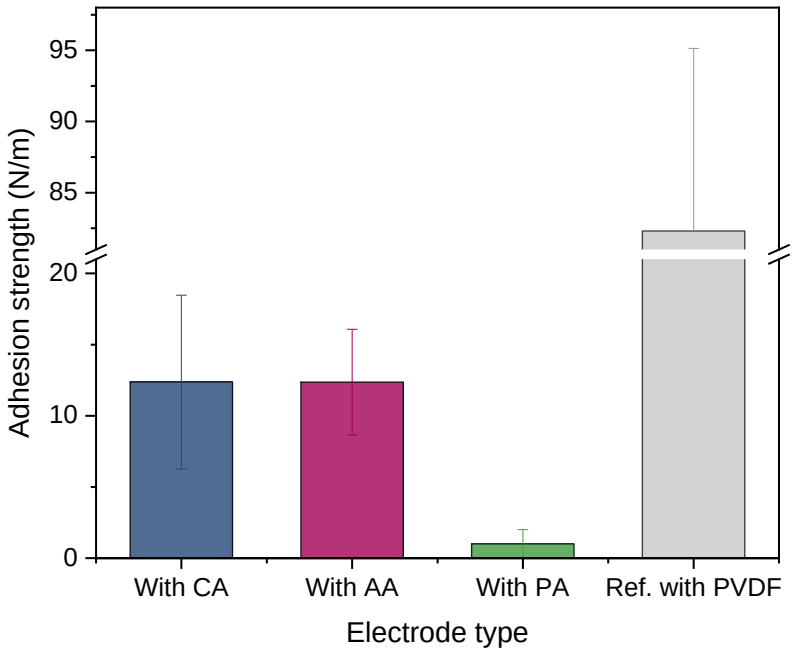

Figure 5-49. Adhesion strength of uncalendered NMC 622 electrodes with different acid additions in contrast to the reference electrode with PVDF binder.

After the peel-off-test, the Al current collectors of uncalendered NMC 622 electrode processed with different acid addition were collected and the peeled side was observed by SEM (Figure 5-50). First of all, no chemical corrosion similar to Figure 5-40-a, c was detected on the Al foil, indicating that at this slurry pH value (9.3 – 9.5), no chemical corrosion between NMC 622 slurry and Al current collector took place. This is consistent with the previous results shown in chapter 5.4.1. Furthermore, residual NMC 622 particles as well as clusters consisting of binder and conductive agent were detached to the Al foil surface of the electrodes processed with CA and AA addition. However, only a small amount of binder and conductive agent were found on the Al foil surface of the electrodes processed with PA, almost no NMC 622 particles was observed. The is in agreement with the results shown in Figure 5-49, where the electrodes processed with CA and AA had higher adhesion strength than those processed with PA.

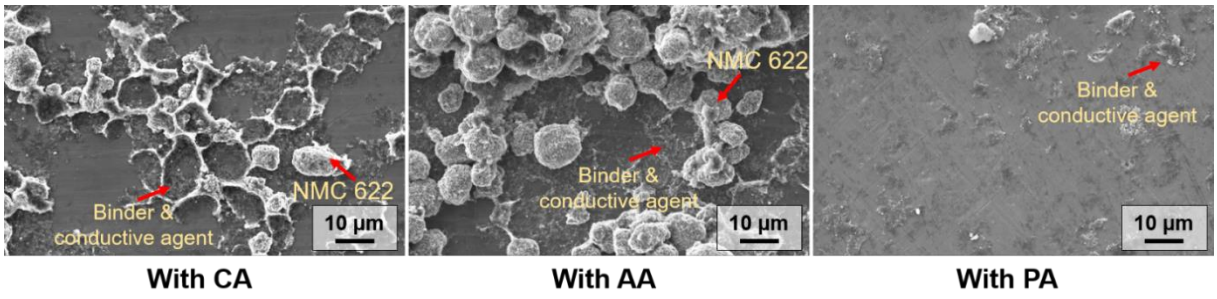

Figure 5-50. SEM images of the Al foils of the NMC 622 electrodes processed with CA, AA and PA addition after peel-off-test.

5.4.4. Impact of acid type on cell performance

The electrochemical performance of cells containing NMC 622 cathodes will be presented and discussed in this chapter with respect to different acid additions in comparison to reference cells containing NMC 622 cathode using PVDF as binder.

CV analyses

CV analyses were performed at a scan rate of 0.02 mV/s to investigate the effect of different acid additions on the electrochemical performance of cells containing different NMC 622 electrodes. In Figure 5-51-a. the specific currents of cells with different thick-film electrodes are plotted vs. voltage. Even with different acid additions during electrode processing, only one anodic and cathodic peak was observed for all cell types, which are related to the redox reaction of Ni^{2+} / Ni^{3+} / Ni^{4+} [92] and the phase change from monoclinic to a hexagonal phase during discharge [187]. This indicates that no new redox reaction appears in cells containing aqueous processed NMC 622 cathodes with different acid additions. Besides, the anodic peak intensity was 1.2 – 1.5 times higher than that of the corresponding cathodic peak, which was also observed in another study [90]. However, the oxidation and reduction peak of the cell containing reference electrode with PVDF binder shifted to lower and higher voltage, respectively, compared to those of cells with aqueous processed electrodes. This phenomenon has also been observed in another study [187]. Besides, the reference cell with PVDF binder exhibited a higher specific current than the other cells. The decrease in specific current of cells containing aqueous processed electrodes must be due to the Li leaching that occurs when NMC 622 comes into contact with water, as discussed in the previous chapter. The voltages corresponding to the oxidation and reduction peaks and the related peak-to-peak separation of cells with different electrodes are summarized in Figure 5-51-b. The cell containing reference electrode with PVDF binder exhibited the lowest peak-to-peak voltage separation of 0.13 V, whereas other cells containing aqueous processed electrodes had a similar voltage difference of 0.20 V. The peak shift and the reduced current intensity indicates that the cells with aqueous processed electrodes have an increased overpotential η compared to cells containing electrodes with PVDF as binder according to equation (3.14) and (3.17), and a low electron transfer rate k_0 smaller than 10^{-2} cm/s [133]. Thus, the cells with aqueous processed electrodes should exhibit higher charge transfer resistance than the cells having cathodes with PVDF as binder. This will be further investigated in chapter 5.4.5.

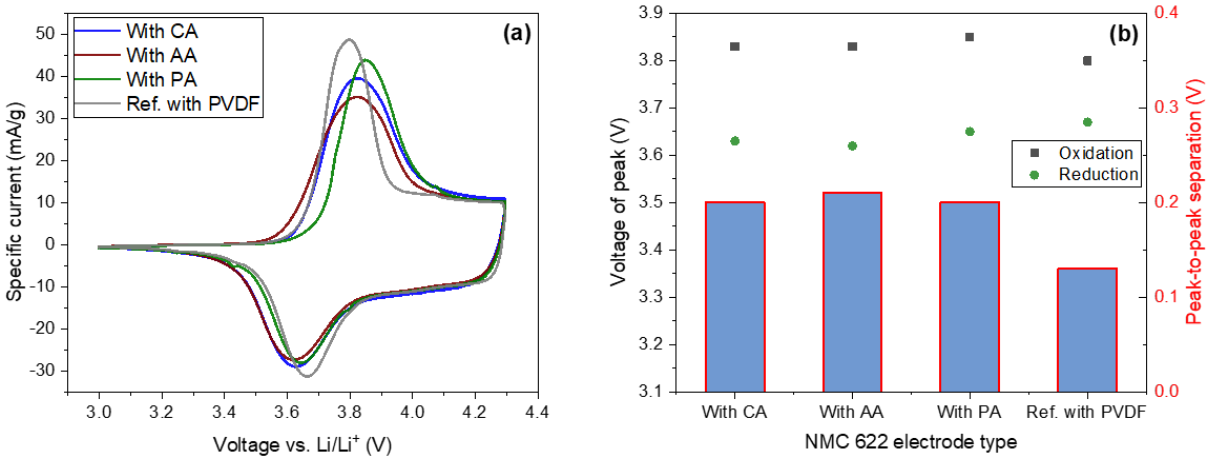

Figure 5-51. The (**a**) CV analyses of half-cells containing NMC 622 cathodes prepared with different acid additions and reference electrodes with PVDF binder; (**b**) The oxidation and reduction peak voltages and peak-to-peak separation of cells with different types of electrodes.

Rate capability analyses

Figure 5-52 shows the discharge capacities of cells with different types of NMC 622 cathodes at C-rates ranging from C/20 to 3C. Each cell was cycled 3 times at C/20 after assembly to establish a stable CEI on the cathode [307]. The cells containing electrodes with PVDF binder and aqueous processed electrodes with AA addition achieved a specific capacity of about 175 – 178 mAh/g, while the cells containing cathodes with CA and PA provided about 170 mAh/g capacity after formation. The initial CE of cells containing electrodes processed with different acids at the first C/20 formation step are listed in Table 5-20. For cells with thin-film electrodes, the initial CE of reference cells using PVDF as binder was 1 – 2 % higher than those containing aqueous processed electrodes with CA and PA addition, while cells containing electrodes with AA addition exhibited the same initial CE. The initial CE of cells containing electrodes with PVDF binder is similar to the results from Tolchard et al. [201], however, in their study the cells containing electrodes with PA addition showed 92 % initial CE, which is higher than that in this work. As discussed before, a lower initial CE indicates a higher electrolyte consumption for CEI formation during charging / discharging [202], which may be resulted from the rough contact surface area between the NMC 622 particles and the liquid electrolyte after acid treatment, as observed in Figure 5-46. The cells with aqueous processed thick-film electrodes showed almost the same initial CE as those with thin-film electrodes, which are similar to the previous results in Table 5-8 using B- and S-NMC 622 with different particle sizes, as well as the study from Kukay et al. [202] using full-cells containing PA treated NMC 811 cathodes and graphite anodes. After the first cycle, the CE rose to 99 – 100 % for all cells at C/20, which suggests adequate CEI formation on the NMC 622 electrodes.

Table 5-20. Initial coulombic efficiency of cells containing aqueous processed NMC 622 electrodes with different acid additions and different film thicknesses.

Electrode type	Initial coulombic efficiency [%]	Capacity retention [%]
With CA, thin-film	88.7 ± 0.1	84.8 ± 1.1
With CA, thick-film	88.8 ± 0.1	96.5 ± 1.7
With AA, thin-film	89.9 ± 0.4	87.0 ± 1.7
With AA, thick-film	90.1 ± 0.2	94.9 ± 1.8
With PA, thin-film	86.8 ± 0.6	96.3 ± 0.5
With PA, thick-film	86.9 ± 1.3	96.9 ± 0.9
Ref. with PVDF, thin-film	89.8 ± 0.6	98.7 ± 0.3
Ref. with PVDF, thick-film	88.8 ± 0.4	98.8 ± 0.4

Figure 5-52-a displays that for cells with thin-film electrodes, the reference cells containing cathodes with PVDF binder had the highest capacities from C/10 to 1C compared to cells with aqueous processed cathodes. For example, the reference cells showed 174 mAh/g specific capacity at C/10, while cells with aqueous processed electrodes with AA addition provided 170 mAh/g capacity. The cells containing electrodes processed with CA and PA addition exhibited a lower discharge capacity of 164 mAh/g. This is similar to the previously reported results [187]. As the C-rate increased from C/2 to 3C, cells containing electrodes with addition of CA and AA exhibited a more pronounced capacity loss compared to ones containing PA or PVDF binder. At 2C, the specific capacities of the reference cells and cells containing electrode with PA remained at 62 mAh/g and 59 mAh/g, respectively, while the capacities of cells containing electrodes with CA and AA decreased to 15 mAh/g in the last cycle of 2C. At 3C, cells with CA and with AA showed more than 95 % loss in capacity, maintaining 5 mAh/g capacity, while the cells with the other two types of electrodes reached a capacity of about 30 mAh/g.

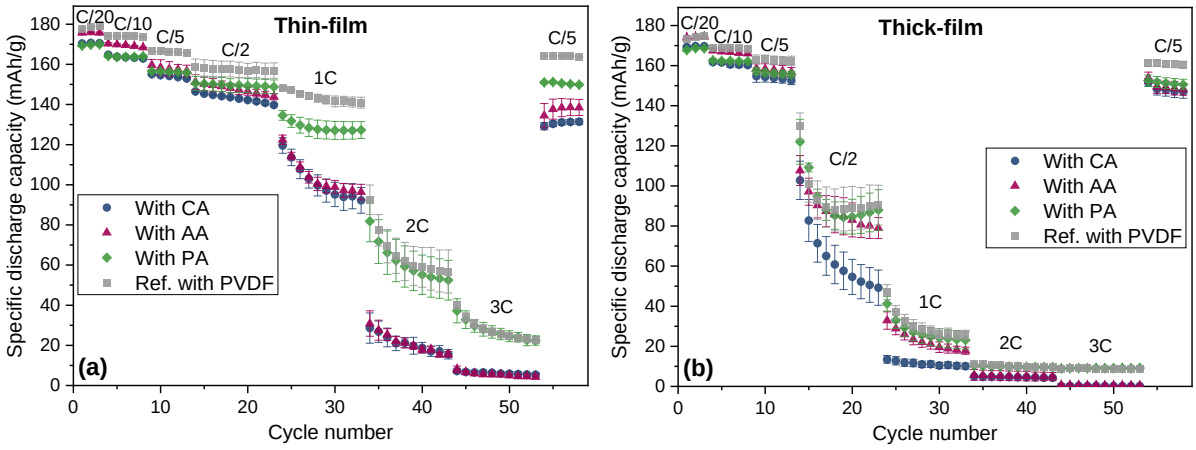

Figure 5-52. Specific discharge capacities of half-cells containing (**a**) electrodes with about 70 µm thickness and (**b**) electrodes with 150 µm thickness at increasing C-rates from C/20 to 3C. For each electrode film thickness, three different acids, i.e., CA, AA, and PA were added during the mixing process of NMC 622 slurry.

Subsequently to charging and discharging at 3C, the cells were cycled again 5 times at C/5 to determine the cell degradation as shown in the last column of Table 5-20. Compared to the previous C/5, the reference cells and the cells containing thin-film electrode with PA addition retained 99 % and 96 % of their capacity, respectively, while the cells with CA and

with AA reached 85 % and 87 % capacity after being cycled at high C-rates. The addition of PA during slurry preparation not only decreases the slurry pH value but could also lead to the formation of phosphates such as Li_3PO_4, Li_2HPO_4, or M_xPO_4 / M_xHPO_4 (M as Mn, Ni, or Co) layer on the surface of NMC 622 particles [30], as concluded from the P 2p spectra of the XPS analyses (Figure 5-47-b). A similar conclusion has been reached in other studies using NMC 111 as the active material [194]. In addition, Jo et al. [188] had reported that cells with PA modified NMC 622 electrodes exhibited a high capacity retention. However, in their study, NMC 622 powders were pre-modified in PA solution and heated at 500 °C prior to slurry preparation, while conventional PVDF binder was subsequently applied for the electrode fabrication. In this work, *in situ* coating of NMC 622 powder was achieved during slurry preparation without additional processing steps.

The rate capabilities of cells with thick-film electrodes are depicted in Figure 5-52-b. The discharge capacity of cells containing reference electrodes and electrodes with AA addition was 4 – 5 mAh/g higher than the others at C/20 and C/10. At C/5, all cells exhibited similar capacities of 155 mAh/g except for the cells with PVDF binder, whose capacities were 5 mAh/g higher. When the C-rate was increased to C/2, the cells with CA-added electrodes displayed the most severe capacity drop, retaining 50 mAh/g after the last C/2 cycle, whereas the cells containing reference electrodes and electrodes with PA addition achieved the highest specific capacity of 90 mAh/g, followed by the cells with AA-added electrodes with 79 mAh/g. From 2C to 3C, all cells lost more than 90 % capacity compared to their initial capacity at C/20. Interestingly, the capacity retention of cells with aqueous processed thick-film NMC 622 electrodes was higher than that of ones with thin-film electrodes. For example, Table 5-20 shows that as the film thickness increases, the capacity retention of cells with CA and AA addition increased significantly from 85 % to 97 % and from 87 % to 95 %, respectively. However, for cells with reference electrodes or with PA addition, the capacity retention for cells with thin-film or thick-film electrodes was similar at 97 % and 99 %, respectively. In contrast, the capacity retention of cells containing electrodes with PVDF binder remained at 99 % (as shown in chapter 5.2.2) and did not vary with increasing film thickness. Rate capability analyses reveal that both phosphoric acid and acetic acid are suitable candidates for enhancing the electrochemical performance of cells with thick-film NMC 622 electrodes.

Lifetime analyses

Lifetime analyses were performed at C/2 to investigate the cycling stability of cells with different electrode types. The cell with thin-film reference electrode provided the highest initial capacity as shown in Figure 5-53-a, followed by the one with PA addition. This is consistent with the previous rate capability analyses at C/2 (Figure 5-52). After 100 cycles, the cell with reference electrode and the one with PA addition maintained the highest specific discharge capacities of 88 % and 80 %, respectively, whereas the cells containing CA- or AA-added electrodes suffered severe degradation, providing less than 20 % of the initial capacity at the end of cycling procedure. The strong capacity fading of cells with CA and AA addition could be resulted from the internal crack formation in NMC 622 particles due to the acid attack [29], and the isolation of grains within the primary NMC 622 particles, since they no longer contribute to the electrochemical performance due to the loss of electrical connectivity [354]. Sun et al. [355]

proposed that the strain and strain gradients that arise in the secondary particles due to Li-ion diffusion can induce the fragmentation of NMC secondary particles after long-term cycling. The decohered primary particles no longer participate in electrochemical reaction, which leads to capacity decay.

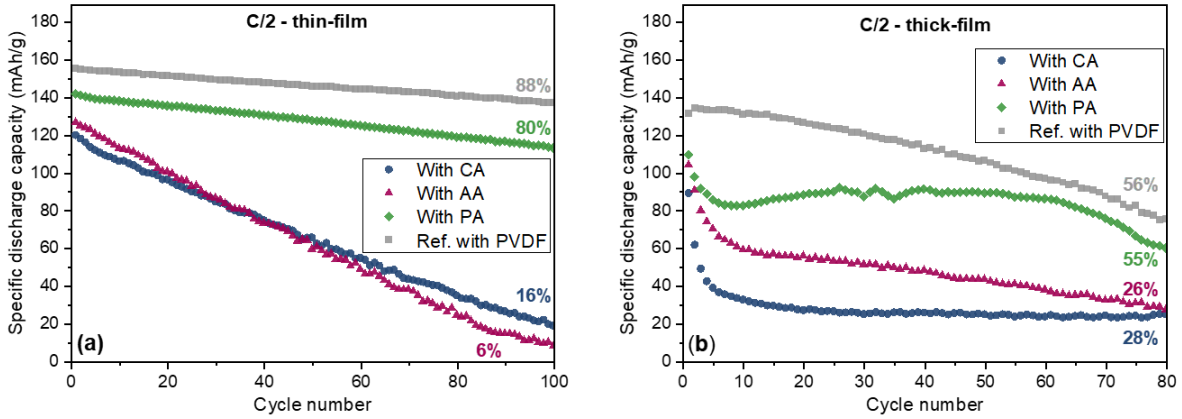

Figure 5-53. Lifetime analyses at C/2 of half-cells containing (**a**) thin-film and (**b**) thick-film NMC 622 electrodes processed with different acid additions or with PVDF binder.

In addition, the effect of porosity and mass loading on the electrochemical performance can be ruled out, since the slurry pH values with different acids were kept the same and the electrode porosity was adjusted to 35 % by calendering. Therefore, the interaction between acid and NMC 622 particles as well as binder has a decisive impact on the electrochemical performance. First of all, cross-linking reaction can occur by adding PA or CA into the slurry with Na-CMC binder. This mechanism was proposed by Kazzazi et al. [31] and Kuenzel et al. [30]. Cross-linked CMC polymers provide a homogenous surface coverage of the active material particle and improve the mechanical integrity of the electrodes. Rigid cross-linked CMC binder, especially PA with short molecule, may provide stress to the secondary particles during cycling and alleviate the separation of primary particles. However, cross-linking may not be the dominant factor affecting the electrochemical performance, since the capacity retention of cells with PA-added electrode was 64 % higher after 100 cycles than those with CA addition. Therefore, the interaction of acid with NMC 622 particles should be considered. XPS analyses proved the presence of phosphates on electrode surface after the addition of PA, and combining with the electrochemical performance data, it can be concluded that not only dried phosphoric acid is present in the electrode, but also a protective layer consisting of phosphate is formed and attached to the surface of NMC 622 particles. This protective layer on the one hand mitigates Li leaching from the NMC 622 surface, and on the other hand prevents secondary particles from cracking during long-term cycling. In addition, another study showed that the capacity retention of cells with NMC 111, modified with 1 wt% PA addition, was higher in comparison to ones with formic acid or without acid [194], which is consistent with the results of this work. Another benefit of using PA addition is that the strong P–O covalent bonds in $(PO_4)^{3-}$ can significantly reduce the rate of oxygen release in NMC 622, thereby increasing the cell safety during operation [187].

Figure 5-53-b displays the discharge capacities of cells with thick-film electrodes. Compared with the cells with standard loaded electrodes, the cells with high mass loaded

electrodes exhibited severe capacity drop, especially for cells containing CA- or AA-added electrodes, which lost almost 50 % of their initial capacity within the first 10 cycles. In contrast, the cells containing electrodes with PVDF binder or with PA addition retained significantly higher capacity and exhibited more stable performance. After 80 cycles, the reference cells and cells with PA-added electrode achieved 56 % and 55 % capacity retention, respectively, while the cells with AA- or CA-added electrodes exhibited 26 % and 28 % capacity at the end compared to their initial capacity. At the end of cycling procedure, the cells were disassembled and the cycled NMC 622 cathodes with CA and PA addition were washed with DMC for 1 h to rinse off the residual electrolyte. Post-mortem analyses of the aged electrodes were performed by means of SEM. Figure S 7 shows that NMC 622 cathode processed with CA addition had more cracks after cycling than those processed with PA addition. The detached NMC 622 grains are probably the result of strain accumulation in the secondary particles during cycling. They can no longer participate in the electrochemical reaction and thus lead to a reduced capacity. As for the cycled cathode with PA addition, the residual PA may react with the electrolyte and produce deposition on the surface of the NMC 622 secondary particles. However, the chemical composition of these products is unknown and deserves further study in the future. In addition, no obvious cracks were found in PA-added NMC 622 cathodes after cycling, which is consistent with their higher discharge capacity than the CA-added cathodes after lifetime analyses. The serious capacity loss of cells with thick-film electrodes comes from reaction inhomogeneity owing to the accumulated Li-ion transport limitation and locally increased ohmic resistance [231]. This means that NMC 622 particles which are located close to the current collector cannot reach the same SOC as the NMC 622 particles which are near the interface between electrode and electrolyte. Thus, the active material particles which are close to the Al current collector take no longer part in the electrochemical reaction and remain at the same SOC regardless of charging or discharging.

In summary, the addition of PA is highly beneficial for enhancing the electrochemical performance, since not only can it adjust the slurry pH value and avoid the chemical corrosion on the Al current collector, but it also significantly enhances the discharge capacity of cells containing electrodes with both standard and high active mass loading at high C-rates higher than C/2, as well as the cycling stability in lifetime analyses.

The EIS analyses and CV analyses will be presented in the next chapter together with the cells containing laser structured NMC 622 electrodes with different acid additions.

5.4.5. Impact of laser structuring on cell performance

Cells containing electrodes processed at different slurry pH values

For the purpose of enhancing Li-ion diffusion kinetics, thick-film electrodes with slurry pH values of 12.1, 10.0, and 9.0 (adjusted using acetic acid) were structured via ultrafast laser ablation. The details of laser structured electrodes are summarized in Table 5-21. The mass loss due to the laser ablation includes the removal of active material, binder, and conductive additive.

Table 5-21. The active mass loading, areal capacity, and respective mass loss of laser structured electrodes compared to unstructured ones.

Electrode type	Active mass loading [mg/cm^2]	Areal capacity [mAh/cm^2]	Mass loss [%]
Slurry pH 12.1	33.3 ± 0.1	5.53 ± 0.02	9.8 ± 1.4
Slurry pH 10.0	44.0 ± 0.1	7.31 ± 0.02	7.2 ± 0.8
Slurry pH 9.0	42.7 ± 0.2	7.10 ± 0.03	3.4 ± 0.5

The SEM images of laser structured electrodes processed with slurry pH values of 12.1, 10.0, and 9.0 are shown in Figure 5-54. The line pitch was kept constant at 200 µm. On the surface of the electrodes prepared with a slurry pH value of 12.1, holes with diameters ranging from 10 µm to 100 µm could be observed. In addition, cracks originated from the holes were observed as well. As the slurry pH value decreased to 10.0, no cracks were formed and holes had diameters smaller than 50 µm. At a slurry pH value of 9.0, no holes or craters were found throughout the electrode. A maximal width of 30 ± 2 µm was achieved at the top of the groove, and the FWHM was 10 ± 1 µm. The sidewalls of the generated channels showed a slight curvature of 7.0 ± 0.3°, which means that the sidewalls were almost perpendicular oriented in relation to the cathode surface.

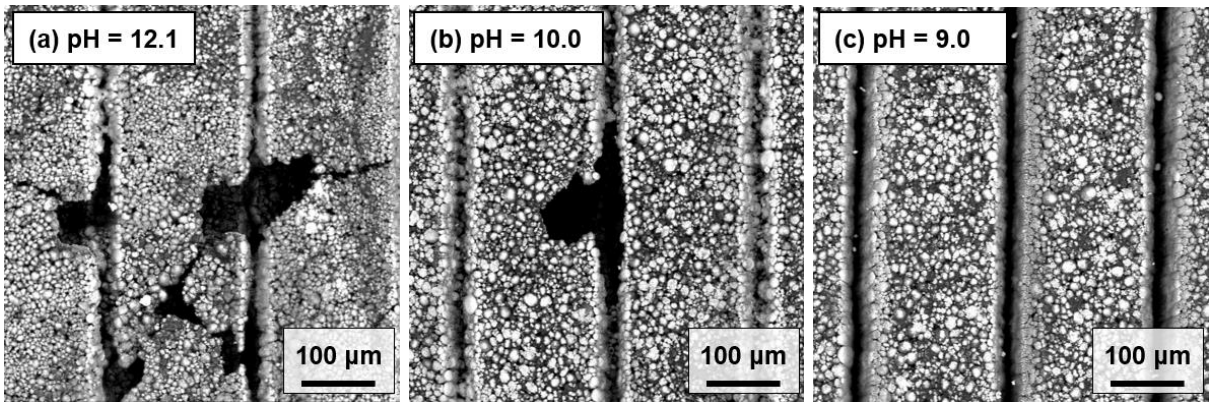

Figure 5-54. SEM images (top view) of laser structured aqueous processed NMC 622 cathodes with slurry pH values of (**a**) 12.1, (**b**) 10.0, and (**c**) 9.0. The slurry pH value was adjusted by adding acetic acid during the mixing process.

Figure 5-55-a exhibits the discharge capacities of cells containing laser structured thick-film electrodes which were produced at slurry pH values of 12.1, 10.0, and 9.0. The discharge capacities of the cells with laser structured electrodes at C/20 and C/10 were similar to that of ones having unstructured electrodes produced with the same slurry pH values. In the following C/5 cycling steps, a capacity increase of 14 mAh/g and 18 mAh/g was observed for cells containing structured cathodes produced with slurry pH values of 9.0 and 10.0 in comparison to the ones with unstructured electrodes, respectively, while cells with laser structured electrodes without acid addition had 3 mAh/g lower capacity than those with unstructured electrodes. However, when the C-rate was increased above C/2, cells with laser structured electrodes began to show enhanced discharge capacities regardless of the slurry pH values used during the electrode preparation. Figure 5-55-b shows increase in specific capacity of cells with laser structured electrodes compared to those with unstructured electrodes. For instance, cells containing structured electrodes prepared with slurry pH values of 9.0 retained

42 mAh/g more capacity at C/2, while cells with electrodes produced with slurry pH values of 12.1 and 10.0 showed an increase in capacity of 17 and 11 mAh/g in comparison to cells containing unstructured electrodes produced with the same respective slurry pH value. This is similar to previous results of cells containing structured electrodes with PVDF binder [268]. This proves that for aqueous processed electrodes at different slurry pH values and with up to 57 % porosity, laser structuring can still further enhance the cell capacity at high C-rates relatively to the ones with unstructured electrodes. This may be due to the connection of cavities inside the electrodes as shown in Figure 5-38, which leads to new diffusion pathways of Li-ions from electrolyte to the bulk electrode and a decreased tortuosity in the electrode. However, due to the presence of cavities inside the NMC 622 cathodes processed with slurry pH value above 10 (see Figure 5-38), the mass loading of the electrodes was uneven. Besides, since the laser fluence was constant during the laser structuring, localized though-holes or slits in the Al current collector occurred due to laser ablation. This can lead to mechanical instability in electrodes.

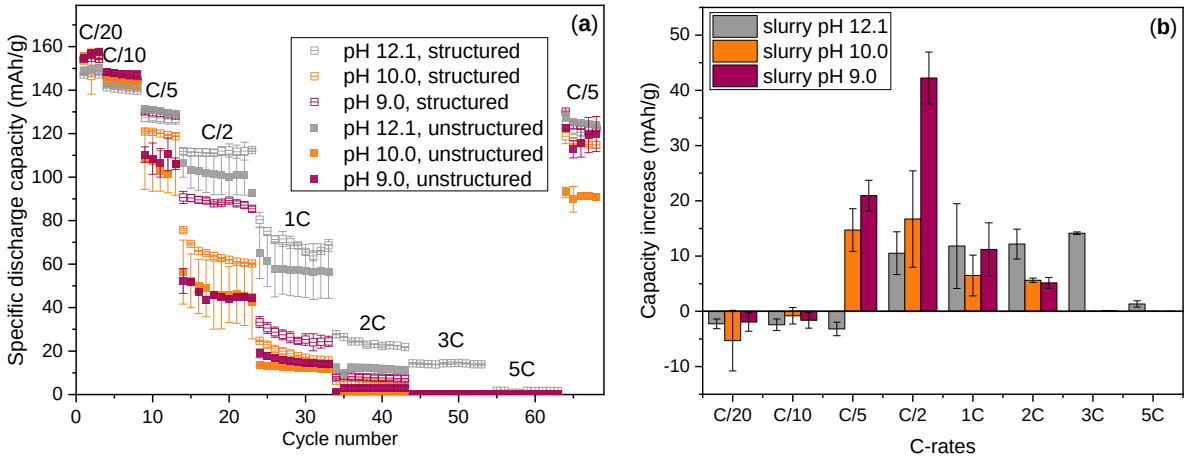

Figure 5-55. Rate capability analyses of (**a**) the half-cells containing unstructured or laser structured thick-film electrodes which were produced at different slurry pH values; And (**b**) the specific discharge capacity increase of cells with laser structured electrodes in contrast to those containing unstructured electrodes.

Cell containing electrodes processed with addition of different acid types

NMC 622 electrodes processed aqueously with different acid additions were structured using ultrafast laser ablation. The setup for laser structuring is shown in Figure 4-8. Cross-sectional analyses of laser structured electrodes processed with different acid additions were performed to determine the laser ablation depth and width of the composite electrodes, as shown in Figure 5-56. The slurry induced corrosion of the Al current collector during coating was suppressed due to pH modification. Therefore, hydrogen generation was suppressed and no cavities with diameter larger than 50 µm were observed within the dried electrodes, which is in agreement with the previous results of electrodes coated at different slurry pH values, as shown in Figure 5-38. The number of laser scans were adjusted to achieve channel structures extending from the electrode surface to the current collector without affecting the current collector. The number of laser scans (15 – 16 passes) were similar for different electrode types, indicating an identical ablation behavior in electrodes regardless of different acid additions. The high-resolution SEM images in Figure S 6 show the edges of the laser generated channels.

No melted particles or obvious HAZ could be detected, which is similar to the results achieved for laser structured electrodes with PVDF binder. Direct sublimation of materials using an ultrafast laser facilitates the acquisition of microstructures with high aspect ratios and sidewalls with smooth surfaces. In addition, the generated channel can accelerate electrolyte wetting due to capillary effect [13]. Meanwhile, electrolyte-filled channels serve as electrolyte reservoirs and can enhance rate capability and lifetime of batteries [16, 268].

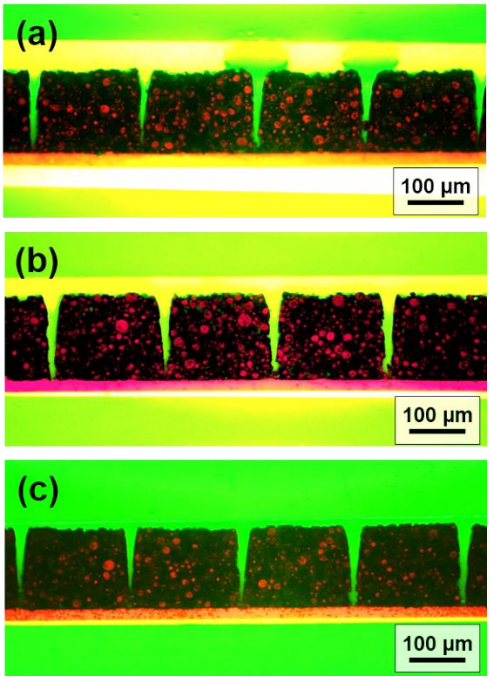

Figure 5-56. Cross-sectional views of aqueous processed and laser structured NMC 622 cathodes with addition of (**a**) CA, (**b**) AA, and (**c**) PA during slurry preparation. An average laser power of 2.5 W and a laser repetition rate of 500 kHz were applied, while the laser scans varied from 15 to 16 for the structuring of different electrodes.

Figure 5-56 displays that all channels are V-shaped with wide openings at the electrode surface, which are similar compared to the structures in electrodes with PVDF binder, as shown in Figure 5-11 and Figure 5-31. The geometric information of the channels in laser structured electrodes and the mass loss due to laser structuring are summarized in Table 5-22. The mass loss is calculated based on equation (5.7). The top width of the channels near the electrode surface is about 30 µm, which is in good agreement with the calculated laser spot size of 29 µm (chapter 5.2.3). For different electrode types, the mass loss is controlled at around 7.5 %, which is slightly higher than the laser structured electrodes with PVDF binder (5.8 ± 1.6 %) shown in Table 5-4.

Table 5-22. Maximum width and FWHM of the channel structures in different types of NMC 622 electrodes and the respective mass loss due to laser structuring.

Electrode type	Max. width [µm]	FWHM [µm]	Mass loss [%]
With CA	31.2 ± 3.8	12.6 ± 1.8	7.5 ± 4.8
With AA	32.7 ± 2.7	13.7 ± 0.3	7.5 ± 2.7
With PA	29.8 ± 3.0	14.9 ± 0.4	7.4 ± 1.5

The rate capabilities of cells with laser structured thick-film electrodes and their capacity increase in contrast to ones containing unstructured electrodes are depicted in Figure 5-57. At

the very first cycle, cells containing laser structured electrodes with CA and PA provided similar initial CE of 86.5 ± 0.2 % and 85.8 ± 0.5 %, respectively, while the ones with AA addition showed an initial CE of 88.2 ± 0.2 %. In comparison to the cells with unstructured electrodes, the cells with laser structured electrodes displayed about 2 % lower initial CE, which should be owing to the formation of CEI on the generated channel surface between electrolyte and laser structured electrode, as discussed in chapter 5.2.3. At C/20 and C/10, the rate capacity of cells with structured electrodes was 5 mAh/g lower than that of the cells with unstructured electrodes, as shown in Figure 5-52-b. As the C-rate was increased to C/5, all cells revealed similar capacities of 153 mAh/g except reference cells having electrodes with PVDF binder, whose capacities were 10 mAh/g higher. The cells with laser structured electrodes started to show excellent performance at C/2. The cells containing structured PA-added electrodes retained the highest specific capacity of 131 mAh/g, followed by the cells with structured AA- and CA-added electrodes with 124 mAh/g and 108 mAh/g, respectively. At C/2, the largest increase in capacity of 44 mAh/g was observed for the cells containing electrodes processed with CA addition, while a capacity increase of 38 and 36 mAh/g was exhibited for the cells containing electrodes processed with PA and AA addition, respectively. At 1C, capacity increases of 21 – 31 mAh/g were shown for all cells with laser structured electrodes, while at 2C and 3C, cells with laser structured electrodes achieved 3 – 4 mAh/g higher capacity compared to ones with unstructured electrodes. Furthermore, all cells using laser structured aqueous processed electrodes exhibited higher specific capacity in comparison to reference cells. For example, in comparison to the reference cells, the cells with structured PA-added electrodes had 32 mAh/g and 26 mAh/g higher discharge capacity at C/2 and 1C (32 % and 87 % higher), respectively. Rate capability analyses reveal that both PA and AA are good candidates for enhancing the electrochemical performance of cells containing laser structured thick-film NMC 622 electrodes, especially at C-rates equal or above C/2. This conclusion is consistent with previous rate capability results of cells containing unstructured electrodes.

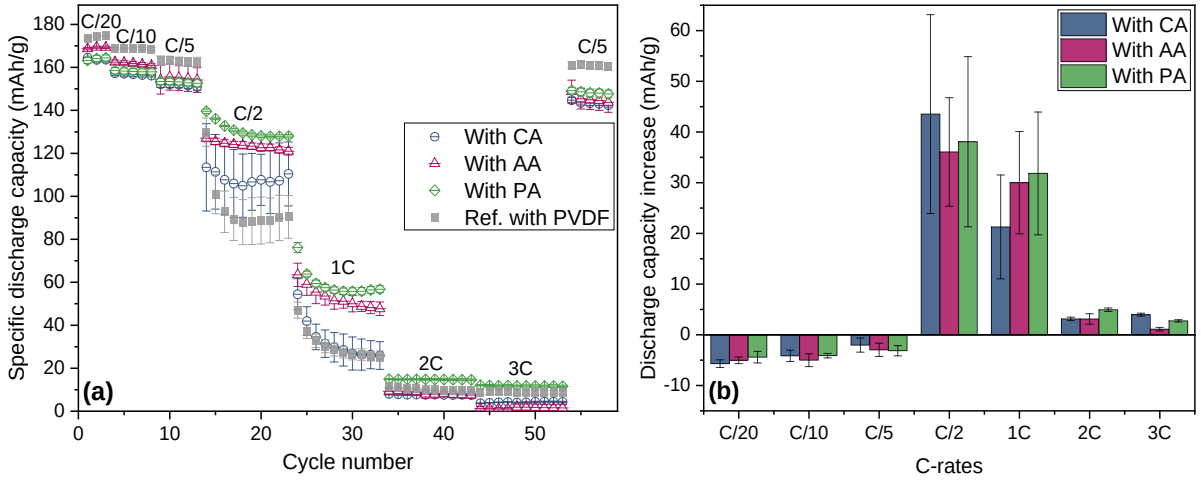

Figure 5-57. Rate capability analyses of (**a**) the half-cells containing laser structured thick-film electrodes which were produced with different acid additions (CA, AA or PA) in comparison to the reference cells containing unstructured electrodes with PVDF binder; and (**b**) the specific discharge capacity increase of cells with laser structured electrodes in contrast to those containing unstructured electrodes shown in Figure 5-52-b at different C-rates ranging from C/20 to 3C.

Several studies have shown that the energy density increases with increasing electrode thickness and decreasing porosity, meanwhile power density is significantly reduced [24, 232, 239]. In this work, the channel structures generated by laser ablation provide extra porosity to the electrodes, while the unstructured parts maintain a low porosity and a high mass loading. As a result, laser structuring can compensate the power density degradation of cells with thick-film electrodes at high C-rates in comparison to cells with unstructured electrodes.

The differential capacity dQ/dV plots of cells with different types of aqueous processed NMC 622 electrodes from the third cycle at C/20 are depicted in Figure S 8. All cells exhibited two peaks during charging and one peak during discharging, indicating an identical phase transition of NMC 622 between H1 and M phases, which are the same in comparison to cells containing electrodes with PVDF as binder (Figure 5-23-b). Furthermore, the two peaks of cells containing electrodes with PA during charging exhibited similar form in contrast to ones containing electrodes with PVDF as binder, as the first peak at 3.68 V was higher than the second peak at 3.75 V. However, the first peak of cells containing AA-added electrodes at 3.67 V was lower and wider in contrast to its second peak at 3.78 V, which is similar to the results from Zhang et al. [301] using NMC 622 cathodes with PVDF as binder. The reason for the lowering of the first peak is unknown. The peak during discharging located at 3.72 V for cells with PA addition and with PVDF as binder, while cells with CA and AA addition exhibited slight lower peak potential at 3.70 V. In contrast to cells with unstructured electrodes, the cells with laser structured electrodes showed a peak shift to lower and higher potential during charging and discharging, respectively. This suggests that the polarization of cells with laser structured electrodes was reduced in comparison to those with unstructured electrodes.

Figure 5-58 presents that at C/10, the discharge profiles of the cells with CA and AA additions were lower compared to the reference cell with PVDF as binder, indicating that these cells were more polarized during the discharging. The discharge profile of the cell with PA addition from 4.3 to 3.7 V is similar to that of the reference cell. Furthermore, the IR drop of cells with CA and AA addition (from 4.3 V to less than 4.2 V with about 170 Ω) was higher in contrast to those with PA addition and with PVDF as binder (from 4.3 to 4.25 V with about 80 Ω), which indicated a higher ohmic resistance of the first two types of electrodes. In addition, for the cells with CA addition, the IR-drop was decreased to 90 Ω after applying laser structuring, as shown in Figure 5-58-a. Besides, the discharge plateau of the cell containing structured CA-added electrode was higher than that of the cells with unstructured electrodes, which means that the cell polarization was decreased. However, no difference in the discharge profiles of cells containing electrodes with AA and PA addition with / without laser structuring was observed at C/10. When C-rate increased to C/2, IR-drop of cells with CA and AA addition increased significantly (from 4.3 to 3.8 V with about 705 Ω), while cells with other two kinds of electrodes showed a lower IR-drop of 4.3 to 4.15 V (with a resistance of about 245 Ω). Besides, all cells with structured electrodes displayed lower cell polarization from 4.3 to 3.0 V at C/2 in comparison to those with unstructured electrodes.

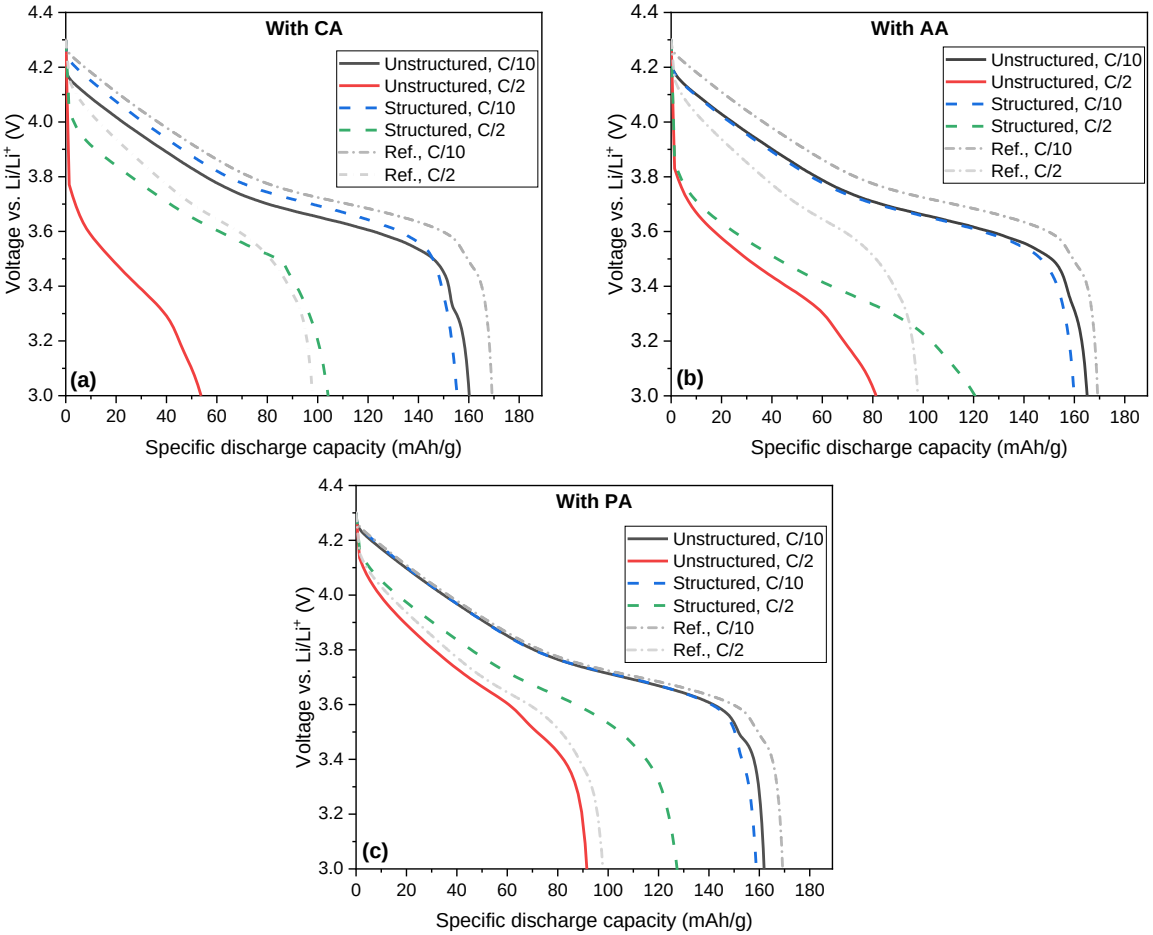

Figure 5-58. Specific discharge capacity vs. voltage (vs. Li / Li^+) of the half-cells containing unstructured and structured thick-film electrodes with addition of (**a**) CA, (**b**) AA, (**c**) PA, in comparison to the reference cell with PVDF binder at C/10 and C/2 [305].

After rate capability analyses, some of the cells were cycled at C/2 to study their long-term stability. Figure 5-59 displays the specific discharge capacity and relative discharge capacity of cells containing laser structured electrodes with different acid additions in contrast to that of the cells with unstructured electrodes. All cells with laser structured electrodes showed significantly less degradation and maintained a high discharge capacity after 80 cycles. The initial and final discharge capacities as well as capacity retention of all cells are summarized in Table 5-23. The cells with laser structured electrodes displayed both higher initial and final capacity in comparison to ones with unstructured electrodes. Furthermore, no sudden drop in capacity within the first 10 cycles was detected for cells with laser structured aqueous processed electrodes. In addition, the cell containing laser structured PA-added electrode surpassed the reference cell at around 60 cycles and achieved 13 mAh/g higher capacity in contrast to the reference cell at the end, holding 72 % capacity after 80 cycles.

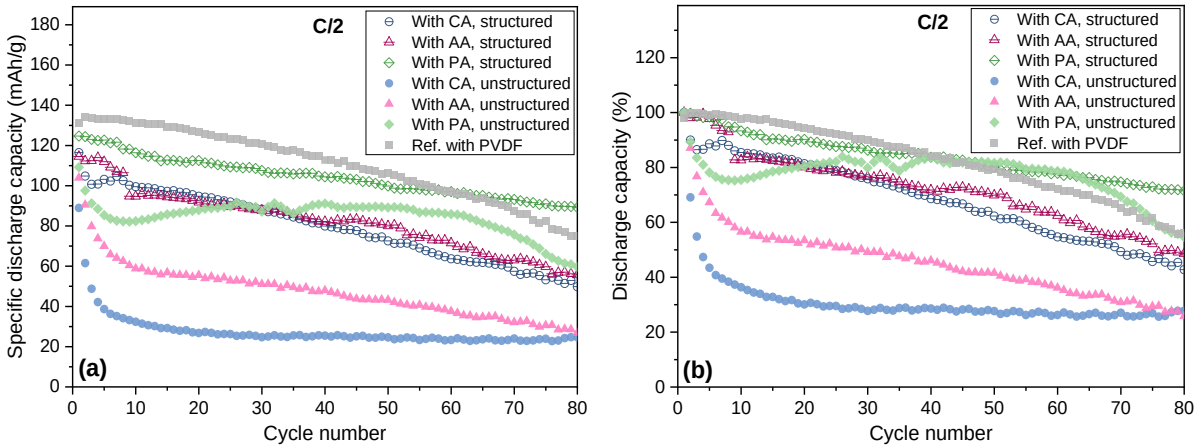

Figure 5-59. Lifetime analyses of half-cells containing thick-film NMC 622 cathodes prepared with different acids during mixing process. (**a**) The specific discharge capacity and (**b**) the relative discharge capacity compared to the initial capacity of the first cycle.

With laser ablation, 3D architectures with channels were generated inside the electrodes, extending all the way to the current collector. The diffusion pathway of Li-ions to the NMC 622 particles at the bottom is no longer through the whole film but through the sidewalls of the channel structures into the electrode. This was verified via laser induced breakdown spectroscopy (LIBS) by Smyrek et al. [313] and Zheng et al. [277], who demonstrated that the laser generated channels provide new Li-ion diffusion pathways from the liquid electrolyte into the active materials, i.e., the Li concentration in cycled 3D thick-film electrodes becomes more homogeneous in comparison to that in unstructured electrodes. As a result, more NMC 622 particles at the bottom of laser structured thick-film electrodes (near the current collector) can actively participate in the electrochemical reaction, since Li-ion diffusion can take place through the vertical interfaces between electrode and electrolyte.

Table 5-23. Initial capacity, final capacity, and capacity retention of cells with different types of thick-film electrodes from lifetime analysis.

	With CA, unstructured	**With CA, structured**	**With AA, unstructured**	**With AA, structured**	**With PA, unstructured**	**With PA, structured**	**Ref. with PVDF**
Initial capacity [mAh/g]	89	116	104	114	109	125	131
Final capacity [mAh/g]	25	51	29	57	61	90	77
Capacity retention [%]	28	44	28	50	56	72	57

CV analyses of cells containing unstructured and laser structured NMC 622 electrodes prepared with PA addition are shown in Figure 5-60-a, b with increasing scan rates ν from 0.02 to 0.12 mV/s. Further measurements from cells containing electrodes with CA or AA addition, and with PVDF binder are displayed in Figure S 9. The effective diffusion coefficient of Li-ions is determined using equation (4.10). The specific surface areas A_m [cm²/g] for the calculation of D_{eff} is given as follows:

$$A_m = S_{BET} \cdot 2/3 \cdot P_{ele} \tag{5.14}$$

where 2/3 of the BET surface area of NMC 622 powder S_{BET} [cm²/g] and the electrode porosity P_{ele} [-] were applied. The use of the factor “2/3” is due to that the Li-ion diffusion pathways in

NMC 622 particles are 2-dimensional [65], while the porosity of the electrode was introduced into the equation (4.10) as a factor to describe the contact surface area of the NMC 622 particles with electrolyte due to the existence of the pores within the electrode. P_{ele} was kept constant at 0.35 for all types of cathodes.

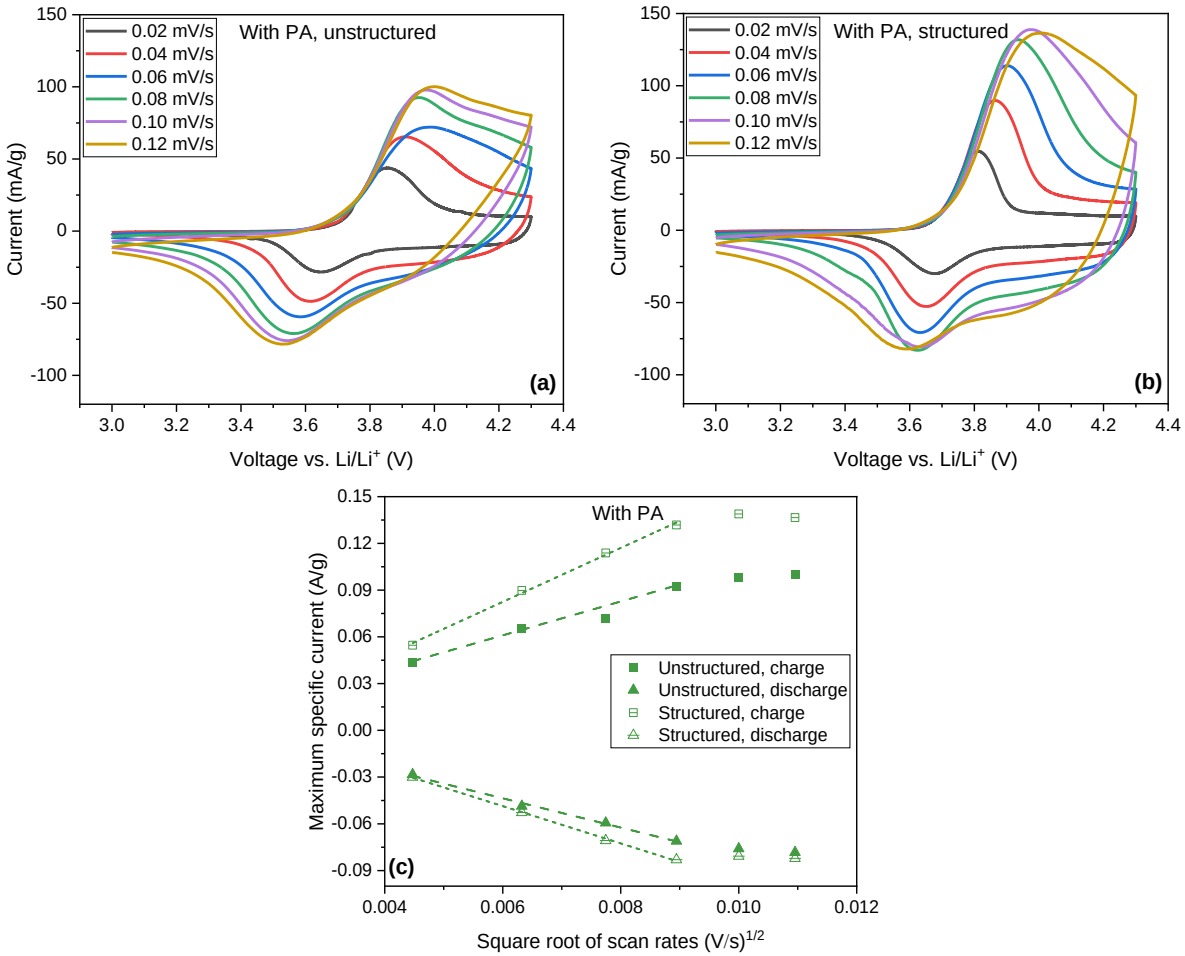

Figure 5-60. CV plots of half-cells containing (**a**) unstructured and (**b**) laser structured NMC 622 cathodes prepared with PA addition, and (**c**) the corresponding maximum specific currents vs. the square root of scan rates.

To calculate the effective Li-ion diffusion coefficient, the specific peak current of each cell is plotted vs. the square root of scan rates, as shown in Figure 5-60-c. A linear relation is found between the maximum specific current and the square root of scan rates at scan rates ranging from 0.02 to 0.08 mV/s, whereas the peak current deviates from the linear fitting at scan rates higher than 0.1 mV/s. This suggests that the critical scan rate for cells with thick-film NMC 622 electrodes is around 0.08 mV/s. The calculated D_{eff} of reference cell with PVDF binder (Table 5-24) is in consistent in the order of magnitude with our previous results using CV [268], but the D_{eff} is lower in comparison to other results using the same active materials but with GITT method at room temperature with a value of 0.7 – 1.0 × 10^{-10} cm^2/s at 50 % SOC [86, 88]. The D_{eff} depends not only on the diffusion of Li-ions in the electrolyte, but also reflects the Li-ions diffusion through the interface between electrode and electrolyte [295]. Table 5-24 shows that for all cells the D_{eff} during charging is higher than during discharging, indicating a faster Li-ion diffusion in the electrolyte from cathode to anode (charging) than from anode to cathode

(discharging). Furthermore, all cells with laser structured electrodes have 14 – 61 % higher D_{eff} during both charging and discharge compared to those with unstructured electrodes, whereas the highest increase in D_{eff} of 61 % belongs to the cell with laser structured PA-added electrode in comparison to the cell with respective unstructured electrode. This can be verified by the rate capability analyses in Figure 5-57, where the cells with laser structured electrodes showed a higher capacity than the ones with unstructured electrodes at C/2 to 2C. In particular, the cells with laser structured PA electrode show 17 % higher D_{eff} during charging and almost the same coefficient during discharging in comparison to those of the reference cell containing unstructured electrode with PVDF as binder.

Table 5-24. Effective Li-ion diffusion coefficient of cells with different types of electrodes during charge and discharge.

	With CA, unstructured	**With AA, unstructured**	**With PA, unstructured**	**With CA, structured**	**With AA, structured**	**With PA, structured**	**Ref. with PVDF**
D_{eff} - charge [cm^2/s]	5.0×10^{-13}	6.0×10^{-13}	5.5×10^{-13}	9.3×10^{-13}	9.3×10^{-13}	1.4×10^{-12}	1.2×10^{-12}
D_{eff} - discharge [cm^2/s]	3.7×10^{-13}	4.2×10^{-13}	4.1×10^{-13}	4.8×10^{-13}	4.8×10^{-13}	6.6×10^{-13}	7.1×10^{-13}

Figure 5-61 displays the Nyquist plots of cells containing unstructured and structured electrodes with different acid additions and the reference cell with PVDF binder. The EIS analyses were performed for all cells at an OCV of 3.6 V (50 % SOC) after the rate capability analyses. The Nyquist plots consist of two semicircles at high frequencies and a tail at low frequency, as described in chapter 5.3.1. The EIS data are fitted using an equivalent circuit model as shown in Figure 5-61.

The fitted parameters of cells employing different types of electrodes are summarized in Table 5-25. Since separator, current collector, electrolyte, and other cell components were the same for all cells, the values of the bulk resistances R_e for all cells are similar. However, the ohmic resistance of cells containing electrodes with PA addition was higher compared to other cells. This might be related to the reduced contact between active material particles with conductive agent, and particles with current collector, since the adhesion strength of aqueous processed electrodes with PA addition was significantly reduced as shown in Figure 5-49.

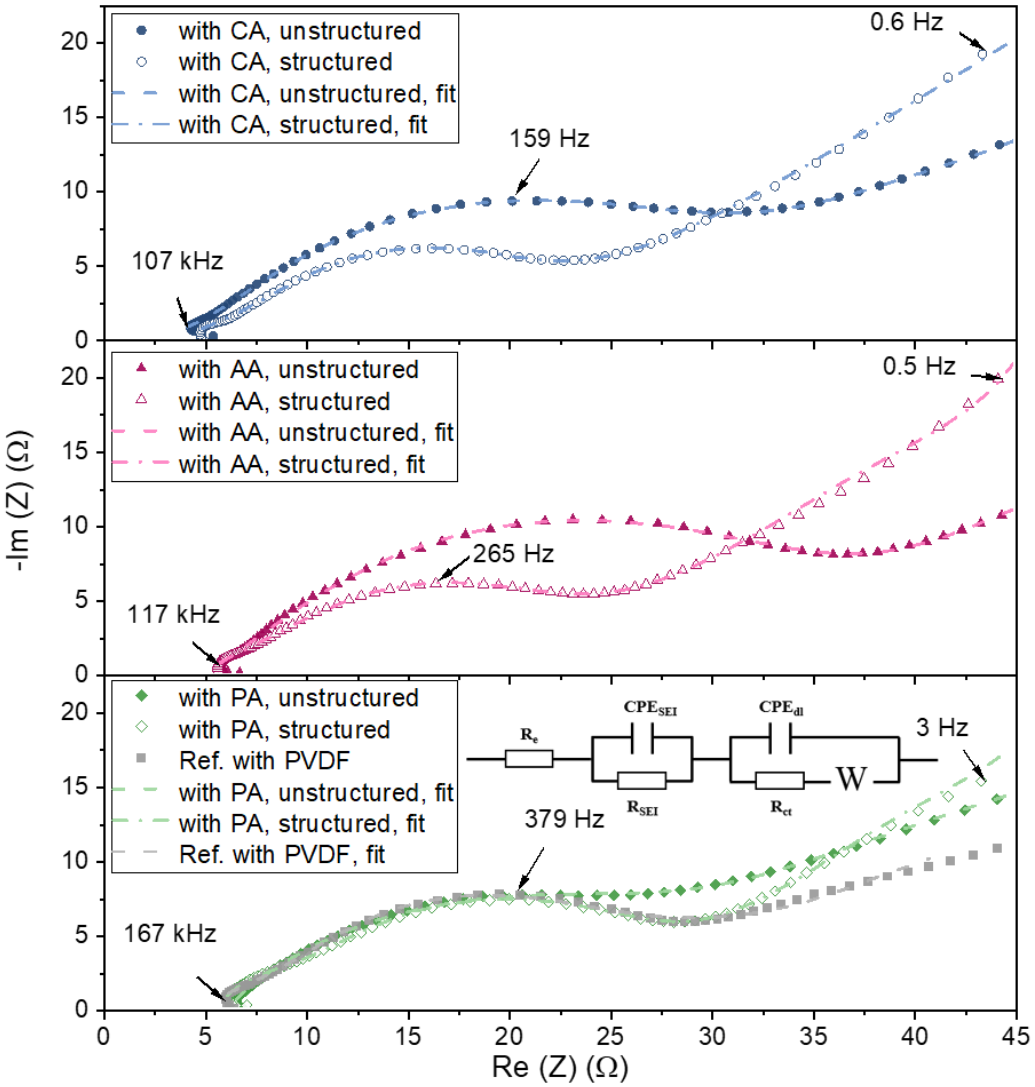

Figure 5-61. Nyquist plots of cells containing thick-film cathodes with different acid additions (CA, AA, PA and with PVDF binder) at an OCV of 3.63 V (50 % SOC) and the fitting curves using the illustrated equivalent circuit model.

In addition, the reference cell with PVDF as binder showed a similar R_{SEI} of 8 Ω compared to recent study [195]. However, the cells containing aqueous processed unstructured electrodes (with CA, AA, and PA addition) showed two to three times higher R_{SEI} compared to the reference cell with PVDF as binder, which suggests that the addition of acid during slurry mixing procedure may affect the interface between the electrolyte and electrode. However, the cells with laser structured electrodes showed 2 – 9 Ω lower SEI resistance in comparison to the respective cells with unstructured electrodes. Nevertheless, all electrodes were assembled vs. Li using half-cell design, thus it cannot be ruled out whether laser structuring would have an impact on the SEI formation on graphite anode side of a full-cells. Therefore, pouch cells with NMC 622 cathode vs. graphite anode will be further investigated in the next chapter. Besides, the increase in τ_{SEI} of the cells containing aqueous processed electrodes compared to the reference cell using PVDF as binder suggests a longer electron transfer time through the interface between the electrode and electrolyte in aqueous processed electrodes.

Table 5-25. Ohmic resistance, SEI resistance, charge transfer resistance, SEI resistance, double-layer resistance, and Warburg resistance of the cells containing aqueous processed thick-film NMC 622 electrodes with different acid additions as well as reference cell with PVDF binder.

	With CA, unstructured	With AA, unstructured	With PA, unstructured	With CA, structured	With AA, structured	With PA, structured	Ref. with PVDF
R_e [Ω]	2.6	5.1	6.2	3.7	4.9	5.7	4.7
R_{SEI} [Ω]	18.0	17.5	24.8	7.5	5.8	5.3	8.1
R_{ct} [Ω]	25.5	20.8	25.4	21.3	18.8	16.6	23.3
Y_{SEI} [$Fs^{\varphi-1}$]	$1.3 \cdot 10^{-4}$	$8.3 \cdot 10^{-5}$	$3.4 \cdot 10^{-4}$	$8.5 \cdot 10^{-5}$	$9.8 \cdot 10^{-5}$	$5.5 \cdot 10^{-5}$	$3.1 \cdot 10^{-5}$
Y_{dl} [$Fs^{\varphi-1}$]	$1.1 \cdot 10^{-2}$	$2.2 \cdot 10^{-3}$	$2.9 \cdot 10^{-3}$	$5.0 \cdot 10^{-3}$	$2.2 \cdot 10^{-3}$	$6.1 \cdot 10^{-5}$	$3.0 \cdot 10^{-3}$
φ_{SEI} [-]	0.77	0.80	0.60	0.90	0.90	0.69	0.97
φ_{dl} [-]	0.28	0.42	0.72	0.34	0.42	0.82	0.37
C_{SEI} [µF]	21.8	16.9	14.3	35.7	43.2	41.5	23.9
C_{dl} [µF]	370.7	33.9	1064.7	64.3	23.2	13.7	29.6
τ_{SEI} [µs]	391.4	295.1	353.8	266.8	270.6	8.0	194.8
τ_{dl} [ms]	9.4	0.7	27.0	1.4	0.4	0.2	0.7
W [Ω]	238.6	58.0	77.4	237.9	60.8	65.9	34.6
χ^2 [-]	0.00014	0.00065	0.00033	0.00023	0.00054	0.00005	0.00051

As for R_{ct}, all cells with unstructured electrodes exhibited similar values of 21 to 26 Ω. However, after lifetime analyses, the charge transfer resistance of the cells with aqueous processed electrodes may increase faster than that of the cells containing electrodes with PVDF binder, which was shown in recent published results using NMC 811 as active material and Li_2SO_4 as pH modifier [195]. In their study, the R_{ct} of cells containing electrodes with PVDF as binder increased from 16 to 19 Ω after 100 cycles at 1C, while cells with aqueous processed electrodes with acid addition showed an increase from 17 to 25 Ω.

The R_{ct} values of cells with laser structured electrodes exhibited reduced 2 – 9 Ω in contrast to the respective cells with unstructured electrodes. This trend has also been reported in full-cells using NMC 622 cathodes and graphite anodes, where the cells with laser structured cathodes exhibited a decrease in R_{ct} of 5 Ω compared to the cells with unstructured electrodes [269]. It might be due to the larger contact area between the liquid electrolyte and the NMC 622 particles in laser structured electrodes, which enhances the Li-ion diffusion and reduces the Li-ion concentration gradient in the electrolyte near the electrode-electrolyte interface. Furthermore, cells with laser structured electrodes exhibited increased C_{SEI} values and reduced C_{dl} values in comparison to cells with respective unstructured electrodes. It is noted that the cell containing laser structured electrode with PA addition showed the lowest characteristic time constant τ_{SEI} and τ_{dl}, indicating that the time to form the CEI layer and double layer is much faster in PA-added NMC 622 electrode in contrast to cells containing other types of electrodes. This must be related to the existence of the thin coating of phosphates on the surface of NMC 622 particles. Besides, the mass transport within the laser structured electrodes is enhanced compared to that in unstructured electrodes. Thus, adding PA into the slurry during mixing can lead to an enhanced electrochemical performance, which is in agreement with rate capability analyses (Figure 5-52) as well as lifetime analyses (Figure 5-59).

Figure S 10 depicts the linear relationship between the real part of impedance Z_{re} and the $\omega^{-1/2}$ from EIS analyses in Figure 5-61. The Warburg impedance coefficient σ_w is derived from the slope and the calculated lithium-ion diffusion coefficient in half-cells are listed in Table 5-26. The calculation of the $D_{eff,EIS}$ has been illustrated in chapter 5.3.1. The $D_{eff,EIS}$ derived from the Warburg element at low frequency range in EIS analyses is about 1/10 than the D_{eff} values obtained by the CV analyses. This is due to that $D_{eff,EIS}$ describes the diffusion of Li-ion in the electrode active material at a given SOC (here is 50 %) in a single-phase region, while the D_{eff} derived from the CV analyses represents the whole charging / discharging process integrally at different SOC [124]. Besides, the lithium-ion diffusion coefficients obtained from GITT are usually higher than the ones from EIS, which is mainly due to its non-equilibrium states, since normally only 10 min is applied before each measuring step in GITT, while at least 30 min is applied before an EIS measurement [124]. The $D_{eff,EIS}$ of all cells with laser structured electrodes were 11 – 32 % higher than those containing respective unstructured electrodes. These data are correlated with the D_{eff} obtained from the CV analyses (Table 5-24). Similar trends were presented by Tran et al. [271], where cells containing laser structured NMC 811 cathodes showed lower charge transfer resistance (108 Ω) and higher $D_{eff,EIS}$ (3.5×10^{-11} cm^2/s) compared to that of the cells with unstructured electrodes (R_{ct} of 137 Ω and $D_{eff,EIS}$ of 1.6×10^{-11} cm^2/s). The difference in $D_{eff,EIS}$ between their work and here could be resulted from many factors, such as the type and amount of the electrolyte, the chemical composition and surface morphology of the active material, the type of separator, or the mechanical pressure inside the cells.

Table 5-26. Warburg impedance coefficient σ_w, and the calculated lithium-ion diffusion coefficient $D_{eff,EIS}$ from EIS analyses in half-cells containing thick-film NMC 622 electrodes processed with different acid additions.

Electrode type	σ_w [Ωs$^{-1/2}$]	$D_{eff,EIS}$ [cm^2/s]
With CA, unstructured	21.9 ± 0.3	2.53×10^{-14}
With AA, unstructured	22.8 ± 0.6	2.34×10^{-14}
With PA, unstructured	34.7 ± 0.5	1.01×10^{-14}
With CA, structured	20.7 ± 0.2	2.83×10^{-14}
With AA, structured	19.8 ± 0.3	3.09×10^{-14}
With PA, structured	33.0 ± 0.2	1.12×10^{-14}
Ref. with PVDF	19.4 ± 0.3	3.22×10^{-14}

The positive effect of the combination of laser patterning and acid modification on electrochemical performance is proved by EIS and CV analyses. On the one hand, EIS analyses showed that after rate capability analyses, the cells containing aqueous processed electrodes with high mass loading had higher R_{SEI} than the reference cells with PVDF as binder, which may be related to the interaction between aqueous processed electrodes and electrolyte. However, the cells with laser structured aqueous processed electrodes exhibited both lower R_{SEI} and R_{ct} compared to those cells with unstructured electrodes. On the other hand, CV analyses and EIS analyses at low frequency range displayed that the effective Li-ion diffusion coefficients in cells with laser structured electrodes were higher than in those with unstructured electrodes. Especially for cell containing laser structured PA-added electrode,

which had a higher D_{eff} during charging and almost the same coefficient during discharging in comparison to the reference cell having unstructured electrodes with PVDF as binder.

Impact of laser structuring strategy on the cell performance

In order to further investigate the impact of different laser structuring strategies on the cell performance, aqueous processed thick-film NMC 622 electrodes with PA addition were structured using different average laser powers and laser scans. In order to adjust the channel width, two strategies were applied, as illustrated in Figure 5-62.

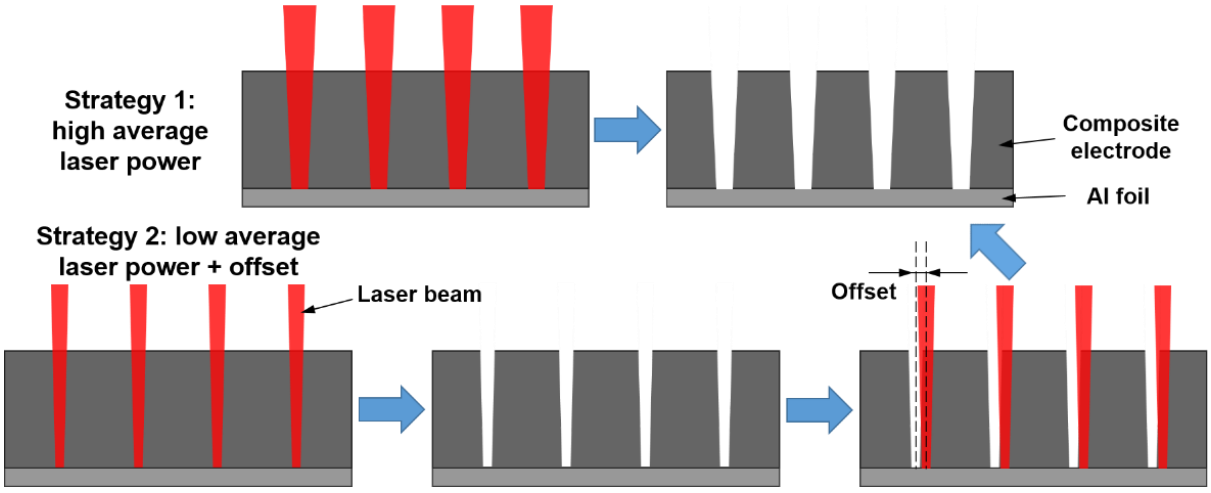

Figure 5-62. Schematic representation of the two laser structuring strategies used to adjust the ablation width.

The first method is to increase the laser power from 2.5 W to 5.0 W. With increasing laser power, the maximum width of the channel structures increases from 30 to 42 µm, as shown in Figure 5-63-a and -b, whereas the FWHM increases from 13 to 26 µm, which is almost twice as much as at low laser power (2.5 W). The mass loss due to laser structuring increases from 7 % to 9 % as summarized in Table 5-27. A higher mass loss is not economically favorable because the cathode material is expensive in comparison to anode and other cell components. However, the laser processing time is significantly shorter due to the reduction of the number of laser scans from 13 to 7, which facilitates the upscaling and the integration of laser processing into large-scale production lines.

The second method is to adjust the channel width by using multiple scans with offset, while keeping the average laser power constant. Four different offset distances varying from 30 µm to 10 µm were applied, as shown in Figure 5-63-c to -f. Since the laser has a spot size of 29 µm, these four offsets correspond to hatch overlaps ranging from 0 % to 67 %. When the offset was set to 30 µm (0 % overlap), the grooves generated by the two laser structuring processes were not connected to each other, resulting in a Π-shaped structure (Figure 5-63-c). As the offset was reduced, the channels were connected and the total channel width was increased in comparison to the single laser structuring with the same average laser power. However, when the offset was reduced to 15 and 10 µm, the channel width was decreased while the ablation depth was increased, affecting the Al current collector, as marked in Figure 5-63-e and -f with dashed circles. In order to avoid the ablation of current collector, 20 µm offset was applied.

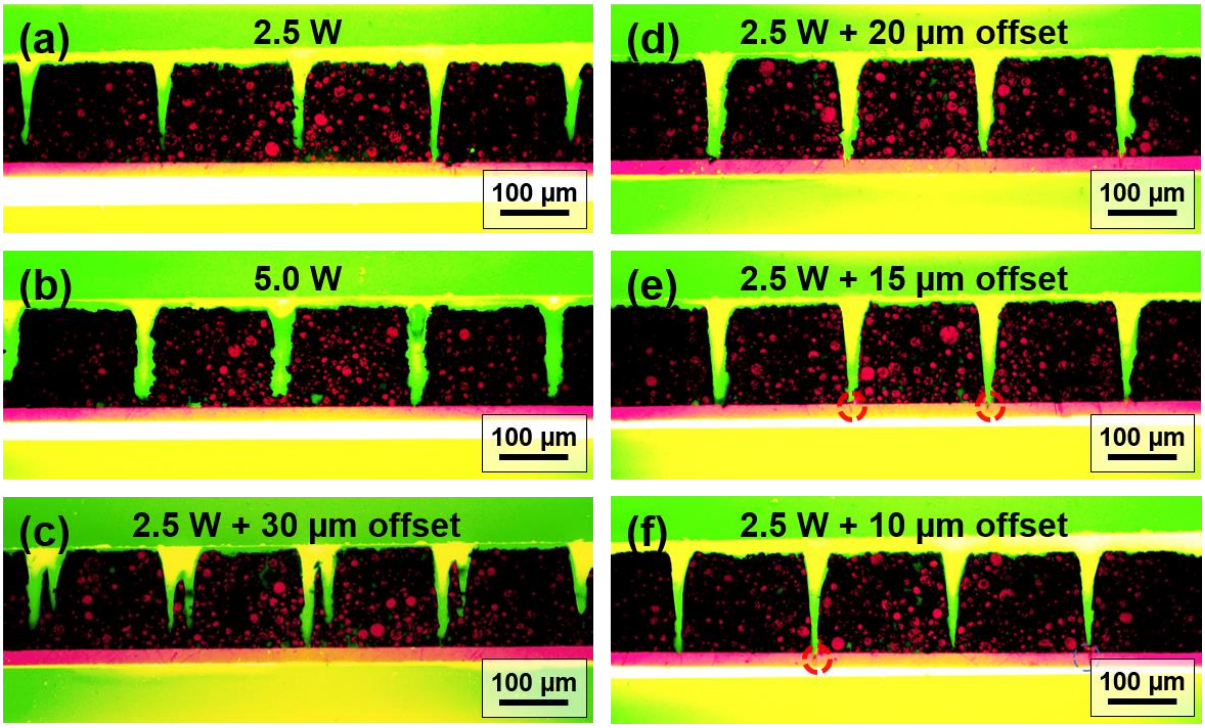

Figure 5-63. Laser structured NMC 622 electrodes with (**a**) 2.5 W and (**b**) 5.0 W average laser power, and double scans with 2.5 W laser power and an offset of (**c**) 30 µm, (**d**) 20 µm, (**e**) 15 µm, and (**f**) 10 µm between two laser structuring processes. For structuring with 2.5 W laser power, 13 scans were applied, while 7 scans were used for laser structuring with 5.0 W. Partial ablation of Al current collector is each indicated by a red dashed circle.

By comparing Figure 5-63-b and -d, it can be observed that a single laser structuring with high average laser power produced channels with a 7 µm narrower maximum width in comparison to the laser structuring processes with 2.5 W and offset. However, the FWHM of the channels using two different structuring strategies remained the same. The highest mass loss of 9.3 % belonged to the electrodes structured using offset scans. Besides, Table 5-27 exhibits that the FWHM of the structured electrodes with offset scans was twice as that of the structured electrode with a single scan and 2.5 W. In addition, Park et al. [265] investigated the impact of laser fluence and laser scans on the morphology of LFP cathodes and reached similar conclusions: The width and ablation depth increases with increasing laser fluence; Low laser fluence and multi-laser scans are effective to achieve groove structures with high aspect ratios. By employing double- or multi-scans strategy with offset at low average laser power, the width of the groove structures (or mass loss) can be flexibly adjusted according to practical needs.

Table 5-27. The active mass loading, areal capacity, and mass loss of NMC 622 cathodes structured with different laser processing strategies.

	Laser scans [-]	**Max. width [µm]**	**FWHM [µm]**	**Active mass loading [mg/cm²]**	**Areal capacity [mAh/cm²]**	**Mass loss [%]**
Unstructured	-	-	-	38.1 ± 0.3	6.33 ± 0.05	-
2.5 W	13	29.8 ± 3.0	13.1 ± 0.5	35.4 ± 0.1	5.89 ± 0.02	7.0 ± 1.1
5 W	7	42.8 ± 3.5	25.7 ± 2.4	34.7 ± 0.3	5.76 ± 0.05	9.0 ± 1.5
2.5 W, with offset	13 + 13	49.7 ± 3.8	24.9 ± 2.9	34.6 ± 0.2	5.75 ± 0.03	9.3 ± 1.2

Figure 5-64-a shows the rate capability of coin cells (half-cells) containing laser structured thick-film NMC 622 electrodes prepared with PA addition using different laser processing strategies. In comparison to the cells containing laser structured electrodes with 2.5 W average laser power, the ones containing electrodes structured at high laser power had a lower discharge capacity of 160 mAh/g at the first cycle at C/20, whereas those with single scan (without offset) structured electrodes achieved 163 mAh/g capacity. Nevertheless, all cells showed a similar initial CE of 86 %. As the C-rate increased from C/10 to C/2, cells with 5.0 W structured electrodes exhibited the lowest capacity in comparison to other cells with laser structured electrodes. Especially at C/10 and C/5, as shown in Figure 5-64-b, the capacity decrease of cells with this type of electrodes was significantly higher. From C/2 to 2C, cells with laser structured electrodes showed a capacity increase of 5 – 64 mAh/g in comparison to the reference cells with unstructured electrodes. In particular, the cells containing structured electrodes with 2.5 W and with offset scans exhibited 39 and 64 mAh/g at C/2 and 1C, respectively. In contrast, cells with 5.0 W structured electrodes showed lower capacity increase at C/2 to 2C. Besides, they retained lower discharge capacity at 3C compared to the reference cells with unstructured electrodes.

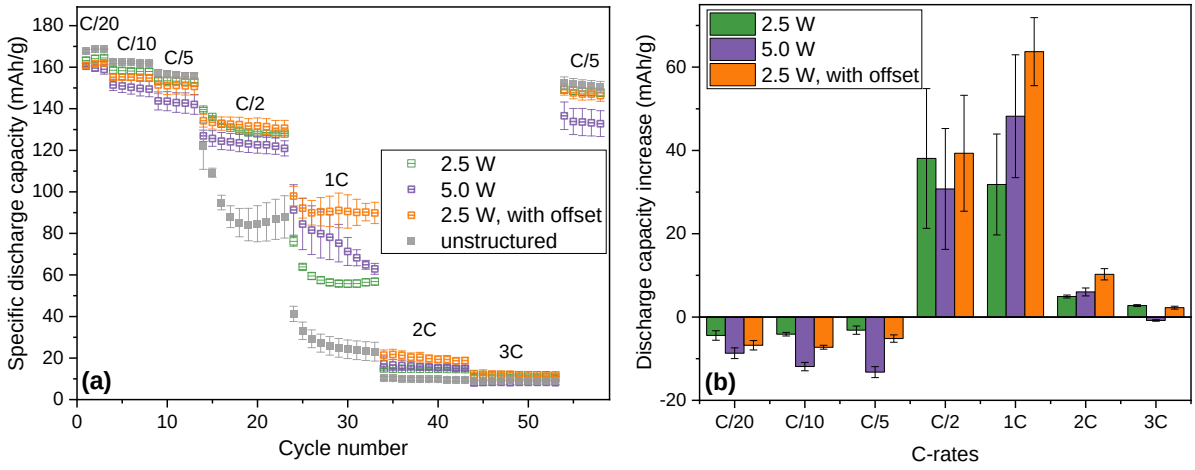

Figure 5-64. Rate capability analyses of (**a**) the half-cells containing laser structured NMC 622 prepared with PA addition with three different laser structuring strategies, and (**b**) the discharge capacity increase of the cells containing laser structured electrodes in contrast to ones with unstructured electrodes.

The lifetime analyses of half-cells containing electrodes with different laser structuring strategies at C/2 are shown in Figure 5-65. The cells containing electrodes structured with 2.5 W average laser power and those structured with 2.5 W and offset scans exhibited around 125 mAh/g initial capacity, while others showed about 110 mAh/g initial capacity. The cells with 2.5 W structured electrodes showed the lowest discharge capacity after 100 cycles, retaining only 9 % in contrast to their initial capacity, while the ones containing structured electrodes with offset scans achieved 60 % capacity after lifetime analyses. The cells with 5.0 W structured electrodes and the reference cells with unstructured electrodes showed similar capacity retention of 40 % after 100 cycles.

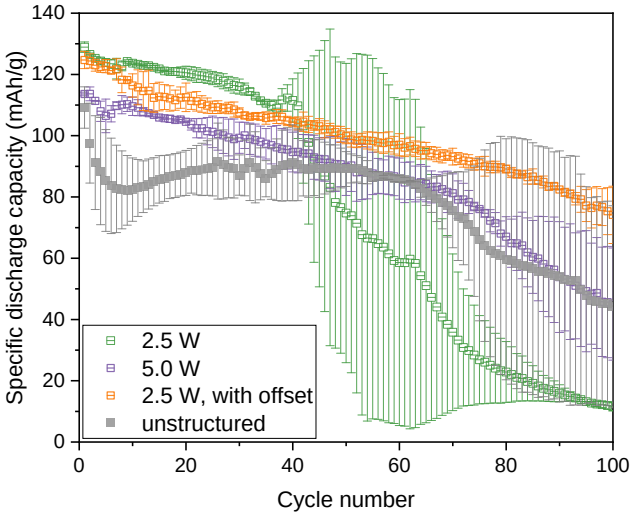

Figure 5-65. Lifetime analyses at C/2 of half-cells containing thick-film NMC 622 electrodes processed with PA addition and laser structured using different strategies in contrast to the reference cells with unstructured electrodes.

Our previous study has shown that for cells containing NMC 622 electrodes with 150 µm thickness, the discharge capacity increased at C-rates ≥ C/2 with decreasing laser generated line pitch. In other words, it is assumed that with increasing mass loss of the laser structured electrodes, an enhanced rate capability at high C-rates should be achieved [268]. However, the electrode mass losses due to laser structuring with 5.0 W and 2.5 W with offset scans were similar, but the cells containing electrode with former structuring strategy displayed less discharge capacity in rate capability and lifetime analyses. The performance deterioration of the cells with high laser power structured electrodes may be resulted from the interaction between laser-induced plasma and active materials. As the laser fluence increases from 1.5 to 3.0 J/cm^2 (average laser power from 2.5 to 5.0 W), the plasma temperature increases and the composite electrode attached to the channel geometry may face an increased temperature due to plasma interaction which is even more pronounced with increasing channel aspect ratios. Although no melt formation was detected in laser structured NMC 622 cathodes, which is similar to the results from Mangang et al. [15] using fs-laser ablation of the LFP cathodes, the increased temperature may lead to selective ablation of binder and conductive agent, which was detected in composite LCO electrode using fs-laser ablation [270] or in NMC 111 electrode with surface treatment using IR-laser radiation [356]. The isolated inactive NMC 622 particles without electrical contact to the current collector could result in the capacity decrease in rate capability analyses and lifetime analyses.

In addition, it was found that there are significant differences in electrochemical stability between half-cells assembled with aqueous processed cathodes from the same electrode sheet [201]. Thus, it is too early to draw conclusions about the optimal laser structuring strategy for thick-film aqueous processed NMC 622 electrodes. Therefore, the original and the optimized laser structuring strategies, i.e., with 2.5 W, and with 2.5 W plus offset, were applied for the structuring of the aqueous processed NMC 622 electrodes, which were assembled in pouch cells vs. graphite anodes. Rate capability, lifetime analyses, and EIS results will be presented in the next chapter.

5.5. Pouch cells with NMC 622 cathodes and graphite anodes

Based on the previous results, two sets of thick-film cathodes were selected for the assembly of pouch cells, which were NMC 622 cathodes processed with state-of-the-art PVDF binder, and ones prepared with water-soluble binders and PA addition during slurry mixing process. In addition, two different laser strategies were applied for the structuring of the PA-added NMC 622 cathodes, which were with 2.5 W average laser power, and 2.5 W with 20 µm offset scans. Since the aqueous processed NMC 622 cathodes had lower areal capacity in comparison to ones with PVDF binder due to Li-leaching, graphite anodes with two different areal capacity were prepared to realize a similar cell-balancing-factor for all pouch cells. The graphite anodes were fabricated using water-soluble binders with 93 wt% active material as described in chapter 4.2.2, and the laser patterning of graphite anodes was performed using setup with high power ultrashort laser as shown in Figure 4-10. The laser parameters such as laser power, repetition rate, scan speed, and the number of laser scans applied to pattern the graphite anodes are given in chapter 4.3.2. For the structuring of graphite anodes, a 6 times beam expansion was applied, while the laser spot size before the BeT was determined as 2.6 mm. Thus, the laser spot size can be determined using equation (3.21):

$$d_f \approx \frac{M^2 f}{d_L}\frac{4\lambda}{\pi} = \frac{1.1 \cdot 255\ mm \cdot 4 \cdot 1030\ nm}{2.6\ mm\ \cdot 6 \cdot \pi \cdot 1000} \approx 24\ \mu m \tag{5.15}$$

The laser pulse energy E_{pulse} and the peak fluence Φ applied for the laser structuring of the graphite anodes with water-based binder can be calculated using equation (5.4) and (5.5):

$$E_{pulse} = \frac{P_L}{f_{rep}} = \frac{37\ W}{1\ MHz} = 37\ \mu J \tag{5.16}$$

$$\Phi = \frac{2E_{pulse}}{\pi\omega_0^2} = \frac{2 \cdot 37\ \mu J}{\pi \cdot (\frac{24\ \mu m}{2})^2} = 16.4\ J/cm^2 \tag{5.17}$$

Compared to the laser pulse energy applied for the structuring of NMC 622 cathodes (5 µJ), the pulse energy for graphite anode structuring was more than 7 times higher, while the peak fluence was 16 times higher. Besides, the laser pulse energy used in this work for the laser structuring of graphite anodes was higher than the parameters reported in other studies [19, 170, 275, 277, 280]. The areal capacities of different cathodes and anodes and the mass loss due to laser structuring are listed in Table 5-28. The dimensions of cathodes and anodes assembled in pouch cells are shown in Figure 4-14. The cell-balancing-factor of all cells were adjusted to 1.1 – 1.2 by matching the areal capacity of anodes with cathodes.

Table 5-28. Areal capacities of different types of electrodes and the mass loss of laser structured electrodes compared to that of unstructured ones. For all aqueous processed NMC 622 cathodes, PA was added during the slurry mixing process and the slurry pH value was adjusted to 9.2.

Electrode type	Areal capacity [mAh/cm^2]	Mass loss [%]
Cathode with PVDF binder, unstructured	6.07 ± 0.08	-
Cathode with PVDF binder, structured	5.80 ± 0.09	3.4 ± 2.2
Cathode, aqueous processed, unstructured	5.93 ± 0.09	-
Cathode, aqueous processed, 2.5 W structured	5.64 ± 0.08	4.2 ± 1.3
Cathode, aqueous processed, 2.5 W + 20 µm offset structured	5.28 ± 0.10	10.2 ± 1.9
Anode, unstructured, thin	6.42 ± 0.11	-
Anode, unstructured, thick	7.26 ± 0.12	-
Anode, structured, thick	6.39 ± 0.13	12.0 ± 3.3

Figure 5-66-a displays the cross-sectional view of a laser structured graphite anode. The pitch between channels was set to 350 µm to match the areal capacity of anodes with that of cathodes, and the channel structures show a maximum width of 46.4 ± 4.9 µm and a FWHM of 27.7 ± 2.3 µm. Compared to the channel structures in NMC 622 cathodes having a V-shapes with wider opening near the electrode surface, structured graphite anodes provide more rectangular type channels and higher mass loss. Besides, from Figure 5-66-b it can be observed that there is no or only a small amount of residual electrode material on the copper foil in the laser generated grooves.

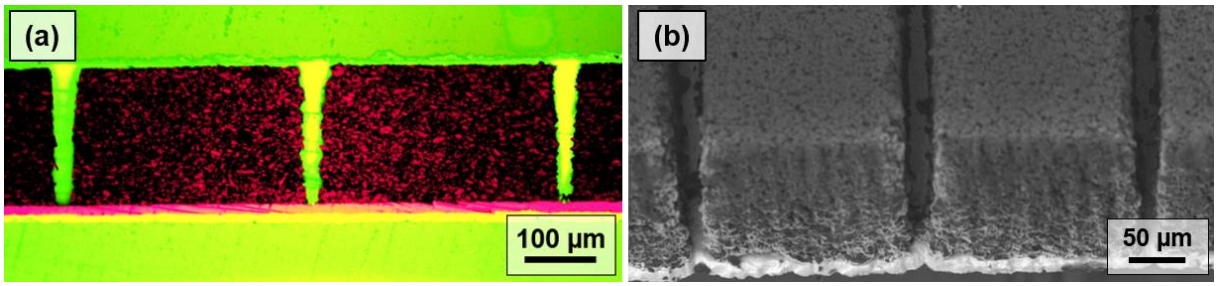

Figure 5-66. The (**a**) cross-sectional view and (**b**) the SEM image of the laser structured graphite anode (laser repetition rate: 1 MHz, average laser power: 37 W, scan speed: 20 m/s, laser scans: 92).

Rate capability analyses of pouch cells containing NMC 622 cathodes prepared with PVDF binder or water-soluble binder with PA addition vs. graphite anodes are shown in Figure 5-67. The reference cells refer to the cells containing NMC 622 cathodes with PVDF binder. As summarized in Table 5-29, pouch cells with unstructured aqueous processed NMC 622 cathodes exhibited the lowest initial discharge capacity of 97 mAh/g, whereas the cells with laser structured aqueous processed NMC 622 cathodes displayed a capacity of 120 – 125 mAh/g, which is similar to those with unstructured NMC 622 cathodes with PVDF binder. The highest initial discharge capacity of 157 mAh/g belonged to the cells with structured NMC 622 cathodes with PVDF binder. In addition, all cells showed a lower initial discharge capacity compared to the second cycle during formation at C/20. The discharge capacity increase in pouch cells with aqueous processed NMC electrodes with increasing cycle number during formation was also observed in another study [200], which may be due to the swapping of Li-ions in the electrolyte with part of the protons on the surface of aqueous processed NMC 622 particles.

Table 5-29. Initial CE and discharge capacity of pouch cells containing different NMC 622 cathodes at C/20.

Cathode type	Initial CE [%]	Initial discharge capacity [mAh/g]
Ref., unstructured	83.3 ± 3.1	126 ± 23
With PA, unstructured	83.8 ± 1.6	97 ± 15
Ref., structured	86.0 ± 3.2	157 ± 12
With PA, structured, 2.5 W	81.7 ± 0.7	120 ± 4
With PA, structured, 2.5 W + offset	84.3 ± 3.3	125 ± 3

The initial CE of pouch cells was lower in contrast to that of coin cells (half-cells). For instance, reference pouch cells with unstructured electrode displayed an initial CE of 83.3 %, whereas coin cells showed an initial CE of 88.8 %. This difference should be owing to the SEI formation on the graphite anodes, which comprises multiple organic and inorganic layers [357]. This suggests that more electrolyte consumption is required to form the SEI on graphite than on Li counter electrode or the CEI formation on NMC 622 cathodes in half-cells during the first charging / discharging at C/20. After the first cycle, the CE rose to 99 – 100 % for all pouch cells, indicating an adequate SEI formation on the graphite anodes.

At C/10 and C/5, the cells having laser structured electrodes had up to 5 mAh/g lower specific discharge capacity compared to those with unstructured electrodes (Figure 5-67-a). The charge and discharge profiles at C/10 of pouch cells with different types of NMC 622 cathodes are displayed in Figure S 11-a, -c, and -e. The IR-drops at the beginning of discharge profile for all cells was about 0.05 V, which is similar to that of the half-cells containing the same cathode types. From 4.2 to about 3.4 V, no difference was observed in specific discharge capacity between cells with unstructured and laser structured electrodes. However, at the end of charging and discharging, the cells with laser structured electrodes reached about 5 mAh/g less capacity in contrast to the cells with unstructured electrodes.

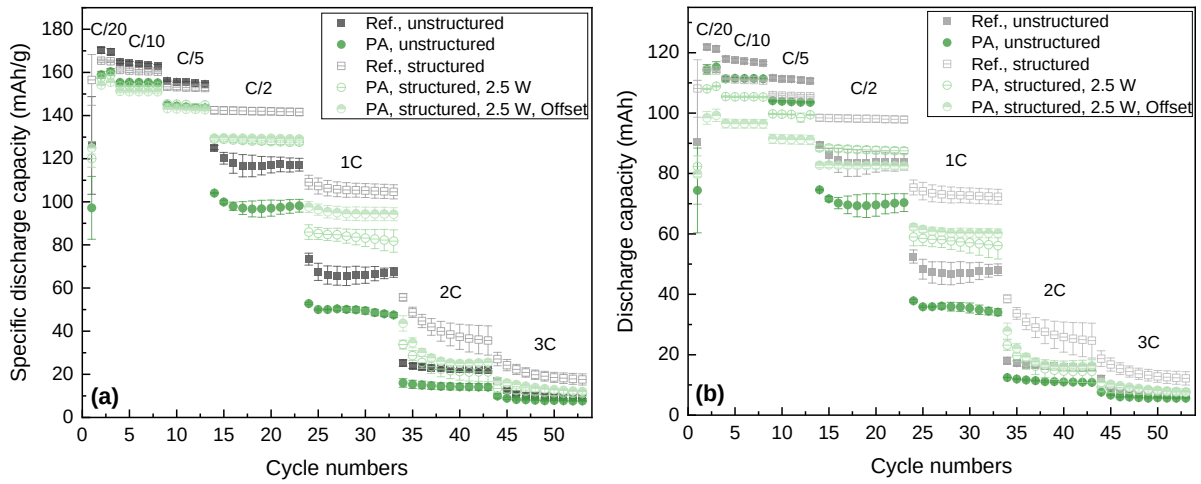

Figure 5-67. Rate capability analyses of pouch cells using different NMC 622 cathodes and graphite anodes. (**a**) The specific discharge capacity with regard to the mass of active material in cathodes, and (**b**) the total discharge capacity of full-cells.

As the C-rate increased to C/5, the difference in specific discharge capacity between the pouch cells with unstructured electrodes and those with laser structured electrodes reduced, while at C/2 to 2C, all cells with laser structured electrodes exhibited higher specific capacity in comparison to cells with unstructured electrodes. For example, for reference cells containing

NMC 622 cathodes with PVDF binder, those with laser structured electrodes showed 25 mAh/g higher specific discharge capacity at C/2, while an increase of 32 mAh/g was observed for cells with aqueous processed cathodes. Figure S 11-b, -d, and -f show the discharge profiles of pouch cells containing different types of NMC 622 cathodes at C/2. Compared to the cells with unstructured electrodes, the ones with laser structured electrodes exhibited a higher discharge plateau (or a lower charge plateau) and reached 20 – 25 mAh/g more capacity after being fully discharged (or charged). This is in line with the rate capability analyses of half-cells using the electrodes from the same batch as shown in Figure 5-58, illustrating that the laser structuring can reduce the cell polarization of full-cells, and is particularly suitable for the cells containing electrodes with high mass loading. A maximal increase of 44 mAh/g was found for cells containing laser structured PA-added cathodes with offset scans in contrast to cells with unstructured electrodes at 1C, whereas the cells containing laser structured PA-added cathodes with single scan showed a specific discharge capacity increase of 34 mAh/g, which is slightly lower in comparison to 40 mAh/g specific capacity increase for reference cells having laser structured cathodes with PVDF binder. As the C-rate increased to 2C, pouch cells with laser structured PA-added NMC 622 cathodes exhibited similar specific capacity in comparison to reference cells containing unstructured electrodes with PVDF binder. The cells with laser structured cathodes with PVDF binder maintained a discharge capacity of 19 mAh/g at 3C, while other cells exhibited 12 mAh/g specific capacity.

Figure 5-67-b shows the total discharge capacities of pouch cells containing different types of electrodes. From C/20 to C/5, Li-leaching during the aqueous processing of NMC 622 slurry led to a discharge capacity decrease of about 6 mAh in comparison to ones with PVDF binder. Besides, for cells containing PA-added cathodes, 2.5 W laser structuring further reduced the cell capacity by 6 mAh, whereas a drop in capacity of about 15 mAh at C/20 to C/5 was observed for cells containing laser structured cathodes with offset scans in contrast to ones using unstructured electrodes. The capacity decreases at low C-rates were proportional to the mass loss due to laser structuring. At C/2, laser structuring began to show its advantage: An increase in capacity of 15 mAh was observed for pouch cells containing laser structured cathodes with PVDF binder in contrast to those with unstructured cathodes, while cells containing laser structured PA-added cathodes with 2.5 W average laser power and with 2.5 W offset scans showed a capacity increase of 24 and 19 mAh, respectively, which is similar or higher than that of the reference cells containing unstructured cathodes with PVDF binder. In addition, the capacity drop of the cells with laser structured electrodes during the first 3 cycles at C/2 was not detected, indicating a higher cycling stability at high C-rates. When the C-rate was increased to 1C, the capacity of the cells containing laser structured PA-added cathodes was 11 – 13 mAh higher in contrast to the reference cells having unstructured cathodes with PVDF binder, while at 2C, cells containing laser structured PA-added cathodes achieved similar capacity compared to the reference cells containing unstructured cathodes with PVDF binder. Thus, by combining laser structuring with aqueous processed thick-film electrodes, it is possible to achieve the same or higher cell capacity than using cathodes with state-of-the-art PVDF binder, especially at high C-rates from C/2 to 2C.

The differential capacity dQ/dV plots of pouch cells with unstructured and laser structured electrodes from the third cycle at C/20 are displayed in Figure 5-68. An interval of 2 mV was

used to acquire the dQ/dV data from rate capability analyses using a self-made Matlab script [*Ulrich Rist, personal communication, April 09, 2024*], the raw data were subsequently smoothed using the ‘‘Adjacent-Averaging’’ filter (with weighted average and points of window of 10) in OriginPro 2019 software. Three peaks were observed during charging and discharging, respectively, which is similar to the previously reported literatures using NMC cathodes vs. graphite anodes [94, 358, 359]. The first distinct peak during charging appeared at 3.46 V (c1), followed by the main peak (c2) at 3.64 V. A third peak (c3) was observed at around 3.85 V, which is significantly weak in contrast to the other peaks. During discharging, the main anodic peak (a2) appeared at 3.58 V for all cells with unstructured electrodes, while the second small peak (a1) located at 3.39 V. After comparing the peak positions obtained for pouch cells to that for half-cells containing the NMC 622 cathodes from as shown in Figure 5-23-b and Figure S 8-c, it is identified that the c2 peak should be ascribed to the phase transition of NMC 622 from hexagonal (H1) to monoclinic (M) phase, as discussed in chapter 5.3.1 and 5.4.5, while the new appeared c1 peak must be associated to the lithiation of graphite ($C_6 \rightarrow LiC_x$), which is in good agreement with another study [94]. The weak c3 peak is associated with the phase transition of NMC 622 from monoclinic (M) to hexagonal (H2) phase [86, 94].In addition, the c1 peaks exhibited similar intensity for cells with laser structured electrodes in contrast to ones with unstructured electrodes, while the intensity of c2 peaks reduced for cells with laser structured electrodes, especially for cells containing aqueous processed cathodes. The peak area of c2 was reported to be proportional to the total cell capacity [359, 360]. In Figure 5-68-b, the intensities of c2 and a2 peaks decreased for cells containing laser structured electrodes with increasing mass loss due to laser structuring compared to those with unstructured electrodes, which is coherent with the capacity loss at C/20 as shown in the rate capability analyses (Figure 5-67). This further indicates that the c2 and a2 peaks are related to the Li-ion de- / intercalation in NMC 622 cathodes.

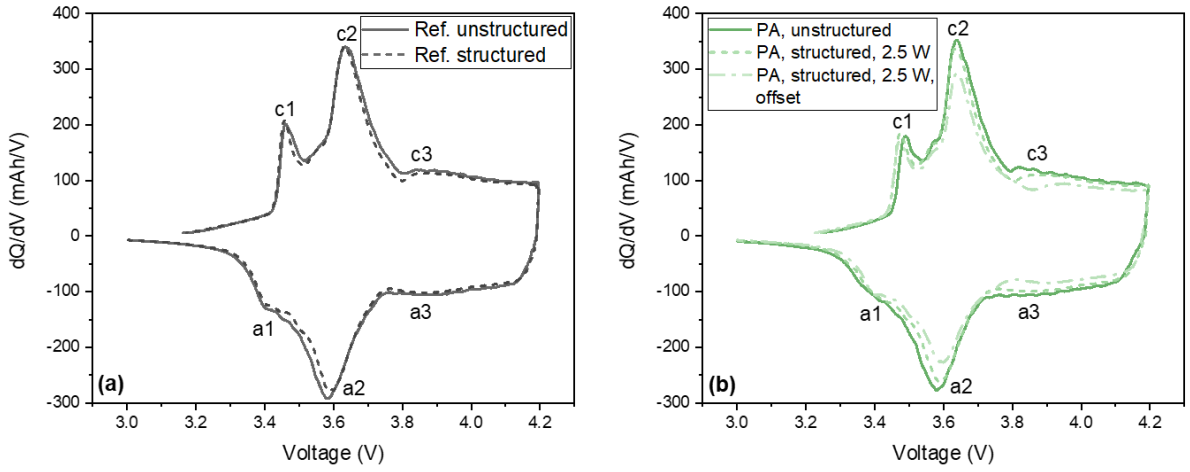

Figure 5-68. The dQ/dV plots of the pouch cells containing unstructured and laser structured NMC 622 cathodes with (**a**) PVDF as binder and (**b**) with PA addition during mixing procedure.

For the applications of LIBs in automobile industry, power density and energy density are more practical metrics to characterize the electrochemical performance of batteries. In order to compare the pouch cells containing thick-film electrodes with PVDF binder and those with water-based binders, as well as the enhanced performance of cells with laser structured

electrodes, the energy density on cell level was calculated from the rate capability analyses and plotted vs. the power density (Figure 5-69), which is also known as Ragone plot. As shown in Figure 4-14, one cathode and one anode were applied for the assembly of each pouch cell in this work. Thus, in order to be more consistent with practical applications in battery industry, the total volume of the composite electrodes with a footprint of 49 × 49 mm^2, separator, plus half volume of Al and Cu current collector, were used to calculate the volumetric energy density and power density of pouch cells. A high capacity (Ah) required for the practical applications can be obtained by stacking this basic unit using double-side coated electrodes. The mass of the cathode and anode, half the mass of the Al and Cu foils, and the entire mass of the electrolyte and separator are taken into account when calculating the gravimetric energy and power density. The calculation and the used data can be found in Appendix C.

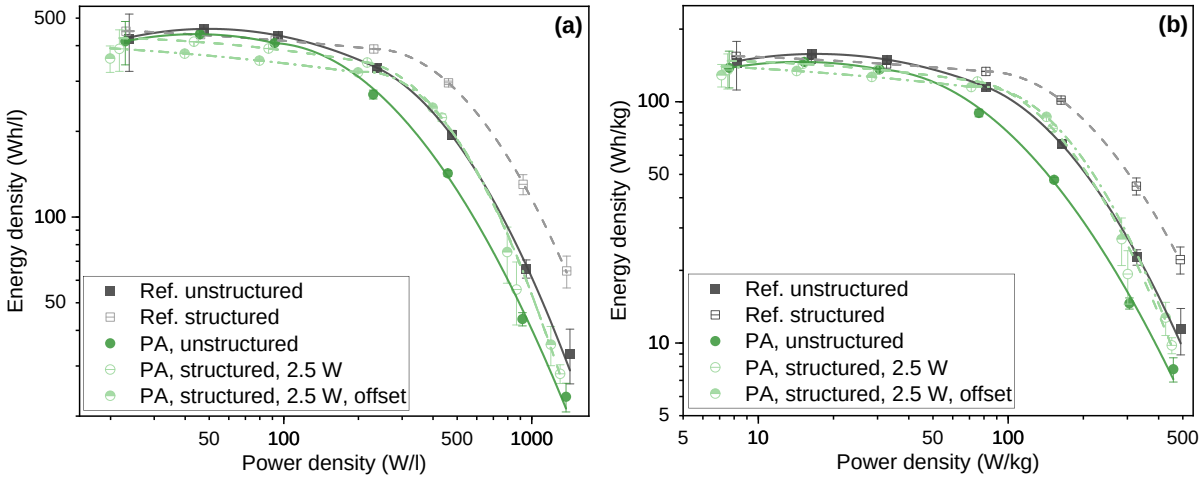

Figure 5-69. Ragone plots for the pouch cells containing unstructured or laser structured thick-film electrodes with PVDF binder or with water-based binder and PA addition. The (**a**) volumetric and (**b**) gravimetric energy densities vs. power densities are plotted taking into account all cell components in full-cells.

The Ragone plot reveals that for pouch cells with thick-film electrodes, both volumetric and gravimetric energy densities decrease as the power density increases. The trade-off between energy density and power density is governed by the Li-ion diffusion kinetics in thick-film electrodes. Figure 5-69-a displays that at power density less than 130 W/l, cells with unstructured thick-film electrodes achieve a higher energy density than those with laser structured electrodes, implying that for low power applications (C-rates below C/2), the enhancement of Li-ion diffusion kinetics in 3D patterned electrodes is insufficient to compensate the mass loss of active materials due to laser structuring. Besides, for cells with PA addition, the crossing point, where the energy density reaches the same value for both cells with unstructured and laser structured electrodes, shifts to a higher power density as the mass loss increases. For example, the crossing point is located at 140 W/l for cells with cathodes structured at 2.5 W, whereas for cells containing cathodes structured with offset scans, the point increases to 190 W/l. This suggests that by reducing the mass loss in electrodes due to laser structuring, laser structuring begins to show its advantages at lower power density. Moreover, for cells with PVDF binder, an increase in energy density of up to 110 Wh/l is observed at power density from 140 to 1300 W/l after laser structuring. In contrast, cells containing unstructured PA-added cathodes exhibit the lowest energy density due to the

irreversible Li-leaching during aqueous slurry preparation. However, from 220 to 600 W/l, the energy densities of the cells containing laser structured aqueous processed cathodes increase to the same level as that of the reference cells containing unstructured electrodes with PVDF binder. The same trend is observed in Figure 5-69-b, where cells with PA-added laser structured electrodes reach a higher gravimetric energy density at 80 to 220 W/kg in contrast to the reference ones containing unstructured cathodes with PVDF. Besides, if only comparing cells containing aqueous processed electrodes, laser structuring can enhance the energy density in the power density range from 140 to 1300 W/l (or 40 – 450 W/kg).

Figure 5-70 exhibits the lifetime analyses of pouch cells which were performed at C/2 (charge and discharge), and after each 100 cycles at C/2, the cells were cycled at C/5 to examine the capacity retention. In comparison to the lifetime analyses using half-cells (Figure 5-53), whose capacity decreased intensively at around 70 to 100 cycles [201], full-cells exhibited extraordinary performance and remained stable after 500 cycles.

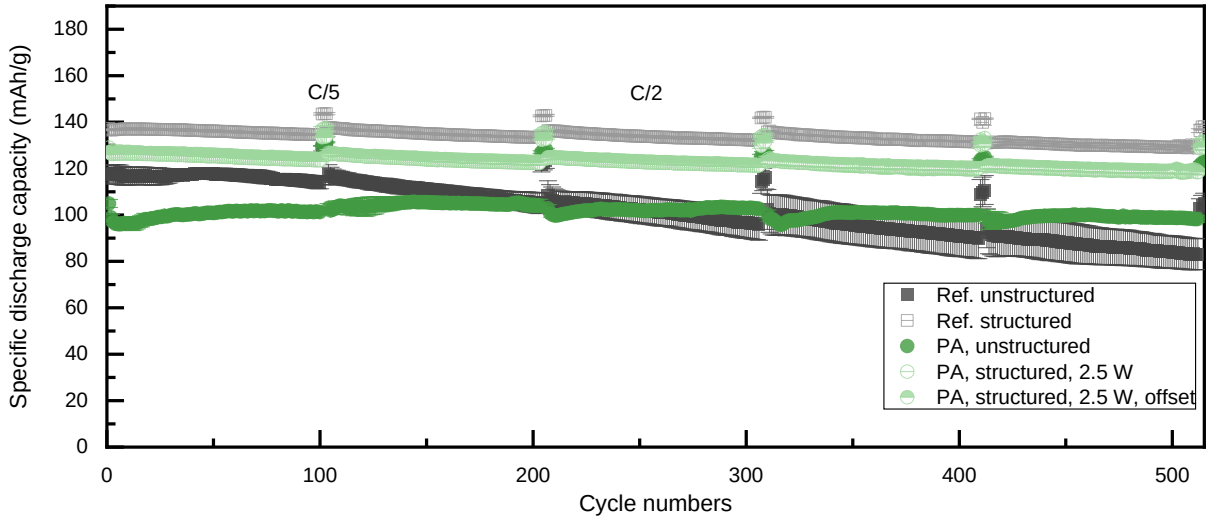

Figure 5-70. Lifetime analyses of pouch cells containing unstructured and laser structured reference cathodes with PVDF binder in comparison to ones containing aqueous processed PA-added NMC 622 cathodes which were structured using two different scan strategies.

At the beginning of the lifetime analyses, cells containing aqueous processed cathodes exhibited 10 mAh/g lower discharge capacity than the reference cells having cathodes with PVDF binder. This must be due to the reaction of the residual water in the aqueous processed cathode with fluorine-based Li salt (e.g., $LiPF_6$), which leads to the formation of hydrofluoric acid (HF) in the cell [361]. The HF attack on the surface of NMC 622 particles can further generate water, which in return accelerates the production of HF; Besides, detached inactive NMC 622 particles can be generated through cracks formation in active materials, and thus the cells show an decrease in capacity [186]. The reference cells containing unstructured thick-film cathodes with PVDF binder displayed continuous capacity drop from 117 to 83 mAh/g, retaining 71 % capacity after 500 cycles, whereas those containing unstructured aqueous processed electrodes with PA addition achieved 94 % capacity after 500 cycles. The enhanced cycling stability of cells containing aqueous processed NMC cathode in contrast to ones containing electrodes with PVDF binder was also observed in other studies [196, 200]. However, the mass loading of the cathode in this work is much higher in comparison to the so

far published literatures. The enhanced lifetime of cells containing aqueous processed cathodes with PA addition indicates that PA can stabilize the surface of NMC 622 particles and may hinder the dissolution of transition metal-ions as suggested in other studies [194, 201].

The SOH of all cells is determined using equation (3.9) and only the cycles at C/2 are shown in Figure S 12. The pouch cells containing laser structured cathodes with PVDF binder exhibited 94 % SOH after 500 cycles, while cells containing laser structured PA-added cathodes with 2.5 W and with 2.5 W plus offset scans showed 92 % and 93 % SOH, respectively.

In order to estimate the EoL of pouch cells with different types of cathodes, a linear fit was applied to the data from the lifetime analyses. As already observed in Figure S 12, reference cells with unstructured electrodes reached EoL after 369 cycles, while the reference cells with laser structured electrodes were expected to survive the longest with 1952 cycles. In contrast, cells containing unstructured PA-added cathodes would last 1664 cycles, whereas the ones containing laser structured cathodes with single scan and offset scans could achieve 1480 and 1815 cycles before reaching their EoL, respectively. This indicates that for the reference cells, laser structuring can significantly extend their EoL by a factor of 4.3 and meanwhile increases the capacity. In addition, the EoL of cells with aqueous processed unstructured cathodes is 3.5 times longer than that of the reference cells, while offset scans strategy can further extend their life by 9 %. However, if we consider the total discharge capacity as displayed in Figure 5-67-b, the structuring strategy with single scan and an average laser power of 2.5 W is preferred for aqueous processed cathodes, since about 5 mAh higher discharge capacity was obtained by reducing the mass loss due to laser structuring.

EIS analyses were performed on all pouch cells at 50 % SOC (3.63 V) after the rate capability analyses and after every 100 cycles during lifetime analyses. In chapter 5.3.1, an equivalent circuit with two R-CPE elements and a resistance connected in series was illustrated, which represent the bulk resistance, SEI resistance and charge transfer resistance. However, in contrast to half-cells, full-cells consist of both graphite anodes and NMC 622 cathodes. In order to distinguish the effects from anode and cathode, an equivalent circuit with three in series connected R-CPE elements are more appropriate for the data fitting [131]. However, due to the limitation of the test frequency, the first semicircle corresponding to the SEI formation could not be detected. Thus in this work, the main focus is on the charge transfer processes of the anode and cathode at middle frequencies [362, 363], and the resistances were fitted using an equivalent circuit as shown in Figure 5-71-a (marked with red rectangle).

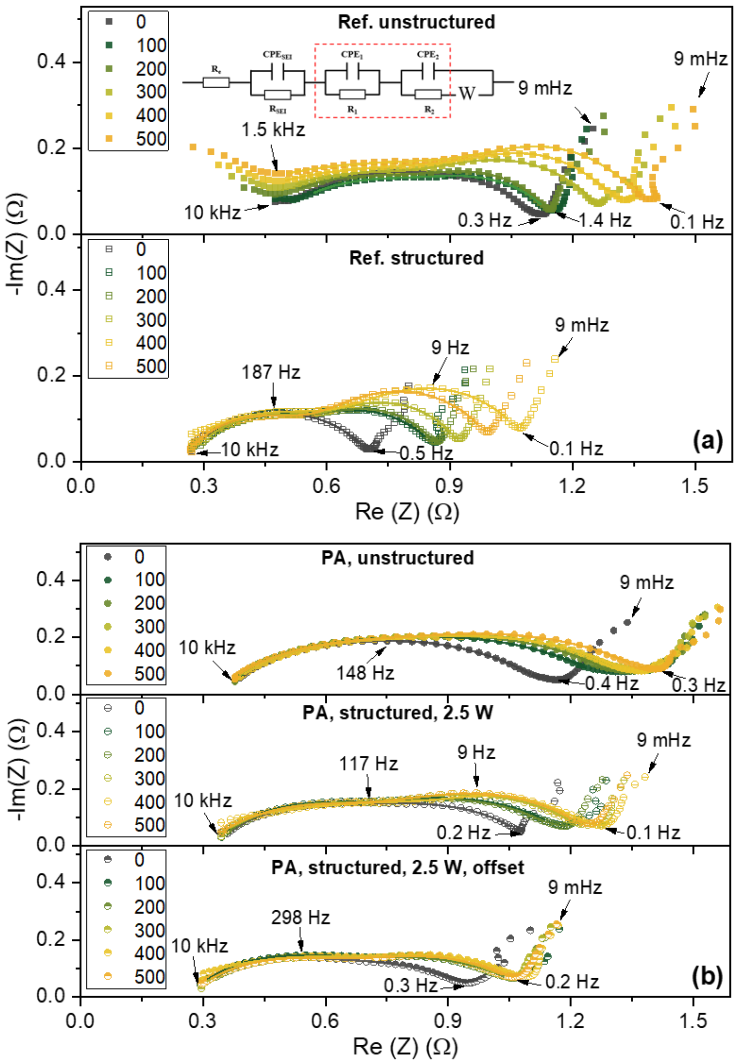

Figure 5-71. Nyquist plots of the pouch cells containing unstructured and laser structured thick-film NMC 622 cathodes with (**a**) PVDF as binder and (**b**) with water-soluble binders and PA addition at 50 % SOC (3.63 V). Measurements were performed subsequently to rate capability analyses and after every 100 cycles during the lifetime analyses. The respective fitting curves were related to the illustrated equivalent circuit model.

The semicircles from 10 kHz to about 0.1 Hz in Figure 5-71 did not display a clear separation between the contribution of anode and cathode and thus resulted in a plateau-shaped form. However, the widening of the total semicircles was observed with increasing cycle number, which is also observed in other studied using half-cells [364] or full-cells [362, 365] containing NMC cathodes. Furthermore, by comparing the semicircles before the lifetime analyses (0 cycle), all pouch cells with laser structured electrodes showed a reduced semicircle in contrast to those with unstructured electrodes, suggesting an overall lower charge transfer resistance in laser structured electrodes. Similar results have been observed in another study [170]. In addition, results from Middlemiss et al. [366] using pouch cells with three-electrode configurations showed that the semicircle corresponding to the charge transfer resistance consisting of anode and cathode, with anode at higher frequencies and cathode at lower frequencies. The characteristic frequencies ($1/\tau_{dl}$) of the fitted resistances R_1 and R_2 were checked to ensure that the resistances were correctly matched to the anode and cathode in full-cells. Other parameters obtained by the fitting using equivalent circuit model are listed in Table S 1.

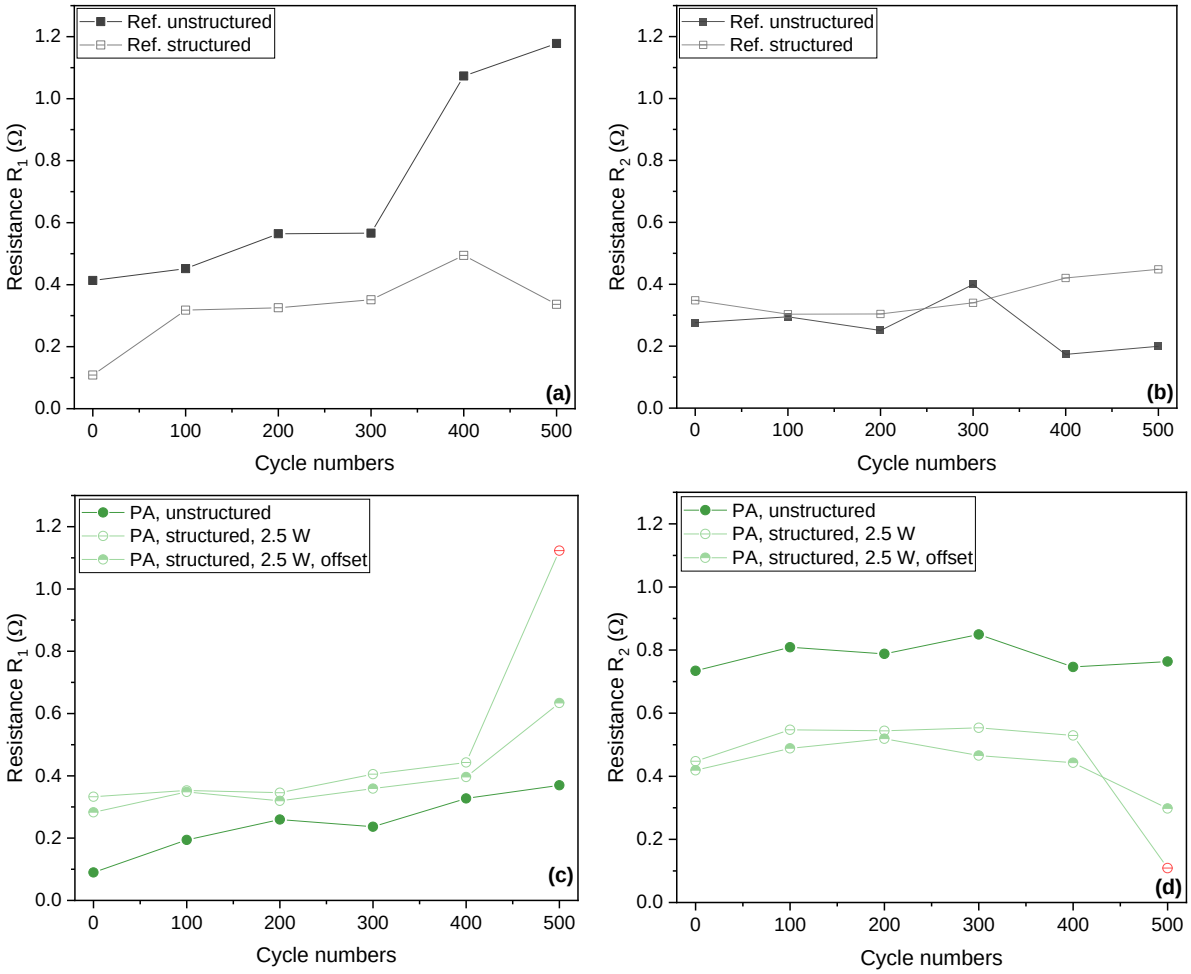

Figure 5-72. Fitted resistances R_1 and R_2 of pouch cells containing unstructured and laser structured NMC 622 cathodes with (**a**), (**b**) PVDF binder and (**c**), (**d**) with water-based binder and PA addition after different cycle numbers.

Figure 5-72-a and –c show that for all cells R_1 increased with increasing cycle number, and cells with aqueous processed electrodes with PA addition exhibited 0.3 – 0.8 Ω lower R_1 compared to the cells containing electrodes with PVDF binder. This is due to that the graphite anodes used for the cells with aqueous processed cathodes had lower mass loading compared to those for the cells containing cathodes with PVDF binder (Table 5-28). The cell containing unstructured cathodes with PVDF binder showed an increase in R_1 by 185 % (from 0.4 to 1.2 Ω) with increasing cycle number, which is in agreement with their severe aging behavior in lifetime analyses. In addition, all pouch cells with laser structured electrodes displayed similar R_1 values from 0 to 400 cycles. The R_1 and R_2 value of the cell containing aqueous processed structured cathodes with 2.5 W after 500 cycles were unusual, which is possibly due to the fact that this cell was placed at open circuit voltage for more than two weeks prior to the last EIS analysis due to technical issue. Thus, these data points marked in red can be neglected.

In contrast to the significant increase in R_1 with increasing cycle number, R_2 of the cells containing cathodes with PVDF as binder exhibited less than 0.1 Ω increase during the lifetime analyses (Figure 5-72-b). Besides, the pouch cell with PA-added unstructured cathodes showed about 0.5 Ω higher R_2 value compared to the cell containing unstructured cathode with PVDF as binder (Figure 5-72-d). Since PA has a melting point of about 40 °C, the residual PA would be dense and highly crystallized after the drying process at 90 °C; Furthermore, PA can

be soluble in organic electrolyte and may consume the CEI on the NMC 622 cathodes, leading to a higher charge transfer resistance [201]. Furthermore, both cells having laser structured aqueous processed cathodes showed about 0.3 Ω lower R_2 compared to the cell with unstructured electrodes, while the cell having structured cathode with offset scans exhibited the lowest R_2 among all cells with aqueous processed electrodes. However, the difference in R_2 between the cells containing laser structured electrodes with different scanning strategies is only 0.03 – 0.09 Ω. Thus, both scan strategies can achieve similar effect of reducing the charge transfer resistance R_2 of the NMC 622 cathodes in the pouch cells.

EIS analyses and lifetime analyses have demonstrated that the combination of laser processing and aqueous processed thick-film NMC 622 cathodes can significantly reduce the charge transfer resistance in pouch cells vs. graphite anodes and mitigates the aging of the cells, thus allowing cells to maintain a high capacity and a long cycle lifetime.

5.6. Laser process upscaling for structuring of NMC 622 cathodes

In order to implement the laser structuring process into existing large-scale electrode production lines, it is necessary to increase the process efficiency for laser structuring of electrodes. Therefore, the laser structuring efficiency and the possibility of reducing the laser processing time will be discussed in this chapter using an example of the PVDF-based NMC 622 cathodes with a thickness of 100 µm and an areal capacity of 4.4 mAh/cm^2, which is comparable to the latest state-of-the-art NMC cathodes used in the battery industry. The cross-sections of laser structured electrodes with different laser setups, laser power, scan speed, and number of scans are shown in Figure 5-73. The laser spot size of the high-power ps-laser is calculated using equation (3.17):

$$d_f \approx \frac{M^2 f}{d_L}\frac{4\lambda}{\pi} = \frac{1.1 \cdot 420\ mm \cdot 4 \cdot 1064\ nm}{3.0\ mm \cdot 2.2 \cdot 2.5 \cdot \pi \cdot 1000} \approx 38\ \mu m \qquad (5.18)$$

the laser beam diameter on the focusing lens d_L [mm] is related to the beam diameter at laser exit (3 mm) and two applied BeT with expanding factors of 2.2 and 2.5 (Figure 4-9).

A first approach to reduce the laser structuring time is to increase the average laser power while reducing the number of laser scans required to ablate the electrode materials. Figure 5-73-a and -b exhibit the cross-sectional views of the laser ablated NMC 622 cathodes using the standard laser parameter mentioned in chapter 5.2.3 and fast laser structuring with one laser scan at the maximal average laser power of 11.3 W, respectively. In order to realize channel structures down to the current collector, the scan speed was reduced to 120 mm/s. However, widening of the channel structures with increasing laser power was observed (FWHM increases from 14 µm to 65 µm), which leads to an increasing mass loss and a decreasing aspect ratio. To minimize the mass loss of cathodes due to the laser structuring while maintaining a high processing speed, a high-power laser together with a 1×5 beam splitter was employed as described in Figure 4-9.

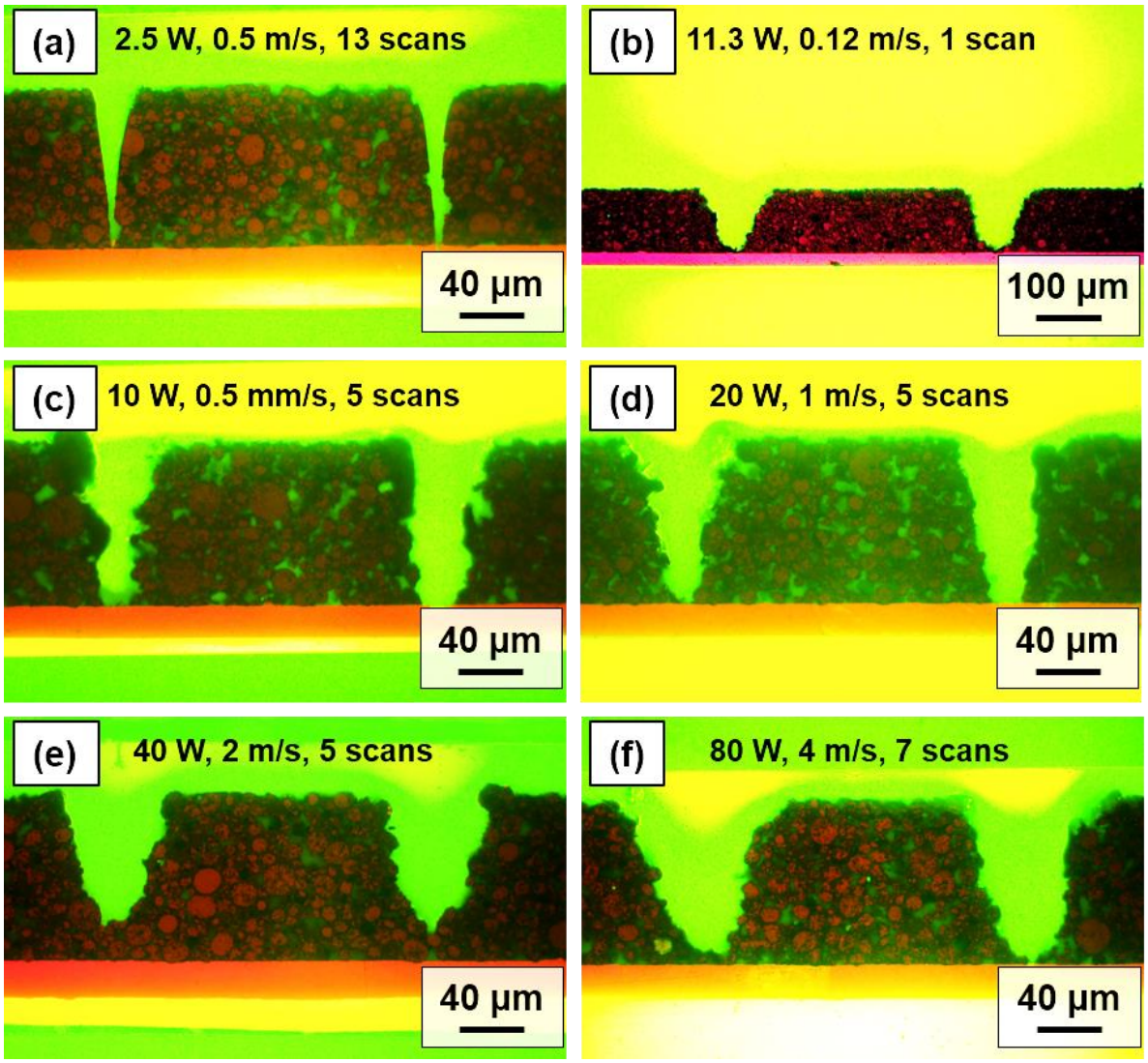

Figure 5-73. Cross-sectional views of a laser structured NMC 622 cathodes processed with an fs-laser with (**a**) 2.5 W, 13 scans and (**b**) a maximum laser power of 11.3 W with one scan using setup shown in Figure 4-8. In addition, a high power fs-laser with a repetition rate of 1 MHz was applied for the structuring of the cathodes (**c**) to (**f**) by adjusting the laser power from 10 W to 80 W while keeping the line energy constant at 20 J/m (laser spot size: 38 µm in diameter).

Two laser scanning strategies can be applied for the laser structuring of electrodes as illustrated in Figure 5-74, namely method 1 with beamlets oriented parallel to the scan direction and method 2 with beamlets oriented horizontal to the scan direction. Method 1 is approximately equivalent to the laser structuring using a single beam and with 5 laser scans, whereas method 2 could be used for laser with 5 times higher average power. Figure 5-73-c to -f display cross-sections of the laser structured cathodes with single beam and 5 scans at various laser power ranging from 10 to 80 W. Although the laser line energy (average laser power divided by scan speed) was kept constant at 20 J/m, the ablation depth at 80 W laser power is not sufficient to reach the current collector, thus the number of laser scan was increased to 7, as shown in Figure 5-73-f.

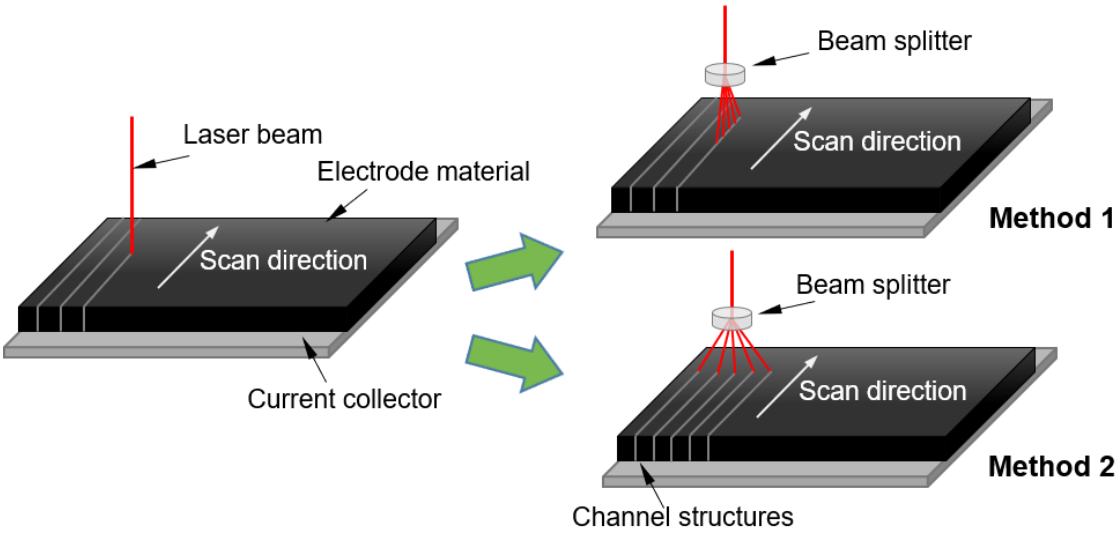

Figure 5-74. Schematic illustrations of laser structuring using a single laser beam or with a beam splitter. Depending on the direction of the beamlets (parallel or horizontal to the scan direction), the scanning strategy can be categorized into two methods.

The maximum width and FWHM of the channel structures in laser structured NMC 622 cathodes with different laser parameters are summarized in Table 5-30. The estimated mass loss is based on the volume of removed material, assuming that the composite electrodes are homogeneous. Furthermore, the cross-sectional geometry is simplified as a rectangle with FWHM multiplied by the film thickness. The mass loss is calculated as follows using a constant channel pitch of 200 µm:

$$Mass\ loss\ (\%) = \frac{V_{channels}}{V_{total}} \cdot 100\% = \frac{n_{channels} \cdot V_{channel}}{V_{total}} \cdot 100\%$$
$$= \frac{\frac{1\ cm}{200\ \mu m} \times b \times h \times 1\ cm}{1\ cm \times 1\ cm \times h} \cdot 100\% = \frac{b}{200\ \mu m} \cdot 100\% \quad (5.19)$$

where $V_{channels}$ [cm³] is the total volume of channels, V_{total} [cm³] the total volume of a unit electrode with a footprint of 1 cm × 1 cm and a film thickness of h [µm], $n_{channels}$ [-] the total number of the channels generated by laser structuring in an electrode per unit area, $V_{channel}$ [cm³] the volume of a single channel, and b [µm] the FWHM of channel structures.

Table 5-30. Different laser parameters and the resulted maximum width and FWHM of the generated channels in NMC 622 cathodes, as well as the processing time per unit area with / without a 1 × 5 beam splitter.

Laser parameters	Max. width [µm]	FWHM [µm]	Processing time with single beam [s/cm²]	Processing time with beam splitter [s/cm²]	Estimated mass loss [%]
2.5 W, 13 scans, 500 mm/s	31.1 ± 1.5	13.9 ± 1.7	13.0	-	7.0 ± 0.9
11.3 W, 1 scan, 120 mm/s	115.2 ± 10.0	64.7 ± 8.1	4.2	0.8	32.4 ± 4.1
10 W, 5 scans, 500 mm/s	51.4 ± 7.3	29.1 ± 2.2	5.0	1.0	14.6 ± 1.1
20 W, 5 scans, 1000 mm/s	62.0 ± 8.6	33.1 ± 5.0	2.5	0.5	16.6 ± 2.5
40 W, 5 scans, 2000 mm/s	62.8 ± 6.9	44.9 ± 5.1	1.3	0.3	22.5 ± 2.6
80 W, 7 scans, 4000 mm/s	91.8 ± 14.2	54.0 ± 3.7	0.9	-	27.0 ± 1.9

By increasing the laser power and slowing down the scan speed, the number of scans can be reduced from 13 to 1, while the laser processing time is decreased from 13.0 to 4.2 s/cm^2. Meanwhile, if a laser with a power of 56.5 W was applied as suggested in Figure 5-74 (method 2), the processing time can be further reduced to 0.8 s/cm^2, which is 94 % less processing time in comparison to the laser structuring using reference parameters (2.5 W, 13 scans, 500 mm/s). However, the maximum width and FWHM have increased by a factor of 4 – 5, resulting in an increase in mass loss from 7 % to 32 %. The increase in ablation depth and width with increasing laser power was also reported in graphite anode by Sterzl et al. [367]. The relationship between laser scan speed and average laser power was given by Neuenschwander et al. [368]:

$$v_s = \frac{4}{\pi e^2} \cdot \frac{1 - \mathrm{PO}}{(d_f/2)\Phi_{th}} \cdot P_L \cdot 100 \tag{5.20}$$

where v_s [mm/s] is the laser scan speed, PO [-] the pulse overlap, d_f [mm] the laser spot diameter, Φ_{th} [J/cm^2] the threshold laser fluence for ablation, and P_L [W] the average laser power. From equation (5.20) it can be concluded that for the same laser spot size and a constant pulse overlap, increasing the average laser power can lead to an increase in scan speed (or a decrease in laser processing time). Neuenschwander et al. [369] reported that with regard to efficiency, the optimum laser fluence Φ_{opt} [J/cm^2] for the ablation of metals using a Gaussian laser beam is given as:

$$\Phi_{opt} = e^2 \Phi_{th} \tag{5.21}$$

where Φ_{th} [J/cm^2] is the material dependent threshold fluence. Besides, the maximum material removal rate $\dot{V}_{max}$ [cm^3/s] is shown as follows [369]:

$$\frac{\dot{V}_{max}}{P_L} = 2\frac{\delta}{\Phi_{opt}} = 2\frac{\delta}{e^2 \Phi_{th}} \tag{5.22}$$

where δ [cm] is the penetration depth as illustrated in equation (3.22). From equation (5.22) it is clear that for electrodes with a defined composition (Φ_{th} remains constant) it is necessary to increase the laser power in order to achieve higher laser ablation rate.

In contrast, when using 5 scans, a high-power laser, and high scan speeds, the processing time can be further reduced from 5.0 s/cm^2 at 10 W to 1.3 s/cm^2 at 40 W. Besides, a further increase in laser power is still available, as the laser used in this work can reach a maximum average laser power of 280 W (measured after the laser scanning optics). Additionally, by combining this strategy with a 1 × 5 beam splitter, the processing time can be further reduced to 0.3 s/cm^2, which means that compared to the reference parameters using single scan at 11.3 W, only 2.3 % of the time is acquired to complete the laser structuring, and the mass loss is 10 % lower in contrast to that strategy. Similar idea was recently studied by Hille et al. [370], they estimated that the processing time could be decreased by about 88 % for the laser structuring of graphite anodes using hole pattern by combining a 3 × 7 beam splitter with kilowatt high power laser.

Another strategy to reduce the processing time is to increase the laser repetition rate. The pulse distance is defined as the scan speed divided by the laser repetition rate. Therefore, by increasing the laser repetition rate, faster scan speeds can be realized while maintaining the

same pulse distance. In order to investigate the effect of laser repetition rate and pulse distance on the laser structuring efficiency, laser ablations using a high power ps-laser were performed on thick-film NMC 622 cathodes with a thickness of 150 µm. Laser repetition rates were varied from 100 kHz to 1 MHz, while pulse distances from 0.5 µm to 10 µm at laser energy of 0.1 mJ and 0.2 mJ with a single scan were applied. The ablation depth and FWHM of the generated groove structures in cathodes were measured using digital microscopy and are shown in Figure 5-75.

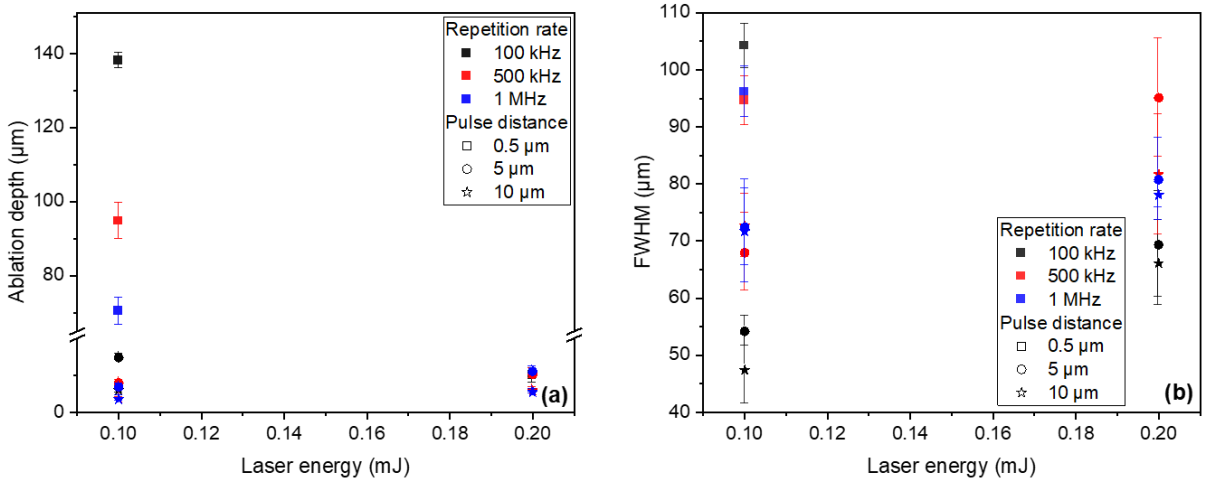

Figure 5-75. The (**a**) ablation depth and (**b**) FWHM of laser structured NMC 622 cathodes at different laser repetition rates and pulse distances.

At 0.5 µm and 5 µm pulse distance with 0.1 mJ laser energy, the ablation depth increased with decreasing repetition rate, this phenomena has been reported in the laser structuring of graphite anodes [367, 371], which can be explained by the fact that the previous pulse may affect the coupling of the subsequent laser pulse to the plasma and the ejected material. Similar results was reported by Habedank et al. [18], they found that for the laser ablation of graphite anode, the ablation depth increased as the repetition rate decreased from 10 kHz to 100 Hz. However, no difference in ablation depth was observed between 10 and 100 Hz. Furthermore, the ablation depth D_{ab} [cm] can be described as follows [18]:

$$D_{ab} = \delta \cdot \ln\left(\frac{\Phi}{\Phi_{th}}\right) \tag{5.23}$$

where δ [cm] is the penetration depth, Φ [J/cm^2] the laser fluence, Φ_{th} [J/cm^2] the material dependent threshold fluence. By combining equation (5.23) with (5.4) and (5.5), the relationship between ablation depth and laser repetition rate f_{rep} [Hz] is obtained:

$$D_{ab} = \delta \cdot \ln\left(\frac{2P_L}{\pi\Phi_{th} f_{rep} (d_f/2)^2}\right) = \delta \cdot \ln\left(\frac{8}{\pi\Phi_{th} d_f^2} \cdot \frac{P_L}{f_{rep}}\right) \tag{5.24}$$

where P_L [W] is the average laser power, d_f [mm] the laser spot diameter. Thus, from equation (5.24) it is concluded that in order to increase the laser ablation depth, it is necessary to either increase the average laser power, or to decrease the laser repetition rate, or using a small laser spot size. However, most recent studies revealed that the material removal rate in NMC

electrodes can be further increased by a factor of 4 – 5 by applying laser with burst mode, while keeping the high repetition rate at 1 – 40 MHz [372, 373].

The maximum ablation depth in Figure 5-75-a was achieved at the pulse distance of 0.5 µm, which may be owing to a thermal ablation behavior, since the heat accumulation is more pronounced at low pulse distances [367]. In addition, the ablation depth decreased with increasing pulse distance because the pulse overlap between laser pulses decreased with increasing pulse distance, leading to a decrease in line energy. At a laser pulse energy of 0.2 mJ, the ablation depth was reduced to about 10 µm, with no difference in the impact of different laser parameters on the ablation depth was found. This indicates that increasing the laser power and repetition rate simultaneously does not achieve the same ablation depth as by lower laser energy. Furthermore, the ablation width increases with decreasing pulse distance. In summary, in the repetition rate range of 100 kHz to 1 MHz, using low laser repetition rates is more effective for the laser structuring of NMC 622 cathodes with PVDF as binder.

In order to verify whether the use of a beam splitter can increase the efficiency of laser structuring as expected, the laser energy was kept constant at 0.15 mJ, i.e., without the use of beam splitter, a laser power of 3 W was used, whereas a laser power of 15 W was applied when the beam splitter was installed, to ensure that the laser energy of each individual beamlet remained the same in contrast to the single beam setup without beam splitter. The ablation depth and width of the laser structured NMC 622 cathodes in combination with a 1 × 5 beam splitter are shown in Figure 5-76. The surface of theses laser structured NMC 622 cathodes using a pulse distance of 1 µm with / without beam splitter are presented in Figure S 13.

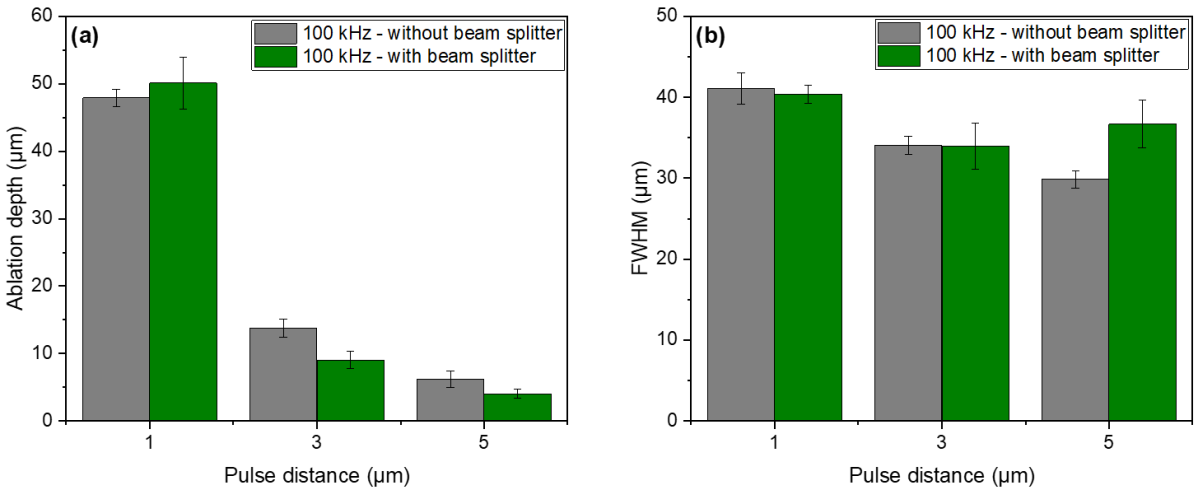

Figure 5-76. The (**a**) ablation depth and (**b**) the FWHM of the laser structured NMC 622 cathodes processed with / without 1 × 5 beam splitter at different pulse distances.

At a pulse distance of 1 µm, the ablation depth with beam splitter was 2 µm higher than that without beam splitter, while at pulse distances of 3 and 5 µm, laser structuring without beam splitter exhibited 2 to 4 µm higher ablation depth per laser scan. Furthermore, at pulse distances of 1 and 3 µm, the beam splitter had no effect on the ablation width, while at the pulse distance of 5 µm, the ablation width with the beam splitter was 7 µm higher than the reference. In addition, in the preliminary laser ablation experiment using a 1 × 6 beam splitter,

the presence of narrow grooves between the major ablative grooves was detected on the stainless steel plate (Figure S 14), which is due to the existence of the secondary maxima after the beam diffraction. However, only 5 beamlets were detected during the laser structuring process with the 1 × 5 beam splitter, which means that no unexpected beamlets (secondary maxima) were generated after the beam diffraction. Therefore, the 1 × 5 beam splitter can be applied in the laser structuring at lower pulse distance to reduce the processing time significantly (by a factor of 5) while maintaining similar ablation depth and width.

6. Conclusion and outlook

Increasing mass loading is a practical strategy to increase the energy density of cells. The first step in this work was to determine the limit of rate capability of cells containing thick-film NMC 622 cathodes processed with state-of-the-art PVDF binder. The slurries were coated onto the Al foil using tape casting with a doctor blade and the electrodes were subsequently dried in the ambient air and calendered in order to achieve higher density. Afterwards, the electrodes were dried in order to remove residual water and assembled vs. Li using coin cell design. Cathodes with film thicknesses ranging from 70 to 200 µm were prepared and electrochemically characterized. Rate capability analyses exhibited that cells suffered severe capacity drop at C/2 to 5C as the film thickness increased. In comparison to other cells, the cells containing cathodes with 200 µm thickness began to show capacity drop at C/2 and lost more than 80 % in contrast to their initial capacity at 1C, whereas the ones containing cathodes with a 150 µm thickness maintained about 50 % capacity at 1C. Besides, cells containing thick-film electrodes with 200 µm thickness exhibited high IR-drop at C/2 and 1C. A similar trend was observed by Heubner et al. [24] for cells containing NMC 622 cathodes with film thicknesses over 200 µm. The induced strain accumulation in thick-film electrodes can lead to cracks formation in NMC 622 secondary particles, causing particle isolation and capacity loss of the cells [309].

In order to enhance the capacity at high C-rates, the cathodes were laser structured with 200 µm line pitch. Capacity increases of 10 % to 50 % were observed in cells with laser structured cathodes compared to ones with unstructured electrodes at C/2 to 3C. Similar results were reported recently for the cells containing NMC 811 cathodes structured using line patterns with 200 µm pitch, and the cells with laser structured cathodes showed lower charge transfer resistance and 3 times higher capacity at 2C in comparison to the ones with unstructured electrodes [271]. In order to further investigate the impact of different laser pattern types on the electrochemical performance, line structures with pitch varying from 200 to 100 µm and hole structures with 200 mm pitch were applied to the structuring of NMC 622 cathodes with a thickness of 150 µm. All cells containing electrodes with different line structures exhibited similar capacity increase at C/2, while the ones with hole structures displayed the least capacity increase. As the C-rate rose to 1C and 2C, the cell capacity increased with decreasing structure pitch, but the cells containing laser structured electrodes with 150 µm and 100 µm pitch showed similar capacity increases. Since the mass loss due to laser structuring increases with decreasing pitch, an appropriate pitch should be determined according to the practical demand. In addition, in contrast to hole structures, the channel structures can accelerate the electrolyte wetting due to the capillary effect [13], thus the line structures were applied in subsequent experiments.

In the next step, monolayer thick-film cathodes containing polycrystalline NMC 622 powders with big (B) and small (S) particle sizes were prepared using PVDF as binder and NMP as solvent. Besides, mechanically blended B&S-cathodes monolayer cathodes were also prepared. ICP-OES and XRD analyses revealed that the two NMC 622 powders had similar chemical composition and same phase, whereas the CV and differential capacity dQ/dV plots indicated that the same redox reaction occurred during charging and discharging. Rate

capability analyses showed that the cells with S-cathodes owned the highest discharge capacity, while the cells with B&S-cathodes displayed an intermediate performance between those with S- or B-electrodes. Furthermore, bilayer NMC 622 cathodes with different hierarchical structures (BS, SB) were fabricated using bilayer coating strategy with different thickness ratio of B- and S-layer. CV analyses showed that cells with S-electrodes had a larger peak-to-peak potential difference in comparison to those with bilayer electrodes, indicating a higher cell polarization for cells with thick-film S-electrodes. EIS analyses revealed that all cells with bilayer or blended B&S-NMC 622 electrodes except for BS – 2:1 exhibited higher charge transfer resistance in comparison to cells with monolayer B- and S-electrodes, which may be due to the presence of the interface between the B- and S-layer within the bilayer electrodes. In addition, it was found that cells containing bilayer electrodes with BS – 1:1 configuration achieved similar rate capability as those with B&S-cathodes, while the latter displayed higher SEI resistance and charge transfer resistance, as well as significantly lower cycling stability. The rate capability and CV analyses suggested that in order to achieve higher discharge capacity at high C-rates using bilayer architectures, the following strategies could be applied:

(i) using the BS-configuration, i.e., bilayer cathodes with large NMC 622 particles as bottom layer and small particles as upper layer, or

(ii) increasing the thickness of the layer with small particles.

The study by Wood et al. [156] using NMC 532 cathodes showed similar results and confirmed that the BS-configuration is beneficial for high power applications. However, if we compare the discharge capacities at low C-rates, an opposite trend was observed, implying that using the SB-configuration and increasing the thickness of B-layer can increase the cell capacity at low C-rates.

Ultrafast laser ablation was applied to generate groove structures inside the bilayer electrodes for the first time. It was found that the mass loss caused by laser structuring could be effectively suppressed by using SB-configurations or by increasing the B-layer thickness in BS-electrodes. At the same time, SB-configurations were conducive to increasing the discharge capacity of cells with laser structured electrodes compared to those with unstructured electrodes. Lifetime analyses showed that all cells with laser structured thick-film electrodes were more stable and retained significantly higher capacity (90°% capacity retention) after long-term cycling in contrast to those without laser structuring.

For the aqueous processing of NMC 622 slurry, acetic acid (AA) was added to balance the slurry pH value, and water-soluble binders CMC and TRD 202A were applied for the slurry preparation. NMC 622 cathodes with different slurry pH values and thicknesses were cast onto the Al-foil and calendered. The corrosion of the Al current collector induced by the unmodified slurry (pH 12.1) was accompanied by hydrogen release during coating [28, 342], which led to the formation of a large number of cavities within the dried cathode film. In addition, more chemical corrosion was observed as the electrode thickness was increased, due to the fact that the drying time inevitably increases with increasing wet film thickness. Furthermore, the cavities inside the dried electrodes led to a decrease in energy density, which is contrary to the original intention of increasing energy density by applying thick-film electrodes.

When the slurry pH was adjusted below 10, no cavities inside the thick-film electrodes or craters on the electrode surface were observed. Besides, the viscosity of cathode slurries

raised with an increasing amount of acid, which is beneficial for thick-film fabrication, since the sedimentation of large NMC 622 particles can be impeded. Cyclic voltammetry demonstrated that the addition of AA did not lead to additional redox reactions. However, the voltage difference increased with decreasing slurry pH values. This occurred as a result of an increased cell polarization caused by a reduced electrode porosity. A strong impact of the slurry pH value and cathode film thickness on the discharge capacity was observed in rate capability analyses. The specific capacity increased with rising slurry pH value when the C-rates were above C/5 for thin-film electrodes and above C/10 for thick-film electrodes. The cells containing thick-film electrodes without acid addition exhibited the highest capacity, whereas the electrodes with the highest amount of acid (pH 8.4) retained less capacity at C/10 to 1C, which was also observed in cells with thin-film electrodes. This is due to an enhanced Li-ion diffusion kinetics inside the electrode with high porosity. Therefore, the slurry pH value should be adjusted between 9 to 10, on the one hand to mitigate the chemical corrosion between the alkaline cathode slurry and the current collector to achieve a higher energy density; and on the other hand, to prevent the capacity decrease at low slurry pH values.

The effect of different acid additions on the electrochemical performance of aqueous processed NMC 622 cathodes was further investigated by comparing three different acid additives at the same slurry pH value, i.e., acetic acid (AA), citric acid (CA), and phosphoric acid (PA). The electrodes with different acid additions during mixing procedure were characterized using XPS and Raman spectroscopy. Two different electrode thicknesses were selected to represent the state-of-the-art electrode thicknesses (70 µm) and the advanced thick-film approach (150 µm). The C 1s spectra from XPS analyses showed that no distinct differences in Li_2CO_3 amount were observed in aqueous processed electrodes with different acid additions. However, this might be due to the low content of detected lithium carbonate in the samples. The addition of PA resulted in an additional peak in P 2p spectra, which is assigned to the formation of phosphates [31, 194, 198]. Raman spectra of different NMC 622 electrode types revealed two Raman-active modes A_{1g} and E_g. After comparing the ratio of A_{1g}/E_g, it could be inferred that Li leaching was more pronounced in the electrodes processed with CA and AA than in the electrodes processed with PA and the reference electrode with PVDF as binder. Combining the results from XPS analyses and Raman spectroscopy, it could be concluded that a protective layer consisting of phosphates was formed on the surface of NMC 622 after adding the PA, which could mitigate the Li leaching from NMC 622 particles during slurry preparation. Rate capability analyses exhibited that for cells containing aqueous processed cathodes with high mass loading, the cells with AA addition reached similar capacity at C/20 to C/5 as the reference cells with PVDF as binder. At higher C-rates, both PA and AA addition could enhance capacity, while cells with CA addition showed the lowest capacity from C/2 to 3C. However, lifetime analyses revealed that cells with PA-added cathodes retained similar capacity after 80 cycles as the reference cells having electrodes with PVDF as binder, while the cells containing CA- and AA-added cathodes exhibited significantly lower capacities at the end of cycling procedure. This trend was observed for cells with both thin- and thick-film electrodes. Besides, post-mortem analyses indicated that more cracks were generated in secondary NMC 622 particles in the cycled electrodes with CA addition in contrast to those with PA addition.

After electrode preparation, laser structuring was carried out on thick-film electrodes with a pitch of 200 µm. A mass loss of 7.5 % was achieved for different electrode types. Rate capability analyses displayed that all cells with structured aqueous processed electrodes showed 20 to 40 mAh/g higher capacities at C/2 and 1C in contrast to the reference cells with respective unstructured electrodes, especially for those with PA and AA addition. Besides, cells containing laser patterned electrodes with PA addition exhibited higher capacity retention and the highest final capacity after 80 cycles at C/2 than cells with other electrode types, including reference cells containing unstructured electrodes with PVDF as binder. The impact of combining laser patterning and acid modification on the electrochemical performance was further proved by EIS and CV analyses. On the one hand, EIS analyses displayed that after rate capability analyses, the cells containing aqueous processed thick-film electrodes exhibited similar or higher charge transfer resistance than the reference cells with PVDF as binder. However, the cells with laser structured aqueous processed electrodes showed both lower SEI resistance and charge transfer resistance compared to the cells with respective unstructured electrodes. On the other hand, CV analyses indicated that the D_{eff} of Li-ions in cells with laser structured electrodes were increased by 14 to 61 % compared to those with unstructured electrodes during both discharging and charging. In addition, an increase of about 110 % in D_{eff} was reported in half-cells containing laser structured NMC 811 cathodes using EIS analyses [271]. In particular, the cells with laser structured PA electrodes showed 17 % higher D_{eff} during charging and almost the same coefficient during discharging in comparison to those of reference cells with PVDF as binder.

In order to investigate the impact of channel width on the performance of cells containing laser structured PA-added cathode, two laser scanning strategies were applied to control the ablation width, i.e., doubling the laser power, or performing double scans with 20 µm offset. The mass loss increased from 7 % to 9 % with increasing laser power. However, the laser processing time was significantly reduced, as only half laser scans were required. As for double scans, an offset of 20 µm was determined in order to avoid affecting the Al foil during the laser structuring process. Rate capability analyses exhibited that double scans with offset could enhance the discharge capacity at C/2 and 1C, while cells containing structured electrodes using high laser power showed less capacity increase from C/2 to 2C and maintained a lower discharge capacity at 3C in contrast to the reference cells with unstructured electrodes. Furthermore, lifetime analyses demonstrated that using offset scans at low laser power could maximize the increase in discharge capacity of the half-cells containing aqueous processed NMC 622 cathodes.

Pouch cells were eventually assembled using PA-added and reference thick-film NMC 622 cathodes vs. graphite anodes. Different structuring strategies were applied for the cathodes. Rate capability analyses proved that by combining laser structuring with aqueous processed thick-film electrodes, it was possible to achieve the same or higher cell capacity than the reference cells, especially at high C-rates from C/2 to 2C. Ragone plots indicated that laser structuring could enhance the energy density of full-cells at power densities ranging from 140 to 1300 W/l (or 40 – 450 W/kg). Furthermore, full-cells exhibited extraordinary performance in lifetime analyses in comparison to the half-cells. The cells with unstructured PA-added electrodes achieved 94 % capacity after 500 cycles, which was 20 % higher than

the reference cells with PVDF as binder. In addition, for the reference cells, laser structuring extended their EoL by a factor of 4.3 and meanwhile increased the capacity. As for the cells with aqueous processed cathodes, offset scans strategy could further extend the EoL of cells by 9 % in contrast to those with unstructured electrodes. However, when total discharge capacity was taken into consideration, single scan strategy was preferred for the aqueous processed cathodes, since about 5 mAh higher discharge capacity was obtained by reducing the mass loss. EIS and lifetime analyses indicated that laser structuring in combination with aqueous processed thick-film NMC 622 cathodes could significantly mitigate the charge transfer resistance increase in pouch cells during cycling, thereby allowing cells to maintain a high capacity and a longer lifetime.

At last, the possibility of upscaling the laser structuring process was investigated. By increasing the laser power and using single laser scan, the processing time could be reduced from 13 to 4.2 s/cm^2. However, this was accompanied by an increase in mass loss from 7 % to 30 %. The increase in ablation depth and width with increasing laser power was also recently reported in graphite anode [367]. By combing high laser power with a 1 × 5 beam splitter, only 2.3 % of the time is theoretically acquired to complete the laser structuring, and the mass loss should be 10 % lower in contrast to that using single scan strategy. A recent study estimated that the processing time could be decreased by about 88 % for the laser structuring of graphite anodes using hole pattern by combining a 3 × 7 beam splitter with kilowatt high power laser [370]. Moreover, the ablation depth and width of NMC 622 cathodes were investigated using different laser repetition rates, and it was found that in the range of 100 kHz to 1 MHz, lower laser repetition rates were more effective in achieving higher ablation depths during the laser structuring. The increase in ablation depth with decreasing repetition rate has also been reported in the structuring of graphite anodes [18, 367, 371]. Besides, it was proven that by combining a 1 × 5 beam splitter with a laser beam having 5 times higher average power at a pulse distance of 1 µm, the processing time could be significantly reduced (by a factor of 5), while maintaining the similar ablation depth and width.

For future studies, the fabrication of thick-film multilayer electrodes with different active materials, different size distributions, binder gradient, or porosity gradient, could be further investigated, while other water-based binders or acids could be applied for the cathode slurry processing. The aging mechanism of cells with aqueous processed electrodes with high mass loading could be further studied using *in situ* techniques such as XRD, SEM, or Raman spectroscopy. The impact of different laser patterns on the electrochemical performance could be investigated while keeping the mass loss constant. This has been reported for NMC 622 cathodes with PVDF binder in our recently published study [374]: The cells containing laser structured thick-film NMC 622 cathodes exhibited the maximum capacity increase of 130 % at 1C compared to the cells with unstructured electrodes, while at 2C, hexagons and hexagonal patterns with a hole in each center showed the maximum increase in capacity of around 20 mAh/g compared to other patterns; Lifetime analyses revealed that the combination of line and hole structures could help the cells to reach the highest capacity retention than those with only holes or lines after cycling. However, whether similar conclusions can be drawn for electrodes with other active materials (such as LFP or LNMO) and other mass loadings still need to be studied, and the pattern optimization using artificial intelligence and machine

learning is also a very interesting topic and deserves more attention. Other characterization methods such as nuclear magnetic resonance spectroscopy can be applied to study lithium-ion diffusion kinetics in the cells with laser structured thick-film electrodes. Another possible study focus is the interaction between the active material and high-power laser beam in order to identify possible phase transitions and critical laser pulse fluence. In addition, ultrafast GHz lasers and lasers with burst modes are new and attractive tools for the electrode structuring and need further investigations. Furthermore, LIBS using laser at UV wavelength can have enhanced sensitivity and reduced background interference, and thus would be a powerful tool to investigate the Li or binder distribution in electrodes.

7. Appendices

Appendix A

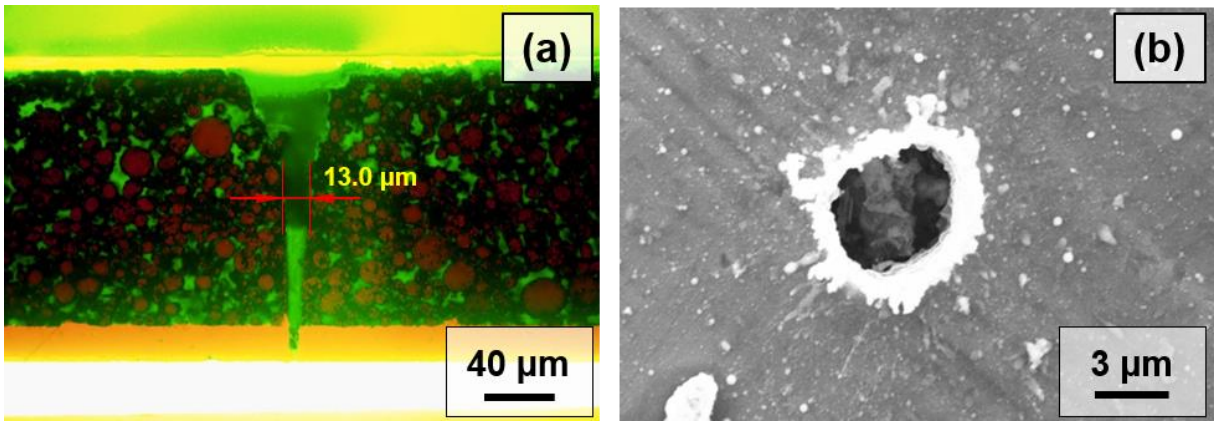

Figure S 1. Details of the through-hole structure in laser structured thick-film NMC 622 cathodes with PVDF binder: (**a**) Cross-sectional view of a hole and (**b**) SEM image of the hole on the rear side of the Al current collector, where the laser exits.

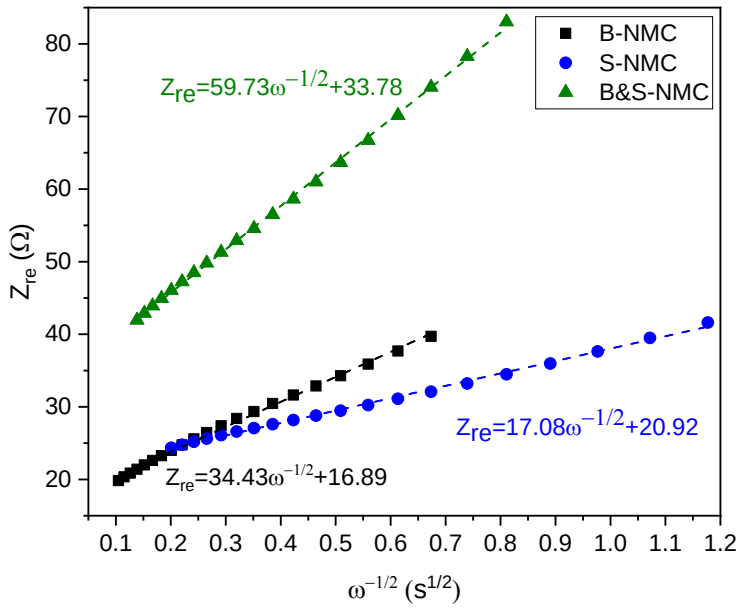

Figure S 2. Relationships between the real impedance Z_{re} [Ω] and $\omega^{-1/2}$ [$s^{1/2}$] at low frequency region for half-cells containing different types of monolayer NMC 622 cathodes. The linear fitting for each cell is displayed.

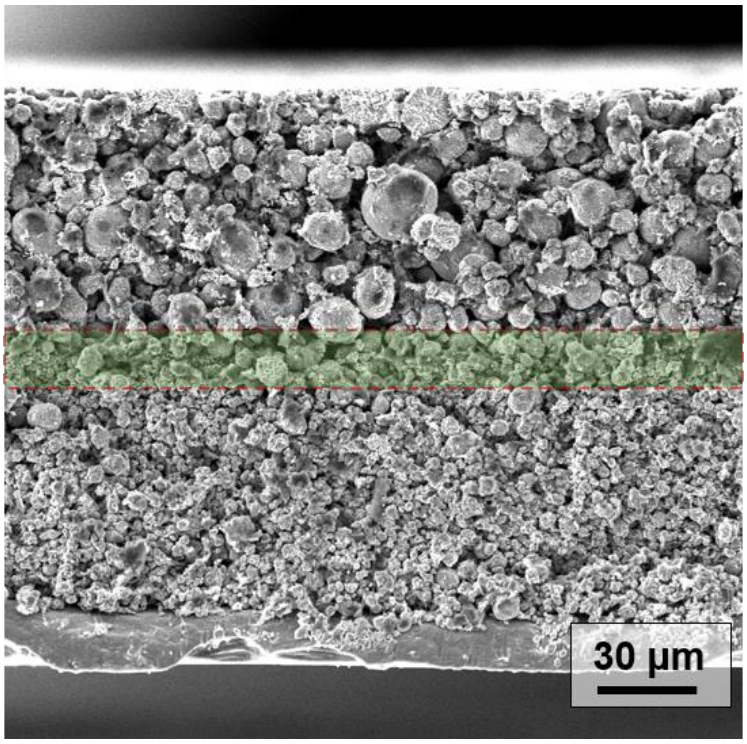

Figure S 3. Cross-sectional SEM images of a bilayer NMC 622 electrode with S:B – 1:1 configuration. The area marked in green is the transition region between the S- and B-layer.

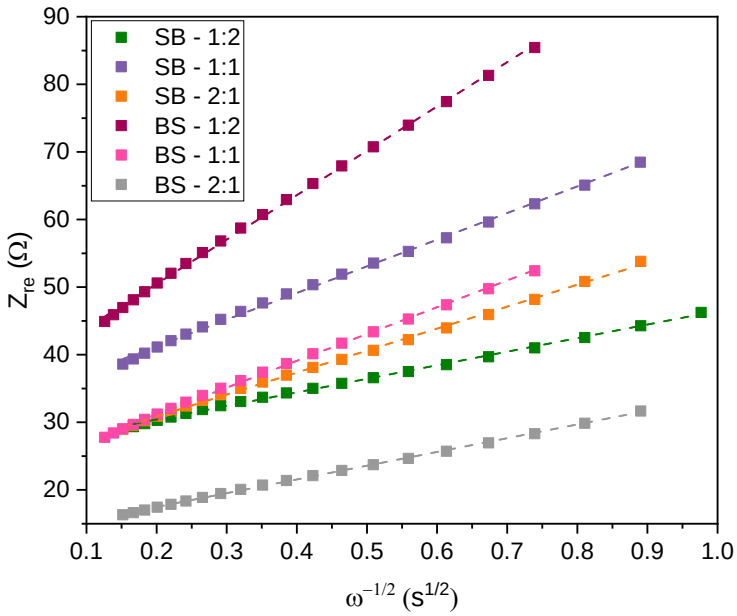

Figure S 4. Relationships between real impedance Z_{re} [Ω] and $\omega^{-1/2}$ [$s^{1/2}$] at low frequency region for half-cells containing different types of bilayer NMC 622 cathodes.

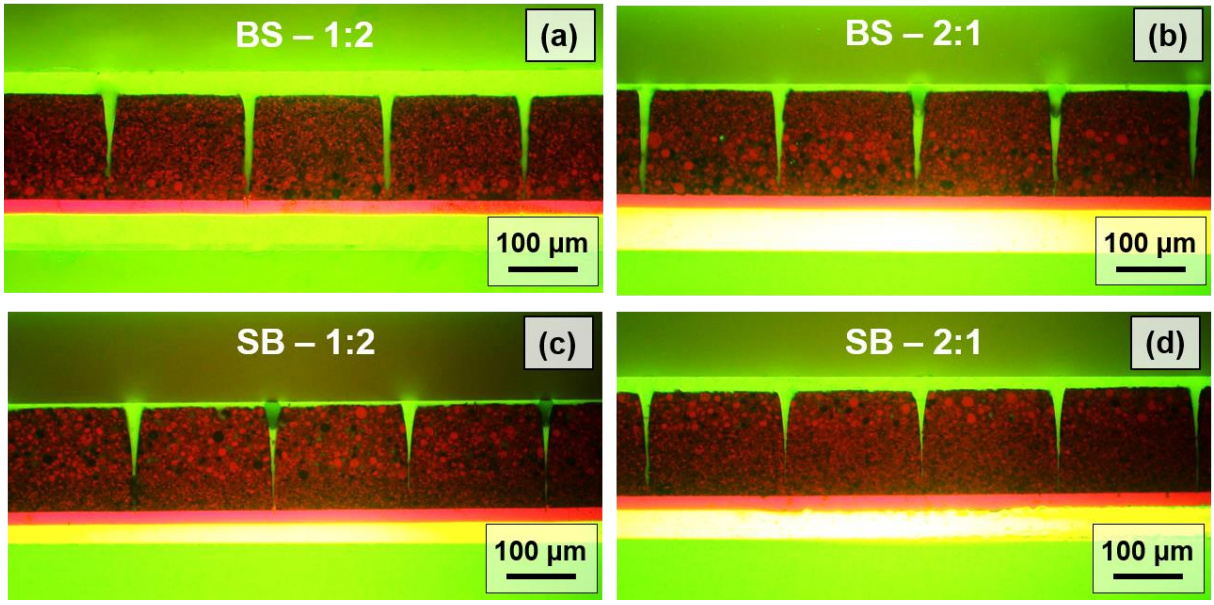

Figure S 5. Cross-sectional views of the laser structured NMC 622 cathodes having bilayer architectures with (**a**) BS – 1:2, (**b**) BS – 2:1, (**c**) SB – 1:2, and (**d**) SB – 2:1 configuration.

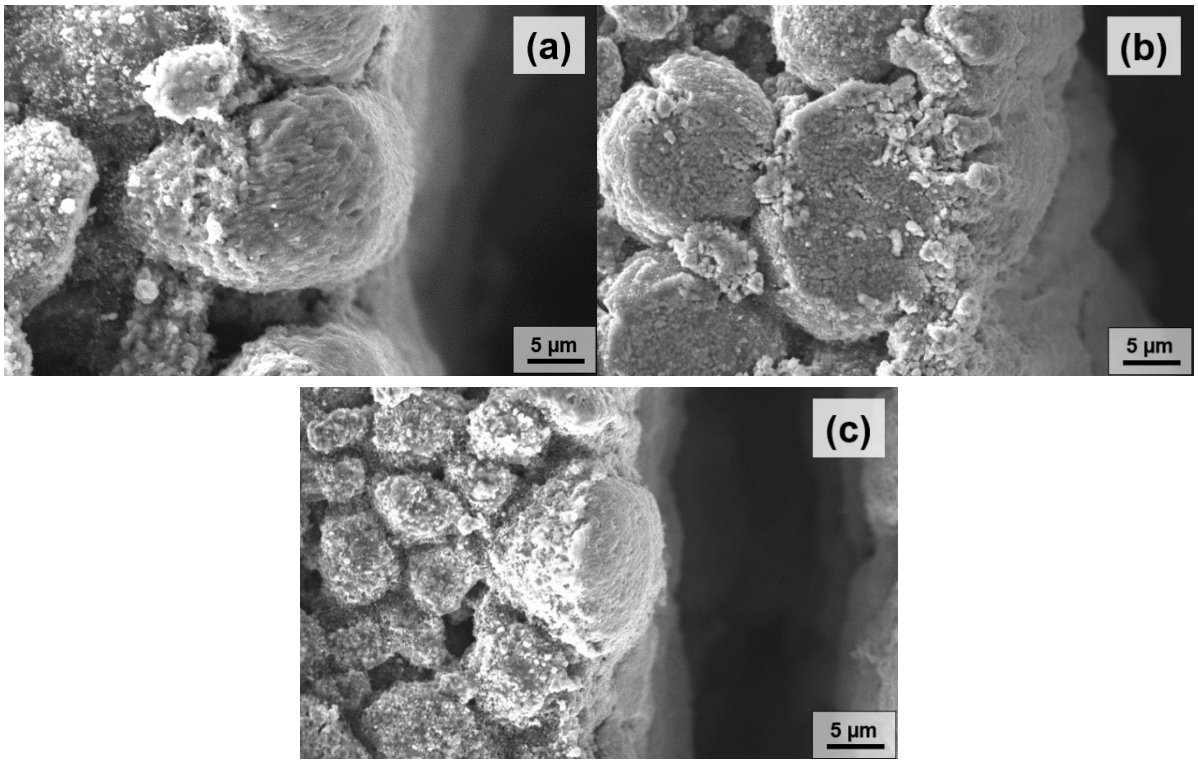

Figure S 6. The edges of channels in the laser structured NMC 622 cathodes with addition of (**a**) citric acid, (**b**) acetic acid, and (**c**) phosphoric acid during mixing procedure, characterized by high resolution SEM.

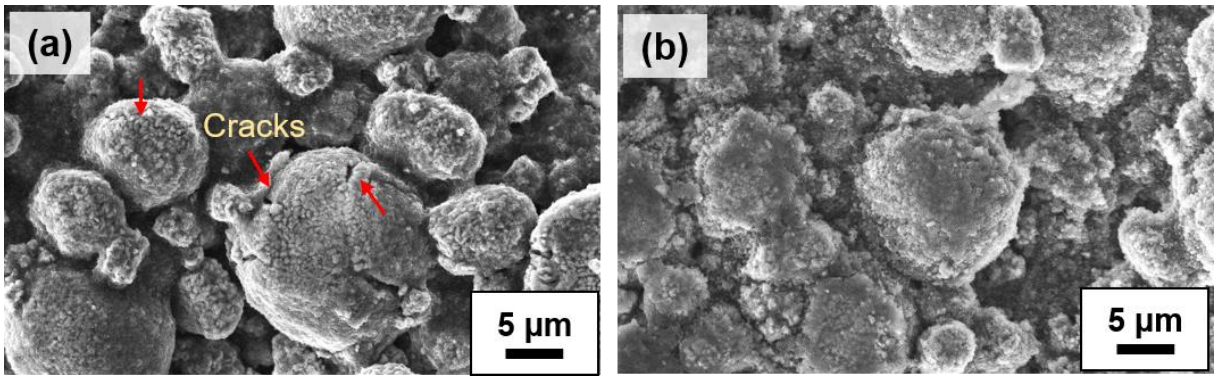

Figure S 7. SEM images of cycled NMC 622 cathodes with addition of (**a**) citric acid and (**b**) phosphoric acid from coin cells after lifetime analyses.

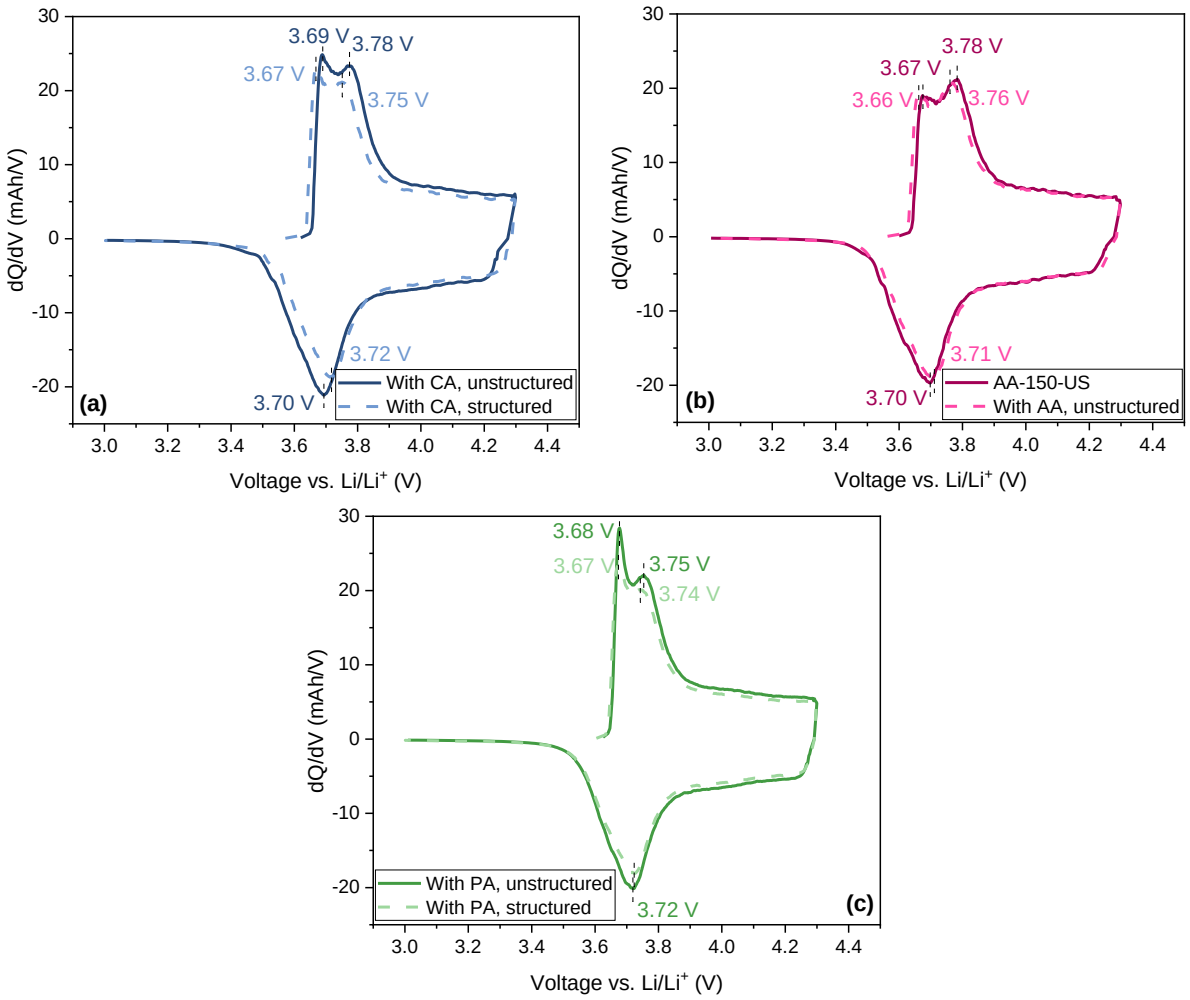

Figure S 8. The differential capacity dQ/dV plots of half-cells containing unstructured / laser structured aqueous processed thick-film NMC 622 cathodes with addition of (**a**) CA, (**b**) AA, and (**c**) PA, from the third cycle at C/20.

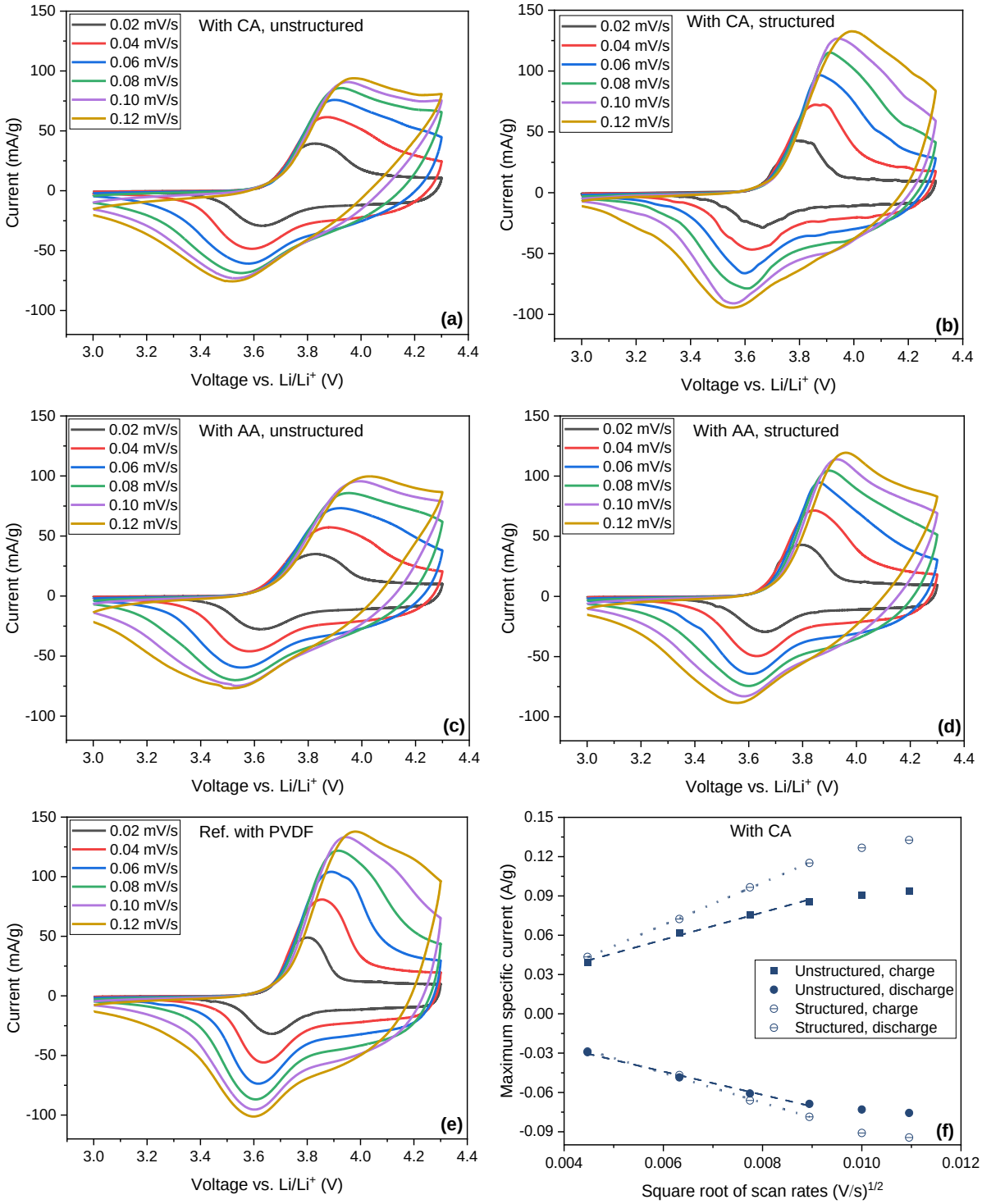
0.02 mV/s
0.04 mV/s
0.06 mV/s
0.08 mV/s
0.10 mV/s
0.12 mV/s
With CA, unstructured
(a)
With CA, structured
(b)
With AA, unstructured
(c)
With AA, structured
(d)
Ref. with PVDF
(e)
Current (mA/g)
Voltage vs. Li/Li+ (V)
With CA
Unstructured, charge
Unstructured, discharge
Structured, charge
Structured, discharge
Maximum specific current (A/g)
Square root of scan rates (V/s)1/2
(f)

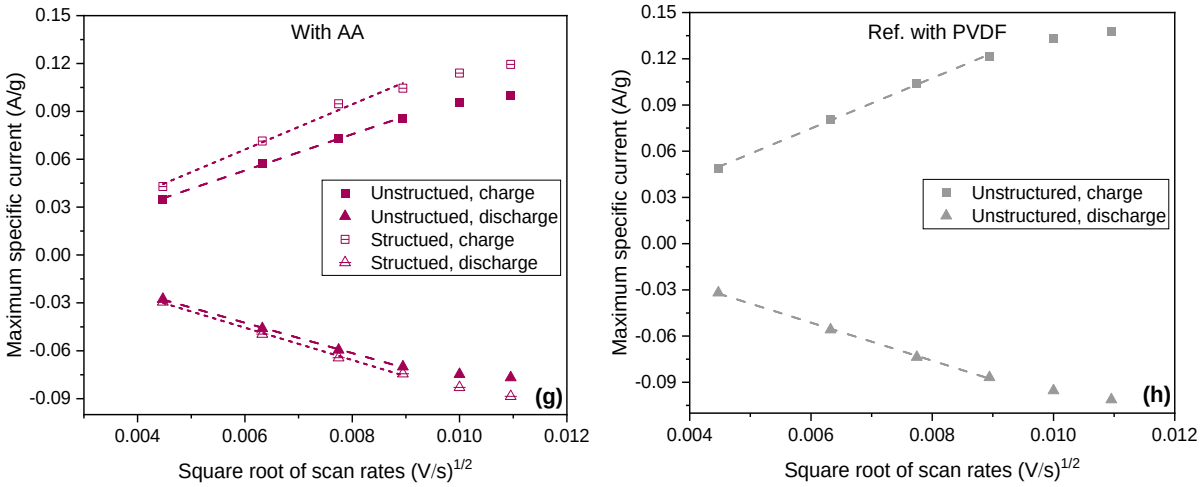

Figure S 9. CV plots of the half-cells containing unstructured NMC 622 electrodes processed with addition of (**a**) CA, (**c**) AA, and (**e**) with PVDF binder. And the CV plots of the cells with laser structured electrodes prepared with addition of (**b**) CA, (**d**) AA. Besides, the maximum specific currents vs. the square root of scan rates of cells containing different electrodes are plotted in (**f**), (**g**), and (**h**).

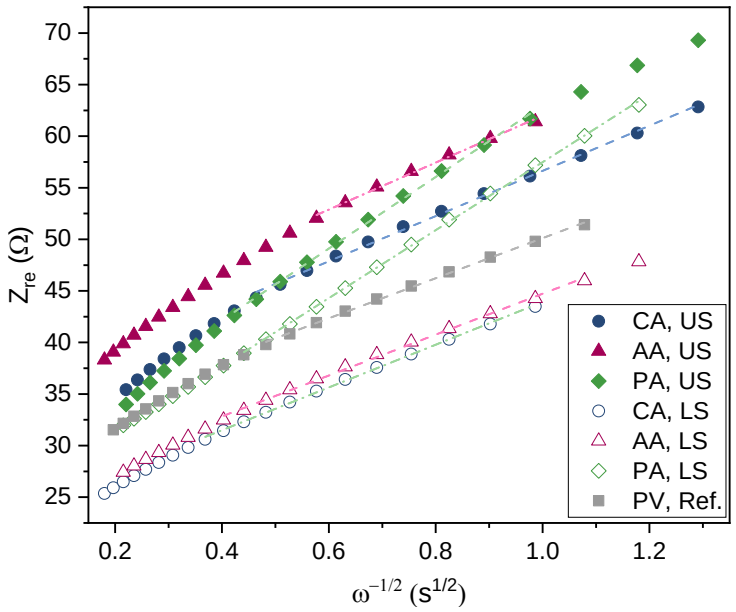

Figure S 10. Relationships between the real impedance Z_{re} [Ω] and $\omega^{-1/2}$ [$s^{1/2}$] at low frequency region for half-cells containing different types of aqueous processed NMC 622 cathodes. “US” indicates cells containing “unstructured” electrodes, while “LS” means cells with “laser structured” electrodes.

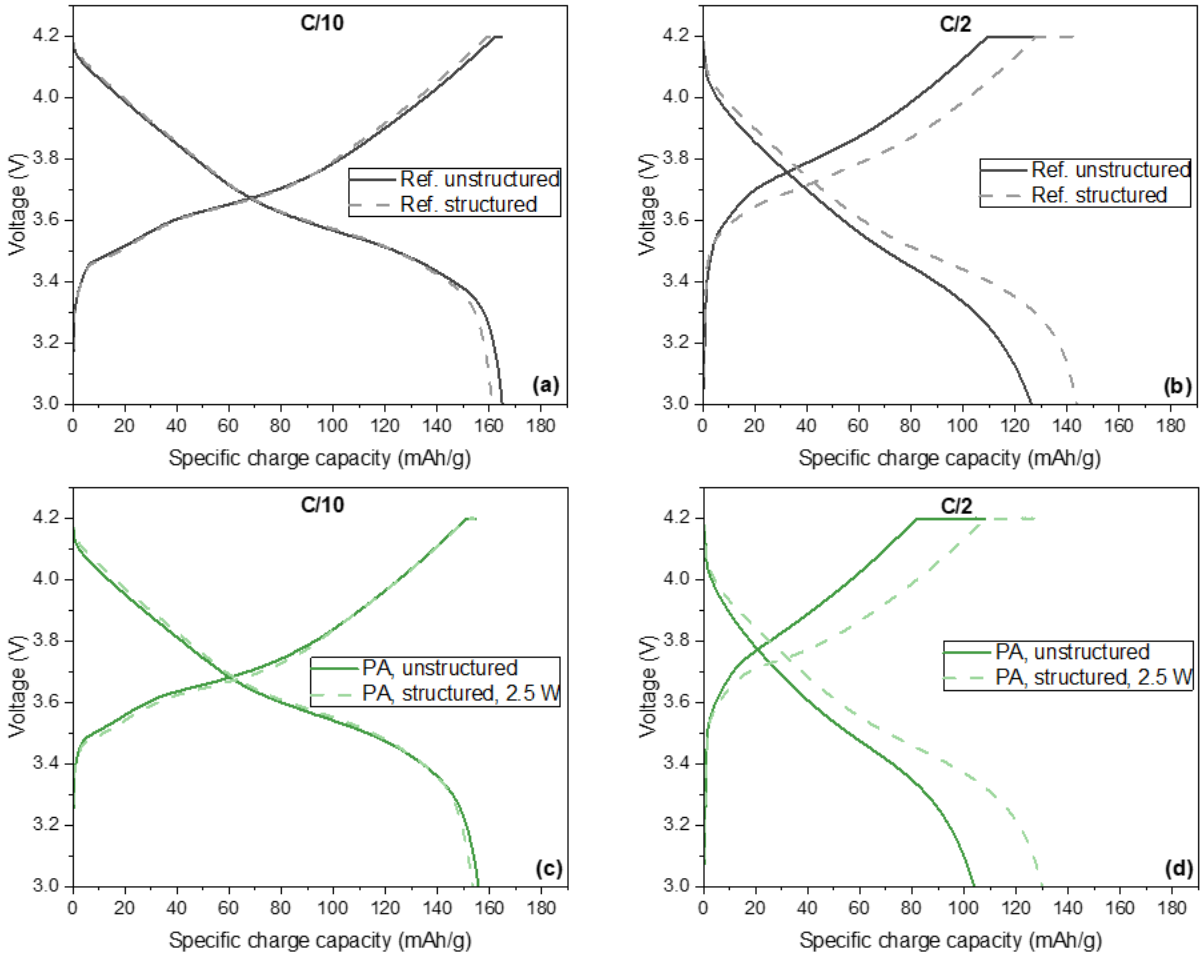

Figure S 11. Discharge profiles of the pouch cells containing unstructured and laser structured reference cathodes with PVDF binder at (**a**) C/10 and (**b**) C/2; And cells containing PA-added cathodes with unstructured and 2.5 W structured at (**c**) C/10 and (**d**) C/2, as well as cells containing laser structured PA-added cathodes with 2.5 W and offset scans in comparison to the cells with unstructured electrodes at (**e**) C/10 and (**f**) C/2.

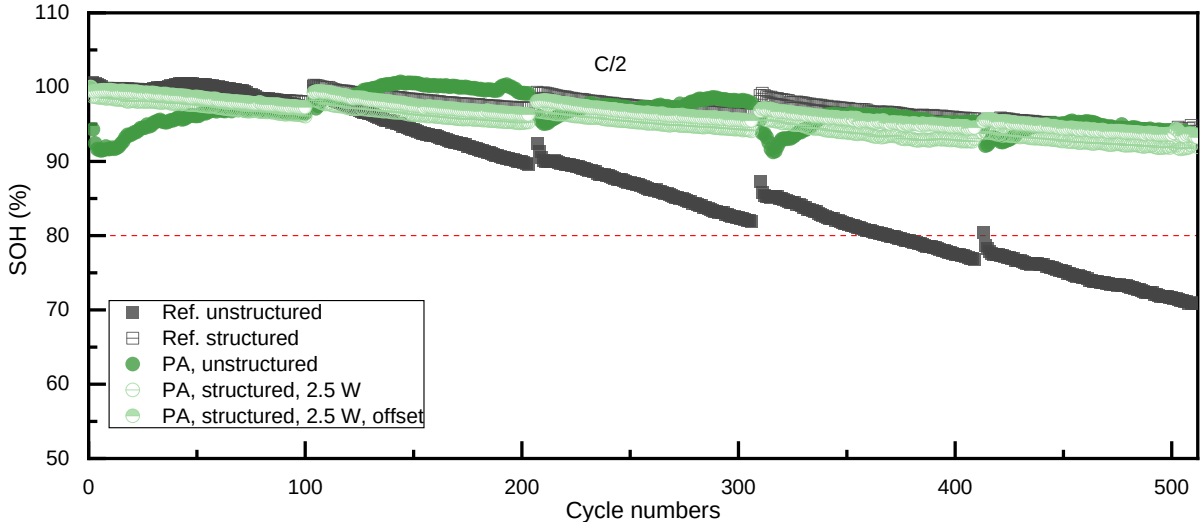

Figure S 12. SOH of the pouch cells containing different types of NMC 622 cathodes (unstructured and laser structured).

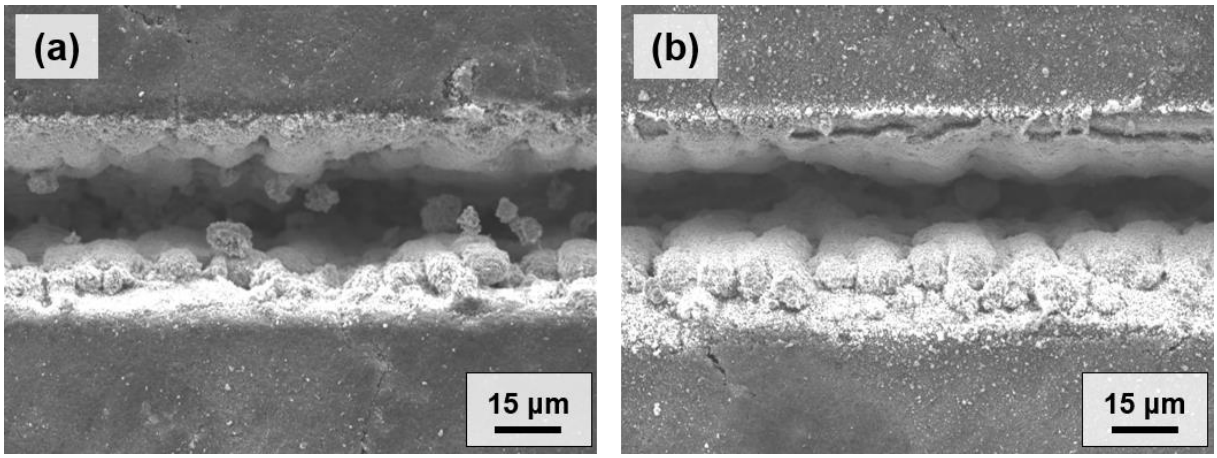

Figure S 13. The laser generated groove structures in the NMC 622 cathodes (**a**) without and (**b**) with a 1 × 5 beam splitter. The laser energy was kept constant at 30 µJ for a single laser beam or for each beamlet after beam splitting.

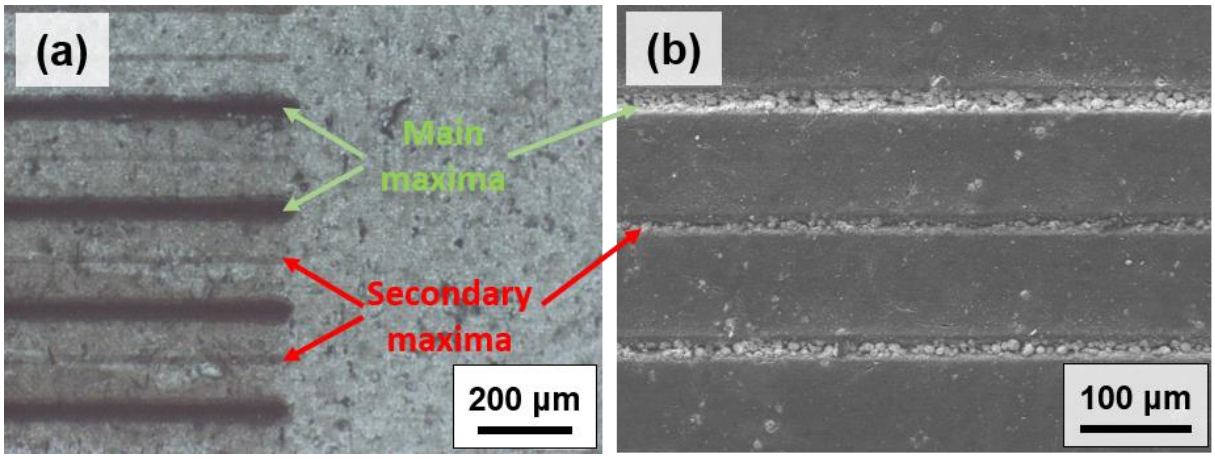

Figure S 14. The main maxima and secondary maxima generated (**a**) on a stainless steel plate (image obtained using an optical microscope) and (**b**) in a NMC 622 cathode (SEM image) after laser ablation process using a 1 × 6 beam splitter.

Table S 1. The fitted charge transfer resistances and obtained parameters for double-layer capacitances derived from the EIS analyses on pouch cells (Figure 5-71) during lifetime analyses. “US” indicates cells with unstructured electrodes, while “LS” means that the cells contain laser structured electrodes.

	With PVDF, US, 0 cycles	**With PVDF, US, 100 cycles**	**With PVDF, US, 200 cycles**	**With PVDF, US, 300 cycles**	**With PVDF, US, 400 cycles**	**With PVDF, US, 500 cycles**	**With PVDF, LS, 0 cycles**	**With PVDF, LS, 100 cycles**	**With PVDF, LS, 200 cycles**	**With PVDF, LS, 300 cycles**	**With PVDF, LS, 400 cycles**	**With PVDF, LS, 500 cycles**
R_1 [Ω]	0.41	0.45	0.56	0.57	1.07	1.18	0.11	0.32	0.33	0.35	0.49	0.34
R_2 [Ω]	0.28	0.29	0.25	0.40	0.17	0.20	0.35	0.30	0.30	0.34	0.42	0.45
Y_1 [$Fs^{\varphi-1}$]	0.02	0.04	0.05	0.04	0.10	0.09	0.02	0.03	0.03	0.03	0.06	0.03
Y_2 [$Fs^{\varphi-1}$]	0.16	0.24	0.25	0.25	0.32	0.32	0.07	0.25	0.27	0.28	0.39	0.32
φ_1 [-]	0.60	0.54	0.50	0.51	0.34	0.33	0.73	0.63	0.62	0.60	0.49	0.62
φ_2 [-]	0.66	0.69	0.78	0.73	0.95	0.95	0.60	0.68	0.72	0.74	0.74	0.73
C_1 [mF]	1.1	1.2	1.3	1.0	1.4	1.2	2.2	1.7	1.7	1.8	1.3	2.2
C_2 [mF]	31.7	73.3	113.9	105.1	275.7	276.7	5.6	72.3	100.0	124.7	205.8	141.8
χ^2 [-]	0.00003	0.00005	0.00003	0.00008	0.00003	0.00003	0.00007	0.00005	0.00004	0.00003	0.00005	0.00010

	With PA, US, 0 cycles	**With PA, US, 100 cycles**	**With PA, US, 200 cycles**	**With PA, US, 300 cycles**	**With PA, US, 400 cycles**	**With PA, US, 500 cycles**	**With PA, LS, 0 cycles**	**With PA, LS, 100 cycles**	**With PA, LS, 200 cycles**	**With PA, LS, 300 cycles**	**With PA, LS, 400 cycles**	**With PA, LS, 500 cycles**
R_1 [Ω]	0.09	0.19	0.26	0.24	0.33	0.37	0.33	0.35	0.35	0.41	0.44	1.12
R_2 [Ω]	0.73	0.81	0.79	0.85	0.75	0.76	0.45	0.55	0.54	0.55	0.53	0.11
Y_1 [$Fs^{\varphi-1}$]	0.01	0.01	0.01	0.01	0.01	0.01	0.01	0.01	0.02	0.02	0.02	0.12
Y_2 [$Fs^{\varphi-1}$]	0.04	0.07	0.08	0.09	0.10	0.11	0.16	0.17	0.19	0.20	0.20	0.29
φ_1 [-]	0.87	0.76	0.72	0.74	0.67	0.66	0.68	0.68	0.66	0.63	0.60	0.32
φ_2 [-]	0.56	0.53	0.54	0.52	0.55	0.56	0.60	0.60	0.60	0.64	0.66	0.90
C_1 [mF]	1.8	1.2	1.0	1.1	0.8	0.8	1.1	1.0	1.0	1.1	1.0	1.6
C_2 [mF]	2.2	5.3	8.1	8.2	11.6	14.7	27.8	36.5	39.2	54.5	66.2	313.9
χ^2 [-]	0.00003	0.00006	0.00007	0.00008	0.00008	0.00007	0.00012	0.00011	0.00012	0.00011	0.00010	0.00006

	With PA, LS, offset, 0 cycles	With PA, LS, offset, 100 cycles	With PA, LS, offset, 200 cycles	With PA, LS, offset, 300 cycles	With PA, LS, offset, 400 cycles	With PA, LS, offset, 500 cycles
R_1 [Ω]	0.28	0.35	0.32	0.36	0.40	0.63
R_2 [Ω]	0.42	0.49	0.52	0.47	0.44	0.30
Y_1 [$Fs^{\varphi-1}$]	0.01	0.01	0.02	0.02	0.02	0.05
Y_2 [$Fs^{\varphi-1}$]	0.22	0.25	0.25	0.25	0.29	0.38
φ_1 [-]	0.69	0.68	0.66	0.66	0.62	0.46
φ_2 [-]	0.52	0.56	0.53	0.61	0.61	0.68
C_1 [mF]	1.2	1.1	1.0	1.1	1.0	0.8
C_2 [mF]	25.2	49.1	41.9	62.2	75.3	140.6
χ^2 [-]	0.00008	0.00008	0.00017	0.00011	0.00010	0.00012

Appendix B

In order to calculate the pressure on the electrode in a CR2032 coin cell with a half-cell configuration vs. Li, the thickness of each cell component was measured and is given in Table S 2.

Table S 2. Thickness of different cell components for CR2032 coin cells.

Cell component	Upper case	Bottom case	Spacer	Wave spring	Lithium
Thickness [µm]	279 ± 4	255 ± 1	486 ± 7	1497 ± 35	250*

* The thickness of lithium foil is derived from the data sheet provided by the supplier.

The displacement of the spring Δx [mm] in the coin cell is calculated as follows:

$$\Delta x = (h_{bot.ca} + h_{up.ca} + 2 \cdot h_{spacer} + h_{elect} + h_{Li} + h_{Sep} + h_{spring} - h_{cell})/1000 \qquad \text{(S1)}$$

where $h_{bot.ca}$ [µm] and $h_{up.ca}$ [µm] is the thickness of the bottom and upper case of the CR2032 coin cell, respectively; h_{spacer} [µm] and h_{elect} [µm] the thickness of the spacer and total thickness of electrode (with current collector) used in the coin cell, respectively; h_{Li} [µm] the thickness of lithium foil, h_{Sep} [µm] the thickness of the separator, h_{spring} [µm] the thickness of spring, and h_{cell} [µm] the total height of the coin cell after sealing. It is assumed that the thickness of other cell components remains constant during the sealing process except for the spring. Thus, for coin cells containing a cathode with a thickness of 150 µm and a wave spring, a Δx of 0.45 ± 0.09 mm is obtained by using the data in Table S 2 into equation (S1).

In order to estimate the pressure on the electrodes in coin cells, the displacement vs. compression curve of the wave spring was measured and fitted using polynomial fitting with 3rd order (Figure S 15). The displacement of 0.45 mm corresponds to a force of 87 – 90 N. Therefore, the pressure applied by the spring on the NMC 622 cathode can be calculated by dividing the force by the electrode surface area (circle with a diameter of 12 mm), which is 0.78 ± 0.10 MPa.

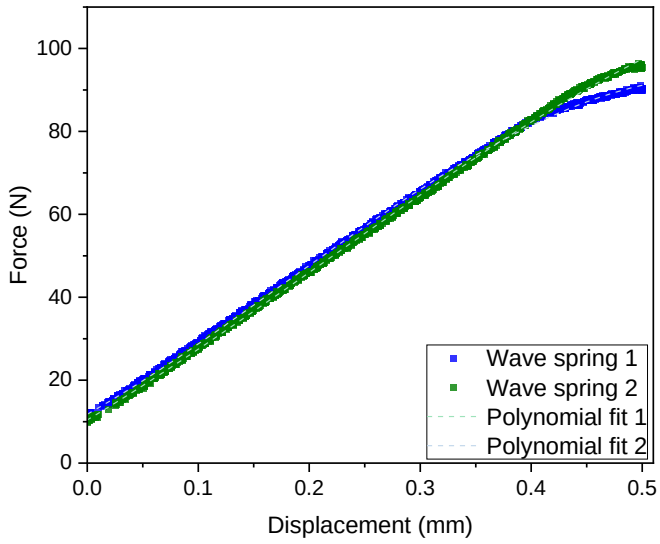

Figure S 15. The force vs. displacement of the wave springs used in CR2032 coin cells and the polynomial fitting of data with 3rd order.

Appendix C

In order to obtain the Ragone plot of pouch cells containing NMC 622 cathodes and graphite anodes (Figure 5-69), the energy density as well as the power density on cell level need to be determined. The gravimetric energy density ED_g [Wh/kg] and volumetric energy density ED_v [Wh/l] are calculated as follows:

$$ED_g = \frac{Q_{cell} \cdot U_{OC}}{m_{cell}} \cdot 1000 \quad \text{S 2}$$

$$ED_v = \frac{Q_{cell} \cdot U_{OC}}{V_{cell}} \quad \text{S 3}$$

where Q_{cell} [Ah] is the cell capacity, U_{OC} [V] the open circuit voltage of the cell, m_{cell} [g] and V_{cell} [l] the total mass and volume of a unit cell, respectively. The Q_{cell} was obtained from the rate capability analyses at different C-rates, while the U_{OC} was 3.6 V for all cells.

The gravimetric power density PD_g [W/kg] and volumetric power density PD_v [W/l] are described as follows:

$$PD_g = \frac{I \cdot U_{OC}}{m_{cell}} \cdot 1000 \quad \text{S 4}$$

$$PD_v = \frac{I \cdot U_{OC}}{V_{cell}} \quad \text{S 5}$$

where I [A] is applied current. The total mass of a unit cell is given as:

$$m_{cell} = m_{Cat} + m_{Ano} + m_{Sep} + m_{Ele} - \frac{1}{2}(m_{Al} + m_{Cu}) \quad \text{S 6}$$

where m_{Cat} [g] is the mass of the cathode with Al foil, m_{Ano} [g] the mass of the anode with Cu foil, m_{Sep} [g] the mass of separator, m_{Ele} [g] the mass of the injected electrolyte, and m_{Al} [g] and m_{Cu} [g] the mass of Al and Cu foil, respectively. By weighing the uncoated current collector, the m_{Al} and m_{Cu} were determined to be 0.120 g and 0.223 g, respectively. The m_{Sep} was 0.043 g, while the total injected electrolyte mass m_{Ele} was 1.166 g (1.1 ml). The measured m_{Cat} and m_{Ano} are summarized in Table S 3 for cells with different types of electrode:

Table S 3. The mass of cathodes and anodes used in different types of pouch cells applied for the calculation of energy density and power density.

Pouch cells type	m_{Cat} [g]	m_{Ano} [g]
Cathode with PVDF binder, unstructured	0.890	0.715
Cathode with PVDF binder, structured	0.872	0.744
Cathode aqueous processed, unstructured	0.895	0.798
Cathode aqueous processed, 2.5 W structured	0.861	0.722
Cathode aqueous processed, 2.5 W + offset structured	0.780	0.707

The total volume of a unit cell is calculated as follows:

$$V_{cell} = A_{foot} \cdot \frac{h_{Cat} + h_{Ano} + h_{Sep} + \frac{1}{2}(h_{Al} + h_{Cu})}{10000} \quad \text{S 7}$$

where A_{foot} [cm^2] is the footprint of the pouch cell (4.9 × 4.9 cm^2), h_{Cat} [µm] and h_{Ano} [µm] the film thickness of the cathode and anode without current collector, respectively; h_{Sep} [µm] the thickness of separator, h_{Al} [µm] and h_{Cu} [µm] the thickness of Al and Cu foil. All the thickness data can be found in chapter 4.5.1 and 5.4.3.

Selbständigkeitserklärung (Statement of authorship)

Hiermit erkläre ich, dass ich die vorliegende Dissertation selbständig angefertigt habe. Es wurden nur die in der Arbeit ausdrücklich benannten Quellen und Hilfsmittel benutzt. Diese Dissertation wurde nicht in gleicher oder ähnlicher Form zur Erlangung einer akademischen Benotung verwendet oder wird anderweitig veröffentlicht.

I hereby declare that I have developed and written this dissertation independently and have not used sources or means without declaration in the text. Any thoughts from others or literal quotations are clearly marked. This dissertation was not used in the same or in a similar version to achieve an academic degree or is being published elsewhere.

Karlsruhe,

Ort, Datum (Location, Date)	Unterschrift (Signature)

List of publications

Patent

1. **P. Zhu,** W. Pfleging, "Elektrodenanordnung und Batterie mit der Elektrodenanordnung", 102023106290.5, Registration date: March 14. 2023.

Publication in journals

1. **P. Zhu**, B. Ebert, P. Smyrek, W. Pfleging, The Impact of Structural Pattern Types on the Electrochemical Performance of Ultra-Thick NMC 622 Electrodes for Lithium-Ion Batteries, Batteries 10 (2024) 58.
2. **P. Zhu**, V. Trouillet, S. Heißler, W. Pfleging, Laser structuring of high mass loaded and aqueous acid processed $Li(Ni_{0.6}Mn_{0.2}Co_{0.2})O_2$ cathodes for lithium-ion batteries, Journal of Energy Storage, 66 (2023) 107401.
3. A. Meyer, **P. Zhu**, A. Smith, W. Pfleging, Gaining a New Technological Readiness Level for Laser-Structured Electrodes in High-Capacity Lithium-Ion Pouch Cells, Batteries, 9(11) (2023) 548.
4. C. Zwahr, N. Serey, L. Nitschke, C. Bischoff, U. Rädel, A. Meyer, **P. Zhu**, W. Pfleging, Targeting new ways for large-scale, high-speed surface functionalization using Direct Laser Interference Patterning in a roll-to-roll process, International Journal of Extreme Manufacturing, 5(3) (2023) 035006.
5. **P. Zhu**, J. Han, W. Pfleging, Characterization and laser structuring of aqueous processed $Li(Ni_{0.6}Mn_{0.2}Co_{0.2})O_2$ thick-film cathodes for lithium-ion batteries, Nanomaterials, 11 (2021) 1840.
6. Z. Song, **P. Zhu**, W. Pfleging, J. Sun, Electrochemical performance of thick-film $Li(Ni_{0.6}Mn_{0.2}Co_{0.2})O_2$ cathode with hierarchic structures and laser ablation, Nanomaterials, 11 (2021) 2962.
7. **P. Zhu**, H.J. Seifert, W. Pfleging, The ultrafast laser ablation of $Li(Ni_{0.6}Mn_{0.2}Co_{0.2})O_2$ electrodes with high mass loading, Applied Sciences, 9 (2019) 4067.

Conference and poster contributions

1. N. Straßburger, **P. Zhu**, & W. Pfleging, (2024, April). Hierarchical structuring of cathodes and anodes for lithium-ion batteries. *Laser Processing for Batteries and Supercapacities* (Paper 13005-20). SPIE.
2. **P. Zhu**, P. Smyrek, B. Ebert, & W. Pfleging, (2023, March). Laser patterning and electrochemical characterization of thick-film cathodes for lithium-ion batteries. *Laser-based Micro-and Nanoprocessing XVII* (Vol. 12409, pp. 92-97). SPIE.
3. W. Pfleging, A. Meyer, U. Rist, P. Smyrek, Y. Sterzl, Y. Zheng, & **P. Zhu**, (2023, March). Laser structuring and functionalization of nanoscaled battery materials. *Nanoscale and*

Quantum Materials: From Synthesis and Laser Processing to Applications 2023 (Vol. 12410, p. 1241002). SPIE.

4. W. Pfleging, P. Smyrek, Y. Zheng, U. Rist, Y. Sterzl, A. Meyer, & **P. Zhu**, (2022, October). 3D Electrode Architectures for High Power and High Energy Lithium-Ion Battery Operation-Recent Approaches and Process Upscaling. *Electrochemical Society Meeting Abstracts 242* (No. 6, pp. 593-593). The Electrochemical Society, Inc..

5. **P. Zhu**, & W. Pfleging (2022, July). Aqueous Processed Thick-Film $Li(Ni_{0.6}Mn_{0.2}Co_{0.2})O_2$ Electrodes with 3D Architectures. *Electrochemical Society Meeting Abstracts 241* (No. 2, pp. 414-414). The Electrochemical Society, Inc..

6. **P. Zhu**, A. Meyer, & W. Pfleging. (2022, March). Ultrafast laser ablation of aqueous processed thick-film $Li(Ni_{0.6}Mn_{0.2}Co_{0.2})O_2$ cathodes with 3D architectures for lithium-ion batteries. *Laser-based Micro-and Nanoprocessing XVI* (Vol. 11989, pp. 116-122). SPIE.

7. A. Meyer, **P. Zhu**, & W. Pfleging. (2021, March). High power ultrafast laser processing of electrodes: Up-scaling in roll-to-roll environment. *Laser-based Micro-and Nanoprocessing XV* (Vol. 11674, p. 116741A). SPIE.

8. **P. Zhu**, A. Meyer, & W. Pfleging. (2021, March). Ultrafast laser structuring $Li(Ni_{0.6}Mn_{0.2}Co_{0.2})O_2$ cathodes for high energy and high power lithium-ion batteries. *Laser-based Micro-and Nanoprocessing XV* (Vol. 11674, p. 116741B). SPIE.

9. A. Meyer, **P. Zhu**, H.J. Seifert, & W. Pfleging. (2020). Recent progress in ultrafast laser structuring of advanced silicon/graphite thick film anodes for Li-ion-cells. *Materials Science and Engineering Congress (MSE 2020), Online, 22.09. 2020–25.09. 2020*.

10. A. Meyer, **P. Zhu**, H.J. Seifert, & W. Pfleging. (2020). Ultrafast Laser Materials Processing of Electrodes for Next Generation Li-Ion Batteries (NextGen-3DBat). *International Battery Seminar and Exhibit (2020), Online, 28.07. 2020–30.07. 2020*.

11. W. Pfleging, P. Smyrek, **P. Zhu**, X. Cheng, Y. Zhang, & Y. Zheng, (2020). Laser Processing of Battery Materials-Process Up-Scaling and Strategies for Tuning of Materials Properties. *14th Laser-based Micro-and Nanoprocessing (2020), San Francisco, CA, USA, 03.02. 2020–06.02. 2020*.

Student research works conducted in conjunction with this thesis

1. Lin Ding, "Manufacturing and characterization of water-based NMC622 cathodes for lithium-ion batteries", master thesis, 04 May 2021, KIT

2. Jiahao Han, "Preparation and characterization of water-based $Li(Ni_{0.6}Mn_{0.2}Co_{0.2})O_2$ thick-film cathodes for Li-ion batteries", master thesis, 18 Feb. 2020, KIT

List of pre-publications with statement of own contribution

1. **P. Zhu**, Y. Sterzl, W. Pfleging, Impact of laser ablation strategies on electrochemical performances of 3D batteries containing aqueous acid processed Li($Ni_{0.6}Mn_{0.2}Co_{0.2}$)O_2 cathodes with high mass loading, Batteries, submitted on 29. Aug. 2024.
   Own contribution: Conceptualization; methodology; validation; investigation; resources; data curation; writing – original draft preparation; writing – review and editing; visualization.

List of figures

List of tables

References

[1] A. Danowitz, K. Kelley, J. Mao, J.P. Stevenson, M. Horowitz, CPU DB: recording microprocessor history, Communications of the ACM, 55 (2012) 55-63.

[2] J. Koomey, S. Berard, M. Sanchez, H. Wong, Implications of historical trends in the electrical efficiency of computing, IEEE Annals of the History of Computing, 33 (2010) 46-54.

[3] M. Armand, P. Axmann, D. Bresser, M. Copley, K. Edström, C. Ekberg, D. Guyomard, B. Lestriez, P. Novák, M. Petranikova, Lithium-ion batteries–Current state of the art and anticipated developments, Journal of Power Sources, 479 (2020) 228708.

[4] B. Dunn, H. Kamath, J.-M. Tarascon, Electrical energy storage for the grid: a battery of choices, Science, 334 (2011) 928-935.

[5] N.E. Parliament, What is carbon neutrality and how can it be achieved by 2050?, (2019) (last access date: 20 Feb. 2023).

[6] J. Wieler, Elektroautos im Test: So hoch ist die Reichweite wirklich, ADAC, (2023) (last access date: 20 Feb. 2023).

[7] W. Zhou, C.J. Cleaver, C.F. Dunant, J.M. Allwood, J. Lin, Cost, range anxiety and future electricity supply: A review of how today's technology trends may influence the future uptake of BEVs, Renewable and Sustainable Energy Reviews, 173 (2023) 113074.

[8] A.M. Andwari, A. Pesiridis, S. Rajoo, R. Martinez-Botas, V. Esfahanian, A review of Battery Electric Vehicle technology and readiness levels, Renewable and Sustainable Energy Reviews, 78 (2017) 414-430.

[9] W. Habla, V. Huwe, M. Kesternich, Electric and conventional vehicle usage in private and car sharing fleets in Germany, Transportation Research Part D: Transport and Environment, 93 (2021) 102729.

[10] J. Li, Z. Du, R.E. Ruther, S.J. An, L.A. David, K. Hays, M. Wood, N.D. Phillip, Y. Sheng, C. Mao, Toward low-cost, high-energy density, and high-power density lithium-ion batteries, Jom, 69 (2017) 1484-1496.

[11] N. Susarla, S. Ahmed, D.W. Dees, Modeling and analysis of solvent removal during Li-ion battery electrode drying, Journal of Power Sources, 378 (2018) 660-670.

[12] J. Pröll, R. Kohler, M. Torge, M. Bruns, M. Przybylski, S. Ulrich, H. Seifert, W. Pfleging, Laser-adjusted three-dimensional Li-Mn-O cathode architectures for secondary lithium-ion cells, Laser-based Micro-and Nanopackaging and Assembly VI, SPIE, (2012), pp. 202-211.

[13] W. Pfleging, J. Pröll, A new approach for rapid electrolyte wetting in tape cast electrodes for lithium-ion batteries, Journal of Materials Chemistry A, 2 (2014) 14918-14926.

[14] R. Kohler, J. Proell, M. Bruns, S. Ulrich, H. Seifert, W. Pfleging, Conical surface structures on model thin-film electrodes and tape-cast electrode materials for lithium-ion batteries, Applied Physics A, 112 (2013) 77-85.

[15] M. Mangang, H. Seifert, W. Pfleging, Influence of laser pulse duration on the electrochemical performance of laser structured $LiFePO_4$ composite electrodes, Journal of Power Sources, 304 (2016) 24-32.

[16] T. Tsuda, N. Ando, K. Matsubara, T. Tanabe, K. Itagaki, N. Soma, S. Nakamura, N. Hayashi, T. Gunji, T. Ohsaka, Improvement of high-rate charging/discharging performance of a lithium ion battery composed of laminated $LiFePO_4$ cathodes/graphite anodes having porous electrode structures fabricated with a pico-second pulsed laser, Electrochimica Acta, 291 (2018) 267-277.

[17] J.B. Habedank, L. Kraft, A. Rheinfeld, C. Krezdorn, A. Jossen, M.F. Zaeh, Increasing the discharge rate capability of lithium-ion cells with laser-structured graphite anodes: Modeling and simulation, Journal of The Electrochemical Society, 165 (2018) A1563.

[18] J.B. Habedank, J. Endres, P. Schmitz, M.F. Zaeh, H.P. Huber, Femtosecond laser structuring of graphite anodes for improved lithium-ion batteries: Ablation characteristics and process design, Journal of Laser Applications, 30 (2018) 032205.

[19] Y. Zheng, H. Seifert, H. Shi, Y. Zhang, C. Kübel, W. Pfleging, 3D silicon/graphite composite electrodes for high-energy lithium-ion batteries, Electrochimica Acta, 317 (2019) 502-508.

[20] R. Schmuch, R. Wagner, G. Hörpel, T. Placke, M. Winter, Performance and cost of materials for lithium-based rechargeable automotive batteries, Nature Energy, 3 (2018) 267-278.

[21] D.L. Wood III, J. Li, C. Daniel, Prospects for reducing the processing cost of lithium ion batteries, Journal of Power Sources, 275 (2015) 234-242.

[22] M. Singh, J. Kaiser, H. Hahn, A systematic study of thick electrodes for high energy lithium ion batteries, Journal of Electroanalytical Chemistry, 782 (2016) 245-249.

[23] Z. Du, D.L. Wood, C. Daniel, S. Kalnaus, J. Li, Understanding limiting factors in thick electrode performance as applied to high energy density Li-ion batteries, Journal of Applied Electrochemistry, 47 (2017) 405-415.

[24] C. Heubner, A. Nickol, J. Seeba, S. Reuber, N. Junker, M. Wolter, M. Schneider, A. Michaelis, Understanding thickness and porosity effects on the electrochemical performance of $LiNi_{0.6}Co_{0.2}Mn_{0.2}O_2$-based cathodes for high energy Li-ion batteries, Journal of Power Sources, 419 (2019) 119-126.

[25] I. Hwang, C.W. Lee, J.C. Kim, S. Yoon, Particle size effect of Ni-rich cathode materials on lithium ion battery performance, Materials Research Bulletin, 47 (2012) 73-78.

[26] R. Chowdhury, Y. Zhao, Y. Xia, M. Ouyang, N. Brandon, A. Banerjee, Revisiting the promise of Bi-layer graded cathodes for improved Li-ion battery performance, Sustainable Energy & Fuels, 5 (2021) 5193-5204.

[27] M. Wood, J. Li, R.E. Ruther, Z. Du, E.C. Self, H.M. Meyer III, C. Daniel, I. Belharouak, D.L. Wood III, Chemical stability and long-term cell performance of low-cobalt, Ni-Rich cathodes prepared by aqueous processing for high-energy Li-Ion batteries, Energy Storage Materials, 24 (2020) 188-197.

[28] S. Li, B. Church, Effect of aqueous-based cathode slurry pH and immersion time on corrosion of aluminum current collector in lithium-ion batteries, Materials and Corrosion, 67 (2016) 978-987.

[29] W. Bauer, F.A. Çetinel, M. Müller, U. Kaufmann, Effects of pH control by acid addition at the aqueous processing of cathodes for lithium ion batteries, Electrochimica Acta, 317 (2019) 112-119.

[30] M. Kuenzel, D. Bresser, T. Diemant, D.V. Carvalho, G.T. Kim, R.J. Behm, S. Passerini, Complementary strategies toward the aqueous processing of high-voltage $LiNi_{0.5}Mn_{1.5}O_4$ lithium-ion cathodes, ChemSusChem, 11 (2018) 562-573.

[31] A. Kazzazi, D. Bresser, A. Birrozzi, J. von Zamory, M. Hekmatfar, S. Passerini, Comparative analysis of aqueous binders for high-energy li-rich NMC as a Lithium-Ion cathode and the impact of adding phosphoric acid, ACS applied materials & interfaces, 10 (2018) 17214-17222.

[32] T. Bashir, S.A. Ismail, Y. Song, R.M. Irfan, S. Yang, S. Zhou, J. Zhao, L. Gao, A review of the energy storage aspects of chemical elements for lithium-ion based batteries, Energy Materials, 1 (2021) 100019.

[33] K. Kubota, M. Dahbi, T. Hosaka, S. Kumakura, S. Komaba, Towards K-ion and Na-ion batteries as "beyond Li-ion", The chemical record, 18 (2018) 459-479.

[34] A. Masias, Lithium-Ion Battery Design for Transportation, Springer International Publishing AG (2018).

[35] R.N. Gonzalez, J.M. Míguez, Y. Xu, A. Laukkanen, O.B. Fernandez, M.G. Agusti, A. Igartua, J.M. Benito, A.Y. Koposov, M. Jahn, M. Kusnezoff, H. Lorrmann, V.D. Noto, K.M. Ryan, P. Mustarelli, A. Frédéric, A.M. Stevenson, T. Bein, S. Christian, F.X. Schwarz, S. Bodoardo, M. Meeus, D. Gloesener, F. Stassin, Roadmap on advanced materials for batteries, European Commission - Website, 2021 (last access date: 25 Feb. 2023).

[36] Z.P. Cano, D. Banham, S. Ye, A. Hintennach, J. Lu, M. Fowler, Z. Chen, Batteries and fuel cells for emerging electric vehicle markets, Nature Energy, 3 (2018) 279-289.

[37] A. Kwade, W. Haselrieder, R. Leithoff, A. Modlinger, F. Dietrich, K. Droeder, Current status and challenges for automotive battery production technologies, Nature Energy, 3 (2018) 290-300.

[38] M.E. Spahr, D. Goers, A. Leone, S. Stallone, E. Grivei, Development of carbon conductive additives for advanced lithium ion batteries, Journal of Power Sources, 196 (2011) 3404-3413.

[39] W. Bauer, D. Nötzel, V. Wenzel, H. Nirschl, Influence of dry mixing and distribution of conductive additives in cathodes for lithium ion batteries, Journal of Power Sources, 288 (2015) 359-367.

[40] X. Qi, B. Blizanac, A. DuPasquier, M. Oljaca, J. Li, M. Winter, Understanding the influence of conductive carbon additives surface area on the rate performance of $LiFePO_4$ cathodes for lithium ion batteries, Carbon, 64 (2013) 334-340.

[41] S. Hein, T. Danner, D. Westhoff, B. Prifling, R. Scurtu, L. Kremer, A. Hoffmann, A. Hilger, M. Osenberg, I. Manke, Influence of conductive additives and binder on the impedance of lithium-ion battery electrodes: effect of morphology, Journal of The Electrochemical Society, 167 (2020) 013546.

[42] S.-L. Chou, Y. Pan, J.-Z. Wang, H.-K. Liu, S.-X. Dou, Small things make a big difference: binder effects on the performance of Li and Na batteries, Physical Chemistry Chemical Physics, 16 (2014) 20347-20359.

[43] M. Bichon, D. Sotta, N. Dupré, E. De Vito, A. Boulineau, W. Porcher, B. Lestriez, Study of immersion of $LiNi_{0.5}Mn_{0.3}Co_{0.2}O_2$ material in water for aqueous processing of positive electrode for Li-ion batteries, ACS applied materials & interfaces, 11 (2019) 18331-18341.

[44] R. Sahore, D.L. Wood III, A. Kukay, K.M. Grady, J. Li, I. Belharouak, Towards understanding of cracking during drying of thick aqueous-processed $LiNi_{0.8}Mn_{0.1}Co_{0.1}O_2$ cathodes, ACS Sustainable Chemistry & Engineering, 8 (2020) 3162-3169.

[45] R. Genieser, S. Ferrari, M. Loveridge, S. Beattie, R. Beanland, H. Amari, G. West, R. Bhagat, Lithium ion batteries (NMC/graphite) cycling at 80 C: Different electrolytes and related degradation mechanism, Journal of Power Sources, 373 (2018) 172-183.

[46] L. Wang, S. Liu, K. Zhao, J. Li, Y. Yang, G. Jia, Improving the rate performance and stability of $LiNi_{0.6}Co_{0.2}Mn_{0.2}O_2$ in high voltage lithium-ion battery by using fluoroethylene carbonate as electrolyte additive, Ionics, 24 (2018) 3337-3346.

[47] L. Liu, Wang, S., Zhang, Z., Fan, J., Qi, W., Chen, S., Fluoroethylene carbonate as an electrolyte additive for improving interfacial stability of high-voltage $LiNi_{0.6}Co_{0.2}Mn_{0.2}O_2$ cathode, Ionics, 25 (2019) 1035-1043.

[48] J. Xia, L. Ma, J. Dahn, Improving the long-term cycling performance of lithium-ion batteries at elevated temperature with electrolyte additives, Journal of Power Sources, 287 (2015) 377-385.

[49] M. Schmidt, U. Heider, A. Kuehner, R. Oesten, M. Jungnitz, N. Ignat'Ev, P. Sartori, Lithium fluoroalkylphosphates: a new class of conducting salts for electrolytes for high energy lithium-ion batteries, Journal of power sources, 97 (2001) 557-560.

[50] S.S. Zhang, A review on electrolyte additives for lithium-ion batteries, Journal of Power Sources, 162 (2006) 1379-1394.

[51] T. Dagger, M. Grützke, M. Reichert, J. Haetge, S. Nowak, M. Winter, F.M. Schappacher, Investigation of lithium ion battery electrolytes containing flame retardants in combination

with the film forming electrolyte additives vinylene carbonate, vinyl ethylene carbonate and fluoroethylene carbonate, Journal of power sources, 372 (2017) 276-285.

[52] H. Lee, M. Yanilmaz, O. Toprakci, K. Fu, X. Zhang, A review of recent developments in membrane separators for rechargeable lithium-ion batteries, Energy & Environmental Science, 7 (2014) 3857-3886.

[53] G. Venugopal, J. Moore, J. Howard, S. Pendalwar, Characterization of microporous separators for lithium-ion batteries, Journal of power sources, 77 (1999) 34-41.

[54] J.A. Morehouse, L.S. Worrel, D.L. Taylor, D.R. Lloyd, B.D. Freeman, D.F. Lawler, The effect of uni-axial orientation on macroporous membrane structure, Journal of Porous Materials, 13 (2006) 61-72.

[55] G.-L. Ji, B.-K. Zhu, Z.-Y. Cui, C.-F. Zhang, Y.-Y. Xu, PVDF porous matrix with controlled microstructure prepared by TIPS process as polymer electrolyte for lithium ion battery, Polymer, 48 (2007) 6415-6425.

[56] D. Djian, F. Alloin, S. Martinet, H. Lignier, Macroporous poly (vinylidene fluoride) membrane as a separator for lithium-ion batteries with high charge rate capacity, Journal of Power Sources, 187 (2009) 575-580.

[57] G.B. Appetecchi, F. Croce, B. Scrosati, High-performance electrolyte membranes for plastic lithium batteries, Journal of power sources, 66 (1997) 77-82.

[58] L.J. Krause, W. Lamanna, J. Summerfield, M. Engle, G. Korba, R. Loch, R. Atanasoski, Corrosion of aluminum at high voltages in non-aqueous electrolytes containing perfluoroalkylsulfonyl imides; new lithium salts for lithium-ion cells, Journal of power sources, 68 (1997) 320-325.

[59] Q. Mao, Y. Liu, Y. Zhao, A review on copper alloys with high strength and high electrical conductivity, Journal of Alloys and Compounds, (2024) 174456.

[60] Y. Gu, J.F. Federici, Fabrication of a flexible current collector for lithium ion batteries by inkjet printing, Batteries, 4 (2018) 42.

[61] M.S. Whittingham, Lithium batteries and cathode materials, Chemical reviews, 104 (2004) 4271-4302.

[62] C. Liu, Z.G. Neale, G. Cao, Understanding electrochemical potentials of cathode materials in rechargeable batteries, Materials Today, 19 (2016) 109-123.

[63] D. Ouyang, J. Weng, M. Chen, J. Wang, Z. Wang, Sensitivities of lithium-ion batteries with different capacities to overcharge/over-discharge, Journal of Energy Storage, 52 (2022) 104997.

[64] R. Gauthier, A. Luscombe, T. Bond, M. Bauer, M. Johnson, J. Harlow, A. Louli, J.R. Dahn, How do depth of discharge, C-rate and calendar age affect capacity retention, impedance growth, the electrodes, and the electrolyte in Li-ion cells?, Journal of The Electrochemical Society, 169 (2022) 020518.

[65] C.M. Julien, A. Mauger, K. Zaghib, H. Groult, Comparative issues of cathode materials for Li-ion batteries, Inorganics, 2 (2014) 132-154.

[66] A.K. Padhi, K.S. Nanjundaswamy, J.B. Goodenough, Phospho‐olivines as positive‐electrode materials for rechargeable lithium batteries, Journal of the electrochemical society, 144 (1997) 1188.

[67] L.-X. Yuan, Z.-H. Wang, W.-X. Zhang, X.-L. Hu, J.-T. Chen, Y.-H. Huang, J.B. Goodenough, Development and challenges of $LiFePO_4$ cathode material for lithium-ion batteries, Energy & Environmental Science, 4 (2011) 269-284.

[68] J. Betz, J.P. Brinkmann, R. Nölle, C. Lürenbaum, M. Kolek, M.C. Stan, M. Winter, T. Placke, Cross talk between transition metal cathode and Li metal anode: unraveling its influence on the deposition/dissolution behavior and morphology of lithium, Advanced energy materials, 9 (2019) 1900574.

[69] M.M. Thackeray, W.I. David, P.G. Bruce, J.B. Goodenough, Lithium insertion into manganese spinels, Materials Research Bulletin, 18 (1983) 461-472.

[70] J.-K. Park, Principles and applications of lithium secondary batteries, John Wiley & Sons (2012).

[71] S. Zhou, H. Han, J. Nie, M. Armand, Z. Zhou, X. Huang, Improving the high-temperature resilience of $LiMn_2O_4$ based batteries: LiFNFSI an effective salt, Journal of The Electrochemical Society, 159 (2012) A1158.

[72] K. Mizushima, P. Jones, P. Wiseman, J.B. Goodenough, $LixCoO_2$ (0< x< -1): A new cathode material for batteries of high energy density, Materials Research Bulletin, 15 (1980) 783-789.

[73] A.R. Armstrong, A.D. Robertson, R. Gitzendanner, P.G. Bruce, The layered intercalation compounds Li $(Mn_{1-y}Co_y)O_2$: positive electrode materials for lithium–ion batteries, Journal of solid state chemistry, 145 (1999) 549-556.

[74] J. Paulsen, C. Thomas, J. Dahn, O2 Structure $Li_{2/3}[Ni_{1/3}Mn_{2/3}]O_2$: A New Layered Cathode Material for Rechargeable Lithium Batteries. I. Electrochemical Properties, Journal of the Electrochemical Society, 147 (2000) 861.

[75] Z. Lu, D. MacNeil, J. Dahn, Layered cathode materials $Li[Ni_xLi_{(1/3-2x/3)}Mn_{(2/3-x/3)}]O_2$ for lithium-ion batteries, Electrochemical and Solid-State Letters, 4 (2001) A191.

[76] Z. Lu, J.R. Dahn, Understanding the anomalous capacity of Li/Li $[Ni_xLi_{(1/3-2x/3)}Mn_{(2/3-x/3)}]O_2$ cells using in situ X-ray diffraction and electrochemical studies, Journal of the Electrochemical Society, 149 (2002) A815.

[77] T. Ohzuku, Y. Makimura, Layered lithium insertion material of $LiNi_{1/2}Mn_{1/2}O_2$: a possible alternative to $LiCoO_2$ for advanced lithium-ion batteries, Chemistry letters, 30 (2001) 744-745.

[78] C. Chen, J. Liu, M. Stoll, G. Henriksen, D. Vissers, K. Amine, Aluminum-doped lithium nickel cobalt oxide electrodes for high-power lithium-ion batteries, Journal of power Sources, 128 (2004) 278-285.

[79] T. Ohzuku, Y. Makimura, Layered lithium insertion material of $LiCo_{1/3}Ni_{1/3}Mn_{1/3}O_2$ for lithium-ion batteries, Chemistry letters, 30 (2001) 642-643.

[80] K. Shaju, G.S. Rao, B. Chowdari, Performance of layered $Li(Ni_{1/3}Co_{1/3}Mn_{1/3})O_2$ as cathode for Li-ion batteries, Electrochimica Acta, 48 (2002) 145-151.

[81] N. Yabuuchi, T. Ohzuku, Novel lithium insertion material of $LiCo_{1/3}Ni_{1/3}Mn_{1/3}O_2$ for advanced lithium-ion batteries, Journal of Power Sources, 119 (2003) 171-174.

[82] Y. Zhu, Y. Huang, R. Du, M. Tang, B. Wang, J. Zhang, Effect of Ni^{2+} on Lithium-ion diffusion in layered $LiNi_{1-x-y}Mn_xCo_yO_2$ materials, Crystals, 11 (2021) 465.

[83] J. Choi, A. Manthiram, Crystal chemistry and electrochemical characterization of layered $LiNi_{0.5-y}Co_{0.5-y}Mn_{2y}O_2$ and $LiCo_{0.5-y}Mn_{0.5-y}Ni_{2y}O_2$ ($0 \leqslant 2y \leqslant 1$) cathodes, Journal of power sources, 162 (2006) 667-672.

[84] M.-H. Kim, H.-S. Shin, D. Shin, Y.-K. Sun, Synthesis and electrochemical properties of $Li[Ni_{0.8}Co_{0.1}Mn_{0.1}]O_2$ and $Li[Ni_{0.8}Co_{0.2}]O_2$ via co-precipitation, Journal of Power Sources, 159 (2006) 1328-1333.

[85] N. Kosova, E. Devyatkina, V. Kaichev, Optimization of Ni^{2+}/Ni^{3+} ratio in layered $Li(Ni,Mn,Co)O_2$ cathodes for better electrochemistry, Journal of power sources, 174 (2007) 965-969.

[86] H.-J. Noh, S. Youn, C.S. Yoon, Y.-K. Sun, Comparison of the structural and electrochemical properties of layered $Li[Ni_xCo_yMn_z]O_2$ (x = 1/3, 0.5, 0.6, 0.7, 0.8 and 0.85) cathode material for lithium-ion batteries, Journal of Power Sources, 233 (2013) 121-130.

[87] W. Ahn, S.N. Lim, K.-N. Jung, S.-H. Yeon, K.-B. Kim, H.S. Song, K.-H. Shin, Combustion-synthesized $LiNi_{0.6}Mn_{0.2}Co_{0.2}O_2$ as cathode material for lithium ion batteries, Journal of Alloys and Compounds, 609 (2014) 143-149.

[88] S. Cui, Y. Wei, T. Liu, W. Deng, Z. Hu, Y. Su, H. Li, M. Li, H. Guo, Y. Duan, Optimized temperature effect of Li-ion diffusion with layer distance in $Li(Ni_xMnyCo_z)O_2$ cathode materials for high performance Li-ion battery, Advanced Energy Materials, 6 (2016) 1501309.

[89] W. Lee, S. Muhammad, T. Kim, H. Kim, E. Lee, M. Jeong, S. Son, J.H. Ryou, W.S. Yoon, New insight into Ni-rich layered structure for next-generation Li rechargeable batteries, Advanced Energy Materials, 8 (2018) 1701788.

[90] Q. Wang, C.-H. Shen, S.-Y. Shen, Y.-F. Xu, C.-G. Shi, L. Huang, J.-T. Li, S.-G. Sun, Origin of structural evolution in capacity degradation for overcharged NMC622 via operando coupled investigation, ACS applied materials & interfaces, 9 (2017) 24731-24742.

[91] S.-J. Cho, C.-C. Chung, S. Podowitz-Thomas, J.L. Jones, Understanding the lithium deficient $Li_xNi_yMn_zCo_{1-y-z}O_2$ (x< 1) cathode materials structure, Materials Chemistry and Physics, 228 (2019) 32-36.

[92] Y. Wei, J. Zheng, S. Cui, X. Song, Y. Su, W. Deng, Z. Wu, X. Wang, W. Wang, M. Rao, Kinetics tuning of Li-ion diffusion in layered $Li(Ni_xMn_yCo_z)O_2$, Journal of the American Chemical Society, 137 (2015) 8364-8367.

[93] A. Van der Ven, G. Ceder, Lithium diffusion in layered Li_xCoO_2, Electrochemical and Solid-State Letters, 3 (2000) 301.

[94] R. Jung, M. Metzger, F. Maglia, C. Stinner, H.A. Gasteiger, Oxygen release and its effect on the cycling stability of $LiNi_xMn_yCo_zO_2$ (NMC) cathode materials for Li-ion batteries, Journal of The Electrochemical Society, 164 (2017) A1361.

[95] J.-H. Kim, K.-J. Park, S.J. Kim, C.S. Yoon, Y.-K. Sun, A method of increasing the energy density of layered Ni-rich $Li[Ni_{1-2x}Co_xMn_x]O_2$ cathodes (x= 0.05, 0.1, 0.2), Journal of materials chemistry A, 7 (2019) 2694-2701.

[96] S. Ahmed, A. Pokle, S. Schweidler, A. Beyer, M. Bianchini, F. Walther, A. Mazilkin, P. Hartmann, T. Brezesinski, J.r. Janek, The role of intragranular nanopores in capacity fade of nickel-rich layered $Li(Ni_{1-x-y}CoxMn_y)O_2$ cathode materials, ACS nano, 13 (2019) 10694-10704.

[97] D. Guerard, A. Herold, Intercalation of lithium into graphite and other carbons, Carbon, 13 (1975) 337-345.

[98] S. Basu, C. Zeller, P. Flanders, C. Fuerst, W. Johnson, J. Fischer, Synthesis and properties of lithium-graphite intercalation compounds, Materials Science and Engineering, 38 (1979) 275-283.

[99] R. Yazami, P. Touzain, A reversible graphite-lithium negative electrode for electrochemical generators, Journal of Power Sources, 9 (1983) 365-371.

[100] R. Fong, U. Von Sacken, J.R. Dahn, Studies of lithium intercalation into carbons using nonaqueous electrochemical cells, Journal of The Electrochemical Society, 137 (1990) 2009.

[101] E. Peled, The electrochemical behavior of alkali and alkaline earth metals in nonaqueous battery systems—the solid electrolyte interphase model, Journal of The Electrochemical Society, 126 (1979) 2047.

[102] P. Verma, P. Maire, P. Novák, A review of the features and analyses of the solid electrolyte interphase in Li-ion batteries, Electrochimica Acta, 55 (2010) 6332-6341.

[103] J. Besenhard, M. Winter, J. Yang, W. Biberacher, Filming mechanism of lithium-carbon anodes in organic and inorganic electrolytes, Journal of Power Sources, 54 (1995) 228-231.

[104] J. Asenbauer, T. Eisenmann, M. Kuenzel, A. Kazzazi, Z. Chen, D. Bresser, The success story of graphite as a lithium-ion anode material–fundamentals, remaining challenges,

and recent developments including silicon (oxide) composites, Sustainable Energy & Fuels, 4 (2020) 5387-5416.

[105] D. Aurbach, B. Markovsky, A. Shechter, Y. Ein-Eli, H. Cohen, A comparative study of synthetic graphite and Li electrodes in electrolyte solutions based on ethylene carbonate-dimethyl carbonate mixtures, Journal of the Electrochemical Society, 143 (1996) 3809.

[106] X. Song, K. Kinoshita, T. Tran, Microstructural characterization of lithiated graphite, Journal of The Electrochemical Society, 143 (1996) L120.

[107] K. Persson, V.A. Sethuraman, L.J. Hardwick, Y. Hinuma, Y.S. Meng, A. Van Der Ven, V. Srinivasan, R. Kostecki, G. Ceder, Lithium diffusion in graphitic carbon, The journal of physical chemistry letters, 1 (2010) 1176-1180.

[108] M. Levi, C. Wang, E. Markevich, D. Aurbach, Z. Chvoj, Noteworthy electroanalytical features of the stage 4 to stage 3 phase transition in lithiated graphite, Journal of Solid State Electrochemistry, 8 (2003) 40-43.

[109] P.P. Magampa, N. Manyala, W.W. Focke, Properties of graphite composites based on natural and synthetic graphite powders and a phenolic novolac binder, Journal of Nuclear Materials, 436 (2013) 76-83.

[110] T. Placke, R. Kloepsch, S. Dühnen, M. Winter, Lithium ion, lithium metal, and alternative rechargeable battery technologies: the odyssey for high energy density, Journal of Solid State Electrochemistry, 21 (2017) 1939-1964.

[111] B.N. Loeffler, D. Bresser, S. Passerini, M. Copley, Secondary lithium-ion battery anodes: From first commercial batteries to recent research activities, Johnson matthey technology review, 59 (2015) 34-44.

[112] D.V. Carvalho, N. Loeffler, G.-T. Kim, M. Marinaro, M. Wohlfahrt-Mehrens, S. Passerini, Study of water-based lithium titanate electrode processing: The role of pH and binder molecular structure, Polymers, 8 (2016) 276.

[113] H. Wu, Y. Cui, Designing nanostructured Si anodes for high energy lithium ion batteries, Nano today, 7 (2012) 414-429.

[114] M.T. McDowell, S.W. Lee, W.D. Nix, Y. Cui, 25th anniversary article: understanding the lithiation of silicon and other alloying anodes for lithium-ion batteries, Advanced Materials, 25 (2013) 4966-4985.

[115] J.W. Choi, D. Aurbach, Promise and reality of post-lithium-ion batteries with high energy densities, Nature Reviews Materials, 1 (2016) 1-16.

[116] J. Yang, Y. Takeda, N. Imanishi, C. Capiglia, J. Xie, O. Yamamoto, SiO_x-based anodes for secondary lithium batteries, Solid State Ionics, 152 (2002) 125-129.

[117] K. Schulmeister, W. Mader, TEM investigation on the structure of amorphous silicon monoxide, Journal of non-crystalline solids, 320 (2003) 143-150.

[118] D. Andre, H. Hain, P. Lamp, F. Maglia, B. Stiaszny, Future high-energy density anode materials from an automotive application perspective, Journal of materials chemistry A, 5 (2017) 17174-17198.

[119] J.B. Goodenough, Y. Kim, Challenges for rechargeable Li batteries, Chemistry of materials, 22 (2010) 587-603.

[120] J.B. Goodenough, K.-S. Park, The Li-ion rechargeable battery: a perspective, Journal of the American Chemical Society, 135 (2013) 1167-1176.

[121] H. Abdi, B. Mohammadi-ivatloo, S. Javadi, A.R. Khodaei, E. Dehnavi, Energy storage systems, Distributed generation systems, 7 (2017) 333-368.

[122] S. Daubner, M. Weichel, D. Schneider, B. Nestler, Modeling intercalation in cathode materials with phase-field methods: Assumptions and implications using the example of $LiFePO_4$, Electrochimica Acta, 421 (2022) 140516.

[123] M. Tang, W.C. Carter, Y.-M. Chiang, Electrochemically driven phase transitions in insertion electrodes for lithium-ion batteries: examples in lithium metal phosphate olivines, Annual Review of Materials Research, 40 (2010) 501-529.

[124] W. Choi, H.-C. Shin, J.M. Kim, J.-Y. Choi, W.-S. Yoon, Modeling and applications of electrochemical impedance spectroscopy (EIS) for lithium-ion batteries, Journal of Electrochemical Science and Technology, 11 (2020) 1-13.

[125] A. Barai, K. Uddin, W.D. Widanage, A. McGordon, P. Jennings, A study of the influence of measurement timescale on internal resistance characterisation methodologies for lithium-ion cells, Scientific reports, 8 (2018) 21.

[126] U. Krewer, F. Röder, E. Harinath, R.D. Braatz, B. Bedürftig, R. Findeisen, Dynamic models of Li-ion batteries for diagnosis and operation: a review and perspective, Journal of the electrochemical society, 165 (2018) A3656.

[127] S.S. Zhang, K. Xu, T. Jow, EIS study on the formation of solid electrolyte interface in Li-ion battery, Electrochimica acta, 51 (2006) 1636-1640.

[128] S. Zhang, K. Xu, T. Jow, Electrochemical impedance study on the low temperature of Li-ion batteries, Electrochimica acta, 49 (2004) 1057-1061.

[129] C. Ho, I. Raistrick, R. Huggins, Application of A-C techniques to the study of lithium diffusion in tungsten trioxide thin films, Journal of The Electrochemical Society, 127 (1980) 343.

[130] H. Xia, L. Lu, G. Ceder, Li diffusion in $LiCoO_2$ thin films prepared by pulsed laser deposition, Journal of Power Sources, 159 (2006) 1422-1427.

[131] U. Westerhoff, K. Kurbach, F. Lienesch, M. Kurrat, Analysis of lithium-ion battery models based on electrochemical impedance spectroscopy, Energy Technology, 4 (2016) 1620-1630.

[132] A. Latz, J. Zausch, Thermodynamic derivation of a Butler–Volmer model for intercalation in Li-ion batteries, Electrochimica Acta, 110 (2013) 358-362.

[133] E.J. Dickinson, A.J. Wain, The Butler-Volmer equation in electrochemical theory: Origins, value, and practical application, Journal of Electroanalytical Chemistry, 872 (2020) 114145.

[134] R. Morasch, H.A. Gasteiger, B. Suthar, Li-Ion Battery Active Material Impedance Analysis I: Comparison of Measured NCM 111 Kinetics with Butler-Volmer Equation Based Predictions, Journal of The Electrochemical Society, 170 (2023) 080522.

[135] M. Doyle, T.F. Fuller, J. Newman, Modeling of galvanostatic charge and discharge of the lithium/polymer/insertion cell, Journal of the Electrochemical society, 140 (1993) 1526.

[136] J.W. Long, B. Dunn, D.R. Rolison, H.S. White, Three-dimensional battery architectures, Chemical Reviews, 104 (2004) 4463-4492.

[137] J. Li, M.C. Leu, R. Panat, J. Park, A hybrid three-dimensionally structured electrode for lithium-ion batteries via 3D printing, Materials & Design, 119 (2017) 417-424.

[138] L. Airoldi, U. Anselmi‐Tamburini, B. Vigani, S. Rossi, P. Mustarelli, E. Quartarone, Additive Manufacturing of Aqueous‐Processed $LiMn_2O_4$ Thick Electrodes for High‐Energy‐Density Lithium‐Ion Batteries, Batteries & Supercaps, 3 (2020) 1040-1050.

[139] P. Zhu, P.R. Slater, E. Kendrick, Insights into architecture, design and manufacture of electrodes for lithium-ion batteries, Materials & Design, 223 (2022) 111208.

[140] L. Li, H. Tan, X. Yuan, H. Ma, Z. Ma, Y. Zhao, J. Zhao, X. Wang, D. Chen, Y. Dong, Direct ink writing preparation of $LiFePO_4$/MWCNTs electrodes with high-areal Li-ion capacity, Ceramics International, 47 (2021) 21161-21166.

[141] V. Gupta, F. Alam, P. Verma, A. Kannan, S. Kumar, Additive manufacturing enabled, microarchitected, hierarchically porous polylactic-acid/Lithium iron phosphate/carbon nanotube nanocomposite electrodes for high performance Li-Ion batteries, Journal of Power Sources, 494 (2021) 229625.

[142] T.P. Plateau, H. Pham, Y. Zhu, M. Leu, J. Park, Enabling Ultrathick Electrodes via a Microcasting Process for High Energy and Power Density Lithium‐Ion Batteries, Advanced Energy Materials, 12 (2022) 2201353.

[143] J. Keilhofer, L.W.F. Schaffranka, A. Wuttke, F.J. Günter, L. Hille, F.A. Dorau, R. Daub, Mechanical Structuring of Lithium‐Ion Battery Electrodes Using an Embossing Roller, Energy Technology, 11 (2023) 2200869.

[144] H. Zhao, Q. Yang, N. Yuca, M. Ling, K. Higa, V.S. Battaglia, D.Y. Parkinson, V. Srinivasan, G. Liu, A convenient and versatile method to control the electrode microstructure toward high-energy lithium-ion batteries, Nano letters, 16 (2016) 4686-4690.

[145] W. Deng, W. Shi, Q. Liu, J. Jiang, X. Li, X. Feng, Constructing gradient porous structure in thick $Li_4Ti_5O_{12}$ electrode for high-energy and stable lithium-ion batteries, ACS Sustainable Chemistry & Engineering, 8 (2020) 17062-17068.

[146] L.L. Lu, Y.Y. Lu, Z.J. Xiao, T.W. Zhang, F. Zhou, T. Ma, Y. Ni, H.B. Yao, S.H. Yu, Y. Cui, Wood-inspired high-performance ultrathick bulk battery electrodes, Advanced Materials, 30 (2018) 1706745.

[147] C. Huang, P.S. Grant, Coral-like directional porosity lithium ion battery cathodes by ice templating, Journal of Materials Chemistry A, 6 (2018) 14689-14699.

[148] C. Huang, M. Dontigny, K. Zaghib, P.S. Grant, Low-tortuosity and graded lithium ion battery cathodes by ice templating, Journal of Materials Chemistry A, 7 (2019) 21421-21431.

[149] D. Parikh, J. Li, Bilayer hybrid graphite anodes via freeze tape casting for extreme fast charging applications, Carbon, 196 (2022) 525-531.

[150] J. Billaud, F. Bouville, T. Magrini, C. Villevieille, A.R. Studart, Magnetically aligned graphite electrodes for high-rate performance Li-ion batteries, Nature Energy, 1 (2016) 1-6.

[151] J. Sander, R.M. Erb, L. Li, A. Gurijala, Y.-M. Chiang, High-performance battery electrodes via magnetic templating, Nature Energy, 1 (2016) 1-7.

[152] S.N. Lauro, J.N. Burrow, C.B. Mullins, Restructuring the Lithium-Ion Battery: A Perspective on Electrode Architectures, eScience, 3 (2023) 100152.

[153] A. Shodiev, M. Chouchane, M. Gaberscek, O. Arcelus, J. Xu, H. Oularbi, J. Yu, J. Li, M. Morcrette, A.A. Franco, Deconvoluting the benefits of porosity distribution in layered electrodes on the electrochemical performance of Li-ion batteries, Energy Storage Materials, 47 (2022) 462-471.

[154] J. Yang, Y. Li, A. Mijailovic, G. Wang, J. Xiong, K. Mathew, W. Lu, B.W. Sheldon, Q. Wu, Gradient porosity electrodes for fast charging lithium-ion batteries, Journal of Materials Chemistry A, 10 (2022) 12114-12124.

[155] X. Zhang, Z. Hui, S.T. King, J. Wu, Z. Ju, K.J. Takeuchi, A.C. Marschilok, A.C. West, E.S. Takeuchi, L. Wang, Gradient architecture design in scalable porous battery electrodes, Nano Letters, 22 (2022) 2521-2528.

[156] M. Wood, J. Li, Z. Du, C. Daniel, A.R. Dunlop, B.J. Polzin, A.N. Jansen, G.K. Krumdick, D.L. Wood Iii, Impact of secondary particle size and two-layer architectures on the high-rate performance of thick electrodes in lithium-ion battery pouch cells, Journal of Power Sources, 515 (2021) 230429.

[157] L.-L. Lu, Y.-Y. Lu, Z.-X. Zhu, J.-X. Shao, H.-B. Yao, S. Wang, T.-W. Zhang, Y. Ni, X.-X. Wang, S.-H. Yu, Extremely fast-charging lithium ion battery enabled by dual-gradient structure design, Science Advances, 8 (2022) eabm6624.

[158] K.B. Hatzell, M.B. Dixit, S.A. Berlinger, A.Z. Weber, Understanding inks for porous-electrode formation, Journal of Materials Chemistry A, 5 (2017) 20527-20533.

[159] S. Tsantilis, S.E. Pratsinis, Soft-and hard-agglomerate aerosols made at high temperatures, Langmuir, 20 (2004) 5933-5939.

[160] J. Mewis, N.J. Wagner, Colloidal suspension rheology, Cambridge university press2012.

[161] A. Saillenfait, F. Gallissot, I. Langonne, J. Sabate, Developmental toxicity of N-methyl-2-pyrrolidone administered orally to rats, Food and Chemical Toxicology, 40 (2002) 1705-1712.

[162] H. Bockholt, W. Haselrieder, A. Kwade, Intensive dry and wet mixing influencing the structural and electrochemical properties of secondary lithium-ion battery cathodes, ECS Transactions, 50 (2013) 25.

[163] B. Nguyen, N. Mariage, R. Fredon, E. Kelder, B. Lestriez, Manufacturing of $LiNi_{0.5}Mn_{1.5}O_4$ positive composite electrodes with industry-relevant surface capacities for lithium ion-cells, Journal of The Electrochemical Society, 162 (2015) A1451.

[164] K.M. Kim, W.S. Jeon, I.J. Chung, S.H. Chang, Effect of mixing sequences on the electrode characteristics of lithium-ion rechargeable batteries, Journal of power sources, 83 (1999) 108-113.

[165] M. Peddi, S.B. Moodakare, M. Kamaraj, G. Sundararajan, G. Raghavan, Effects of Nano-Micro Hierarchical Architecture Intraparticle Connectivity and Carbon Black-$LiNi_{1/3}Mn_{1/3}Co_{1/3}O_2$ Interaction: An Energy-Power Tradeoff In Lithium-Ion Batteries, Journal of The Electrochemical Society, 169 (2022) 020576.

[166] W. Bauer, D. Nötzel, Rheological properties and stability of NMP based cathode slurries for lithium ion batteries, Ceramics International, 40 (2014) 4591-4598.

[167] W.B. Hawley, J. Li, Electrode manufacturing for lithium-ion batteries—Analysis of current and next generation processing, Journal of Energy Storage, 25 (2019) 100862.

[168] G. Kim, S. Jeong, M. Joost, E. Rocca, M. Winter, S. Passerini, A. Balducci, Use of natural binders and ionic liquid electrolytes for greener and safer lithium-ion batteries, Journal of Power Sources, 196 (2011) 2187-2194.

[169] M. Zackrisson, L. Avellán, J. Orlenius, Life cycle assessment of lithium-ion batteries for plug-in hybrid electric vehicles–Critical issues, Journal of cleaner production, 18 (2010) 1519-1529.

[170] A. Meyer, F. Ball, W. Pfleging, The Effect of Silicon Grade and Electrode Architecture on the Performance of Advanced Anodes for Next Generation Lithium-Ion Cells, Nanomaterials, 11 (2021) 3448.

[171] C.-C. Li, J.-T. Lee, Y.-L. Tung, C.-R. Yang, Effects of pH on the dispersion and cell performance of $LiCoO_2$ cathodes based on the aqueous process, Journal of materials science, 42 (2007) 5773-5777.

[172] J.-H. Lee, J.-S. Kim, Y.C. Kim, D.S. Zang, Y.-M. Choi, W.I. Park, U. Paik, Effect of carboxymethyl cellulose on aqueous processing of $LiFePO_4$ cathodes and their electrochemical performance, Electrochemical and Solid-State Letters, 11 (2008) A175.

[173] J. Li, B.L. Armstrong, J. Kiggans, C. Daniel, D.L. Wood, Lithium ion cell performance enhancement using aqueous $LiFePO_4$ cathode dispersions and polyethyleneimine dispersant, Journal of the Electrochemical Society, 160 (2013) A201-A206.

[174] N.P. Pieczonka, V. Borgel, B. Ziv, N. Leifer, V. Dargel, D. Aurbach, J.H. Kim, Z. Liu, X. Huang, S.A. Krachkovskiy, Lithium polyacrylate (LiPAA) as an advanced binder and a passivating agent for high-voltage Li-ion batteries, Advanced Energy Materials, 5 (2015) 1501008.

[175] M. Kuenzel, H. Choi, F. Wu, A. Kazzazi, P. Axmann, M. Wohlfahrt-Mehrens, D. Bresser, S. Passerini, Co-Crosslinked Water-Soluble Biopolymers as a Binder for High-Voltage $LiNi_{0.5}Mn_{1.5}O_4$|Graphite Lithium-Ion Full Cells, ChemSusChem, 13 (2020) 2650-2660.

[176] F.A. Cetinel, W. Bauer, Processing of water-based $LiNi_{1/3}Mn_{1/3}Co_{1/3}O_2$ pastes for manufacturing lithium ion battery cathodes, Bulletin of Materials Science, 37 (2014) 1685-1690.

[177] Q. Wu, S. Ha, J. Prakash, D.W. Dees, W. Lu, Investigations on high energy lithium-ion batteries with aqueous binder, Electrochimica Acta, 114 (2013) 1-6.

[178] Z. Du, K. Rollag, J. Li, S.J. An, M. Wood, Y. Sheng, P. Mukherjee, C. Daniel, D. Wood Iii, Enabling aqueous processing for crack-free thick electrodes, Journal of Power Sources, 354 (2017) 200-206.

[179] R. Demiryürek, N. Gürbüz, G. Hatipoglu, M. Er, H. Malkoc, O. Guleryuz, G. Uyar, D. Uzun, M.N. Ateş, Roll-to-roll manufacturing method of aqueous-processed thick $LiNi_{0.5}Mn_{0.3}Co_{0.2}O_2$ electrodes for lithium-ion batteries, International Journal of Energy Research, 45 (2021) 21182-21194.

[180] I.A. Shkrob, J.A. Gilbert, P.J. Phillips, R. Klie, R.T. Haasch, J. Bareno, D.P. Abraham, Chemical weathering of layered Ni-rich oxide electrode materials: evidence for cation exchange, Journal of The Electrochemical Society, 164 (2017) A1489.

[181] X. Zhang, W. Jiang, X. Zhu, A. Mauger, C. Julien, Aging of $LiNi_{1/3}Mn_{1/3}Co_{1/3}O_2$ cathode material upon exposure to H_2O, Journal of Power Sources, 196 (2011) 5102-5108.

[182] J.h. Park, J.k. Park, J.w. Lee, Stability of $LiNi_{0.6}Mn_{0.2}Co_{0.2}O_2$ as a Cathode Material for Lithium-Ion Batteries against Air and Moisture, Bulletin of the Korean Chemical Society, 37 (2016) 344-348.

[183] Z. Chen, J. Wang, J. Huang, T. Fu, G. Sun, S. Lai, R. Zhou, K. Li, J. Zhao, The high-temperature and high-humidity storage behaviors and electrochemical degradation mechanism of $LiNi_{0.6}Co_{0.2}Mn_{0.2}O_2$ cathode material for lithium ion batteries, Journal of power sources, 363 (2017) 168-176.

[184] L. Azhari, X. Zhou, B. Sousa, Z. Yang, G. Gao, Y. Wang, Effects of Extended Aqueous Processing on Structure, Chemistry, and Performance of Polycrystalline $LiNi_xMn_yCo_zO_2$ Cathode Powders, ACS Applied Materials & Interfaces, 12 (2020) 57963-57974.

[185] W.B. Hawley, A. Parejiya, Y. Bai, H.M. Meyer III, D.L. Wood III, J. Li, Lithium and transition metal dissolution due to aqueous processing in lithium-ion battery cathode active materials, Journal of Power Sources, 466 (2020) 228315.

[186] I. Hamam, N. Zhang, A. Liu, M. Johnson, J. Dahn, Study of the reactions between Ni-rich positive electrode materials and aqueous solutions and their relation to the failure of Li-ion cells, Journal of the Electrochemical Society, 167 (2020) 130521.

[187] M. Hofmann, M. Kapuschinski, U. Guntow, G.A. Giffin, Implications of aqueous processing for high energy density cathode materials: part I. Ni-rich layered oxides, Journal of The Electrochemical Society, 167 (2020) 140512.

[188] C.-H. Jo, D.-H. Cho, H.-J. Noh, H. Yashiro, Y.-K. Sun, S.T. Myung, An effective method to reduce residual lithium compounds on Ni-rich $Li[Ni_{0.6}Co_{0.2}Mn_{0.2}]O_2$ active material using a phosphoric acid derived Li_3PO_4 nanolayer, Nano Research, 8 (2015) 1464-1479.

[189] K. Notake, T. Gunji, H. Kokubun, S. Kosemura, Y. Mochizuki, T. Tanabe, S. Kaneko, S. Ugawa, H. Lee, F. Matsumoto, The application of a water-based hybrid polymer binder to a high-voltage and high-capacity Li-rich solid-solution cathode and its performance in Li-ion batteries, Journal of Applied Electrochemistry, 46 (2016) 267-278.

[190] T. Tanabe, T. Gunji, Y. Honma, K. Miyamoto, T. Tsuda, Y. Mochizuki, S. Kaneko, S. Ugawa, H. Lee, T. Ohsaka, Preparation of water-resistant surface coated high-voltage $LiNi_{0.5}Mn_{1.5}O_4$ cathode and its cathode performance to apply a water-based hybrid polymer binder to Li-ion batteries, Electrochimica Acta, 224 (2017) 429-438.

[191] N. Loeffler, J. von Zamory, N. Laszczynski, I. Doberdo, G.-T. Kim, S. Passerini, Performance of $LiNi_{1/3}Mn_{1/3}Co_{1/3}O_2$/graphite batteries based on aqueous binder, Journal of Power Sources, 248 (2014) 915-922.

[192] M. Kuenzel, D. Bresser, G.-T. Kim, P. Axmann, M. Wohlfahrt-Mehrens, S. Passerini, Unveiling and amplifying the benefits of carbon-coated aluminum current collectors for sustainable $LiNi_{0.5}Mn_{1.5}O_4$ cathodes, ACS Applied Energy Materials, 3 (2019) 218-230.

[193] I. Doberdò, N. Löffler, N. Laszczynski, D. Cericola, N. Penazzi, S. Bodoardo, G.-T. Kim, S. Passerini, Enabling aqueous binders for lithium battery cathodes–Carbon coating of aluminum current collector, Journal of power sources, 248 (2014) 1000-1006.

[194] N. Loeffler, G.T. Kim, F. Mueller, T. Diemant, J.K. Kim, R.J. Behm, S. Passerini, In situ coating of $Li[Ni_{0.33}Mn_{0.33}Co_{0.33}]O_2$ particles to enable aqueous electrode processing, ChemSusChem, 9 (2016) 1112-1117.

[195] M. Heidbüchel, T. Schultz, T. Placke, M. Winter, N. Koch, R. Schmuch, A. Gomez-Martin, Enabling Aqueous Processing of Ni-Rich Layered Oxide Cathode Materials by Addition of Lithium Sulfate, ChemSusChem, 16 (2022) e202202161.

[196] Y. Cui, J. Chen, J. Zhao, Z. Ma, Y. Tan, J. Xue, H. Xu, J. Nan, Aqueous Lithium Carboxymethyl Cellulose and Polyacrylic Acid/Acrylate Copolymer Composite Binder for the $LiNi_{0.5}Mn_{0.3}Co_{0.2}O_2$ Cathode of Lithium-Ion Batteries, Journal of The Electrochemical Society, 169 (2022) 010513.

[197] Z. Chen, G.-T. Kim, D. Chao, N. Loeffler, M. Copley, J. Lin, Z. Shen, S. Passerini, Toward greener lithium-ion batteries: Aqueous binder-based $LiNi_{0.4}Co_{0.2}Mn_{0.4}O_2$ cathode material with superior electrochemical performance, Journal of Power Sources, 372 (2017) 180-187.

[198] K. Sahni, M. Ashuri, Q. He, R. Sahore, I.D. Bloom, Y. Liu, J.A. Kaduk, L.L. Shaw, H_3PO_4 treatment to enhance the electrochemical properties of $Li(Ni_{1/3}Mn_{1/3}Co_{1/3})O_2$ and $Li(Ni_{0.5}Mn_{0.3}Co0.2)O_2$ cathodes, Electrochimica Acta, 301 (2019) 8-22.

[199] L. Ibing, T. Gallasch, A. Friesen, P. Niehoff, A. Hintennach, M. Winter, M. Börner, The role of the pH value in water-based pastes on the processing and performance of Ni-rich $LiNi_{0.5}Mn_{0.3}Co_{0.2}O_2$ based positive electrodes, Journal of Power Sources, 475 (2020) 228608.

[200] I. de Meatza, I. Urdampilleta, I. Boyano, I. Castrillo, I. Landa-Medrano, S. Sananes-Israel, A. Eguia-Barrio, V. Palomares, From Lab to Manufacturing Line: Guidelines for the Development and Upscaling of Aqueous Processed NMC622 Electrodes, Journal of The Electrochemical Society, 170 (1) (2023).

[201] J.R. Tolchard, P.E. Vullum, B. Arstad, N.P. Wagner, New insights into orthophosphoric acid assisted rapid aqueous processing of NMC622 cathodes, RSC Sustainability, 1 (2023) 378-387.

[202] A. Kukay, R. Sahore, A. Parejiya, W.B. Hawley, J. Li, D.L. Wood III, Aqueous Ni-rich-cathode dispersions processed with phosphoric acid for lithium-ion batteries with ultra-thick electrodes, Journal of colloid and interface science, 581 (2021) 635-643.

[203] L. Neidhart, K. Fröhlich, N. Eshraghi, D. Cupid, F. Winter, M. Jahn, Aqueous Manufacturing of Defect-Free Thick Multi-Layer NMC811 Electrodes, Nanomaterials, 12 (2022) 317.

[204] M. Schmitt, M. Baunach, L. Wengeler, K. Peters, P. Junges, P. Scharfer, W. Schabel, Slot-die processing of lithium-ion battery electrodes—Coating window characterization, Chemical Engineering and Processing: Process Intensification, 68 (2013) 32-37.

[205] J. Park, K. Shin, C. Lee, Roll-to-roll coating technology and its applications: A review, International Journal of Precision Engineering and Manufacturing, 17 (2016) 537-550.

[206] P. Zhu, J. Han, W. Pfleging, Characterization and laser structuring of aqueous processed $Li(Ni_{0.6}Mn_{0.2}Co_{0.2})O_2$ thick-film cathodes for lithium-ion batteries, Nanomaterials, 11 (2021) 1840.

[207] S. Jaiser, M. Müller, M. Baunach, W. Bauer, P. Scharfer, W. Schabel, Investigation of film solidification and binder migration during drying of Li-Ion battery anodes, Journal of Power Sources, 318 (2016) 210-219.

[208] F. Font, B. Protas, G. Richardson, J.M. Foster, Binder migration during drying of lithium-ion battery electrodes: Modelling and comparison to experiment, Journal of Power Sources, 393 (2018) 177-185.

[209] M. Stein, A. Mistry, P.P. Mukherjee, Mechanistic understanding of the role of evaporation in electrode processing, Journal of The Electrochemical Society, 164 (2017) A1616.

[210] Y.S. Zhang, J.J. Bailey, Y. Sun, A.M. Boyce, W. Dawson, C.D. Reynolds, Z. Zhang, X. Lu, P. Grant, E. Kendrick, Applications of advanced metrology for understanding the effects of drying temperature in the lithium-ion battery electrode manufacturing process, Journal of Materials Chemistry A, 10 (2022) 10593-10603.

[211] D.L. Wood, J.D. Quass, J. Li, S. Ahmed, D. Ventola, C. Daniel, Technical and economic analysis of solvent-based lithium-ion electrode drying with water and NMP, Drying technology, 36 (2018) 234-244.

[212] H. Bockholt, M. Indrikova, A. Netz, F. Golks, A. Kwade, The interaction of consecutive process steps in the manufacturing of lithium-ion battery electrodes with regard to structural and electrochemical properties, Journal of Power Sources, 325 (2016) 140-151.

[213] E.N. Primo, M. Chouchane, M. Touzin, P. Vázquez, A.A. Franco, Understanding the calendering processability of $Li(Ni_{0.33}Mn_{0.33}Co_{0.33})O_2$-based cathodes, Journal of Power Sources, 488 (2021) 229361.

[214] H. Zheng, L. Tan, G. Liu, X. Song, V.S. Battaglia, Calendering effects on the physical and electrochemical properties of $Li[Ni_{1/3}Mn_{1/3}Co_{1/3}]O_2$ cathode, Journal of Power Sources, 208 (2012) 52-57.

[215] Y. Sheng, C.R. Fell, Y.K. Son, B.M. Metz, J. Jiang, B.C. Church, Effect of calendering on electrode wettability in lithium-ion batteries, Frontiers in Energy Research, 2 (2014) 56.

[216] A. Davoodabadi, J. Li, H. Zhou, D.L. Wood III, T.J. Singler, C. Jin, Effect of calendering and temperature on electrolyte wetting in lithium-ion battery electrodes, Journal of Energy Storage, 26 (2019) 101034.

[217] J. Li, C. Daniel, S.J. An, D. Wood, Evaluation residual moisture in lithium-ion battery electrodes and its effect on electrode performance, MRS advances, 1 (2016) 1029-1035.

[218] Y. Zhang, S. Lu, Z. Wang, V. Volkov, F. Lou, Z. Yu, Recent technology development in solvent-free electrode fabrication for lithium-ion batteries, Renewable and Sustainable Energy Reviews, 183 (2023) 113515.

[219] A. Gyulai, W. Bauer, H. Ehrenberg, Dry Electrode Manufacturing in a Calender: The Role of Powder Premixing for Electrode Quality and Electrochemical Performance, ACS Applied Energy Materials, 6 (2023) 5122-5134.

[220] F. Degen, O. Krätzig, Future in battery production: An extensive benchmarking of novel production technologies as guidance for decision making in engineering, IEEE Transactions on Engineering Management, 71 (2022) 1038-1056.

[221] B. Ludwig, Z. Zheng, W. Shou, Y. Wang, H. Pan, Solvent-free manufacturing of electrodes for lithium-ion batteries, Scientific reports, 6 (2016) 23150.

[222] G. Schälicke, I. Landwehr, A. Dinter, K.-H. Pettinger, W. Haselrieder, A. Kwade, Solvent-Free Manufacturing of Electrodes for Lithium-Ion Batteries via Electrostatic Coating, Energy Technology, 8 (2020) 1900309.

[223] X. Han, M.R. Funk, F. Shen, Y.-C. Chen, Y. Li, C.J. Campbell, J. Dai, X. Yang, J.-W. Kim, Y. Liao, Scalable holey graphene synthesis and dense electrode fabrication toward high-performance ultracapacitors, ACS nano, 8 (2014) 8255-8265.

[224] D.J. Kirsch, S.D. Lacey, Y. Kuang, G. Pastel, H. Xie, J.W. Connell, Y. Lin, L. Hu, Scalable dry processing of binder-free lithium-ion battery electrodes enabled by holey graphene, ACS Applied Energy Materials, 2 (2019) 2990-2997.

[225] H. Ragones, S. Menkin, Y. Kamir, A. Gladkikh, T. Mukra, G. Kosa, D. Golodnitsky, Towards smart free form-factor 3D printable batteries, Sustainable Energy & Fuels, 2 (2018) 1542-1549.

[226] C. Reyes, R. Somogyi, S. Niu, M.A. Cruz, F. Yang, M.J. Catenacci, C.P. Rhodes, B.J. Wiley, Three-dimensional printing of a complete lithium ion battery with fused filament fabrication, ACS Applied Energy Materials, 1 (2018) 5268-5279.

[227] C. Wang, R. Yu, H. Duan, Q. Lu, Q. Li, K.R. Adair, D. Bao, Y. Liu, R. Yang, J. Wang, Solvent-free approach for interweaving freestanding and ultrathin inorganic solid electrolyte membranes, ACS Energy Letters, 7 (2021) 410-416.

[228] M. Al-Shroofy, Q. Zhang, J. Xu, T. Chen, A.P. Kaur, Y.-T. Cheng, Solvent-free dry powder coating process for low-cost manufacturing of $LiNi_{1/3}Mn_{1/3}Co_{1/3}O_2$ cathodes in lithium-ion batteries, Journal of Power Sources, 352 (2017) 187-193.

[229] X. Wu, S. Xia, Y. Huang, X. Hu, B. Yuan, S. Chen, Y. Yu, W. Liu, High-performance, low-cost, and dense-structure electrodes with high mass loading for lithium-ion batteries, Advanced Functional Materials, 29 (2019) 1903961.

[230] L. Ibing, T. Gallasch, P. Schneider, P. Niehoff, A. Hintennach, M. Winter, F.M. Schappacher, Towards water based ultra-thick Li ion battery electrodes–a binder approach, Journal of Power Sources, 423 (2019) 183-191.

[231] K.-Y. Park, J.-W. Park, W.M. Seong, K. Yoon, T.-H. Hwang, K.-H. Ko, J.-H. Han, Y. Jaedong, K. Kang, Understanding capacity fading mechanism of thick electrodes for lithium-ion rechargeable batteries, Journal of Power Sources, 468 (2020) 228369.

[232] W. Pfleging, Recent progress in laser texturing of battery materials: A review of tuning electrochemical performances, related material development, and prospects for large-scale manufacturing, International Journal of Extreme Manufacturing, 3 (2020) 012002.

[233] H. Hügel, T. Graf, Laser in der Fertigung, Vieweg+Teubner, Germany, (2009).

[234] J. Eichler, L. Dünkel, B. Eppich, Die Strahlqualität von Lasern–Wie bestimmt man Beugungsmaßzahl und Strahldurchmesser in der Praxis?, Laser Technik Journal, 1 (2004) 63-66.

[235] D. Lee, J. Suk, Laser cutting characteristics on uncompressed anode for lithium-ion batteries, Energies, 13 (2020) 2630.

[236] J. Chen, D. Tzou, J. Beraun, A semiclassical two-temperature model for ultrafast laser heating, International journal of heat and mass transfer, 49 (2006) 307-316.

[237] L. Lu, Y. Shi, C. Xu, G. Xu, J. Wang, B. Xu, The influence of pulse width and energy on temperature field in metal irradiated by ultrashort-pulsed laser, Physics Procedia, 32 (2012) 39-47.

[238] J. Dutta Majumdar, I. Manna, Laser material processing, International materials reviews, 56 (2011) 341-388.

[239] W. Pfleging, A review of laser electrode processing for development and manufacturing of lithium-ion batteries, Nanophotonics, 7 (2018) 549-573.

[240] H. Hügel, F. Dausinger, Fundamentals of laser-induced processes, Springer (Berlin etc.) (2004).

[241] R. Weber, T. Graf, P. Berger, V. Onuseit, M. Wiedenmann, C. Freitag, A. Feuer, Heat accumulation during pulsed laser materials processing, Optics express, 22 (2014) 11312-11324.

[242] H.J. Eichler, J. Eichler, O. Lux, Lasers: Basics, Advances and Applications, Springer Series in Optical Sciences2018.

[243] P.A. Schmidt, P. Schmitz, M.F. Zaeh, Laser beam welding of electrical contacts for the application in stationary energy storage devices, Journal of Laser Applications, 28 (2016) 022423.

[244] M.J. Brand, P.A. Schmidt, M.F. Zaeh, A. Jossen, Welding techniques for battery cells and resulting electrical contact resistances, Journal of Energy Storage, 1 (2015) 7-14.

[245] T. Sakagawa, S.-i. Nakashiba, H. Hiejima, Laser micro welding system and its application to seam welding of rechargeable battery, Physics Procedia, 12 (2011) 6-10.

[246] M. Kirchhoff, Laser applications in battery production—From cutting foils to welding the case, 2013 3rd international electric drives production conference (EDPC), IEEE, (2013), pp. 1-3.

[247] M. Luetke, V. Franke, A. Techel, T. Himmer, U. Klotzbach, A. Wetzig, E. Beyer, A comparative study on cutting electrodes for batteries with lasers, Physics procedia, 12 (2011) 286-291.

[248] T. Reincke, S. Kreling, K. Dilger, The influences of pulse overlap on cut quality during fiber laser cutting of electrodes for Lithium-ion batteries, Proceedings of the Lasers in Manufacturing Conference, Berlin, Germany, (2015), pp. 22-25.

[249] M.G. Berhe, H.G. Oh, S.-K. Park, D. Lee, Laser cutting of silicon anode for lithium-ion batteries, Journal of Materials Research and Technology, 16 (2022) 322-334.

[250] D. Lee, R. Patwa, H. Herfurth, J. Mazumder, High speed remote laser cutting of electrodes for lithium-ion batteries: Anode, Journal of Power Sources, 240 (2013) 368-380.

[251] C. Vedder, D. Hawelka, M. Wolter, D. Leiva, J. Stollenwerk, K. Wissenbach, Laser-based drying of battery electrode layers, International Congress on Applications of Lasers & Electro-Optics, Laser Institute of America, (2016), pp. N501.

[252] D. Neb, S. Kim, H. Clever, B. Dorn, A. Kampker, Current advances on laser drying of electrodes for lithium-ion battery cells, Procedia CIRP, 107 (2022) 1577-1587.

[253] Y. Zheng, Z. An, P. Smyrek, H. Seifert, T. Kunze, V. Lang, A.-F. Lasagni, W. Pfleging, Direct laser interference patterning and ultrafast laser-induced micro/nano structuring of current collectors for lithium-ion batteries, Laser-based Micro-and Nanoprocessing X, SPIE, (2016), pp. 271-277.

[254] C. Zwahr, N. Serey, L. Nitschke, C. Bischoff, U. Rädel, A. Meyer, P. Zhu, W. Pfleging, Targeting new ways for large-scale, high-speed surface functionalization using Direct Laser Interference Patterning in a roll-to-roll process, International Journal of Extreme Manufacturing, 5(3) (2023).

[255] J. Pröll, R. Kohler, M. Torge, S. Ulrich, C. Ziebert, M. Bruns, H. Seifert, W. Pfleging, Laser microstructuring and annealing processes for lithium manganese oxide cathodes, Applied Surface Science, 257 (2011) 9968-9976.

[256] R. Kohler, W. Pfleging, J. Pröll, Elektrodenmaterial für Lithium-Ionen-Batterien und Verfahren zu seiner Herstellung, in: W.f.g. Eigentum (Ed.), Deutsches Patent- und Markenamt, Germany, (2013), pp. 12.

[257] N. Zhang, Y. Zheng, A. Trifonova, W. Pfleging, Laser structured Cu foil for high-performance lithium-ion battery anodes, Journal of Applied Electrochemistry, 47 (2017) 829-837.

[258] W. Dong, K. Wang, J. Han, Y. Yu, G. Liu, C. Li, P. Tong, W. Li, C. Yang, Z. Lu, Regulating lithium electrodeposition with laser-structured current collectors for stable lithium metal batteries, ACS Applied Materials & Interfaces, 13 (2021) 8417-8425.

[259] J. Pröll, B. Schmitz, A. Niemoeller, B. Robertz, M. Schäfer, M. Torge, P. Smyrek, H. Seifert, W. Pfleging, Femtosecond laser patterning of lithium-ion battery separator materials: impact on liquid electrolyte wetting and cell performance, Laser-based Micro-and Nanoprocessing IX, SPIE, (2015), pp. 329-335.

[260] B. Ketterer, H. Vasilchina, K. Seemann, S. Ulrich, H. Besser, W. Pfleging, T. Kaiser, C. Adelhelm, Development of high power density cathode materials for Li-ion batteries, International Journal of Materials Research, 99 (2008) 1171-1176.

[261] R. Kohler, J. Proell, S. Ulrich, V. Trouillet, S. Indris, M. Przybylski, W. Pfleging, Laser-assisted structuring and modification of $LiCoO_2$ thin films, Laser-based Micro-and Nanopackaging and Assembly III, SPIE, (2009), pp. 69-79.

[262] R. Kohler, P. Smyrek, S. Ulrich, M. Bruns, V. Trouillet, W. Pfleging, Patterning and annealing of nanocrystalline $LiCoO_2$ thin films, J. Optoelectron. Adv. Mater, 12 (2010) 547-552.

[263] R. Kohler, M. Bruns, P. Smyrek, S. Ulrich, M. Przybylski, W. Pfleging, Laser annealing of textured thin film cathode material for lithium ion batteries, Laser-based Micro-and Nanopackaging and Assembly IV, SPIE, (2010), pp. 214-224.

[264] J.B. Habedank, F.J. Günter, N. Billot, R. Gilles, T. Neuwirth, G. Reinhart, M.F. Zaeh, Rapid electrolyte wetting of lithium-ion batteries containing laser structured electrodes: in situ visualization by neutron radiography, The International Journal of Advanced Manufacturing Technology, 102 (2019) 2769-2778.

[265] D. Park, D. Lee, Effect of fluence and multi-pass on groove morphology and process efficiency of laser structuring for 3D electrodes of lithium-ion batteries, Materials, 14 (2021) 1283.

[266] T. Tsuda, Y. Ishihara, T. Watanabe, N. Ando, T. Gunji, N. Soma, S. Nakamura, N. Hayashi, T. Ohsaka, F. Matsumoto, An improved high-rate discharging performance of “unbalanced” $LiFePO_4$ cathodes with different $LiFePO_4$ loadings by a grid-patterned micrometer size-holed electrode structuring, Electrochemistry, 87 (2019) 370-378.

[267] J. Park, S. Hyeon, S. Jeong, H.-J. Kim, Performance enhancement of Li-ion battery by laser structuring of thick electrode with low porosity, Journal of Industrial and Engineering Chemistry, 70 (2019) 178-185.

[268] P. Zhu, H.J. Seifert, W. Pfleging, The ultrafast laser ablation of $Li(Ni_{0.6}Mn_{0.2}Co_{0.2})O_2$ electrodes with high mass loading, Applied Sciences, 9 (2019) 4067.

[269] N. Dunlap, D.B. Sulas-Kern, P.J. Weddle, F. Usseglio-Viretta, P. Walker, P. Todd, D. Boone, A.M. Colclasure, K. Smith, B.J.T. de Villers, Laser ablation of Li-ion electrodes for fast charging: Material properties, rate capability, Li plating, and wetting, Journal of Power Sources, 537 (2022) 231464.

[270] J. Park, C. Jeon, W. Kim, S.-J. Bong, S. Jeong, H.-J. Kim, Challenges, laser processing and electrochemical characteristics on application of ultra-thick electrode for high-energy lithium-ion battery, Journal of Power Sources, 482 (2021) 228948.

[271] M.X. Tran, P. Smyrek, J. Park, W. Pfleging, J.K. Lee, Ultrafast-Laser Micro-Structuring of $LiNi_{0.8}Mn_{0.1}Co_{0.1}O_2$ Cathode for High-Rate Capability of Three-Dimensional Li-ion Batteries, Nanomaterials, 12 (2022) 3897.

[272] R. Dubey, M.D. Zwahlen, Y. Shynkarenko, S. Yakunin, A. Fuerst, M.V. Kovalenko, K.V. Kravchyk, Laser Patterning of High‐Mass‐Loading Graphite Anodes for High‐Performance Li‐Ion Batteries, Batteries & Supercaps, 4 (2021) 464-468.

[273] L. Hille, H.-C. Toepper, C. Schriever, J. Kriegler, J. Keilhofer, M.P. Noecker, M.F. Zaeh, Influence of Laser Structuring and Calendering of Graphite Anodes on Electrode Properties and Cell Performance, Journal of The Electrochemical Society, 169 (2022) 060518.

[274] L. Hille, L. Xu, J. Keilhofer, S. Stock, J. Kriegler, M.F. Zaeh, Laser structuring of graphite anodes and NMC cathodes–Proportionate influence on electrode characteristics and cell performance, Electrochimica Acta, 392 (2021) 139002.

[275] M.-J. Kleefoot, J. Sandherr, M. Sailer, S. Nester, J. Martan, V. Knoblauch, M. Kumkar, H. Riegel, Investigation on the parameter dependency of the perforation process of graphite based lithium-ion battery electrodes using ultrashort laser pulses, Journal of Laser Applications, 34 (2022) 042003.

[276] L. Hille, M.P. Noecker, B. Ko, J. Kriegler, J. Keilhofer, S. Stock, M.F. Zaeh, Integration of laser structuring into the electrode manufacturing process chain for lithium-ion batteries, Journal of Power Sources, 556 (2023) 232478.

[277] Y. Zheng, L. Pfäffl, H.J. Seifert, W. Pfleging, Lithium distribution in structured graphite anodes investigated by laser-induced breakdown spectroscopy, Applied Sciences, 9 (2019) 4218.

[278] Y. Zheng, D. Yin, H.J. Seifert, W. Pfleging, Investigation of Fast-Charging and Degradation Processes in 3D Silicon–Graphite Anodes, Nanomaterials, 12 (2022) 140.

[279] J.B. Habedank, J. Kriegler, M.F. Zaeh, Enhanced fast charging and reduced lithium-plating by laser-structured anodes for lithium-ion batteries, Journal of The Electrochemical Society, 166 (2019) A3940.

[280] J. Kriegler, L. Hille, S. Stock, L. Kraft, J. Hagemeister, J.B. Habedank, A. Jossen, M.F. Zaeh, Enhanced performance and lifetime of lithium-ion batteries by laser structuring of graphite anodes, Applied Energy, 303 (2021) 117693.

[281] L. Schweighofer, B. Eschelmüller, K. Fröhlich, W. Pfleging, F. Pichler, Modelling and Optimisation of Laser-Structured Battery Electrodes, Nanomaterials, 12 (2022) 1574.

[282] D.C. Harris, Lehrbuch der quantitativen Analyse, Springer-Verlag (2014).

[283] W. Gruner, Determination of oxygen in oxides by carrier gas hot extraction analysis with simultaneous CO_x detection, Fresenius' journal of analytical chemistry, 365 (1999) 597-603.

[284] S. Brunauer, P.H. Emmett, E. Teller, Adsorption of gases in multimolecular layers, Journal of the American chemical society, 60 (1938) 309-319.

[285] D. Dollimore, P. Spooner, A. Turner, The BET method of analysis of gas adsorption data and its relevance to the calculation of surface areas, Surface Technology, 4 (1976) 121-160.

[286] M. Balakrishnan, R. John, Impact of Ni metal ion concentration in TiO_2 nanoparticles for enhanced photovoltaic performance of dye sensitized solar cell, Journal of Materials Science: Materials in Electronics, 32 (2021) 5295-5308.

[287] J.H. Scofield, Hartree-Slater subshell photoionization cross-sections at 1254 and 1487 eV, Journal of Electron Spectroscopy and Related Phenomena, 8 (1976) 129-137.

[288] A.J. de Jesus Silva, M.M. Contreras, C.R. Nascimento, M.F. da Costa, Kinetics of thermal degradation and lifetime study of poly(vinylidene fluoride) (PVDF) subjected to bioethanol fuel accelerated aging, Heliyon, 6 (2020).

[289] M. El-Sakhawy, H.-A.S. Tohamy, A. Salama, S. Kamel, Thermal properties of carboxymethyl cellulose acetate butyrate, Cellul. Chem. Technol, 53 (2019) 667-675.

[290] S. El-Sayed, K. Mahmoud, A. Fatah, A. Hassen, DSC, TGA and dielectric properties of carboxymethyl cellulose/polyvinyl alcohol blends, Physica B: Condensed Matter, 406 (2011) 4068-4076.

[291] W. Shen, T.T. Vo, A. Kapoor, Charging algorithms of lithium-ion batteries: An overview, 2012 7th IEEE conference on industrial electronics and applications (ICIEA), IEEE, (2012), pp. 1567-1572.

[292] V. Mueller, R. Kaiser, S. Poller, D. Sauerteig, Importance of the constant voltage charging step during lithium-ion cell formation, Journal of Energy Storage, 15 (2018) 256-265.

[293] M. Jafari, A. Gauchia, S. Zhao, K. Zhang, L. Gauchia, Electric vehicle battery cycle aging evaluation in real-world daily driving and vehicle-to-grid services, IEEE transactions on transportation electrification, 4 (2017) 122-134.

[294] N. Elgrishi, K.J. Rountree, B.D. McCarthy, E.S. Rountree, T.T. Eisenhart, J.L. Dempsey, A practical beginner's guide to cyclic voltammetry, Journal of chemical education, 95 (2018) 197-206.

[295] Y. Denis, C. Fietzek, W. Weydanz, K. Donoue, T. Inoue, H. Kurokawa, S. Fujitani, Study of $LiFePO_4$ by cyclic voltammetry, Journal of the electrochemical society, 154 (2007) A253.

[296] J. Xie, N. Imanishi, T. Matsumura, A. Hirano, Y. Takeda, O. Yamamoto, Orientation dependence of Li–ion diffusion kinetics in $LiCoO_2$ thin films prepared by RF magnetron sputtering, Solid State Ionics, 179 (2008) 362-370.

[297] H.H. Ku, Notes on the use of propagation of error formulas, Journal of Research of the National Bureau of Standards, 70 (1966).

[298] C.D. Quilty, D.C. Bock, S. Yan, K.J. Takeuchi, E.S. Takeuchi, A.C. Marschilok, Probing sources of capacity fade in $LiNi_{0.6}Mn_{0.2}Co_{0.2}O_2$ (NMC622): an operando XRD study of Li/NMC622 batteries during extended cycling, The Journal of Physical Chemistry C, 124 (2020) 8119-8128.

[299] C.D. Quilty, G.P. Wheeler, L. Wang, A.H. McCarthy, S. Yan, K.R. Tallman, M.R. Dunkin, X. Tong, S. Ehrlich, L. Ma, Impact of Charge Voltage on Factors Influencing Capacity

Fade in Layered NMC622: Multimodal X-ray and Electrochemical Characterization, ACS Applied Materials & Interfaces, 13 (2021) 50920-50935.

[300] M. Stein IV, C.-F. Chen, M. Mullings, D. Jaime, A. Zaleski, P.P. Mukherjee, C.P. Rhodes, Probing the effect of high energy ball milling on the structure and properties of $LiNi_{1/3}Mn_{1/3}Co_{1/3}O_2$ cathodes for Li-ion batteries, Journal of electrochemical energy conversion and storage, 13 (2016) 031001.

[301] N. Zhang, J. Li, H. Li, A. Liu, Q. Huang, L. Ma, Y. Li, J.R. Dahn, Structural, Electrochemical, and Thermal Properties of Nickel-Rich $LiNi_xMn_yCo_zO_2$ Materials, Chemistry of Materials, 30 (2018) 8852-8860.

[302] X. Zhang, W. Jiang, A. Mauger, F. Gendron, C. Julien, Minimization of the cation mixing in $Li_{1+x}(NMC)_{1-x}O_2$ as cathode material, Journal of Power Sources, 195 (2010) 1292-1301.

[303] F. Jeschull, Y. Surace, S. Zürcher, G. Lari, M.E. Spahr, P. Novák, S. Trabesinger, Graphite particle-size induced morphological and performance changes of graphite–silicon electrodes, Journal of The Electrochemical Society, 167 (2020) 100535.

[304] B. Ameduri, From vinylidene fluoride (VDF) to the applications of VDF-containing polymers and copolymers: recent developments and future trends, Chemical reviews, 109 (2009) 6632-6686.

[305] P. Zhu, V. Trouillet, S. Heißler, W. Pfleging, Laser structuring of high mass loaded and aqueous acid processed $Li(Ni_{0.6}Mn_{0.2}Co_{0.2})O_2$ cathodes for lithium-ion batteries, Journal of Energy Storage, 66 (2023) 107401.

[306] F. Günter, N. Wassiliadis, State of the art of lithium-ion pouch cells in automotive applications: Cell teardown and characterization, Journal of The Electrochemical Society, 169 (2022) 030515.

[307] K. Edstroem, T. Gustafsson, J.O. Thomas, The cathode–electrolyte interface in the Li-ion battery, Electrochimica Acta, 50 (2004) 397-403.

[308] S.S. Zhang, The effect of the charging protocol on the cycle life of a Li-ion battery, Journal of power sources, 161 (2006) 1385-1391.

[309] S.S. Choi, H.S. Lim, Factors that affect cycle-life and possible degradation mechanisms of a Li-ion cell based on $LiCoO_2$, Journal of Power Sources, 111 (2002) 130-136.

[310] C.L. Li Songyuan, Wang Jingbo, Xiao Rongshi, Huang Ting, Femtosecond Laser Texturing Process for NCM811 Thick Film Cathodes in Lithium Ion Batteryies, Chinese Journal of Lasers, 50 (2023) 1202401-1202401-1202408.

[311] J.C. Gandert, M. Müller, S. Paarmann, O. Queisser, T. Wetzel, Effective Thermal Conductivity of Lithium‐Ion Battery Electrodes in Dependence on the Degree of Calendering, Energy Technology, 11(8) (2023).

[312] F. Matsumoto, M. Yamada, M. Tsuta, S. Nakamura, N. Ando, N. Soma, Review of the structure and performance of through-holed anodes and cathodes prepared with a

picosecond pulsed laser for lithium-ion batteries, International Journal of Extreme Manufacturing, 5 (2022) 012001.

[313] P. Smyrek, T. Bergfeldt, H.J. Seifert, W. Pfleging, Laser-induced breakdown spectroscopy for the quantitative measurement of lithium concentration profiles in structured and unstructured electrodes, Journal of Materials Chemistry A, 7 (2019) 5656-5665.

[314] A. Meyer, P. Zhu, A. Smith, W. Pfleging, Gaining a New Technological Readiness Level for Laser-Structured Electrodes in High-Capacity Lithium-Ion Pouch Cells, Batteries, 9 (2023) 548.

[315] M.G. Berhe, H.G. Oh, S.-K. Park, M. Mondal, D. Lee, Effect of laser-induced groove morphology on the wettability and performance of Lithium-ion batteries, Materials & Design, 231 (2023) 112020.

[316] M. Yamada, N. Soma, M. Tsuta, S. Nakamura, N. Ando, F. Matsumoto, Development of a roll-to-roll high-speed laser micro processing machine for preparing through-holed anodes and cathodes of lithium-ion batteries, International Journal of Extreme Manufacturing, 5 (2023) 035004.

[317] C. Fongy, A.-C. Gaillot, S. Jouanneau, D. Guyomard, B. Lestriez, Ionic vs electronic power limitations and analysis of the fraction of wired grains in $LiFePO_4$ composite electrodes, Journal of the Electrochemical Society, 157 (2010) A885.

[318] M. Rudolph, D.P. Reddy, S.W. Feldberg, A simulator for cyclic voltammetric responses, Analytical chemistry, 66 (1994) 589A-600A.

[319] W. Li, J. Reimers, J. Dahn, In situ x-ray diffraction and electrochemical studies of $Li_{1-x}NiO_2$, Solid State Ionics, 67 (1993) 123-130.

[320] W. Du, A. Gupta, X. Zhang, A.M. Sastry, W. Shyy, Effect of cycling rate, particle size and transport properties on lithium-ion cathode performance, International Journal of Heat and Mass Transfer, 53 (2010) 3552-3561.

[321] A. Soloy, D. Flahaut, J. Allouche, D. Foix, G. Salvato Vallverdu, E. Suard, E. Dumont, L. Gal, F. Weill, L. Croguennec, Effect of particle size on $LiNi_{0.6}Mn_{0.2}Co_{0.2}O_2$ layered oxide performance in Li-Ion batteries, ACS Applied Energy Materials, 5 (2022) 5617-5632.

[322] S. Sheu, C. Yao, J. Chen, Y. Chiou, Influence of the $LiCoO_2$ particle size on the performance of lithium-ion batteries, Journal of power sources, 68 (1997) 533-535.

[323] Y. Ali, N. Iqbal, S. Lee, Simultaneous effect of particle size and location on stress development in the electrodes of lithium‐ion batteries, International Journal of Energy Research, 44 (2020) 12145-12157.

[324] L. Wang, J. Zhao, X. He, J. Gao, J. Li, C. Wan, C. Jiang, Electrochemical impedance spectroscopy (EIS) study of $LiNi_{1/3}Co_{1/3}Mn_{1/3}O_2$ for Li-ion batteries, Int. J. Electrochem. Sci, 7 (2012) 345-353.

[325] J.-M. Atebamba, J. Moskon, S. Pejovnik, M. Gaberscek, On the interpretation of measured impedance spectra of insertion cathodes for lithium-ion batteries, Journal of the Electrochemical Society, 157 (2010) A1218.

[326] D.D. Macdonald, M. Urquidi-Macdonald, Application of Kramers-Kronig Transforms in the Analysis of Electrochemical Systems: I. Polarization Resistance, Journal of the Electrochemical Society, 132 (1985) 2316.

[327] J. Luo, X. Liang, Y. Zhang, C. Liang, H. Yassine, G. Leroy, J.-C. Carru, M. Mascot, Application of the Kramers–Kronig relationships in the electrochemical impedance models fit, Journal of Solid State Electrochemistry, 25 (2021) 2225-2233.

[328] B.-Y. Chang, The Effective Capacitance of a Constant Phase Element with Resistors in Series and Parallel, Available at SSRN 4079679, (2022).

[329] A. Lasia, The origin of the constant phase element, The Journal of Physical Chemistry Letters, 13 (2022) 580-589.

[330] V. Charbonneau, A. Lasia, G. Brisard, Impedance studies of Li^+ diffusion in nickel manganese cobalt oxide (NMC) during charge/discharge cycles, Journal of electroanalytical chemistry, 875 (2020) 113944.

[331] H. Nara, K. Morita, D. Mukoyama, T. Yokoshima, T. Momma, T. Osaka, Impedance analysis of $LiNi_{1/3}Mn_{1/3}Co_{1/3}O_2$ cathodes with different secondary-particle size distribution in lithium-ion battery, Electrochimica Acta, 241 (2017) 323-330.

[332] K.X. Wang, X.H. Li, J.S. Chen, Surface and interface engineering of electrode materials for lithium-ion batteries, Advanced Materials, 27 (2015) 527-545.

[333] A.C. Wagner, N. Bohn, H. Geßwein, M. Neumann, M. Osenberg, A. Hilger, I. Manke, V. Schmidt, J.R. Binder, Hierarchical Structuring of NMC111-Cathode Materials in Lithium-Ion Batteries: An In-Depth Study on the Influence of Primary and Secondary Particle Sizes on Electrochemical Performance, ACS Applied Energy Materials, 3 (2020) 12565-12574.

[334] Z. Song, P. Zhu, W. Pfleging, J. Sun, Electrochemical performance of thick-film $Li(Ni_{0.6}Mn_{0.2}Co_{0.2})O_2$ cathode with hierarchic structures and laser ablation, Nanomaterials, 11 (2021) 2962.

[335] H. Zheng, J. Li, X. Song, G. Liu, V.S. Battaglia, A comprehensive understanding of electrode thickness effects on the electrochemical performances of Li-ion battery cathodes, Electrochimica Acta, 71 (2012) 258-265.

[336] J.-H. Lee, J.-S. Kim, Y.C. Kim, D.S. Zang, U. Paik, Dispersion properties of aqueous-based $LiFePO_4$ pastes and their electrochemical performance for lithium batteries, Ultramicroscopy, 108 (2008) 1256-1259.

[337] X.H. Yang, W.L. Zhu, Viscosity properties of sodium carboxymethylcellulose solutions, Cellulose, 14 (2007) 409-417.

[338] J.-H. Lee, Y.-M. Choi, U. Paik, J.-G. Park, The effect of carboxymethyl cellulose swelling on the stability of natural graphite particulates in an aqueous medium for lithium ion battery anodes, Journal of electroceramics, 17 (2006) 657-660.

[339] V. Michailova, S. Titeva, R. Kotsilkova, E. Krusteva, E. Minkov, Influence of aqueous medium on viscoelastic properties of carboxymethylcellulose sodium, hydroxypropyimethyl cellulose, and thermally pre-gelatinized starch gels, Colloids and Surfaces A: Physicochemical and Engineering Aspects, 149 (1999) 515-520.

[340] P. Liu, M. Zhai, J. Li, J. Peng, J. Wu, Radiation preparation and swelling behavior of sodium carboxymethyl cellulose hydrogels, Radiation Physics and Chemistry, 63 (2002) 525-528.

[341] N. Sukiman, X. Zhou, N. Birbilis, A. Hughes, J. Mol, S. Garcia, X. Zhou, G. Thompson, Durability and corrosion of aluminium and its alloys: overview, property space, techniques and developments, Aluminium Alloys-New Trends in Fabrication and Applications, 5 (2012) 47-97.

[342] B.C. Church, D.T. Kaminski, J. Jiang, Corrosion of aluminum electrodes in aqueous slurries for lithium-ion batteries, Journal of materials science, 49 (2014) 3234-3241.

[343] N. Ogihara, Y. Itou, T. Sasaki, Y. Takeuchi, Impedance spectroscopy characterization of porous electrodes under different electrode thickness using a symmetric cell for high-performance lithium-ion batteries, The Journal of Physical Chemistry C, 119 (2015) 4612-4619.

[344] N. Hornsveld, B. Put, W. Kessels, P. Vereecken, M. Creatore, Plasma-assisted and thermal atomic layer deposition of electrochemically active Li_2CO_3, RSC advances, 7 (2017) 41359-41368.

[345] A.T. Appapillai, A.N. Mansour, J. Cho, Y. Shao-Horn, Microstructure of $LiCoO_2$ with and without "$AlPO_4$" nanoparticle coating: combined STEM and XPS studies, Chemistry of Materials, 19 (2007) 5748-5757.

[346] R. Franke, T. Chassé, P. Streubel, A. Meisel, Auger parameters and relaxation energies of phosphorus in solid compounds, Journal of electron spectroscopy and related phenomena, 56 (1991) 381-388.

[347] X. Zhang, A. Mauger, Q. Lu, H. Groult, L. Perrigaud, F. Gendron, C. Julien, Synthesis and characterization of $LiNi_{1/3}Mn_{1/3}Co_{1/3}O_2$ by wet-chemical method, Electrochimica Acta, 55 (2010) 6440-6449.

[348] E. Flores, P. Novák, U. Aschauer, E.J. Berg, Cation Ordering and Redox Chemistry of Layered Ni-Rich $Li_xNi_{1-2y}Co_yMn_yO_2$: An Operando Raman Spectroscopy Study, Chemistry of materials, 32 (2019) 186-194.

[349] E. Flores, P. Novák, E.J. Berg, In situ and Operando Raman Spectroscopy of Layered Transition Metal Oxides for Li-ion Battery Cathodes, Frontiers in Energy Research, 6 (2018).

[350] C. Julien, Local cationic environment in lithium nickel–cobalt oxides used as cathode materials for lithium batteries, Solid State Ionics, 136 (2000) 887-896.

[351] W.B. Hawley, H.M. Meyer III, J. Li, Enabling aqueous processing for $LiNi_{0.80}Co_{0.15}Al_{0.05}O_2$ (NCA)-based lithium-ion battery cathodes using polyacrylic acid, Electrochimica Acta, 380 (2021) 138203.

[352] E. McCafferty, Lewis acid/Lewis base effects in corrosion and polymer adhesion at aluminum surfaces, Journal of the Electrochemical society, 150 (2003) B342.

[353] J. Mattisson, The Influence of Carboxylic Acid in Packaging Materials, Master of Science Thesis, Lund University, (2016).

[354] D.J. Miller, C. Proff, J. Wen, D.P. Abraham, J. Bareño, Observation of microstructural evolution in Li battery cathode oxide particles by in situ electron microscopy, Advanced Energy Materials, 3 (2013) 1098-1103.

[355] G. Sun, T. Sui, B. Song, H. Zheng, L. Lu, A.M. Korsunsky, On the fragmentation of active material secondary particles in lithium ion battery cathodes induced by charge cycling, Extreme Mechanics Letters, 9 (2016) 449-458.

[356] M. Bolsinger, M. Weller, S. Ruck, P. Kaya, H. Riegel, V. Knoblauch, Selective surface treatment by means of IR-laser–A new approach to enhance the rate capability of cathodes for Li-ion batteries, Electrochimica Acta, 330 (2020) 135163.

[357] X. Yu, A. Manthiram, Electrode–electrolyte interfaces in lithium-based batteries, Energy & Environmental Science, 11 (2018) 527-543.

[358] I. Landa-Medrano, A. Eguia-Barrio, S. Sananes-Israel, S. Lijó-Pando, I. Boyano, F. Alcaide, I. Urdampilleta, I. de Meatza, In situ analysis of NMC｜graphite Li-ion batteries by means of complementary electrochemical methods, Journal of The Electrochemical Society, 167 (2020) 090528.

[359] T. Plattard, N. Barnel, L. Assaud, S. Franger, J.-M. Duffault, Combining a fatigue model and an incremental capacity analysis on a commercial NMC/graphite cell under constant current cycling with and without calendar aging, Batteries, 5 (2019) 36.

[360] C. Weng, Y. Cui, J. Sun, H. Peng, On-board state of health monitoring of lithium-ion batteries using incremental capacity analysis with support vector regression, Journal of Power Sources, 235 (2013) 36-44.

[361] M. Stich, M. Göttlinger, M. Kurniawan, U. Schmidt, A. Bund, Hydrolysis of $LiPF_6$ in carbonate-based electrolytes for lithium-ion batteries and in aqueous media, The Journal of Physical Chemistry C, 122 (2018) 8836-8842.

[362] S.J. An, J. Li, Z. Du, C. Daniel, D.L. Wood III, Fast formation cycling for lithium ion batteries, Journal of Power Sources, 342 (2017) 846-852.

[363] D. Andre, M. Meiler, K. Steiner, H. Walz, T. Soczka-Guth, D. Sauer, Characterization of high-power lithium-ion batteries by electrochemical impedance spectroscopy. II: Modelling, Journal of Power Sources, 196 (2011) 5349-5356.

[364] L. Liang, G. Hu, F. Jiang, Y. Cao, Electrochemical behaviours of SiO_2-coated $LiNi_{0.8}Co_{0.1}Mn_{0.1}O_2$ cathode materials by a novel modification method, Journal of Alloys and Compounds, 657 (2016) 570-581.

[365] M. Heinrich, N. Wolff, N. Harting, V. Laue, F. Röder, S. Seitz, U. Krewer, Physico‐chemical Modeling of a lithium‐ion battery: an ageing study with electrochemical impedance spectroscopy, Batteries & Supercaps, 2 (2019) 530-540.

[366] L.A. Middlemiss, A.J. Rennie, R. Sayers, A.R. West, Characterisation of batteries by electrochemical impedance spectroscopy, Energy Reports, 6 (2020) 232-241.

[367] Y. Sterzl, W. Pfleging, Extending the 3D-battery concept: large areal ultrashort pulsed laser structuring of multilayered electrode coatings, Laser-based Micro-and Nanoprocessing XVII, SPIE, (2023), pp. 114-122.

[368] M. Gafner, S.M. Remund, M.W. Chaja, B. Neuenschwander, High-rate laser processing with ultrashort laser pulses by combination of diffractive elements with synchronized galvo scanning, Advanced Optical Technologies, 10 (2021) 333-352.

[369] B. Neuenschwander, B. Jaeggi, M. Zimmermann, G. Hennig, Influence of particle shielding and heat accumulation effects onto the removal rate for laser micromachining with ultra-short pulses at high repetition rates, International Congress on Applications of Lasers & Electro-Optics, AIP Publishing, (2014), pp. 218-226.

[370] L. Hille, J. Kriegler, A. Oehler, M. Chaja, S. Wagner, M.F. Zaeh, Picosecond laser structuring of graphite anodes—Ablation characteristics and process scaling, Journal of Laser Applications, 35 (2023).

[371] A. Meyer, Y. Sterzl, S. Xiao, U. Rädel, W. Pfleging, Ablation behavior of electrode materials during high power and high repetition rate laser structuring, Laser-based Micro-and Nanoprocessing XVI, SPIE, (2022), pp. 123-132.

[372] M. Trenn, T. Keller, K. Voigt, A. Werwein, K. Lange, C. Heubner, L. Pongratz, Efficiency enhancement of Li-ion battery electrode structuring by pulse burst processing: results of an automated study, Laser-based Micro-and Nanoprocessing XVIII, SPIE, (2024), pp. 124-141.

[373] A. Sikora, L. Gemini, M. Faucon, G. Mincuzzi, Benefits of Femtosecond Laser 40 MHz Burst Mode for Li-Ion Battery Electrode Structuring, Materials, 17 (2024) 881.

[374] P. Zhu, B. Ebert, P. Smyrek, W. Pfleging, The Impact of Structural Pattern Types on the Electrochemical Performance of Ultra-Thick NMC 622 Electrodes for Lithium-Ion Batteries, Batteries, 10 (2024) 58.